Frequency Stabilization of 4.7 THz Quantum Cascade Lasers

Doctoral Thesis

Accepted by the
Faculty of Mathematics and Natural Sciences
of the University of Cologne

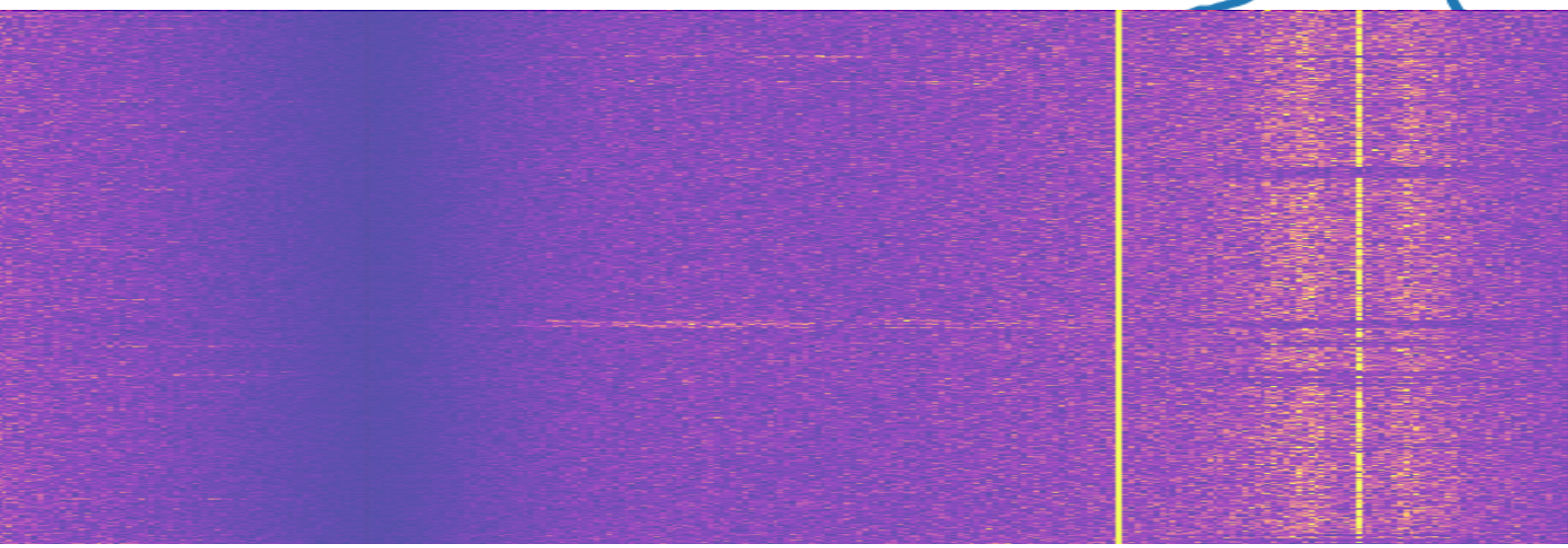

Sajjad Mahdizadeh
from Qom, Iran

I. Physikalisches Institut
Universität zu Köln

November 2023

Eidesstattliche Versicherung

Hiermit versichere ich an Eides statt, dass ich die vorliegende Arbeit selbstständig und ohne die Benutzung anderer als der angegebenen Hilfsmittel angefertigt habe. Alle Stellen, die wörtlich oder sinngemäß aus veröffentlichten und nicht veröffentlichten Schriften entnommen wurden, sind als solche kenntlich gemacht. Die Arbeit ist in gleicher oder ähnlicher Form oder auszugsweise im Rahmen einer anderen Prüfung noch nicht vorgelegt worden. Ich versichere, dass die eingereichte elektronische Fassung der eingereichten Druckfassung vollständig entspricht.

Die Strafbarkeit einer falschen eidesstattlichen Versicherung ist mir bekannt, namentlich die Strafandrohung gemäß § 156 StGB bis zu drei Jahren Freiheitsstrafe oder Geldstrafe bei vorsätzlicher Begehung der Tat bzw. gemäß § 161 Abs. 1 StGB bis zu einem Jahr Freiheitsstrafe oder Geldstrafe bei fahrlässiger Begehung.

Sajjad Mahdizadeh

Köln, den 18.06.2023

reviewers:

Prof. Dr. Jürgen Stutzki
Prof. Dr. Andreas Eckart

Disputation: 20. Sep 2023

Dedicated to

Roya: my best friend, my love, who has walked every step of this journey with me.

To my Mom and Dad, who gave me the gift of dreams and the ability to realize them

To my brother, Yasin, and my sister, Kosar, their constant love and joy empowers me.

and

To those who have inspired me, and saw in me what I failed to see in myself:
My Mom, Daii Yaser, Mr. Mehri, Javad Kazemi, Richard, Urs and Al-Biruni

Acknowledgment

My warmest gratitude to Prof. Dr. Jürgen Stutzki for his support during my Ph.D. years. Jürgen has a vast area of expertise including instrumentation. In the seven years that I have been in his group, I mostly saw him in the astronomer and manager mode, having the steam and courage to lead his team to make the GREAT running, and even now after his retirement, to run the wheel of CCAT-prime/FYST telescope. His deep kindness and belief in me became more apparent as time passed. My deepest thanks to Dr. Urs Graf, for being way more than a supervisor, he was a 2nd father for me. Hundreds of times I have admired your knowledge and expertise in astronomical instrumentation; it was amazing to see how you understand a radio telescope/receiver from the hardware, measurement, and physical point of view. You were available with extreme patience and care beyond a supervisor for a Ph.D. student. My special thanks to Dr. Matthias Justen, for being such a nice and supportive postdoc to work with. I have definitely enjoyed our discussions about the challenges that we faced in the lab. You were indeed a pillar of the receiver group, and your views, perceptions, and advice had a big impact on this work. I would also like to thank Prof. Dr. Andreas Eckart, for accepting the role of the reviewer for this thesis, but also for inspiring me, as an honorable, humble, and professional scientist. I appreciate Prof. Dr. Thomas Michely for accepting the chair role for my disputation and thank Prof. Dr. Lucas Labadie for being on my thesis advisory committee and for the valuable comments I received from him.

Seven years of Ph.D. is a long time, and I was fortunate to get to know many people and enjoy the time with them. My office mate Pablo Tapia was a kind help when I moved to Germany. The company of (now Dr.) Marc Mertens and (now Dr.) Xiaodong Ren was great; quality chats while drinking "club-mate" in summer or Chinese tee in the winter afternoons. After COVID, to be able to keep the laboratory work alive while keeping the distance, and partially for the need for deep work, I moved from the office to the receiver lab. Kateryna Vynokurova joined the receiver group later, like a new breath into the air, passionate and enthusiastic. Among students of the detector group, I recall great memories of (now Dr.) Johanna Böhm, Sina Widdig, (now Dr.) Sina Fathi and Ignacio Barrueto (Nacho). Dr. Netty Honingh, detector group's leader, I am so grateful for our instructive discussions, and your inspiring scientist character. Dr. Karl Jakobs, in the few discussions that I had the chance of, was door-opening. More from the detector group thanks to technicians Michael and Stephan, for their

help, like handling pure Helium for the compressor. I would like to name the astronomers of Jürgen's group. Dr. Ronan Higgins, please accept my deepest gratitude for all the discussions, and support and also for proofreading this thesis. Priv. Doz. Dr. Volker Ossenkopf-Okada, is indeed an inspiring scientist to me that I learned a lot from. There are many others, from whom I also learned and enjoyed time with. I can name Aleena, Christian, Craig, Monika, Parit, Yoko and many more. Among other colleagues, I would like to thank Dr. Frank Lewen, for his generosity and helpful discussions, and especially for giving me the mixers that I used for my experiments. Dr. Frank Schlöder is always available with his expertise and unconditional institution-wide support. During methanol spectroscopy I also had nice discussions with Dr. Sven Thorwirth and Prof. Dr. Stephan Schlemmer. I am grateful to you all.

Another wonderful colleague's team which I have been enjoying being with them is Urs's engineering team. This includes Ayyaz Mahmood, Bernhard Schmidt, Hanna Krüger, Henning Adams, Lars Weikert, Peter Rossman and Sasha Varghese, together with another engineer of institute Micheal Wiest. With some of them I have spent lots of quality time, especially while developing the cryostat; screw by screw and nut by nut. It has been amazing that lots of instrumentation is developed and built in-house, and that is impossible without our mechanical and electrical workshops, from which I would like to mention and thank Alireza, Aree, Christoph, Damian, Julian, Jürgen, Marcus, Markus, Michael, Michael, Pandalis, Thomas and Uwe. I especially enjoyed working with Damian Beaujean, a very passionate technician, who once repaired my rotary vacuum pump by opening it to its heart just in front of my eyes. Working 7 years in a nice atmosphere is never possible without a group of supportive administrative staff. My gratitude to all the work they did and the support they provided for me as a colleague, plus those I specifically needed, when I moved to Germany: Bettina, Isabelle, Maria, Matteo, Petra, Stefanie, Susanne, Tanja and Theresa. Much of the work done in this thesis was only possible in the light of relevant in-depth books. My warm gratitude to our cooperative librarian, Ute Graffenberger, for all her support to me, buying and borrowing books, which opened my way in this project. Thank you very much, all.

Finishing my Ph.D. could never have come to reality, if I had not started journaling and practicing self and project management by being part of a Scrum work group. For two years during the pandemic, we started our day with an online meeting, reviewing our work progress and status, and planning the day. For this a big thanks to Roya (more to come), Zahra who introduced Scrum to us, to Alvaro and Veena, and later on joining Andreas. I learned a lot during that time, and I deeply miss it now. SBF 956 offered a great networking and

collaborating opportunity within the institute since I have started. Among them are colloquiums and student seminars and all-members and student retreats. I could join the SFB student retreats to Leiden and Prague to shape nice memories with my fellow students. To these memorable events, I can add the Nowruz, and Yalda, Persian celebrations, and also Onam that we observed together with Indian/Kerala friends with Veena in the center. I also remember baking different Persian confectioneries like Qhorabieh, Shirini Keshmeshi, Naan-e-Berenji, and Shirini Nokhodchee, on the occasions of good news from my Ph.D., like the day I handed in the thesis, or the day I submitted my first paper. I will definitely miss the luxury of having amazing cafes and restaurants in Cologne. The Persian cafe-confectionery Nobel (I am a worthy competitor now), the Turkish restaurant Sultan, and the Meister Gerhard, where we gathered and celebrated for our group Christmas parties.

During my Ph.D. years, I used to listen to some of the courses from some best lecturers from Iran, available on the Maktabkhoone website. I am grateful to their team, and especially to the courses: Radio Frequency Integrated Circuits by Dr. Mehrdad Sharif Bakhtiar (I extremely enjoyed and learned from this course, especially about the PLL), Optoelectronics by Prof. Dr. Vahid Ahmadi (I learned about solid-state lasers), and Solid State Devices by Dr. Reza Sarvari (Such a great teacher, making me loud laughing while biking to uni and listening to his lecture). The fourth lecture series was the Analog Circuit Design by Prof. Dr. Ali Hajimiri (on YouTube, I learned about noise analysis there). During the years I visited Sharif University for few times and my warm thanks to Dr. Mehrdad Sharif Bakhtiar, for the time he spent once to discussing my Ph.D. project.

I could not write this acknowledgment without mentioning the RadioJove project and the fundamental role it played in my professional career path. I was a teenager when I got to know about it, and I was very lucky to start to develop my own radio telescope for 15-meter wavelength (It is 5 orders of magnitude different from 63 μm in this work). I am grateful to this project, and especially to Richard for his generous support. During the last year of Ph.D., I joined a help telecon of RadioJove project and learned about IF band measurement with SDRs, I needed and used that idea a few weeks later in the lab (see title page), a great example of what you learn for your own interest becoming almost an immediate help in your project. I can not forget the summer times of my youth ages, working in a radio-television repair shop, under the supervision of Mr. Hosseini (calling him "Oosta"), which was definitely a relevant experience for taking steps into radio astronomy.

Participating in different symposiums and meetings was a great chance during

these years. I took part in ISSTTs in Cologne (hosting), in Gothenburg (Sweden), and in Beaze (Spain). They were all amazing experiences, fruitful with seeing high-impact developments and credible scientists from around the globe that initiated collaborations within my Ph.D. project. Memories of getting lost in Gothenburg and the astonishing Flamenco performance we remember; Johanna, Sina, Marc, Matthias, Netty, Urs, Xiaodong, Nacho, and Roya. I should specifically thank the organizers of ISSTT 2022 in Baeza (José V. Siles and colleagues), for holding such a well-coming symposium that upgraded our expectations, thank you! The online meeting option for many SOFIA and FYST projects made it feasible for me to attend them, credit of the COVID virus. I would like to name and thank Dr. Andrey Khudchenkov and Dr. Demitry Paveliev for visiting us at some stages. Demitry thank you for providing us with the Superlattice devices and helping us with setting them up. Andrey thank you for your help on the very first phase lock that we did together, that was a point of confidence for me, believing that despite the problems, the challenges are possible to overcome.

The chance to teach the master's experimental course: "Radio Astronomy with a satellite dish", was good practice for me. I would like to thank Urs and Frank for giving me this opportunity in the last four years. I would also like to mention the experience of "Schnupper Praktikum" which aims to familiarize 10th-grade school girls with physics and studying physics at university, I took the role of experiment developer for one of these events. It was also a pleasure to get to know about a group of astronomers who are concerned about our planet. With this, I would like to thank Dr. Leonard Burtscher for giving an online talk for our institute and giving me the opportunity to know and interact with other astronomers to share about what is happening to our planet: "There is really no planet B!" In the last year of my Ph.D., I got to know Mr. Azarinejad (koodakroosta.ir) and it was a pleasure for me to join him for a rural trip depth into the Zagros ridge from Dehdasht, and it was such a touching experience to bring telescopes and a microscope to the rural kids and to tell and share about science to them. I am grateful to him for making this experience possible. I am also grateful to the people and kids of Zagros, for sharing their simplicity, friendliness, and honesty with me.

I would like to thank (now Dr.) Mahya Sadaghiani, for being a great company in expanding the borders. Among them, the legendary memory of moping and vacuum cleaning the stairs of the astrophysics institute for the DFG/SFB evaluation in 2017 is a highlight. Stairs still witness our extreme effort on that day, and the next time that I became aware of stairs getting proper cleaning, was only October this year (2023). We share many astrophotography nights, like the one in Unicenter when German police came after a neighbor called to report

our suspicious activity! The police ended up staying with us watching the lunar eclipse until after midnight. Thank you so much Mahya for all that makes you unique. Memories of stargazing and astrophotography Roya and I share, (now Dr.) Tianwai Zang on a visit to Tenerife National Park. Tianwai thank you for your company! The PhD years were also fruitful in terms of bright comets passing by with Neuwise in 2020, and ZTF and Nishimura in 2023! Special thanks to Roya for always being up to drive hundreds of kilometers away to hunt them.

It is not all about what went well, but also what went wrong and difficult. I would like to mention the headache and fear of finding an apartment when I moved to Cologne, only a few times getting close to the danger of staying under the bridge!! Thank you so much Pablo and Mathias for accommodating us generously at your places, and a big thanks to Jürgen, for calling the head of the dormitory office. Only after you called them, they made a contract with us on a Sunday afternoon!! (Are they doing their job only when they have to, with some external authority coming to act?) After that, a bitter thanks to the Unicenter's dormitory section powered by Kölner Studentenwerk for drilling for two years, 7 a.m. every morning into the concrete Unicenter structure in that endless renovation activities making a nightmare for all the habitats, and for once putting the key into the door and illegal attempt on entering our property at around 7:30 am!

I can also not forget the damaged window of our apartment, making our place cold for the 2022/23 winter while writing this thesis. A bitter thanks to our dishwasher and washing machine for making lots of quality trouble for us. The troubles of relying on temporary residence permits and extending them come on top, especially when we had to travel to Bergheim for that, taking at least half a day. Coming to the lab the next morning and missing a simple voltmeter, a poor piece of cable, or a sophisticated frequency synthesizer, was not uncommon in the receiver lab! A bitter thanks to a colleague for making this possible! Last but not least, I would like to mention the Iranian ban on entering NASA territories, including the SOFIA telescope which this thesis has worked for. Developing technology for a telescope that I am banned from, was such an odd experience. I would like to bitter thank NASA for teaching me the meaning of exclusion. During these years, three colleagues, Bettina, Heiko, and Richard passed away, together with my grandmother "Maman Bozorg" and aunt "Ame Zohreh". Some of these were not the easiest to bear, and may they all rest in peace.

The transitional situation of Iran and the Iranian community has been a source of shock, sorrow, and weak hope. We remember the Plasco building fire, and the brave firefighters during the rescue operation, hugging death. We remember the PS752 flight with all the 176 innocent passengers; we were passengers of the

same flight when traveling to Iran, and it hurts, every time fly back to Iran, and remember that aircraft, people, crew, and Kiev. On top of these and many other sorrows, each of them needs months to be resolved; if they ever are, happened the death of Mahsa Amini, raising another strong wave of sorrow and emptiness in our hearts.

My hearty thanks to the Persian gang we made and had in Cologne: Andisheh, Dana, Elaheh, Hassan, Iman, Nafiseh, Negin, Qhazaleh, Roozbeh, Samaneh and Zahra. As immigrants, it is so important to have friends and space to share the new world we are all experiencing, and you have offered me great support in this respect; To some of you, I almost feel like a family member; thank you for being there. Our hiking tours are unforgettable, well worth remembering all, including the Narcissus fields in the Eifel. Friendship of course knows no border, my inmost thanks to Alvaro, Veena, Shashwata, Sabine and Shiraz. With our German teacher, Frau Plath, our speaking ability improved. Her friendliness and kindness turned her into a true friend of ours in the last years.

I can not finish this acknowledgment without remembering many dear friends living in Iran or elsewhere on the planet. It is a strong support to know some of you are not too far: Amirhossein, Faezeh, Faezeh, Hossein, Mahmood, Mina, Mohammadamin, Mohammadmahdi, Morteza and Rasul. There are many many friends that growing up and immigrating has so strongly separated us, still you are all so kind, not to forget me. There are so many names to appear here, it is impossible to put them all. I would still mention the Sharif and Khaabgaah gangs, especially "311, 415 and guests" friends with both Hamidrezas and Hossein in the core. Thank you so much guys for all the company and joyful moments we share. I would also like to thank the friends and company in my channel, for being there, for reading and re-sharing.

Words are not enough when it comes to expressing my gratefulness to my family. Roya, eshghe man, you have been enormously patient and offered me constant support during all these years. That I have managed to finish it and write these sentences, I owe it to you, to light the candle of our home, such that I feel there is always a home that I go back to, and receive love, calmness, and appreciation. Thank you Roya for being on my side. Maman, thank you massively for all I have received from you, for all of it. Thank you for believing in me, for supporting me, for giving me the taste of science and experimenting. You were always with me, for polishing a telescope mirror, for listening to the noise when I was 15 and thinking that I was receiving Jupiter's decametric emission. I am grateful for all the energy and encouragement you gave me throughout all these years. At the beginning of my Ph.D. I had the chance to support you in publishing your research about Abū Isḥāq Ibrāhīm b. Nawbakht, I do not forget

those days. I feel proud of you. Baba, thanks for the lessons you gave me and for believing in me. Yasin my lovely brother, and Kosar, my darling little sister you both brought so much joy and meaning to my life. Thanks for being there. My kind gratitude to Daii Yaser for his mentoring and excellent support, way beyond a typical uncle, thank you so much, Daii. For almost a decade, you have believed in my abilities and been a great source of encouragement. Thank you so much for this, my parents-in-law, Baba Mehdi and Parvin Khanoom.

During these busy Ph.D. years I could spend less time than I would love to with my family, friends, and all other loved ones, hanging out and chatting for hours with ease. Sorry for this. I want to tell you, that I more think about and love you.

The future is bright, exciting, and challenging. I am looking forward to starting my postdoctoral position at Durham University, where I will continue my journey in multi-wavelength astronomical instrumentation, this time in astrophotonics. I see Roya's thesis and Ph.D. disputation on the horizon. All the lessons I have learned in the last years have empowered me, and I am confident we will build upon that.

Abstract

Heterodyne receivers for astronomy observing at 4.7 THz use Quantum Cascade Lasers (QCLs) as the local oscillator. QCLs are compact, powerful, and easy to use but prone to frequency instability from current noise, temperature fluctuations, and optical feedback, and they also lack absolute frequency reference. This work presents several solutions to this problem.

A heterodyne laboratory receiver at 4.7 THz has been developed to host all the experiments. The receiver shows an uncorrected receiver noise temperature of around 5000K at an IF frequency of 5.1 GHz and a total power Allan stability time of around 500 seconds. With this receiver, measuring methanol's emission lines helped to frequency calibrate one of the QCLs. The first experiment uses a methanol absorption line for frequency discrimination and a Hot Electron Bolometer (HEB) as a total power detector. In an active control loop, the experiment locks the laser's frequency to the dip of the absorption line. This method applies a known modulation to the QCL's frequency, dominating the QCL's linewidth with an FWHM of 2.1 MHz.

The second and the third experiments down-convert the QCL's frequency with a Superlattice Device (SLD) harmonic generator and mixer. A diode multiplier chain produces a 182.5 GHz signal to pump the SLD. The 26th harmonic is generated and mixed with the 4.7 THz QCL signal. The resulting IF signal at the SLD's output is 10 dB over the noise floor.

The second experiment feeds the IF signal into a delay line frequency discriminator to produce the QCL frequency's error information. A power divider divides the amplified and filtered SLD's IF into two. Only one is delayed in 10 meters of coax cable, and homodyne mixing produces a DC voltage as a function of the QCL's frequency. The control electronics turn this into a correction current to the QCL. This method stabilized the QCL with more than 10 MHz of frequency deviations, to an FWHM of 780 kHz, for hours. The experiment even works at very low signal-to-noise conditions, such as 2 dB, and revealed that the optical feedback is the dominant QCL line broadening mechanism caused by the pulse tube refrigerator's forced motions.

The third experiment uses a Phase Locked Loop (PLL). A phase detector compares QCL's phase with a reference, producing an error voltage. The loop filter transfers this to a correcting current, compensating the QCL's frequency disturbances. Phase locking is more challenging than frequency locking, and an exact understanding had to be developed on transfer functions and noise modeling. The experiment locked the QCL's phase, reducing the linewidth FWHM from 1.4 MHz to less than 7 kHz, stable for half an hour, and occasionally los-

ing the lock for a few seconds. With the demonstrated works, it is possible to stabilize the frequency of 4.7 THz QCLs.

Contents

1 Introduction

This thesis presents different solutions to stabilize frequency of 4.7 THz QCLs, and this chapter is the introduction. This chapter starts with the importance of sub-millimeter astronomy and the SOFIA telescope's role in this field. After that, the heterodyne technique is introduced, followed by the GREAT instrument of the SOFIA telescope, which initiated this work. A sample of GREAT observation is presented afterward to connect the reader better to GREAT's capabilities and needs. Since the following chapters will dive directly into the experiments, this chapter also includes a broader introduction to essential experimental elements of this work. These will be the Quantum Cascade Laser (QCL), the superlattice harmonic generator and mixer (SLD), the Hot Electron Bolometer (HEB), and the diode frequency multiplier chain. This chapter ends with the motivation and needs that this work arises from and should satisfy.

1.1 Sub-millimeter astronomy

The sub-millimeter part of the electromagnetic spectrum is one of the least studied in astrophysics, caused by the opaqueness of the atmosphere for the ground-based observatories from one hand, and the difficult technological development at this part of the spectrum, called the THz-gap, on the other hand. Only for high and dry altitude conditions such as the Atacama desert in Chile, few and narrow windows are exceptions. However the sub-millimeter spectrum is where many rotational transition levels of molecules and fine structure transitions of atomic species exist, together with the thermal emission of the dust continuum. One great example is to study the gas kinematics of the cold interstellar medium utilizing high spectral resolution spectroscopy at these wavelengths. In particular, there are several spectral lines of high importance, such as the brightest fine structure lines of ionized carbon (CII) at 1.901 THz and atomic oxygen (OI) at 4.745 THz (Stutzki & Güsten, 2022; Zhang et al., 2008; Risacher, Güsten, Stutzki, Hübers, Bell, et al., 2016); These are important cooling lines of the interstellar medium. Not only high-resolution spectroscopy of gas makes the sub-mm astronomy interesting, but also the fact that in this part of the spectrum, the emission from the dust peaks. Dust is generally opaque at shorter wavelengths such as visible light, but it gets clear at Far-IR and sub-mm lights, which makes the sub-millimeter band even more powerful to study the interstellar medium (Ennico et al., 2018). Figure 1 shows the dust continuum emission and the important spectral lines from the interstellar medium, together with the atmospheric transmission situation for ALMA's site and SOFIA's observing flight altitude.

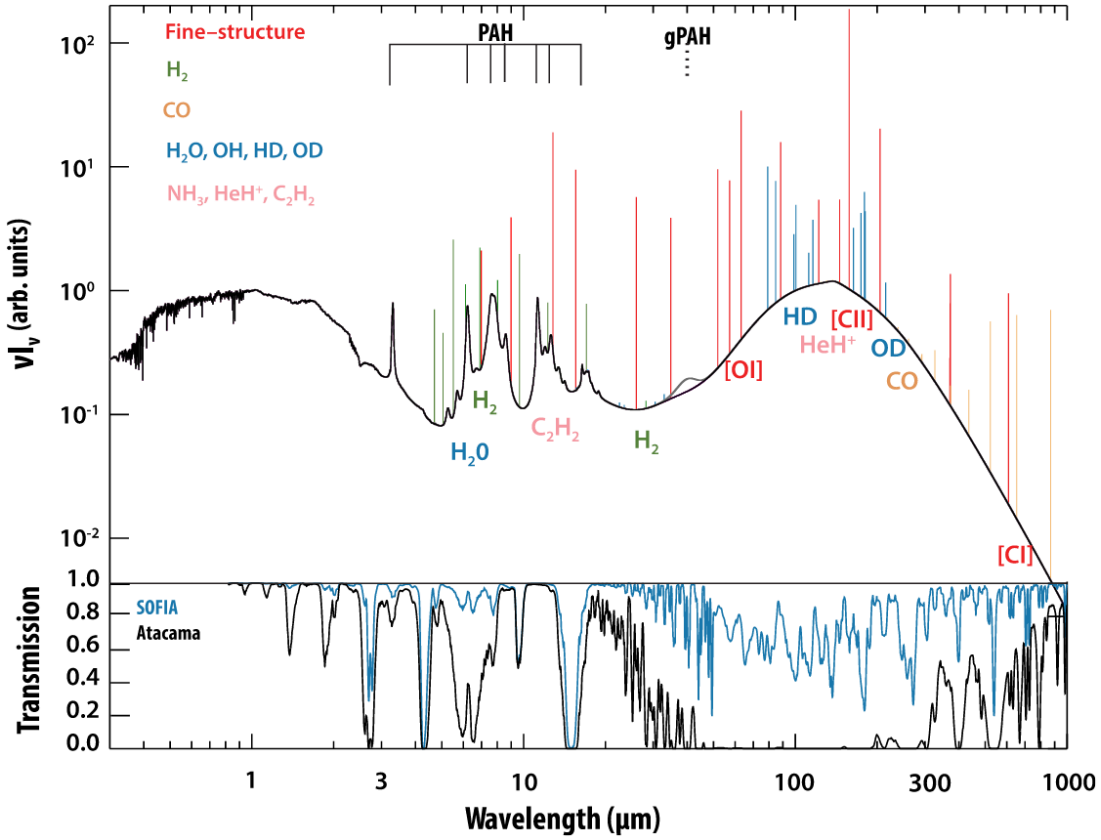

Figure 1: Top: In black is the spectral density of a model Photo Dissociation Region (PDR), and in colors are sample spectral lines from different surveys as they will be observed at a spectral resolving power of 10^5. Bottom: Atmospheric transmission for SOFIA flying at an altitude of 12.3 km and precipitable water vapor (pwv) of 10 μm compared to the ALMA site at an altitude of 4.8 km with a pwv of 0.5 mm. (Ennico et al., 2018)

1.2 SOFIA observatory

Figure 2: SOFIA observatory, after an observation night, has landed in California.

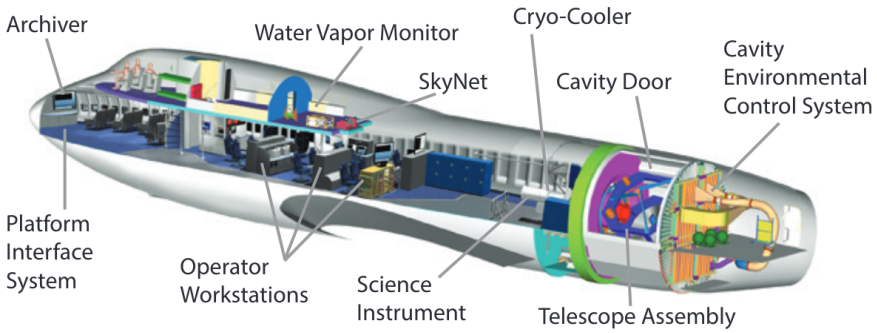

Figure 3: The important elements of the SOFIA observatory.

Stratospheric Observatory For Infrared Astronomy (SOFIA) is an airborne observatory with an effective primary mirror diameter of 2.5 m, installed in the fuselage of a Boeing 747SP aircraft. The letters SP refer to a particular short body version modified to be 14.6 m shorter than the original 747-100. This modification has extended the aircraft's flight range and maximum altitude, therefore, suitable for observatory application. The aircraft and operation is provided by the US side and the telescope by Germany. The telescope is a Cassegrain with a Nasmyth focus. While the telescope is open to the stratosphere, the science instrument flange is located in the pressurized part of the aircraft cabin.

The Nasmyth reflector is a dichroic mirror, and behind that, there is a second mirror that reflects the visible light to the telescope's Focal Plane Imager instrument (FPI). FPI provides signals for the control mechanism of tracking the target. Two other cameras, the Wide Field Imager (WFI) and Fine Field Imager (FFI), provide images for telescope pointing. They are both installed on the front ring of the telescope body. As driving a telescope requires extreme pointing and tracking accuracy, inertial stability of the telescope is done by both FPI camera signal as feedback and fiber optics gyroscopes installed on the telescope. The actuating elements for stabilization movements are magnetic torquers around the 1.2 m diameter pressurized spherical oil bearing.

The telescope has an elevation range of 23-58° and an azimuth range of ±3°. Flight trajectory defines the course selection of azimuth angle. Flights are typically 10 hours long, around six hours above 12.5 km altitude. Usually, a few targets are planned to be observed in one night, and optimization is done based on target positions, priorities, water vapor, and weather conditions. Figure 3 shows the most important inner units of the observatory.

1.3 Heterodyne principle and heterodyne receivers

An important family of radio receivers is called heterodyne receivers. In these receivers, a signal generated in them, called the local oscillator (LO), is mixed

with the incoming radio frequency (RF) signal, which will be measured or used (Kraus, 1986). Almost all the radio devices we know, including car radios, mobile networks, and WiFi, use this technique. The same has been used for radio telescopes for a long time. For astronomy at sub-mm and THz waves, because of no amplifier for these frequencies, to reach very high spectral resolution such as 10^7 (possible after achieving very small LO linewidths with techniques such as phase locking), and to avoid feedback and unstable receiver, it is essential to use the heterodyne technique. In astronomy, this allows for resolving the velocity profile of even cold interstellar medium structures made of atomic and molecular gas. Otherwise, such spectral line profiles can not be resolved with any other spectrometer type at the mm and sub-mm frequencies. The critical element of such a spectrometer is a nonlinear device called the mixer. Mixers for radio astronomy can be room temperatures, such as Schottky diode mixers, or cooled ones, like Superconductor Insulator Superconductor (SIS) and Hot Electron Bolometer (HEB) devices (Graf, Honingh, Jacobs, & Stutzki, 2015).

1.3.1 Mixer principle of operation

The mixer plays the role of mixing the two RF and LO signals. If the RF and LO electric field signals are $E_{RF}(t) = E_{RF}\cos(\omega_{RF}t + \phi_{RF})$ and $E_{LO}(t) = E_{LO}\cos(\omega_{LO}t + \phi_{LO})$, then applying the two electric fields to a nonlinear device will create the following current terms in the device (Pozar, 2005):

$$i(t) = I_0 \; + \; G_1[E_{RF}(t) + E_{LO}(t)] + G_2[E_{RF}(t) + E_{LO}(t)]^2 + \; ... \qquad (1)$$

Generally, as a result of the process, many different terms are created. They are constants, leakage of the LO and the RF to the output, the frequency sum, the frequency difference, and many terms of higher harmonics of the LO and the RF frequencies. Often the constant, the leakages, the sum term, and all higher harmonic terms are averaged out, and only the difference term can pass to the output. For this, if one considers the square term in 1 then:

$$\begin{aligned} i(t) &= G_2[E_{RF}(t) + E_{LO}(t)]^2 \\ &= G_2[E_{RF}\cos(\omega_{RF}t + \phi_{RF}) + E_{LO}\cos(\omega_{LO}t + \phi_{LO})]^2 \\ &= G_2[E_{RF}^2(\cos(\omega_{RF}t + \phi_{RF}))^2 + E_{LO}^2(\cos(\omega_{LO}t + \phi_{LO}))^2 + \\ &\qquad 2E_{RF}E_{LO}\cos(\omega_{RF}t + \phi_{RF})\cos(\omega_{LO}t + \phi_{LO})] \end{aligned}$$

Using trigonometric identities, one can rearrange it as follows:

$$
\begin{aligned}
i(t) = G_2[&\frac{E_{RF}^2}{2}(1+\cos(2\omega_{RF}t+2\phi_{RF}))+\\
&\frac{E_{LO}^2}{2}(1+\cos(2\omega_{LO}t+2\phi_{LO}))+\\
&E_{RF}E_{LO}(\cos((\omega_{RF}-\omega_{LO})t+(\phi_{RF}-\phi_{LO}))+\\
&\cos((\omega_{RF}+\omega_{LO})t+(\phi_{RF}+\phi_{LO})))]
\end{aligned}
$$

The Intermediate Frequency (IF) circuit filters out the constant and high-frequency terms, so they will not reach the mixer's output. In case of RF frequency being close to the LO frequency, only the difference term, which is called IF, will be present at the output:

$$
\begin{aligned}
i(t) \approx& G_2 E_{RF} E_{LO} \cos(|\omega_{RF}-\omega_{LO}|t+(\phi_{RF}-\phi_{LO}))\\
=& G_2 E_{RF} E_{LO} \cos(\omega_{IF}t+(\phi_{RF}-\phi_{LO}))
\end{aligned}
$$

The weak high-frequency signal of the source of interest at ω_{RF} is now converted to a weak but low-frequency signal at ω_{IF}. The advantage is that this signal can now be significantly amplified and handled by the rest of the radio receiver, with much smaller losses than the losses at ω_{RF}, together with the possibility of measuring the phase of the incoming RF signal. In this method, the LO's phase spectral density convolves with the incoming signal's spectral density, but LOs are often made greatly good that this does not affect the quality of the received data.

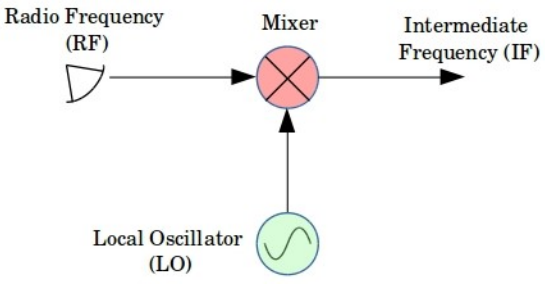

Figure 4: Schematic diagram for the role of the mixer in a heterodyne setup: to mix the incoming RF signal with the LO, and form the IF frequency at the frequency difference of RF and LO.

1.4 GREAT instrument

German REceiver for Astronomy at Terahertz frequencies (GREAT) is a heterodyne receiver with its first light on April 1st, 2011. GREAT kept its original

configuration until January 2015, in which the receiver could accommodate two single-pixel channels at the same time. The selection was possible among four wet cryostats for four bands called L1, L2, Ma, and H with center frequencies of 1.37, 1.86, 2.51, and 4.7 THz, respectively. Thanks to the airborne nature of the observatory, continuous instrument upgrades have been possible, such that from 2011 to 2015, upgrades have been done on optics, detectors, and local oscillators.

UpGREAT, a completely new version of the receiver, was successfully commissioned on May 12th, 2015. It is the first array spectrometer at THz frequencies installed on a telescope. It consists of the two LFA and HFA channels at frequencies of 1.9 to 2.5 THz and 4.7 THz, respectively (Risacher, Güsten, Stutzki, Hübers, Büchel, et al., 2016). LFA is mainly used to observe the ionized carbon (CII) fine structure line at 1.9 THz, while HFA is dedicated to observing the atomic oxygen fine structure line (OI). LFA's cryostat hosts two sub-arrays of seven pixels for H and V polarizations, each on a hexagon shape plus the center point. HFA's cryostat contains a similar pixel arrangement but for one polarization only. Migrating from GREAT to upGREAT has been challenging, especially when one compares the pixel count of the two receivers: from 2 upgraded to 21. Mixers for both upGREAT channels are HEBs with waveguide feedhorn antenna coupling. They provide an IF band from 0.2 to 4 GHz (D. Büchel et al., 2015), with a goal receiver noise temperatures of 1000 and 1500 K for LFA and HFA, respectively. LO technology for LFA is solid-state diode multiplier chain. LO technology of HFA is Quantum Cascade Laser, and the goal of this thesis is frequency stability and improvements of this LO(Risacher, Güsten, Stutzki, Hübers, Büchel, et al., 2016). Fast Fourier Transform Spectrometers from model

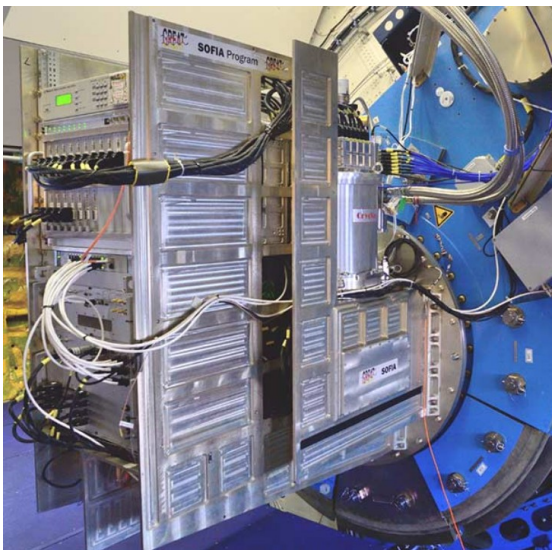

Figure 5: The upGREAT instrument as installed on the Science Instrument (SI) flange of the SOFIA telescope.

FFTS-4G developed by MPIfR have been the choice for back-ends of upGREAT. They read and record the IF spectrum into 32K channels, resulting in a channel width of 122 kHz (Klein et al., 2012).

4GREAT is the last member of the GREAT family and had its first light on July 13th, 2017 (Durán et al., 2021). The main idea behind 4GREAT is to provide single pixel observations capable of direct comparison with the data from the HIFI instrument of the Herschel space telescope. 4GREAT is based on the revival of the original GREAT instrument's L1 and M frequency channels, plus adding two new frequency channels at 0.55 and 1 THz. 4GREAT integrates all these four single-pixel channels in one cryostat, such that this can be installed and commissioned along with the upGREAT's HFA. 4GREAT utilizes the HEB mixers of the GREAT development from KOSMA for the two higher frequency bands while using the spare SIS mixers of the HIFI instrument from the Herschel space telescope for the two lower frequency channels. The LO for all these four channels are solid-state multiplier chains developed by VDI (Virginia Diodes, Inc., 2022). There are two LO units for this receiver, LO-U, which is housed on top of the main warm optics compartment of upGREAT, while LO-L installs into the original underneath LO compartment. Frequency band separation is done by two Dichroic filters and a polarizer grid. As for the back end, 4GREAT uses two types of Fast Fourier Transform Spectrometers (FFTS) configured to read the spectrum into 16k channels at a channel size of 244 kHz, developed by MPIfR. They measure an instantaneous bandwidth of 4 GHz, either from 0 to 4 GHz (baseband), for the higher frequency channels with HEB detectors. In contrast, for the SIS mixer channels, measurement is done from 4 to 8 GHz in the second Nyquist band (Klein et al., 2012).

1.4.1 Detection of atomic oxygen (OI) at 4.7 THz with GREAT instrument: an observational case

Atomic oxygen has been successfully observed in the Martian atmosphere using the OI channel of the GREAT instrument at 4.7 THz (Rezac et al., 2015). The transition is happening in the fine structure of the oxygen ground electronic state: it is the $(^3P_1 - ^3P_2)$ transition associated with a photon of 63 μm/4.745 THz. The Martian observation was done on the 14th of May, 2014, in double-beam chopped mode with a total integration time of 45 minutes. The observed spectrum can be seen in figure 7. The deeper absorption line is the telluric absorption of the same transition happening in the earth's atmosphere. The shallower dip is the Martian absorption line detected at a signal-to-noise ratio of 35. After all corrections and with the help of models, this observation yielded an OI column density of $1.1 \pm 0.2 \times 10^{17}\ cm^{-2}$. This value is double the results from the current Martian

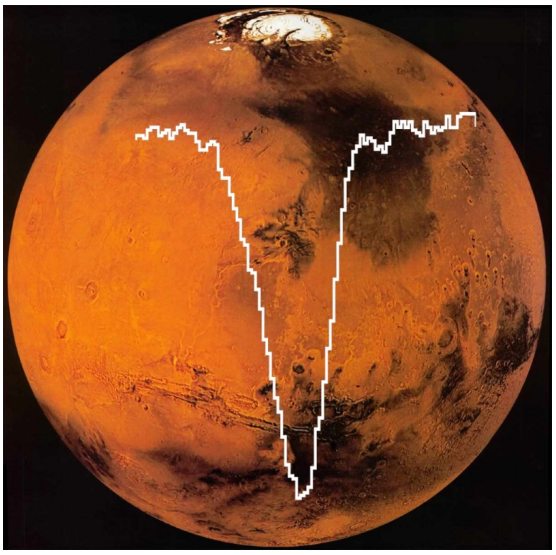

Figure 6: Overlay of the detected Martian OI line shape on top of a Viking I mosaic image of Mars. Credits: NASA/ DLR/ USRA/ DSI/ MPIfR/ SOFIA/ GREAT/(Rezac et al., 2015).

atmospheric model and reveals that the formation of this line is happening at a somewhat higher altitude of 70-120 km in the atmosphere of Mars.

Interestingly from this observation, the linewidths for both telluric and Martian lines are broader than the expected value from pure Doppler broadening of lines. This reflects the effect of LO linewidth on the observation, which has broadened both lines. Removing this unwanted broadening is one of the driving needs for this thesis. In addition to that, due to the lack of absolute frequency reference and, at the same time, frequency drift of LO, this observation had to

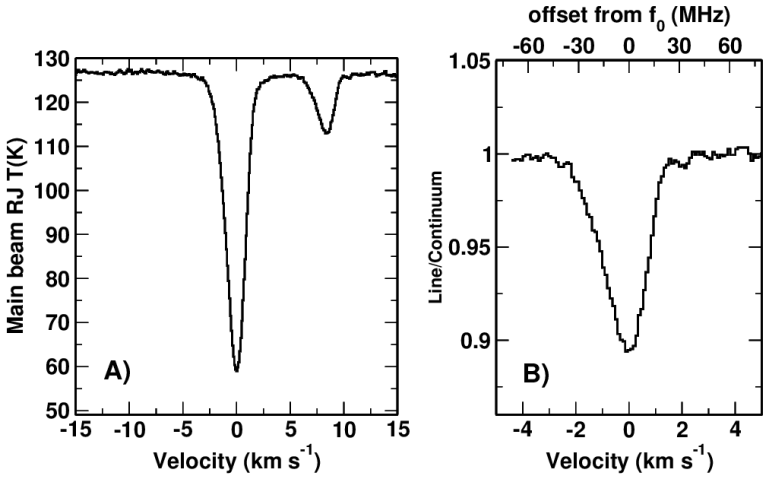

Figure 7: Observed OI spectra of the Martian atmosphere. Left: deeper line is the same transition from the earth's atmosphere (telluric line), and its center is taken as a reference. The shallower line is the detected line from Mars. Right: A zoom into the Martian line corrected for Doppler velocity (Rezac et al., 2015).

be corrected in reference to the telluric line position. The lack of an absolute frequency reference is another fundamental driving need. Sub-section 1.9 of this chapter will present the scientific requirements.

1.5 4.7 THz Quantum Cascade Laser as local oscillator

Quantum Cascade Lasers (QCLs) are the most liked devices to produce milliwatts of THz spectrum power, due to their low power, ease of use, compactness and good beam quality. In 1970, Tsu and Esaki first showed that a stack of thin semiconductor films could simulate a one-dimensional crystal with a much larger crystal lattice constant (Esaki & Tsu, 1970). They predicted that in contrast to typical crystalin structures with bandgapes in the eV range, minigap and minibands, corresponding to photon energies at THz, could be introduced and engineered by the design of a periodic structure. A year later, Kazarinov and Suris proposed the possibility of light amplification with intersubband devices (Kazarinov & Suris, 1971). In 1994 Faist and colleagues demonstrated the first Quantum Cascade Laser (Faist et al., 1994). Their device was lasing at wavelength of 4.2 μm with output power of 8 milliwatts in pulsed mode. Later two breakthroughs happened in the field. The first was the demonstration of the first room-temperature single-frequency distributed feedback laser (Faist et al., 1997). The second breakthrough was a continuous wave operation of a QCL at room temperature (Beck et al., 2002). Nowadays, research work on the topic of QCLs has been hugely expanded, and QCLs have opened their applications in vast fields such as remote sensing, security, laboratory spectroscopy, and communication.

Like all other lasers, QCL also consists of an active medium and a resonator. In a typical semiconductor laser, lasing relies on the recombination of electron-hole pairs across the semiconductor's bandgap, an interband transition, with the bandgap being a material-dependent quantity. Unlike them, QCLs operate based

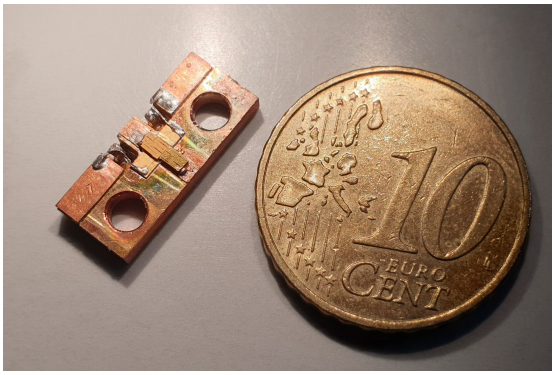

Figure 8: The chip holding one of the QCLs used in this work compared to a 10 cents coin.

on intersubband transitions created within the conduction band. The intersubband energy levels are engineered as requested; therefore, the laser's operating wavelength is determined only by the design of the superlattice structure: such as layer thickness and doping. The layered structure of semiconductors creates quantum wells with design-defined depths and potentials. This enables the wavelength to vary over a wide range from THz to mid-infrared. The word Cascade in their name arises from the fact that: in contrast to other laser types, in QCLs, each electron will undergo all the quantum well structures. Each electron undergoing several quantum wells leads to several photon generations, resulting in higher efficiency.

For a laser to pump an array of THz heterodyne mixers, QCLs have many advantages compared to other THz sources. One of them is the continuous wave (CW) operation capability of the QCL, which makes them suitable for LO application with a very small linewidth. Since celestial objects are located in different parts of our galaxy and even in other galaxies, in order to observe a particular line, some tunability is needed to accommodate the Doppler shifted frequency. Thanks to the tuning mechanisms, the frequency of QCL emission has some tuning range. QCLs are compact especially compared to other THz emission sources such as gas lasers or Backward Wave Tubes (BWO) (Richter, Greiner-Bär, et al., 2010) (Philipp et al., 2007). QCLs are also low-power devices and efficient in producing THz. They do not need high voltage for their operation, but they still need the cryogenic environment, which nowadays can be compact like Stirling cooling machines. For the application of heterodyne spectroscopy, a narrow linewidth and single mode operation are also needed where QCLs satisfy both (Faist, 2018).

Single-mode operation can be achieved via different methods. One is called Distributed feedback (DFB) laser (Faist et al., 1997), in which a periodic structure modulates the refractive index of the active medium all along the laser ridge and creates a one-dimensional Bragg grating. This grating selects only specific modes and frequencies for the reflection that laser needs to lase. These lasers have no implicit reflector, but reflection is distributed throughout the active medium via the Bragg condition, which satisfies only some discrete wavelengths. Another method to achieve single-mode operation is to use a Distributed Bragg Reflector (DBR) (Bonzon et al., 2014). Similar to the DFB structure, these reflectors are modulations in the active medium's refractive index, but they are only introduced at the ends of the laser ridge. Bragg reflectors provide high reflectivity only for discrete modes and they can be used to achieve a single-mode laser.

In this work, two QCLs have been used. The table below shows a brief comparison of the two.

Table 1: A comparison of the two lasers that have been used in this work.

	laser #1	**laser #2**
name in laboratory	upGREAT spare	rocket V1
frequency	4745 GHz	4784 GHz
operating temperature	32 K	33 K
Maximum output power	n/a	1.06 mW
multi-modding	not observed	has been observed
mode jumping	not observed	has been observed

1.5.1 Design

Figure 9 shows the main design elements of these QCLs. The design is called the rocket laser, which receives its name from the appearance of the laser ridge's shape. The design has five main elements: the DBR back reflector, the amplification section, the tapering section, the front reflector, and finally, the patch array antenna (Justen et al., 2016)(Bosco et al., 2016) (Bosco, 2019). Except for the antenna, the rest of the structure is an alternating sandwich of AlGaAs/GaAs made by forming a four quantum-well superlattice. It is grown by Molecular Beam Epitaxy (MBE) with a thickness of 9.2 μm. In the following, all the elements are shortly introduced. The DBR is four periods of 14.6 μm length made of alternating GaAs and Benzocyclobutene (BCB). This section provides high reflectivity of 90% over a wide frequency band of 3 to 6 THz. The broader part of the laser ridge is the active medium with the dimension of 600×52 μm. It has a second-order lateral grating primarily to suppress transversal modes. On the other hand, this has little effect on the desired fundamental longitudinal mode of the laser. Considering only the amplification section as an approximation, the longitudinal free spectral range is:

$$\begin{aligned} \Delta\nu_{FP} &= \frac{c}{2Ln_{eff}} \\ &\approx 60\ GHz \end{aligned}$$

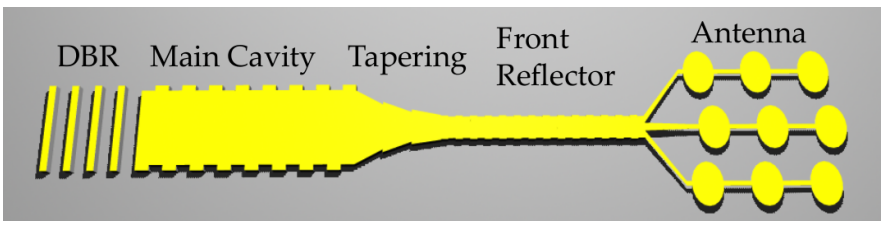

Figure 9: Design of the 4.7 THz QCLs with the main elements labeled. (Bosco, 2019)

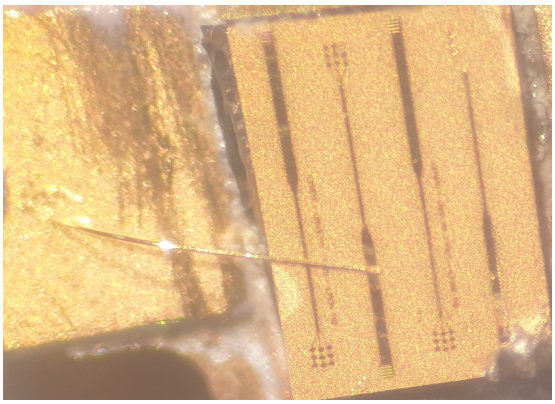

Figure 10: Photo of the QCL nr.2. Among all four, the one with bonding wire is the selected QCL to work.

with n_{eff} being the effective refractive index of the laser's gain medium, this relation sets an upper limit on the longitudinal mode spacing. Tapering has the role of impedance matching between the amplification section and the front reflector consisting of three subsequent sections of trapezoids, with the dimensions being optimized using simulation. The front reflector consists of 70 pieces of laser medium with first-order lateral width modulation between 14.1 μm and 15.3 μm. With a total length of 644 μm, it creates a peak reflectivity of $\approx 35\%$ sharp at 4.745 THz with FWHM of only 70 GHz. The laser ridge is embedded in BCB, a low-loss THz material. After the front reflector, the top metal contact with its three-by-three patch array, the BCB, and the substrate form a THz patch array antenna. This antenna, in turn, radiates the laser emission into a Gaussian beam. A photo of the device nr.2 is shown in figure 10.

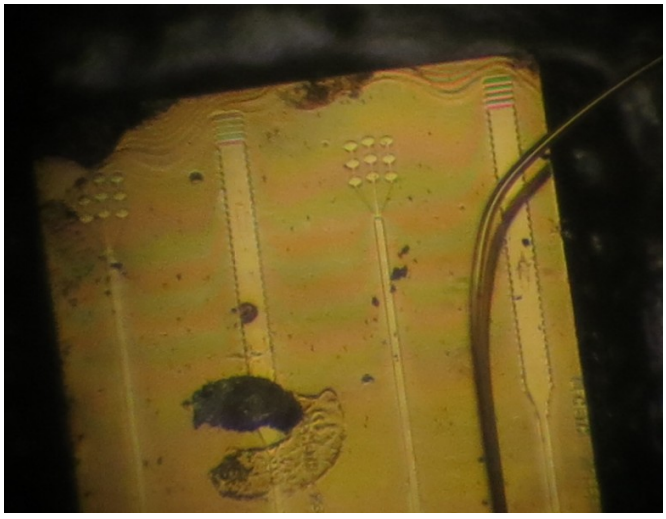

Figure 11: Photo of another QCL with the same design. Thanks to higher magnification, this photo shows the actual primary elements of these lasers: DBR, amplification section with width modulation, transition stage, front reflector, and patch array antenna.

1.5.2 DC and output power characteristics

THz Focal plane arrays consisting of many pixels need LO power that scales with pixel count, and can be in the order of several mWs. The needed power usually multiplies by a factor of few to account for window and radiation shield losses, and then also another time by a factor of around 10 to account for beam combiner loss where as an example only 10% of LO power is coupled to the mixers along with 90% of power that telescope has gathered. The mixer design depicts the latter, where both LO and sky waves should be coupled to the device from the same input port. On the other hand, it has been a challenge to produce even one mW of power at THz frequencies. This contrasts toward both ends of the electromagnetic spectrum where photonics and microwave devices are well available at much more significant power. At THz as of now, only the QCLs can produce several mWs of cw power in a single mode with good spectral purity and beam behavior.

Figure 12 shows the DC performance of QCL nr. 2 during a downward current scan. The red curve shows the QCL bath temperature, which changes only by 2.5 K. The blue dashed curve is the measured power from the device with a pyroelectric detector. To the first approximation, the device shows a monotonic output power increase versus input current. The device power was at maximum when the sweep started at 300 mA, meaning that the device's maximum power is probably at a somewhat larger current than 300 mA. Another feature apparent on the power curve is the threshold current at which the lasing starts: this happens when the laser gain overcomes all the losses in the laser. For this QCL at this particular temperature of 33.5 K, the lasing current threshold is $I_{th} = 120\ mA$. The third curve shows this sample's current-voltage relation, which is far from

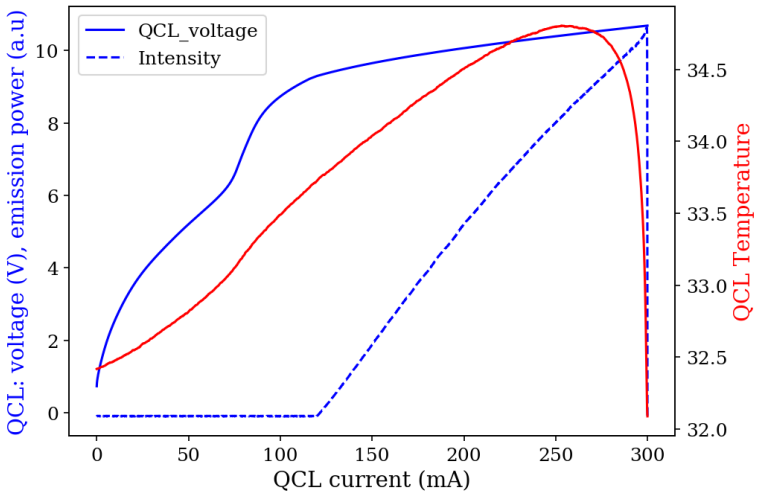

Figure 12: Light Current Voltage (LIV) measurement of the QCL nr.2.

Table 2: A short comparison of a few known 4.7 THz lasers to the ones used in this work.

QCL	**CW power**	**DC power**	**Temp**	**efficiency**
this work nr.1		not tested	32 K	
this work nr.2	1.06 mW	1.9 W	33 K	0.05 %
(Ohtani et al., 2016)	11 mW	29 W		0.04 %
(Richter et al., 2015)	0.15 mW			0.002 %
(Kloosterman et al., 2013)	0.25 mW	0.7 W	10 K	0.04 %
(Khalatpour et al., 2022)	8 mW		55 K	1 %
(Schrottke et al., 2020)	4.4 mW		55 K	

an Ohmic (linear) curve. The device shows large resistances at small currents, whereas, at larger currents, this decreases.

For the QCLs of this work, due to the limited availability of mm-wave power meter, absolute power measurements have been done only for the QCL nr.2. Power measurement was done with an Erickson mm-wave power meter and indicated power of 1.06 mW for this laser. At this output power, the input DC power was 2 W. Table 2 compares a few known single mode 4.7 THz QCLs regarding their power capability. Throughout this thesis, despite this once absolute power measurement, relative power measurements are done with a pyroelectric detector.

1.5.3 Temperature tuning

There are two mechanisms for temperature tuning in a QCL. One of them is the thermal expansion/ contraction of the QCL ridge, which changes the mode spacing of the laser cavity. The expansion increases the cavity length, thus, reduces the lasing frequency of a particular mode. Another effect is the refractive index of the gain medium, which is also a function of temperature. In a general format, gain medium refractive index is a complex quantity:

$$\tilde{n} = n + i\kappa \tag{2}$$

Where both real and imaginary parts are functions of temperature. For GaAs, the slope of the real part is positive, which means an increase in temperature will increase the optical path length of the laser cavity, which affects the laser frequency in the same way that cavity length expansion works: decreasing lasing frequency. Figure 14 shows how increasing the temperature of the laser changes the frequency and can be used to perform a frequency sweep to measure methanol absorption lines.

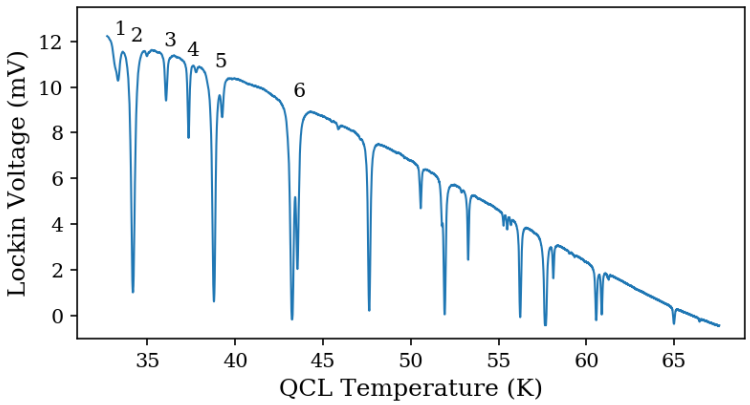

Figure 13: The obtained raw data of absorption lines during a temperature scan of QCL nr.1 at a fixed current of 160 mA. The lines with numbers are again identifiable in the current scan of figure 14. This data set is also used later in section 1.5.5 for frequency calibration.

1.5.4 Current tuning

Changes in the QCL current affect the laser frequency in three different ways. Change in current directly changes the carrier density in the laser, which varies the QCL's active medium gain. This can also be understood as a change in the medium's absorption coefficient α, which is the imaginary part of the complex refractive index. The second phenomenon is the Stark effect which changes the spacing between the intersubband energy levels of the active medium, and this shifts the gain profile of the laser. For a single-mode device small shifts can shift the laser's frequency within the lasing mode. In the extreme case, significant shifts in the gain profile can cause the QCL to jump to the next lasing mode. QCL nr.2 showed mode jumping in this study, and will be briefly presented in the frequency calibration sub-section 1.5.5.

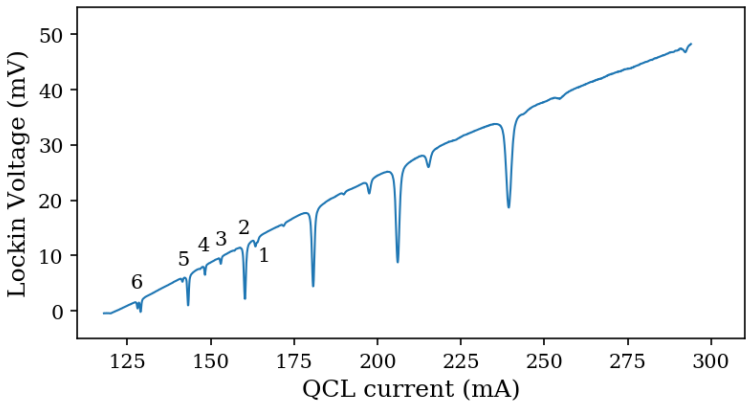

Figure 14: The measured raw data of absorption line strength vs. current of QCL nr.1 in a current scan. Temperature changes are small and have played negligible effects. The lines with numbers are identifiable against figure 13

The third mechanism that the current can tune the QCL frequency is changing the device temperature. Since the laser dissipates different thermal powers at different currents, the device's temperature will vary accordingly. In the devices of this study, a current increase has always increased the QCL's frequency. Figure 14 shows the result of detected power in a current sweep when QCL light is passed through a methanol-filled gas cell. One can identify the same pattern for lines nr.1 to 6 from figure 13. Comparing the patterns demonstrates the opposite sign of the net temperature vs. current frequency tuning.

1.5.5 Frequency calibration

In the previous sub-sections, it has been shown how different tuning mechanisms can be used to tune the frequency of the laser. Due to the complexity and sensitivity of the manufacturing process, it is impossible to get devices precisely as designed, meaning that frequency calibration is essential. In fact, in the layout of the MBE mask, a chirp is introduced that slowly modulates the production parameters of devices across the wafer. This chirp assures that, in the end, few devices will meet the required frequency (Bosco, 2019). The frequency calibration process follows: a gas rich in spectral lines at the design frequency fills a gas cell. In this work, Methanol has always been the choice. Then through absorption or emission spectroscopy, several spectral lines are observed. If not all, some of them can fit well to the known methanol lines near the design frequency. In practice, there are differences between absorption and emission spectroscopy setups. The following covers the absorption, while chapter 5 presents the emission spectroscopy.

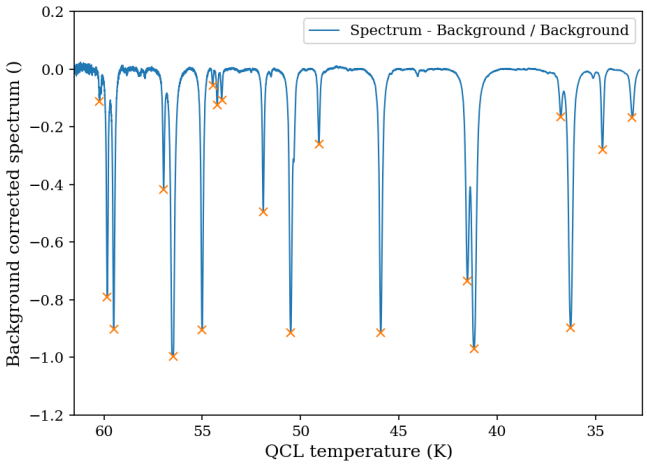

Figure 15: The normalized line strength as a function of temperature for the same data presented in figure 13. Calibration will be successful if the lines can be identified and assigned to known frequencies. Figure 16 shows the result of this calibration.

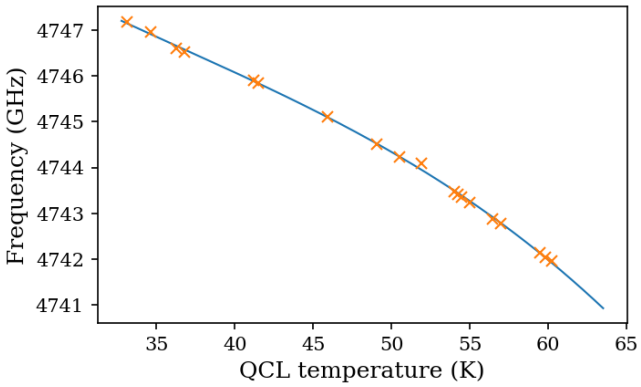

Figure 16: Obtained calibration curve for QCL nr.1 after a successful frequency calibration. As the product of the process, frequency is known for each temperature at the fixed current of 160mA.

The absorption spectroscopy method passes the total light from the QCL through the gas cell. Keeping the path length through the air short minimizes the absorption loss of THz wave traveling in the air. Gas cells used in this work were usually between 40 to 60 cm long, with HDPE optical windows on both sides. The pyro detector is installed Just after the gas cell. When possible, Pyro and windows of the gas cell were installed with a tilt angle to minimize the on-axis back reflection and corresponding standing wave and optical feedback. Since a pyro detector was used, an optical chopper had to chop the beam. A frequency sweep scan is possible with a current sweep to the QCL and simultaneously reading the pyro detector via a lock-in amplifier. Alternatively, fixing the QCL current and turning the cryo cooler off; hence a temperature sweep does the same job. Such measurements look like figures 13 and 14, which can be background corrected to form spectra like 15. This recorded pattern is then tried to cross-match the known methanol spectrum, including spacing and depth of the lines (Jet Propulsion Laboratory (JPL) database for molecular spectroscopy, 2022). Notably, neither temperature nor current scans are linear, making the cross-match challenging. Luckily, many times the cross-match has been possible. When matched, the frequency of each line, temperature, and the current of the same line are recorded. Thus depending on the scan type, points are known from the scan quantity vs. frequency. With this known, a polynomial fit is handy, and this polynomial fit is the calibration curve for the QCL within the scan range. Figure 16 shows an example of such a successful calibration. Another useful database for molecular spectra is the Cologne Database for Molecular Spectroscopy (CDMS), but unfortunately it does not contain methanol data for 4.7 THz (Cologne Database for Molecular Spectroscopy (CDMS), 2019).

QCL nr.2 showed strange behavior during this study. This QCL used to oper-

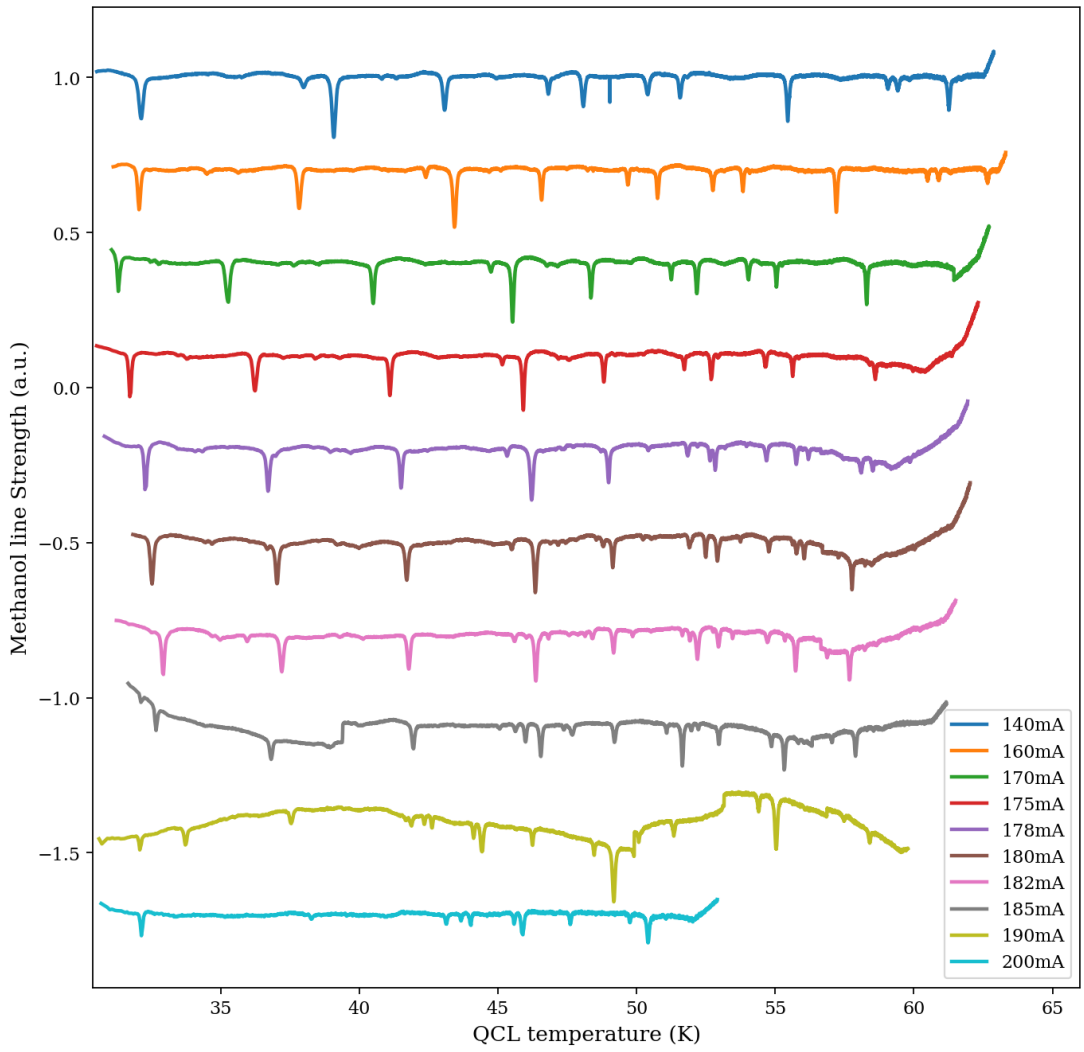

Figure 17: A series of temperature scans at different QCL currents to perform frequency calibration for QCL nr.2. These experiments revealed that QCL is misbehaving: doing multi-mode emission after a non-reversible mode-jump has happened.

ate in the design frequency, passing many thermal cycles. After another thermal cycle, all attempts to detect the QCL's down-converted signal at the IF output from the heterodyne experiment failed. It took months of work with no progress. Since finding the mixer product itself is a multi-dimensional laboratory parameter space, only in the end, the guess was made that the frequency is changed. After installing a gas cell filled with methanol, interestingly, the line pattern had no similarity with what it used to show. More work revealed that this is even worse, and the line pattern changed unexpectedly at different currents. This could be interpreted as a combination of mode hopping and multi-modding. Figure 17 shows the obtained methanol spectrum of this laser showing the misbehavior. For example, 185 and 190 mA traces show strong abrupt jumps that can be understood as mode hopes. Finally, further attempts with a heterodyne laboratory

receiver experiment (presented in chapter 5) to calibrate this laser was successful. Frequency was understood to undergo a jump of 40 GHz, which is in good agreement to this laser's expected value of longitudinal mode spacing.

1.5.6 Optical Feedback

Laser frequency, amplitude, and gain threshold are functions of any existing back reflections to the laser's main cavity. One can consider an external cavity extended after the laser device. The laser's output reflector and the reflected wave from the external reflector at the laser's output reflector's position can be considered a new unified reflector with a new net reflection coefficient (Petermann, 1988) (Lang & Kobayashi, 1980) (Ravaro et al., 2013). For the round trip phase change, one has:

$$\Delta\phi_L = 2\pi\tau_L(\nu - \nu_{th}) + \kappa_{ext}\sqrt{1+\alpha^2}\sin\left(2\pi\tau_{ext}\nu_{th} + \arctan\alpha\right) \tag{3}$$

with $\Delta\phi_L, \tau_L, \tau_{ext}, \nu, \nu_{th}, \kappa_{ext}$ *and* α being total photon's round trip phase, photon's round trip delay, emission frequency, emission frequency of solitary laser at threshold critical current density, external cavity's coupling coefficient and Henry's parameter for the complex refractive index of the gain medium with a typical value of 0.5 for THz QCLs (Green et al., 2008). The external cavity's coupling coefficient is defined as:

$$\kappa_{ext} = \frac{r_{2ext}}{r_{2s}}\ (1\ -\ |r_{2s}|^2) \tag{4}$$

with r_{2ext} and r_{2s} being the external and output amplitude reflection coefficients. A feedback coefficient C can be defined as:

$$C = \frac{\tau_{ext}}{\tau_L}\ \kappa_{ext}\ \sqrt{1+\alpha^2} \tag{5}$$

this feedback coefficient is a useful quantity in describing the laser behavior with optical feedback. For the cases with C $<$ 1, solving equation 3 for zero results in only one emission frequency, and optical feedback only induces frequency shifts. Whereas with C $>$ 1, equation 3 undergoes several zeros, and as a result, more than one external cavity mode can oscillate around the ν_{th}. For the case of monotonic emission frequency with C $<$ 1, 3 can be rearranged into:

$$\nu - \nu_{th} = \Delta\nu_{max}\ sin(\phi_{ext} + \arctan\alpha) \tag{6}$$

with

$$\phi_{ext} = 2\pi\nu\tau_{ext} \tag{7}$$

being the feedback phase and

$$\Delta\nu_{max} = \frac{\kappa_{ext}\ \sqrt{1+\alpha^2}}{2\pi\tau_L} \tag{8}$$

being the maximum frequency shift induced by the optical feedback. The frequency shifts due to the optical feedback are a well-observable quantity throughout the heterodyne experiments of this work.

1.5.7 Beam map

Some QCLs have been shown to produce a beam with good Gaussicity (Justen et al., 2016). The 4.7 THz lasers of this work have a patch array antenna to couple the THz emission to the free space, similar to a design for a 1.9 THz QCL (Justen et al., 2016). The beam shape of QCL is essential for efficient power coupling to the following elements of the receiver, within this work, the superlattice. Every time that the cryostat is switched on, a series of beam map measurements for the QCL beam were performed to check the beam shape and position of the beam waist. For that, a 0.5 mm iris cut on brass foil was installed in front of the pyro detector to increase the spatial resolution of the pyro detector. The detector was installed on an XY stage equipped with two stepper motors to scan the beam. A lock-in amplifier measures the Pyro detector's voltage and communicates the data with the PC. Figure 18 shows an exemplary beam measurement result. The beam is not a perfect Gaussian, but with nonsymmetric solid side-lobes. For further investigations, a direct measurement on the top of the laser should be done, with no intermediate optical elements between the laser and the pyro detector.

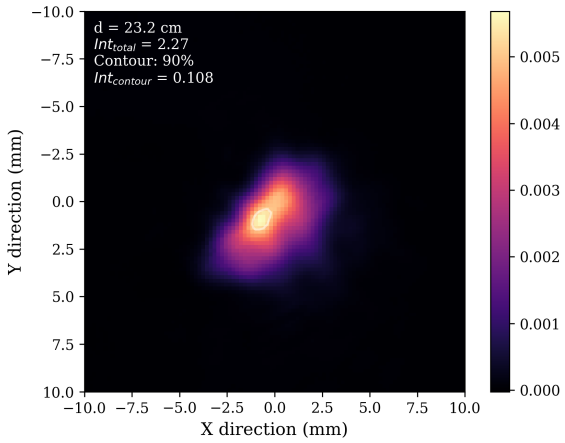

Figure 18: QCL Beam measurement example done to locate the beam around the setup.

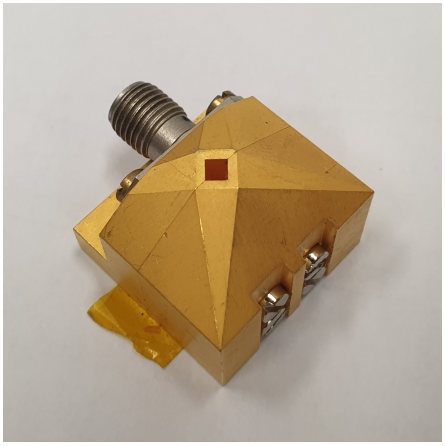

Figure 19: Photograph of the superlattice device. The diagonal horn and SMA port for IF are visible. The LO input waveguide port is on the face touching the table.

1.6 Superlattice harmonic generator and mixer

The principle of operation for this device relies on the solid non-linearity of current voltage (I-V) characteristics of the superlattice diode (SLD) (following subsection). The superlattice is the stack of 6 periods of the structure: 18 monolayers of GaAs followed by four monolayers of AlAs (Pavelyev et al., 2018). The growth of the structure is done by molecular beam epitaxy (MBE) on GaAs substrate. The superlattice region is only a couple of μm long, 1 μm wide, and 70 nm thick. The device is installed inside a split block where a WR06 waveguide enters from one side to carry the LO pump power. A short waveguide, followed by a diagonal horn, exits on the opposite side, serving as the device's high-frequency (RF) port. The device is installed with the help of silver glue epoxy in between the two waveguides and couples the signal to the LO waveguide using a finline antenna. The low-frequency IF connection is provided from the SMA connector's end to the inside of the superlattice device. Figure 19 shows the SLD block.

In total, for this work, four superlattice devices were supplied. First, only one

Table 3: Some specifications and basic measurements from the superlattice devices.

parameter	**value**	**comments**
LO power max	13 dBm	
input freq range	175-210 GHz	
output freq cut-off	1 THz	
nominal input power	8-11 dBm	
Used input power (SLD nr.4N)	10 dBm	
SNR_{max} harmonic 26 (SLD nr.4N)	10 dB over noise	RBW = 3 MHz
SNR_{max} harmonic 22 (SLD nr.1-1)	12 dB over noise	RBW = 3 MHz

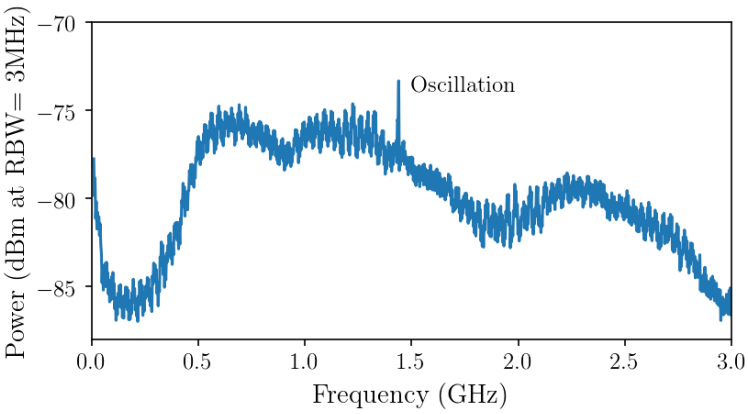

Figure 20: Oscillation observable at the IF output of the SLD with no signal coupled to the RF port. It is marked against the wavy standing wave pattern in the data.

came and was used from March 2017 for two years. That unit was mainly used at nominal power level. One day while experimenting and watching the signal on the spectrum analyzer, the signal disappeared, and the noise floor went down. With further tries, superlattice could not be pumped anymore. However, a check with a Pyro detector and a horn installed on the output of the multiplier diode chain showed power. This case has been the only superlattice failure that happened during this project. After that, the device inventor was invited and brought three new superlattices for the project. Two of them were from the same older design but a new one with a more significant height and diagonal horn. This last new device (nr. 4N) was used during the rest of the project. Table 3 presents the specification and some measured data from the superlattice device.

Table 4: Summary of literature reported values for THz harmonic mixers that have been used to down-convert the QCL's frequency. The mixer column shows the mixer technology with SD being Schottky Diode and the harm column shows the harmonic that has been used. The CL column presents the conversion loss of the harmonic mixer. Freq stands for QCL's frequency (in THz), and SNR is the reported signal to noise ratio, in resolution bandwidth of RBW.

Work	**mixer**	**harm**	**freq**	**CL**	**SNR**	**RBW**
(Hayton et al., 2013)	SLD	18	3.4	80	30dB	100kHz
(Khudchenko et al., 2014)	SLD	24	4.7	100	10dB	100kHz
(Bulcha et al., 2015)	SD	4	2.52	35		
(A. Danylov et al., 2015)	SD	23	2.32		33dB	300kHz
(A. Danylov et al., 2015)	SD	22	2.52	83		
(A. Danylov et al., 2015)	SD	31	2.96		30dB	300kHz
(A. Danylov et al., 2015)	SD	27	3.1	93		
(A. Danylov et al., 2015)	SD	37	4.25	106		
(A. A. Danylov et al., 2012)	SD	21	2.32	∼105	25dB	

The SLD has been shown to suit three different roles: harmonic generation, harmonic mixing, and oscillation (D. G. Paveliev et al., 2008) (Pavelyev et al., 2018) (D. Paveliev et al., 2012) (Renk & Stahl, 2011). Based on the inventor's specifications, the DC bias condition determines the SLD role: a DC bias is needed only for oscillation. In contrast, on many occasions during typical operations for harmonic mixing, an oscillation could be observed in the IF output monitored on the spectrum analyzer display at lower power levels than needed for harmonic mixing, with no DC bias. The observed oscillation was present with no signal present at the RF port. It could be a down-conversion with a harmonic of the LO pump signal, and further investigations are needed. Previously others have reported oscillations in the range of mm-waves in the SLDs (Renk et al., 2005) (Schomburg et al., 1998). In figure 20, a sample plot of such oscillation's peak in the IF is visible.

superlattice devices of this work are neither designed nor optimized to operate at 4.7 THz, and they are lossy at these frequencies. Table 4 shows examples of the conversion loss of similar devices (Khudchenko et al., 2018). In this project, a measured value of 103 dB of conversion loss could be estimated for the superlattice, although values as low as 70 can be found in literature, which does not seem realistic (Pavelyev et al., 2017). Complications are predominantly due to unknown power coupling from the QCL beam to the over-moded input horn of the SLD.

Due to the limited input waveguide frequency band, a list of input LO frequencies can be made to pump the SLD for the target frequency of 4.7 THz. Table 5 presents these frequencies plus the overall possibilities and results from this work.

The role of SLD as a pure harmonic generator has also been used in few cases to stabilize the frequency of THz QCLs. Table 6 contains more general brief data from some QCL phase locking experiments using a non-harmonic mixer. This table is a complement to the table 4.

Table 5: List of the possible input frequencies to generate a harmonics at 4.745 THz.

LO frequency (GHz)	**harmonic**	**tested**	**mixing product**
215.68	22	yes	observed with AMC-S108b
206.30	23	no	
197.71	24	no	
189.80	25	no	
182.50	26	yes	observed with AMC-S177
175.74	27	yes	not observed

Table 6: A summary of experiments using other THz reference sources than harmonic mixers. The mixer column presents the mixer technology, the T column indicates if the mixer was warm or cryogenic cold, ref column presents the type of reference signal, freq presents the QCL frequency in THz, and SNR is the reported signal to noise ratio, in resolution bandwidth of RBW.

work	**mixer**	**T**	**ref**	**freq**	**SNR**	**RBW**
(Rabanus et al., 2009)	HEB	C	SLD harm	1.5		
(Betz et al., 2005)	GaAs SD	W	FIR laser	3.06	26dB	100kHz
(Khosropanah et al., 2009)	HEB	C	SLD harm	2.74	16dB	100kHz

1.6.1 Superlattice I-V curve

Esaki and Tsu predicted a strong non-linearity of current-voltage (I-V) relation for a semiconductor superlattice via the miniband conduction electrons (Esaki & Tsu, 1970). In their prediction, a negative differential resistance will also show after a critical voltage has been reached. The two features put them among the best candidates for harmonic generation, oscillation, and mixing at mm-waves and THz frequencies. Figure 21 is an example of the I-V curve. At low voltages, behavior is linear, i.e., resistive (Pavelyev et al., 2018). For voltage magnitudes more significant than the critical voltage $U_c \approx 100\ mV$, the behavior starts to be non-linear, and the negative differential resistance can be observed. They appear as two regions of drop in the I-V curve and are called first and second drops.

1.6.2 Operation steps

If one wants to operate the superlattice as a mixer/receiver, observation of behaviors are possible when pump power from the diode frequency multiplier chain increases gradually. Table 7 Shows the different steps on pumping the SLD, from no pump power to the optimum point. These observations are made for a pump frequency of 182.5 GHz.

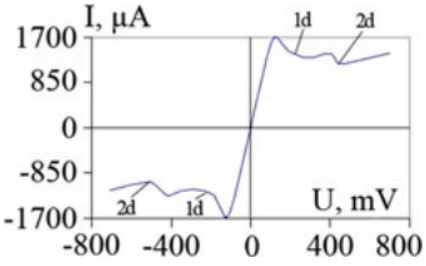

Figure 21: A measurement of superlattice current-voltage (I-V) curve. Plot after (Pavelyev et al., 2018).

Table 7: The sequence of pumping the SLD together with the observed outcome.

step	mixing product	SLD noise	comments
1		appears	SLD reacts to power
2		first maxima	oscillation observable
3		large	
4		second maxima	
5	appears	medium	
6	maximum	small	optimum operating point
7	disappears	medium	

Generally, applying LO pump power to SLD has always been a cautious point throughout this work. In a few cases, more enormous pump powers were also tried with the experimental setup. For SLD nr.1-1, there were two other regions where the mixing product arose over the noise floor, and full power of the diode frequency multiplier chain was applied to the device without damaging it. As a result, it was understood that not much of a signal-to-noise ratio could be gained by further increasing the pump power. After that, devices were rarely tried at more extensive pump powers needed than the first sweet point (step 6 in table 7).

Interestingly the shape of the two noise maxima is different. Figure 22 shows both noise maxima measured for SLD nr.4N. In the first noise maximum peak of generated noise is more potent at lower frequencies in the IF (> 0.5 GHz), whereas, in the second noise maximum, noise generation has more power in higher frequencies (> 1 GHz). An explanation for this behavior could not be done so far.

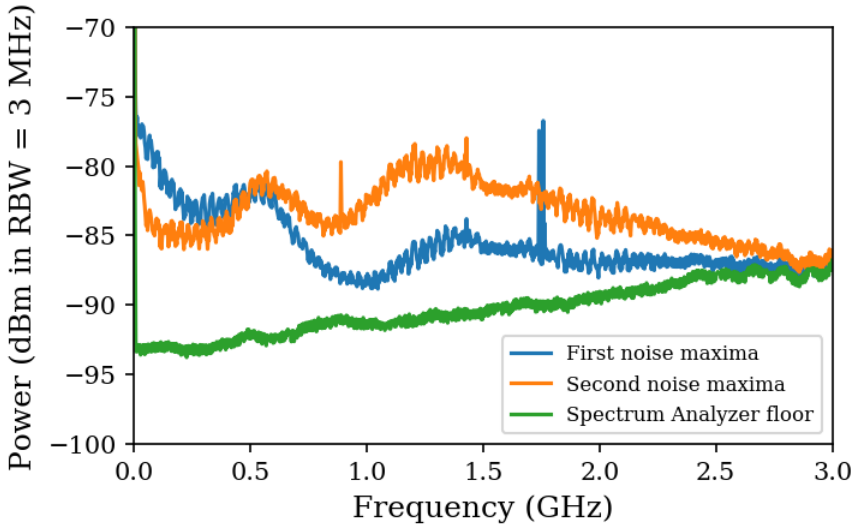

Figure 22: The spectrum of the two noise maxima generated by the SLD before reaching the optimum pumping point. For reference, the spectrum analyzer's noise floor is also plotted.

1.6.3 Generated noise

One of the limiting factors in the signal quality of the SLD's output is the amount of noise that this device produces. Figure 23 compares the noise floor of the unpumped and the pumped SLD. the earlier is the noise floor from the first amplifier afterward, but the latter is the noise floor that will be propagated through the IF system and limits the signal to noise ratio. An IF frequency between 0.3 to 0.5 GHz was often used in this work, and one can see that an additional noise of 5 to 6 dB atop the spectrum analyzer's noise floor is present in the optimally pumped SLD's output. In these measurements, the spectrum analyzer was a very low-noise one, and only one amplifier was placed between SLD and the spectrum analyzer.

During experiments with the heterodyne experiments using the SLD as a harmonic generator and mixer, it was noticed that blocking the optical path to the SLD changes the IF total power of the receiver. This observation triggered the idea to check and quantify this difference. In astronomical radio receivers, a well-known method called hot-cold measurement is done by placing hot and cold blackbody absorbers at the receiver's input. The receiver's output power ratio is reported as the Y factor. For the experiment performed, the Hot source was an absorber piece at a room temperature of 299 K, and the cold source was the cryostat's thermal bath made out of copper at a temperature of 37 K with the cryostat window and two focusing mirrors in between. Figure 24 shows the receiver's output power when the hot source was inserted in or was out of the beam. The measured power values give a Y factor of $\frac{P_{hot}}{P_{cold}} = 1.0059$. Due to the

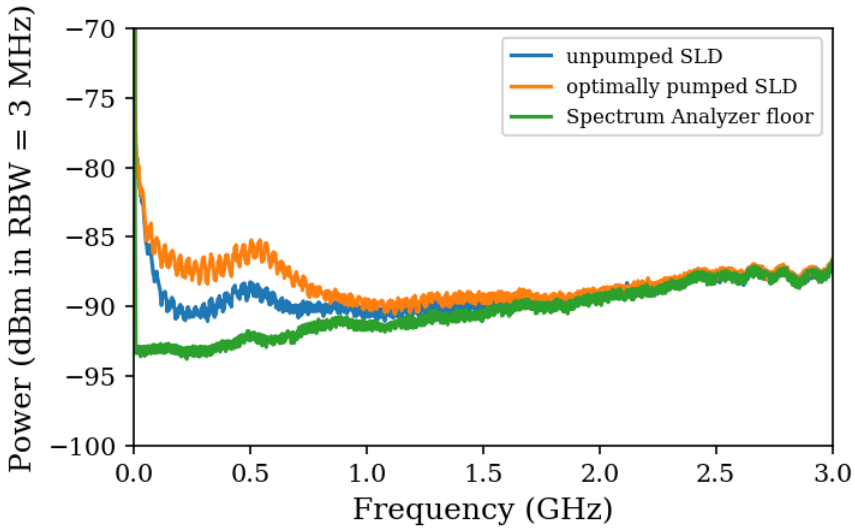

Figure 23: The noise spectrum measurements from the SLD, comparing the pumped SLD vs. the unpumped.

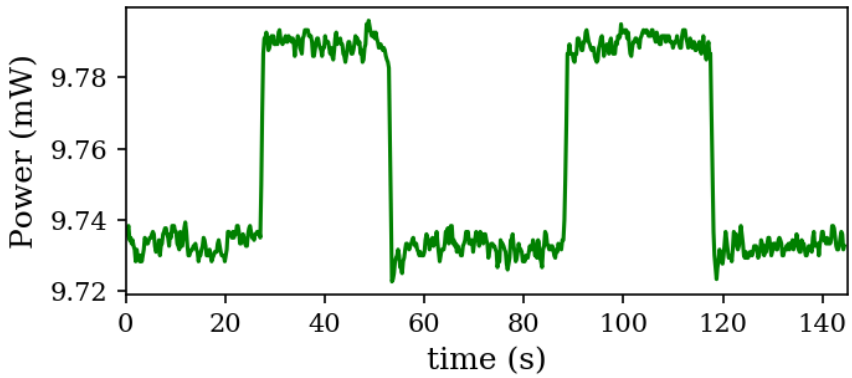

Figure 24: Raw data of SLD Hot-Cold measurement. The lower parts are the power readout of the receiver when looking at the cold cryostat thermal bath made of copper, while the upper parts are the result of a warm absorber inserted into the SLD's beam.

complexity of the cryostat setup, no further effort was made to estimate the total noise temperature of the SLD. More investigations remain open for future works.

One natural way to reduce the generated noise, thus gaining a better signal-to-noise ratio, is to cool the superlattice down to cryogenic temperatures. For example, a successful demonstration of such an idea is done by (Khudchenko et al., 2014), where they have demonstrated phase locking of a 4.7 THz QCL with the superlattice cooled to cryogenic temperatures. Within the frame of this work, since the HFA channel of upGREAT is running at the end performance with many key elements having failure risks, the idea of cooling the superlattice was rejected from the beginning. Specifically, the device's design has yet to be fully known, and not much long-term performance data is available. Therefore putting the superlattice in the failure risk of cryogenic cool-down and warm-up cycles was rejected, and no cooled SLD experiments have been done.

1.6.4 Beam map

Chapter 3 will show how a heterodyne receiver can be formed with the superlattice simultaneously acting as a collecting optics and mixer. This setup is able to easily down-convert the powerful emission from the SLD and, therefore, enables to measure the beam map of the superlattice device. The SLD and attached multiplier diode chain has been scanned with a motorized XY stage to map the SLD beam. An underlying assumption is that the beam of the QCL is converged to a reasonable extent. Since convolution is done between the two beams, the size from the resulting map should be corrected if necessary. For the interest of this project, getting an idea about the size and shape of the SLD beam was critical. An example result can be seen in figure 25. It shows that the beam is a distorted

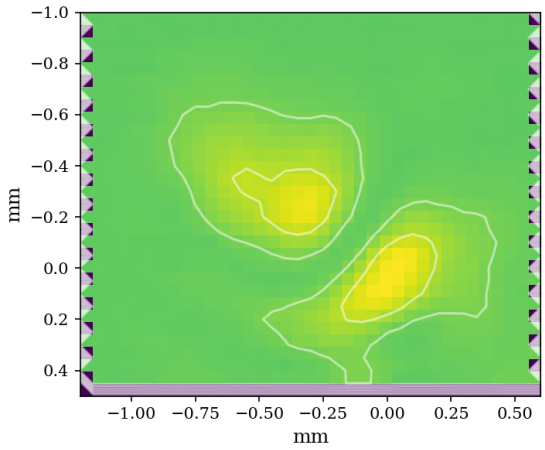

Figure 25: Beam map measurement of the superlattice at 4.7 THz. To create this map source was a fixed and focused QCL beam, and superlattice was moved from each position to every other point. At each position, the corresponding IF power from the receiver was recorded.

and double peak, far away from a fundamental Gaussian beam. This poor beam quality results from the device's over-modded RF input waveguide and horn. The latter is an important reason for less efficiency throughout the work done in this thesis.

1.7 Hot Electron Bolometer (HEB)

Hot Electron Bolometers (HEB) show the best performance in sensitivity among heterodyne detector devices for frequencies beyond 1.2 THz (D. Büchel et al., 2015). The heart of the HEB mixer is the HEB junction: a thin superconductor film that detects the beat note from the two incoming THz radiation. The time constant of the detector is not fast enough to react to the individual THz electric fields, but the difference heterodyne term can be 'seen' and extracted from such a detector. These detectors need an LO power of less than one uW to be pumped and ready to down-convert the faint THz signal to be detected.

Both pump power and signal are coupled to the detector from the input horn where the horn cut is a spline curve (D. F. Büchel, 2017). A sense probe is located at the end of the horn and at the beginning of a waveguide structure. The latter are directly metal machined into the mixer block. After the probe, the HEB junction detects the beat note and down-converts the RF and the LO signals into an IF signal. Junction is a thin film micro-bridge; it is 3600 nm wide and 300 nm long, made of NbN. Following the junction is an RF choke to prevent any high-frequency signals from getting through the rest of the detector elements and being dissipated. The detected signal is finally coupled to a 50 Ohm IF and DC board and gets out of the block via an SMA connector. Figure 26 shows the

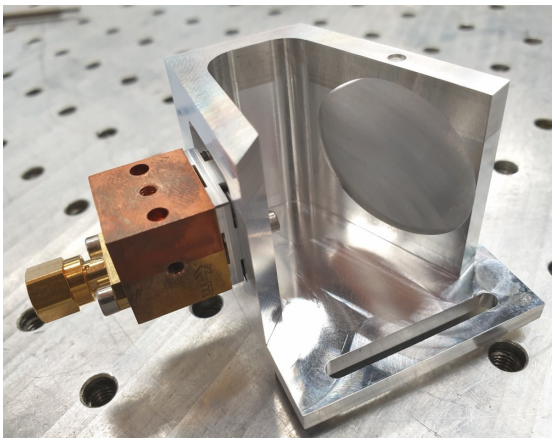

Figure 26: The HEB detector is the copper-colored block installed on the aluminum block that contains the HEB's coupling mirror (the oval cut).

HEB block installed on the corresponding first mirror.

1.7.1 DC behavior

In order to characterize and to operate an HEB detector, one needs to do DC characterization and apply the proper DC bias condition to the HEB junction. The fundamental DC figure would be the I-V curve, which shows the device's current and voltage dependency. The plot of figure 27 shows the unpumped I-V curve, where no LO power has been applied to the detector. As seen in the plot, HEB shows hysteresis effects in this condition, with current behaving differently in the two visible loop areas depending on the previous condition of the superconducting junction. With applying LO power, the hysteresis effect becomes weaker up to a level that it entirely disappears, and also, the curve will mitigate from strong break points to a smoother one(under-pumped). Increasing the LO power results in a nice round bend on both sides of the I-V curve; the

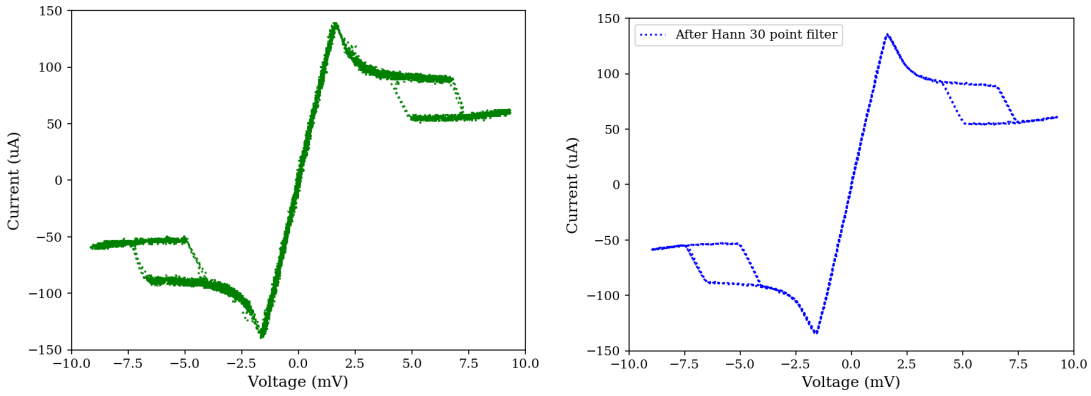

Figure 27: I-V curve of an unpumped HEB detector; Left: original data points. Right: after applying a Hann smoothing filter. The hysteresis effects are evident in both plots.

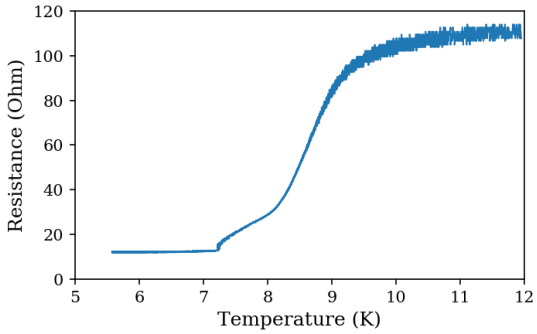

Figure 28: HEB detector's resistance as a temperature function with no pump power.

optimum LO power. With the further increase, the I-V curve tends to move toward a straight line (over-pumped). Studies have shown that the optimum operating point is at $V = 1.2mV$ and $I = 20\mu A$, where the receiver shows the lowest noise temperature (D. F. Büchel, 2017).

Since HEB is a superconducting device, the critical temperature is one of its fundamental parameters. Plot 28 shows a measurement example of device resistance vs. temperature. For this, the HEB is voltage biased at 1.0 mV, and the temperature is scanned up by turning off the cryo-cooler. Simultaneously HEB current is recorded via the current monitor output. In this test, no pump power was applied to the HEB (unpumped).

1.8 Diode multiplier chain

Diode multiplier chains are the most common sources of continuous mm and sub-mm waves (Maiwald et al., 2005). The principle of operation is the generation of harmonics in the non-linear current-voltage response of a diode. Each diode in the chain receives a signal from the previous stage, where the electric field drives a non-linear current in the diode (REF). Due to non-linearity, second and third harmonics are produced with efficiencies like 9 and 3.5 % for frequency generation at 60 GHz(Virginia Diodes, Inc., 2022). The harmonic is selected through filtering and is guided to the output of that diode stage. For example, the frequency multiplier chains of the upGREAT instrument can generate a peak power of 3.5 μW at 2.5 THz (Durán et al., 2021). One limitation of these frequency multiplier chains is that the output power drops fast at higher frequencies (Ward et al., 2004). Currently, highest frequency diode that VDI offers is the WR0.34X3 tripler with an output frequency of 2.2 to 3.3 THz with input power level of 3 mW and an efficiency of 0.05%. A photo of the VDI-AMC-S177 diode chain as a crucial element of heterodyne experiments done in this thesis, can be seen in figure 29.

In this work, the VDI-AMC-S177 diode chain serves the role of generating

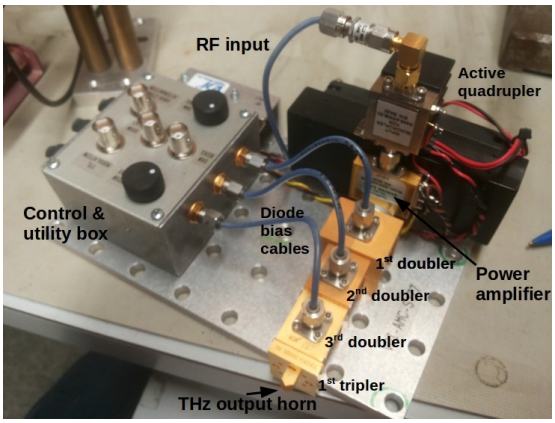

Figure 29: Photograph of the VDI-AMC-S177 diode multiplier chain in complete configuration.

an mm-wave to pump and drive the superlattice from its LO port. This diode multiplier chain is designed to deliver monochromatic wave at 1 THz. It has a frequency quadrupler at the input, with the active quadrupler element implemented with GaAs MMIC technology. After this stage, a power amplifier amplifies the generated signal to a power level of around 1 watt. After that, there are three doubler diode stages, followed by a diode tripler as the last stage. Table 8 shows some specifications of this diode multiplier chain. Output from the second doubler diode matches the optimum frequency range of the superlattice device, therefore this work has involved many measurements at this output point. The VDI-AMC-S177 has a built in bias voltage control unit for two doublers, and also a built-in variable attenuator.

1.8.1 VDI-AMC-S177 output power

In order to safely drive the superlattice, it is crucial to know how much power the diode chain is delivering to the device, and if needed, use the power attenuator

Table 8: A selected specifications and measurements of the AMC-S177 diode multiplier chain. The upper part specifies the parameters for the whole chain, whereas the lower part focuses on the second doubler output.

parameter	**value**	**comments**
target frequency	1 THz	
peak output power	97 uW	at 1.04 THz
number of multiplier elements	5	
number of amplifier elements	1	
specified relative bandwidth	7 %	
maximum output power	25 mW	for 182.5 GHz
input saturation power	15 dBm	for 182.5 GHz
tested bandwidth	161.6 to 187.5 GHz	at 2nd doubler's output

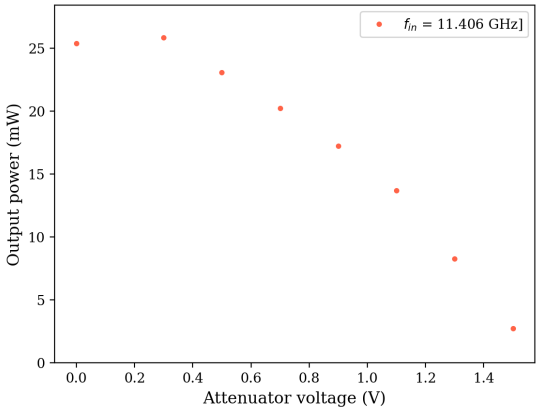

Figure 30: Measured output power after the second doubler diode in the AMC-S177 diode multiplier chain as a function of the attenuator voltage.

to regulate the power value. In an experiment, the output power after the second diode was measured using an mm-wave Erickson power meter. During the test, the chain generated mm-wave power between frequencies of 161.6 GHz to 187.2 GHz, dropping efficiency at around 163 GHz to 165 GHz. In order to get the maximum available power, the bias voltage of the D80 doubler had to be adjusted; only to end limits of -18.9 V and -13.1 V, was enough. Figure 30 shows the output power at the frequency of 182.5 GHz as a function of the attenuator voltage.

1.8.2 VDI-AMC-S177 diode chain utilities

As mentioned earlier, this chain is equipped with a voltage-tunable power attenuator, which accepts a voltage between 0 to 5 volts and attenuates the output from zero to maximum, respectively. Another available utility in this chain is a TTL modulation input that can be used to perform amplitude modulation on the wave. Amplitude modulation frequencies of up to 200 Hz are accepted. The chain also has two knobs to change the bias voltage of the first (D80) and third (D350) doubler diodes for maximum power generation efficiency. In order to be able to read those two bias voltages, there are also monitor outputs to be connected to voltmeters.

1.9 Motivation of this work

The local oscillator's quality is crucial in a heterodyne measurement system. In the following several aspects of LO quality are introduced. In the following chapters when different stabilization methods are presented, these aspects will serve as quality measures.

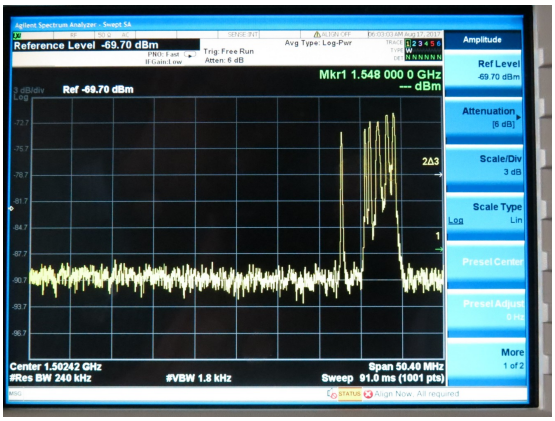

Figure 31: The jitter the QCL suffers from is visible on the spectrum analyzer during a heterodyne experiment. A spectrum analyzer sweeps measurement frequency to cover the band of measurement. During the sweep, the frequency of the laser did not stay stable. As a result, the line in the spectrum has jittered around. In this particular measurement, the QCL line has jittered for 6.5 MHz.

1.9.1 Increase spectral resolution

The fact that in a heterodyne system, LO line-shape will be convolved with the elements building up the spectrum has a downside: Line-shape and linewidth of LO can limit the narrowest possible spectral element that a heterodyne system can measure from the source of interest. In the GREAT spectrometer, 4 GHz of bandwidth is sampled with XFFTS spectrometers into 32K channels, resulting in a single channel bandwidth of 125kHz. If the LO linewidth is meaningfully larger than this, it will be the LO that is limiting the linewidth in the measured data.

Several mechanisms can broaden the QCL's linewidth. As discussed earlier in this chapter, changes in the following quantities of current, temperature, and optical feedback to the QCL will affect the frequency of the laser. Modulations of these quantities will result in QCL's frequency modulation, increasing the laser linewidth (Barkan et al., 2004). An example of such disturbances has been measured with the help of chapter three's experimental setup and can be seen in figure 31. The figure shows how the narrow line of the QCL is broadened to 6.5 MHz with the effects of modulation mechanisms. If the modulation is canceled in a control loop, the linewidth will be reduced; thus, the spectrometer will benefit from a better spectral resolution.

1.9.2 Provide absolute frequency reference

The channel of 4.7 THz on GREAT is dedicated to observing atomic oxygen, and this atom also exists in the stratosphere of the earth itself. This presence results in a telluric absorption or emission line in the observed spectrum, in

addition to the oxygen line from the astronomical source. [1] The telluric line is a good frequency marker in observations done with this channel of the GREAT instrument. The limit is that in the stratosphere, strong winds also exist. Due to the Doppler effect frequency of the resulting telluric line from high-velocity oxygen atoms can be Doppler shifted. This unknown possible Doppler shift increases the uncertainty of the absolute frequency of OI observations done with GREAT when using the telluric line as a frequency marker. Thus an independent stable frequency reference will improve the frequency accuracy of observations.

1.9.3 Spectral purity

Another aspect of a local oscillator is its spectral purity. In many cases in mm and sub-mm astronomy, it is the case that LO has some spurious content. An example is the CII channel of GREAT at 1.9 THz, where many spurious peaks also exist close to the primary wave in the LO. Again because LO is convolved with astronomical sources, especially in observations of strong sources, The LO 'spurs' show up in the data spectrum and can be misleading for an astronomer who wants to analyze the data.

1.10 Scope of this thesis

The introduction was done in this chapter from the astronomical point of interest and SOFIA's and GREAT instrument's point of view. This chapter also included primary content about this work's essential elements, including QCL, superlattice, and Diode multiplier chain. In the subsequent three chapters, frequency stabilization efforts from different methods are presented, each method in a separate chapter. They are Frequency locking to a methanol gas cell line, Frequency locking to a delay line (A heterodyne experiment), and phase locking efforts using the superlattice as a harmonic-mixer. Chapter 5 presents the 4.7 THz heterodyne laboratory receiver as an essential setup for the phase-locking experiment planned with the HEB as the mixer. The thesis concludes with a conclusion chapter that compares results from different methods.

[1] Word telluric has roots in Terra, which was the name of the goddess of earth in roman times.

2 Frequency Stabilization to a molecular line

Frequency stabilization using an absorption gas line is a well-known method to stabilize the frequency of lasers. This method was the first to stabilize the QCL's frequency successfully within the scope of the presented work. Principle of operation is that, in an absorption line, the slope sign changes on different sides of the minimum. This allows to detect how far and on which side of the minimum the source frequency is located. Eventually, it is possible to stabilize the laser frequency to stay at the absorption line's minimum. This chapter is dedicated to this method. In the beginning, some preliminary introductory material is presented. Method, results, and discussion follow that.

2.1 Methanol absorption line

Methanol (CH3OH) is a molecule with a complex and rich spectrum, and at THz, this rich spectrum makes the molecule interesting for frequency calibration and absorption line measurement. The dominant line broadening mechanism of methanol at pressures around one mbar combines the Doppler and pressure broadening. The Doppler broadening arises from the fact that molecules of the gas have a velocity distribution. When emitting a photon, their velocities can blue and red shift the frequency of the emitted photon, resulting in a broadened line. Since the velocity profile of molecules in the gas is a Gaussian profile, and the Doppler shift is a linear function with respect to velocity, the same Gaussian distribution is also reflected in the line shape. Doppler broadening is in-homogeneous because not all contributing molecules are affected in the same way. For FWHM of the Doppler broadened line, one can write (Gordy & Cook, 1984):

$$\Delta\nu_{1/2}^{D} = \nu_0 \times 7.15 \times 10^{-6} \times \sqrt{\frac{T}{m}} \tag{9}$$

presenting the FWHM of Doppler broadened line as a function of the line frequency ν_0, T being temperature in Kelvin and m being the molecular mass in the atomic mass unit (amu). For methanol at room temperature, this results in an FWHM of 10.4 MHz for lines at 4.75 THz. In addition to the Doppler broadening, pressure broadening is also relevant for this experiment. This broadening arises from the disturbed coherence of the emitting molecules due to the short average collision time of the molecules. Pressure broadening results in a Lorentzian line profile and is, in contrast to Doppler broadening, a homogeneous broadening mechanism. For the Lorentzian line shape, one has:

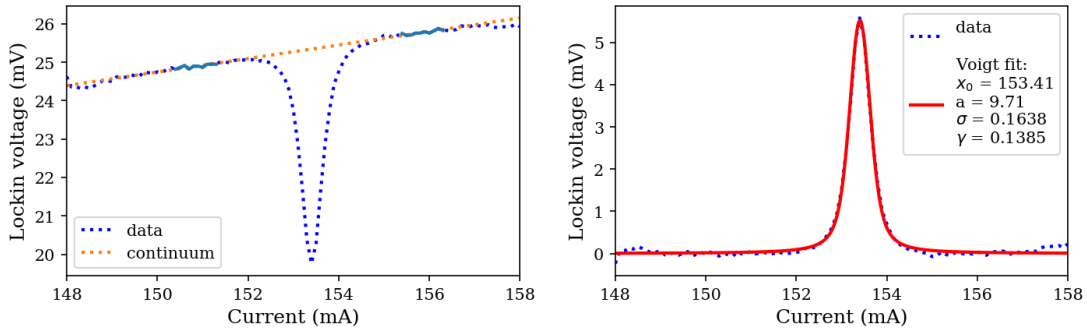

Figure 32: Left: dotted blue curve is the raw measurement from the absorption line used in this chapter. With the help of the solid blue parts where the absorption line has vanished, the dotted orange line is fitted to help the continuum subtraction of the absorption line. Right: dashed blue curve is the reversed continuum subtracted data, and the solid red curve is the Voigt function fit.

$$S(\nu, \nu_0) = \frac{1}{\pi} \frac{\gamma}{\gamma^2 + (\nu - \nu_0)^2} \tag{10}$$

with γ being Half Width at Half Maximum of the Lorentzian line. At low pressures, the linewidth of a pressure-broadened line is expected to be a linear function of pressure. Combination of the Doppler and pressure broadening leads to a Voigt line profile. For example, for the absorption line used in this chapter, a Voigt function could be fitted, which is visible in figure 32. The methanol pressure for this measurement was 1.2 mbar. The σ and γ of the fit correspond directly to the Gaussian and Lorentzian widths. Since current tuning of the laser is used to scan the lines, the initial current values are shown, instead of having them converted to frequencies. Assuming a current tuning value of 34.2 MHz/mA, the 10.4 MHz Doppler broadened line is expected to appear with $\sigma = 0.13$ mA, which is close to the value from the fit. Measurements at different frequencies has determined different pressure broadening constants for methanol (P. Minguzzi, Tonelli, Carrara, & di Lieto, 1985) (Eichholz et al., 2013) (Slocum, Xu, Giles, & Goyette, 2015). One should remember the following points: 1) the real methanol pressure is unknown since the vacuum gauge does not have a methanol calibration curve and, 2) QCL is additionally broadened by unknown shape and value, due to the different broadening mechanisms.

As a side product, the experimental setup of this chapter has made it possible to investigate the linewidth of the methanol line as a function of the methanol pressure. Albeit the real methanol pressure stays unknown, the experimental data could be interesting for molecular physics. Figure 33 presents this result. Interestingly, the y-intercept agrees with the expected 0.3 mA Doppler broadening of the methanol line.

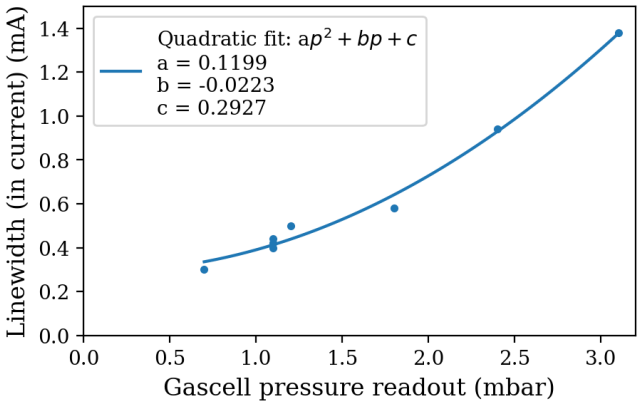

Figure 33: Solid dots present the measured linewidth of a methanol absorption line as a function of pressure gauge readout. The solid line is a fit of a quadratic function to the data.

2.1.1 Role as frequency discriminator

In this experiment, the role of the absorption line is to form a frequency discriminator to detect the QCL frequency disturbances against it. Suppose a tiny current modulation is applied in addition to the Direct Current (DC) that the QCL needs to operate. In this case, a small frequency modulation is created due to current frequency tuning. Figure 34 left helps in understanding this. With the tiny current modulation being applied to the QCL, if there is an absorption line at the operating current/frequency of the laser, the output power from the gas cell will show variations with the following results (table 9):

Far from the absorption line, there is no amplitude modulation. However, there is amplitude modulation around the center of the absorption line with a sign change at the line center. Measurements of the resulting amplitude modulation are best realized with a Lock-In Amplifier (LIA) that compares the amplitude and phase of the resulting amplitude modulation with the original frequency modulator current, producing the derivative signal. One can look at this as a fast frequency modulated signal that probes the transmission's slope through the gas

QCL frequency	**result**
far away lower	no amplitude modulation
in the line slope but lower	amplitude modulation with opposite phase
at the line center	no amplitude modulation
in the line slope but higher	amplitude modulation in phase
far away higher	no amplitude modulation

Table 9: The result of passing a frequency modulated signal through a gas cell with an absorption line within the frequency span of the source (QCL). The source frequency is referenced to the frequency of the absorption line center.

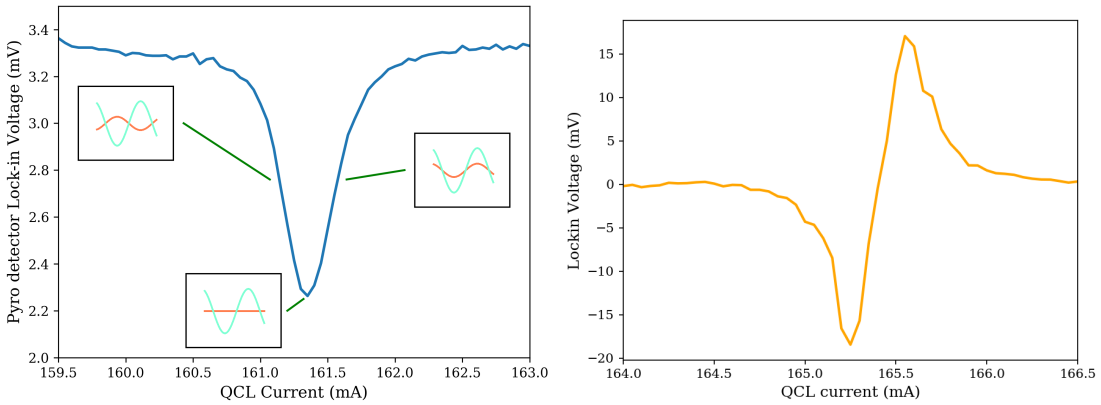

Figure 34: Left: the absorption line, with insets showing the effect of frequency modulation (in cyan) and the resulting amplitude modulation (in red) at the gas cell's output. Note the change in the sign of the resulting amplitude modulation. Right: same absorption line, measured in the first derivative with the help of frequency modulation and detection with a Lock-in amplifier. In the middle, where the high slope line passes the zero, is where the absorption line center is located and where the QCL frequency lock will settle.

cell. An example of the produced derivative signal can be seen in figure 34 right. Table 10 presents some of the relevant numbers about the methanol line and the formed derivative slope from the HEB current monitor output.

2.2 Experimental Setup

The experimental setup consists of cold cryogenic parts and warm room temperature ones. The QCL and the HEB (here used as total power detector) are both cooled to cryogenic temperatures inside the cryostat. The gas cell is filled with methanol and is located between the QCL and the HEB detector. There are also some electronics to drive the QCL, to form the control loop, and to read the HEB's output. A detailed schematic can be seen in figure 35.

QCL needs cryogenic temperatures to be operable, requiring a cryostat that houses the QCL: to provide the QCL with low temperature and extract the heat that the QCL generates. Since the experiment is needed to be operational for

parameter	**value**
frequency	4784620.463 ± 0.122 MHz
lower state energy	570.1880 cm^{-1}
upper state degeneracy	51
typical measured derivative slope	170 $\frac{mV}{mA}$

Table 10: A summary of parameters regarding the methanol line. Data obtained from JPL database for molecular spectroscopy (Jet Propulsion Laboratory (JPL) database for molecular spectroscopy, 2022)

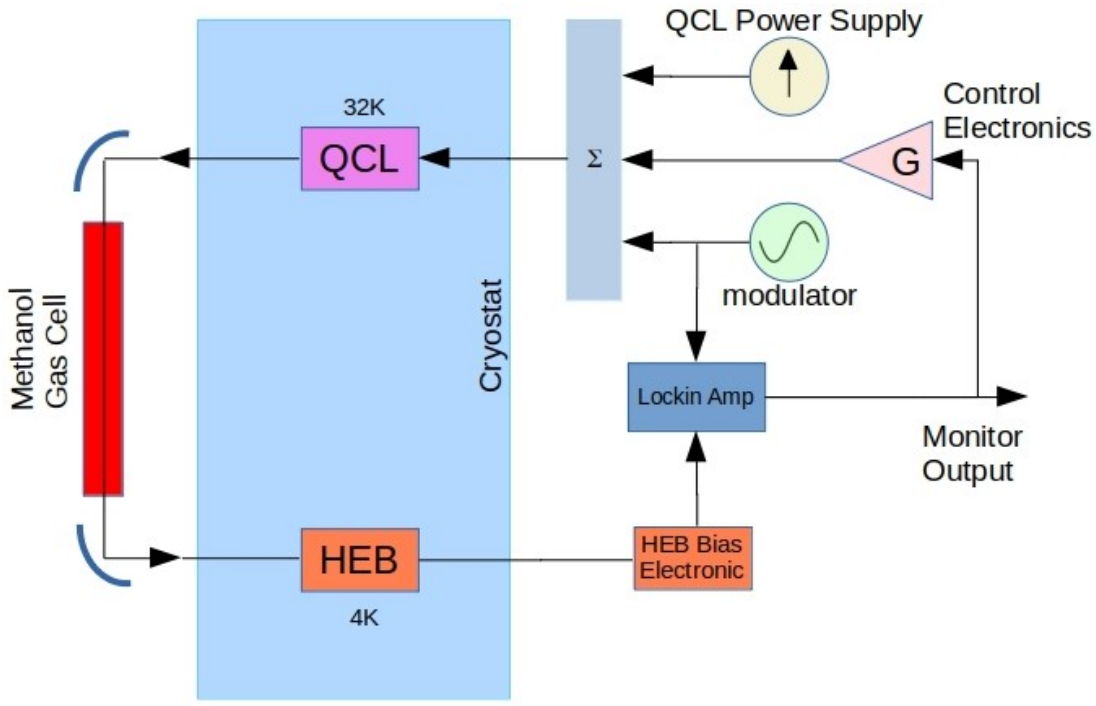

Figure 35: Schematic of the methanol absorption line frequency stabilization experiment. The blue area represents the cryostat environment providing 32K to the QCL and 4K to the HEB detector, enabling them to operate. The yellow disc represents the constant current power supply to drive the QCL; the green disc represents the modulation signal applied to the QCL to form the frequency discriminator; and the box with sigma represents the summing box that adds the three incoming currents. The third signal is the Lock-in amplifier's output, which is further processed in control electronic to correct QCL frequency disturbances.

a long time, a closed cycle pulse tube refrigerator was the choice of the cooling machine. Based on this choice, the development of the cryostat has been done, as presented in chapter 5. The critical fact is that the QCL is cooled, and its thermal power dissipation is managed. Thanks to the mechanical isolation, this design reduces the forced motions of the pulse tube at the QCL; Nevertheless, not entirely. The QCL is housed close to the pulse tube's first cooling stage with a stable temperature of 33 K.

An HEB detector has also been integrated in the same cryostat from the beginning. As a side possibility, the HEB is also usable and is used here as a THz total power detector. Similar to the QCL, the HEB detector also needs cryogenic temperature, and it is housed close to the 2nd stage of the pulse tube at a stable temperature of 4.3 K. Electric current for the QCL as well as the bias voltage of the HEB are inserted to the cryostat with the help from a vacuum feedthrough. The optical beam from both QCL and HEB are guided outside the cryostat using a couple of cold mirrors: on top of the QCL chip and on the side of the HEB detector.

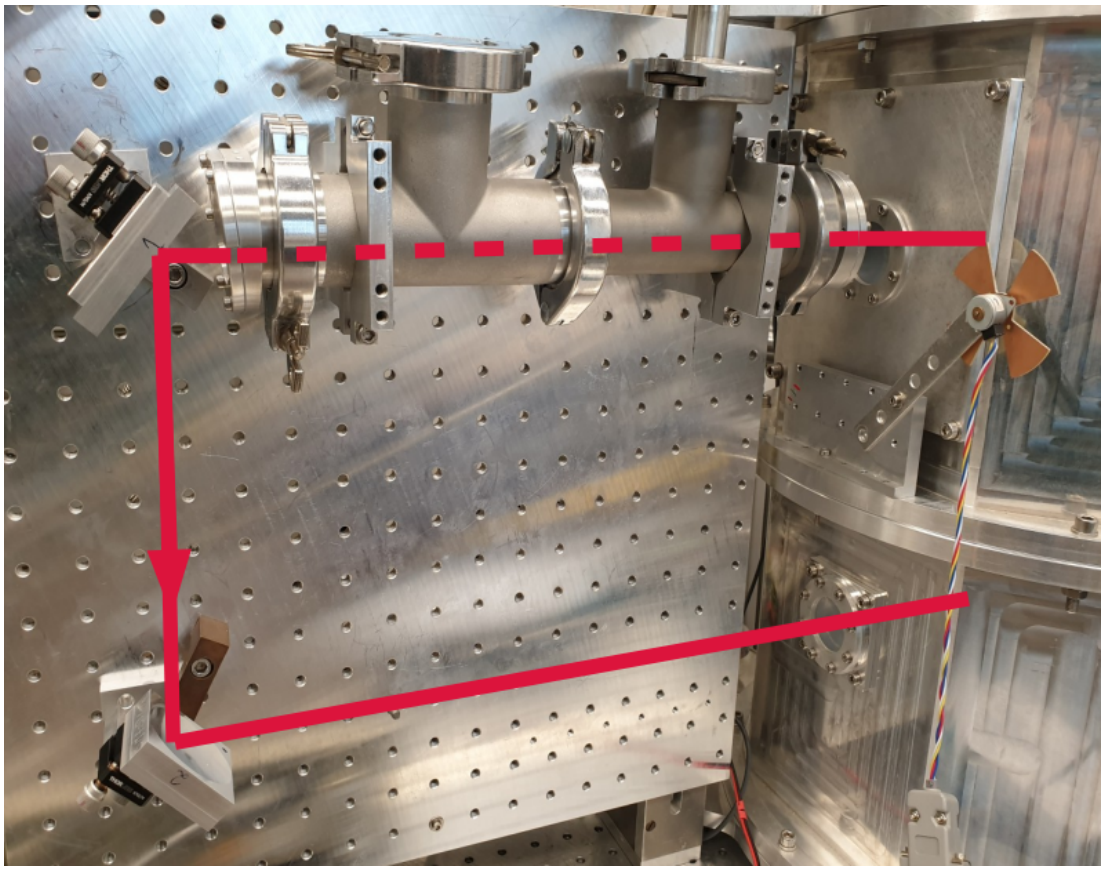

Figure 36: Part of the experimental setup. Cryostat with the QCL and the HEB windows are visible on the right side. The beam path is marked with a thick red line, and the part passing through the gas cell is dashed. The Gas cell, as evident, is located in the top middle, and the two mirrors to reflect the beam are on the left.

2.2.1 Gas cell

Directly after the cryostat QCL window, the methanol gas cell is horizontally placed in the beam. Using a long gas cell in a horizontal position meant that the QCL beam had to travel long away from the cryostat. The same also implied that the beam had to travel back for total power detection by the HEB detector. Luckily the powerful QCL and sensitive HEB detector could overcome the beam attenuation caused by the air. The gas cell via a long vacuum hose was connected to a quad vacuum splitter, with three other ways connected to 1) the methanol container via a needle valve, 2) Leybold TRIVAC D4B rotary pump via a gate valve, and 3) the MPT100 Pirani vacuum gauge. In order to fill the gas cell with methanol, first, both valves were opened such that all contamination and residual gases were evacuated. After a few minutes, both valves were closed, so the gas cell was clean and evacuated. At last, the needle valve was used to open in regulated steps such that a small amount of methanol got into the gas cell. Table 11 briefs some of the numbers regarding the gas cell. It is also worth mentioning

parameter	value
Length	31 cm
Window diameter	4 cm
Window material	High Density Poly Ethylene (HDPE)
Leakage rate	0.08 $mbar/h$
typical methanol pressure	1.1 mbar

Table 11: A summary of parameters regarding the gas cell.

that a shorter gas cell was also tried with vertical installation, resulting in a more compact setup. Nevertheless, the resulting frequency locking could have been more satisfactory because of the weak frequency discriminator due to weak absorption depth.

2.2.2 Optics

The need for a horizontal long gas cell resulted in adding two mirrors in the setup. They were not specially designed for this experiment but were found suitable such that HEB could receive enough THz radiation. All vacuum windows of this experiment have been chosen to be HDPE due to its higher transmission compared to PTFE and silicon windows. For the alignment, the laser beam was always detected with the help of a pyroelectric detector. The pyroelectric detector was small and usually held with hands, and it was easy to move it around the expected beam position and check for maximum detected value. To maximize the beam coupling to the HEB detectors and regulate it, fine adjustment screws of the mirror stages were used.

2.2.3 HEB as a total power detector

The total THz power that the HEB receives in constant voltage bias strongly affects the device's bias current, this is the detection principle. Similar experiments of gas line QCL frequency stabilization with the help of HEB as a total power detector have been demonstrated earlier for QCLs at lower frequencies (Ren, Hovenier, et al., 2012) (Ren, Hayton, et al., 2012). The critical feature of the HEB for this experiment is the low-noise nature of this detector with Noise Equivalent Power (NEP) $\sim 10^{-12} - 10^{-13} W/\sqrt{Hz}$ (van Marrewijk et al., 2015). HEB has only one IF port, which is where both bias DC and the measured IF frequency band are carried along. The essential bias-T electronic that separates these two was integrated into the bias-T at the input port of the HEB's Low Noise Amplifier (LNA). From there, the HEB bias lines were all connected to one of the DB25 vacuum feed-throughs of the cryostat via thin phosphor bronze wires, finally leading to the HEB bias box.

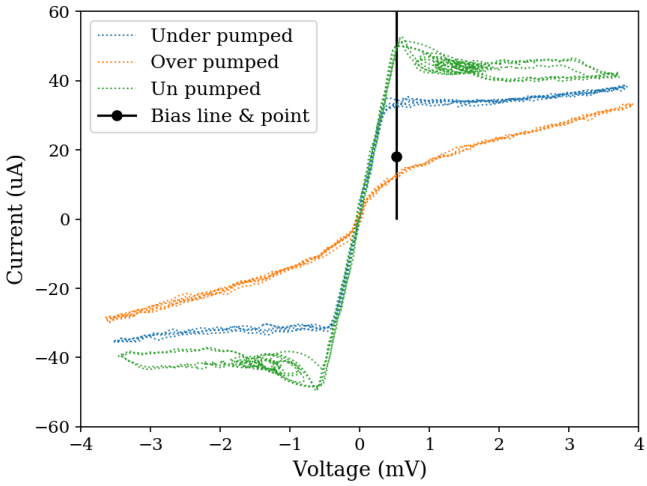

Figure 37: The IV curve of the HEB as a function of the total THz pump power for three cases, including without pump power, under-pumped, and over-pumped device. The solid vertical line shows the bias line of HEB for this experiment, illustrating how different THz power results in different HEB currents. The hysteresis behavior of the HEB for the unpumped curve is also notable.

The primary function of the HEB bias box is to provide a safe tiny current or voltage bias to the HEB. The bias box also provides buffered and amplified voltage and current monitor outputs as replicas of the corresponding quantities. For this experiment, the current monitor output is taken as an indirect measure of the total THz power incident on the HEB. The monitor outputs are created with the help of instrumentation operational amplifiers (OPAMPs); therefore, the noise generated in these OPAMPs was also present in the output. At a selected bias voltage, the current monitor output reacts to the incident THz power as the following: with a large amount of THz power, the current of the HEB is minimum (HEB is over-pumped). With reduced THz power, the current rises until a limit, where any further decrease in THz power results in HEB entering the hysteresis region of the superconducting device, where oscillations dominate the current, and the voltage from the current monitor output is not stable anymore. The current of the HEB becomes more sensitive at lower power levels. Optical beam coupling was used to set the device at lower bounds, but the hysteresis was avoided. Figure 37 presents the IV curve of the HEB at different currents, showing the possibility of total power detection at a chosen particular voltage bias. The hysteresis region of the device is also visible as regions with round curves on the unpumped trace. The stable bias point of HEB for QCL stabilization experiment can be found in table 12.

parameter	value
V_{HEB}	0.53 mV
I_{HEB}	18 uA

Table 12: Exemplary bias point of HEB when the QCL frequency is locked to the methanol line.

2.2.4 QCL power supply, oscillator and summing box

Since QCL frequency is voltage tunable, any noise density present in the supply current will modulate the frequency of the laser and, in turn, will result in extra line broadening. Therefore a dedicated low-noise power supply was developed in-house to produce the low-noise current to drive the QCL. The main element of the current supply is an IRLIB9343 Metal Oxide Silicon Field Effect Transistor (MOSFET) that is used as a tunable constant current source for the QCL.

In subsection 2.1.1, it was introduced that for the scheme of frequency stabilization with an absorption line, one has to apply a small modulation on the QCL current/frequency. This tiny modulation originates from a sinusoidal waveform generated with a laboratory signal generator. The amplitude of this signal determines the maximum frequency deviation of the QCL due to this modulation, and its frequency is chosen to be away from the known strong laboratory noise sources. The QCL line broadening due to the applied frequency modulation can be estimated with Carson's rule (Oppenheim et al., 1996):

$$BW = 2K_i\Delta i \tag{11}$$

with K_i being the current tuning constant of QCL and Δi being the amplitude of the modulating current, BW is approximately the frequency band that contains 98% of the QCL's power. The modulator waveform is fed to the QCL's current via a resistive current combiner, and at the same time, it is sent to the Lock-in Amplifier as a reference signal. Table 13 briefs some of the parameters related to the frequency modulator.

parameter	value
modulation frequency f_m	70 Hz
modulation amplitude A_m	310 mV
expected peak frequency deviation Δf	2.12 MHz

Table 13: Parameters of intentional modulation to form the frequency discriminator to detect the QCL frequency.

parameter	value
τ_{pre}	10 ms
τ_{post}	none
coupling	DC
sensitivity	5 mV
Dynamic range	low
50 Hz filter	on
100 Hz filter	on

Table 14: Parameters set on the lock-in amplifier to demodulate the QCL frequency disturbances and to generate the final correction signal.

2.2.5 Lock-in amplifier

The Lock-in Amplifier (LIA) completes the role of slope detection. It checks the amplitude and phase of the HEB's current monitor output against the original modulator phase. Therefore with its help, a slowly varying voltage appears at the output as:

1. zero when QCL frequency coincides with the methanol absorption line frequency
2. negative when QCL frequency is below the absorption line center frequency
3. positive for QCL lasing at a higher frequency than the absorption line's center

This voltage waveform is a demodulation of QCL frequency disturbances and can be used directly to stabilize the QCL frequency. It only needs a sign conversion, considered in the LIA reference phase settings. The voltage is then fed back to the QCL, creating a correction current that pushes or pulls the frequency of QCL in such a way that it always stays around the absorption line's center frequency. The applied settings on LIA are listed in table 14.

2.3 Result

The unlocked QCL showed strong periodicity with a period of 580 ms, corresponding to 1.72 Hz, the same as the pulse tube period, at the demodulator output which is visible in the red trace of figure 38. The trace shows sharp spikes on both negative and positive sides, happening close to each other, and during the rest of the time, the QCL frequency stays within a smaller variation range. Such a waveform can be understood as a result of pulses from the pulse tube, creating disturbances when each pulse of Helium is released at the core of the cryostat and mechanically disturbs the setup. With the availability of the demodulator

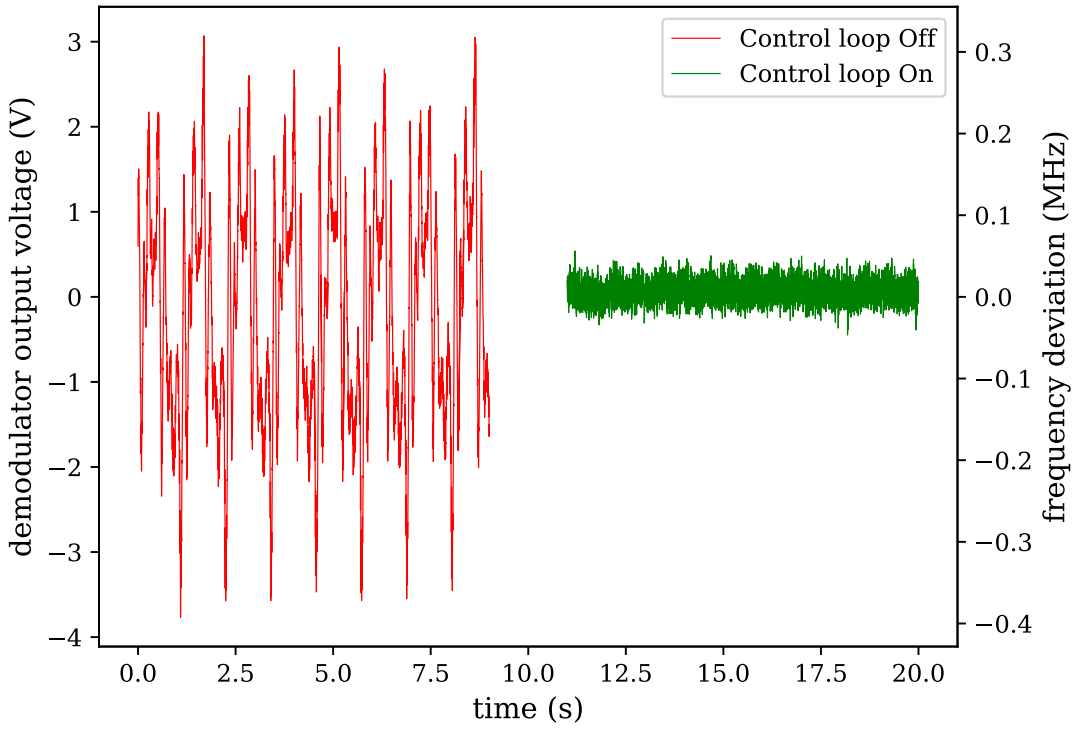

Figure 38: Frequency demodulator output. Red trace: showing the frequency disturbances that QCL suffered without a stabilization control loop. Green trace: the same measurement but with the stabilization control loop in action.

output signal, after the help of a variable gain buffer stage, the correction signal to be injected into the correction port of the resistive current combiner was made. As a result, the control loop was complete, and stabilization was achievable. The green trace of figure 38 shows the resulted demodulator output when the control loop is complete and detected disturbances are used for a live correction. Comparing the traces shows how frequency stabilization reduced the strength of the disturbances.

2.3.1 effect of stabilization in frequency domain

With the Fourier analysis, a periodic set of short pulses in the time domain results in many harmonics in the frequency domain for the demodulator output's signal. The FFT measurement function of the oscilloscope helped with the frequency domain measurement, and figure 39 shows the spectra. Many harmonics of the pulse tube up to a modulation frequency of around 20 Hz are visible. The stabilization effect is evident by comparing the two plots: the power of the disturbance peaks are reduced by at least 20 dB, a factor of ten in demodulated voltage. Since it is shown in subsection 2.1.1 that close to the absorption line, the demodulator output voltage has a linear relation with frequency deviation from the absorption line's center; it can be concluded that closing the control loop has reduced the

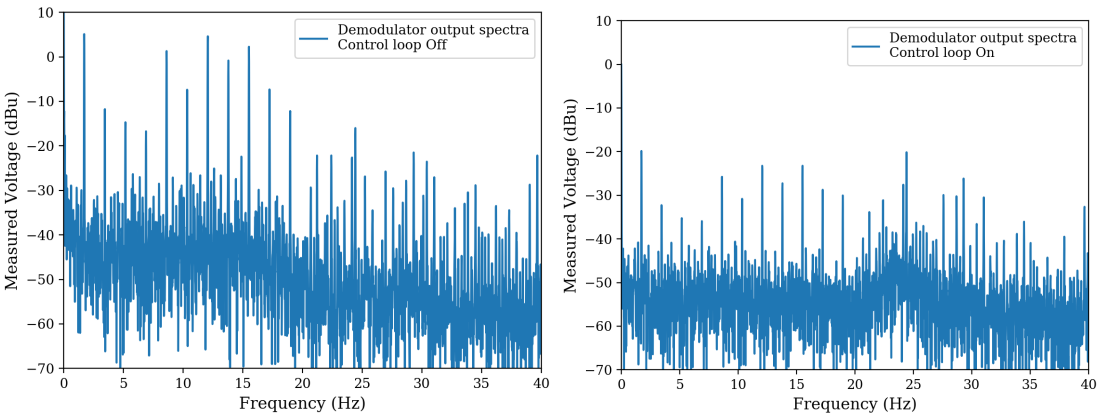

Figure 39: The spectra of the demodulator output. Left: in case of not stabilized QCL, showing solid and rich harmonic content from the pulse tube. Right: harmonics' strength are reduced by at least 20 dB for frequency-stabilized QCL.

parasitic disturbance harmonics in the laser frequency by a factor of at least ten. Still, one should consider that in this analysis, the frequency demodulator range itself is limited. Therefore it can be that stabilization is, in fact, much more effective than this estimation. In addition to the parasitic harmonics, the noise floor of the frequency-modulated components is also reduced by 10 dB. Last but not least, the low-frequency drifts of the unstabilized QCL, which show on the left curve of 39 in the vicinity of 0 Hz, are also removed in the stabilized plot, meaning that the stabilization of frequency has compensated the slow frequency drifts of QCL.

2.3.2 frequency deviations

Figure 40 presents histograms for the identical waveforms of figure 38. The plot on the left shows the line shape for the unstabilized QCL, which consists of a couple of dominant peaks plus a broad tail, far from an excellent real laser line shape. In contrast, the right plot shows how the correction of frequency instabilities changes the disturbed line shape into a single line that resembles a Gaussian. The Full Width at Half Maximum (FWHM) can be investigated as a quantifying measure. From the presented plots, one can read an FWHM = 3.07 V and FWHM = 0.34 V for the unstabilized and stabilized QCL lines, respectively. Since the voltage variation range here is smaller than the expected linear range of frequency demodulators, one can consider them as unstabilized and stabilized QCL line shapes, excluding the demodulator-induced line broadening.

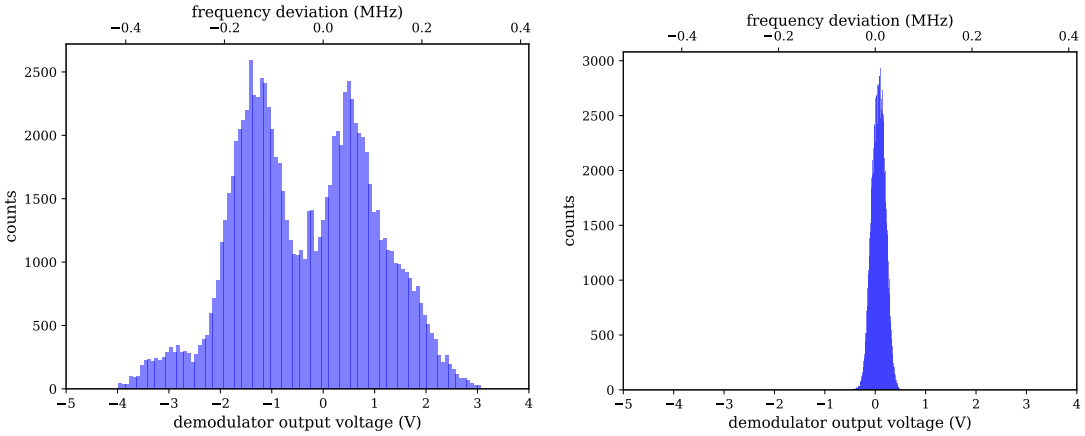

Figure 40: Histograms of the signal at the output of the frequency discriminator. Left: the unlocked QCL shows a wide spread of demodulator voltage corresponding to the original frequency spread and disturbances of the QCL. Right: locked QCL shows a much narrower demodulator signal spread.

2.3.3 Total linewidth estimation

In the past subsection for locked QCL linewidth, an estimation of FWHM = 0.34 V was found, with a demodulator constant of 9.6 V/MHz, corresponding to an FWHM of 36 kHz. One should be careful that this value contains contributions from all the disturbances on top of QCL frequency after stabilization, but excluding the modulator component. As described in subsection 2.2.4, the sinusoidal waveform is used to frequency modulate the QCL to form the absorption line frequency discriminator with the help of the LIA. Both linewidths are present for the final stabilized QCL linewidth: the modulator broadened component and the residual from the stabilization method. Only as an approximation, one can consider Carson's bandwidth as the FWHM of modulator-induced frequency deviations. With this, one can put an upper limit for the total QCL linewidth as:

$$FWHM^2_{total} = FWHM^2_{modulator} + FWHM^2_{residual} \tag{12}$$

When numbers are applied, an FWHM of 2.12 MHz is found, identical to the modulator-induced line broadening. This means that the modulator broadening fully dominates the linewidth in this experiment.

2.4 Limitations

In this section some of the main limitations of this experiment are presented.

2.4.1 HEB current monitor output noise

The limiting noise source for this experiment is the noise present in the HEB bias box's current monitor output. Since the HEB is cooled to cryogenic temperature, it is expected to create little noise on the bias current. However, the device's very small current is extracted from the cryostat, and an OPAMP reads the current value. This room-temperature OPAMP generates some noise that stays present in this experiment. For similar experiments, an HEB bias box with a low-noise current monitor readout design would be preferable.

2.4.2 Gas cell leakage and absorption line selection

The gas cell had a relatively large leakage and could not keep the methanol pressure constant. Additional air leaking into the cell creates additional collision with methanol molecules resulting in broader linewidth, which decreases the absorption line frequency discriminator slope. In the performed experiments, this effect has been the limiting factor regarding stabilization time. Nevertheless, stabilization of about 10 minutes was still achievable. For improvement, a professional low-leakage gas cell would be advantageous. Another factor has been the length of the gas cell and available strong absorption lines in the spectrum of the gas. Before reaching saturation, the stronger the absorption line, the higher the frequency discrimination slope. A direct method of obtaining a deeper absorption line would be to increase the gas cell length. As seen in the plots of figure 34, the absorption line of choice has a relative depth of about 30%. This means that the gas cell's length could be doubled to achieve an absorption line depth of 60% while still far away from line saturation. A more compact gas cell design that still keeps the path length long can be useful for compact setups (Higgins, Teyssier, Pearson, Risacher, & Trappe, 2010).

2.5 Further possibilities

There are many possibilities for improving this experiment. Any low-noise, not very slow (at least 40 Hz of bandwidth), total power detector can replace the HEB detector. For example, cooled Ge-Ga detectors have been shown to be a good option (Richter, Pavlov, et al., 2010). There have even been reports on using a room temperature pyroelectric detector ($NEP \sim 10^{-9}W/\sqrt{Hz}$) in similar works (van Marrewijk et al., 2015). A good low-noise detector electronic will make a difference as well, since essential for an excellent high signal-to-noise ratio. A good signal-to-noise ratio also means achieving good results with smaller signal values. This means the modulator amplitude can be reduced, so the QCL line broadening from the modulator can therefore be reduced. Regarding the gas

cell, the length of the cell, selection and pressure of the gas, and finally, careful construction to avoid significant leakages are points one can consider to improve. With the choice of stronger absorption lines and longer path length through the cell, even using a multiple reflection cell, apart from helping in the compactness of the setup, helps for further reduction in the modulator's amplitude, improving the total linewidth of the QCL.

3 Delay Line Frequency Stabilization

This chapter presents the method of delay line frequency discrimination used to stabilize the frequency of a QCL. In contrast to the last chapter, this method uses a heterodyne beat note from the QCL and a synthesized and harmonic-generated reference wave, where the frequency of the beat note still carries the instability of the original QCL emission. This unstable ∼GHz signal can be used in a feedback loop to correct the QCL frequency's instabilities. In short: this method is powerful and robust: a laser linewidth of less than a MHz could be achieved while keeping the laser frequency locked for hours. [2]

3.1 Description of Method

As presented in chapter 2, the cryostat houses the QCL, and a cold mirror couples the QCL's emission to the outside. Outside the cryostat, two warm mirrors couple the QCL beam into the high-frequency input horn of the Superlattice Device (SLD) harmonic generator and mixer block. This horn serves the role of the Radio Frequency (RF) port when SLD operates as both a harmonic generator and mixer. A diode multiplier chain generates a continuous wave at 182.5 GHz that enters the SLD's Local Oscillator (LO) waveguide port and pumps it. The multiplier chain itself receives input from a precision centimeter wave synthesizer. The SLD generates the 26th harmonic of 182.5 GHz at 4.745 THz and, at the same time, acts as a mixer to mix this with the power received from the QCL via the diagonal horn of the device (Renk et al., 2006). The product of the mixing is the beat note of the two signals, which is present at the IF output of the SLD and is used for frequency stabilization.

The signal level of the beat note at the output of the SLD is very small, in the order of a pW or even less. First, this tiny signal should be amplified in a chain of amplifiers so that power and voltage levels are large enough to be handled and used. Such an intermediate frequency (IF) chain serves different roles to amplify the beat note signal, filter the surrounding noise, monitor the power levels continuously as a means of system performance and a measure of signal to noise, copy the frequency band of interest in an IF band monitor output to measure the performance of frequency stabilization and status of the experiment.

At the output of the IF chain, the signal is large enough and ready for frequency stabilization with the help of a frequency discriminator. A power divider divides the signal into two paths. One path directly goes to a radio frequency

[2] From the work presented in this chapter, a journal paper (Mahdizadeh et al., 2023) and a conference proceedings paper (Mahdizadeh et al., 2022) have been published. The same figures of this chapter have been used in these two papers.

mixer which is playing the phase comparator/detector role. The other path goes through a delay line of length L, thus being delayed by τ, and then it ends with the other mixer input. The mixer multiplies the two and produces a voltage sensitive to the two inputs phase difference. A frequency sum product of the two also exists, which is not interesting and is dumped in some way. If the incoming frequency deviates, the signal's phase at the delay line output also deviates; thus, the final phase differences at the mixer change. This, in turn, results in a change in the output DC from the mixer. Equation (13) presents this idea:

$$\Delta V(f_m) = K_{FD}\Delta f(f_m) \tag{13}$$

in this way, deviations of the output voltage from zero ΔV at any given rate are proportional to the frequency deviation at that rate $\Delta f(f_m)$ of the incoming signal, with K_{FD} being the frequency discriminator proportionality constant. This demodulation scheme can be used for Frequency Modulation (FM) measurement and frequency stabilization applications.

After detecting the frequency deviations, it is easy to correct them via the current tuning effect of the QCL. After amplification and bandwidth limitations, there is a voltage there that can be fed back to the QCL current, locking its frequency and eliminating the frequency drifts and disturbances. This process has been presented in more depth in the following sections, with experimental results to follow.

3.2 Some relations and concepts from frequency modulation theory

As a starting point, let us imagine an oscillator continuously oscillating at a frequency of f_c, called the carrier frequency (often such a signal carries a message or a signal using modulations). Here the amplitude of this continuous wave is fixed and denoted with V_c. The oscillator's frequency is variable and Frequency Modulated (FM); for example, a sinusoidal of frequency f_m is the modulating function. The output voltage of such an oscillator can be written as (product note 11729C-2, 1985) (Robins, 1991):

$$V(t) = V_c \sin(2\pi f_c t + \frac{\Delta f}{f_m}\sin(2\pi f_m t)) \tag{14}$$

the term $\frac{\Delta f}{f_m}$ is such written, so if one calculates the derivative, the left carrier frequency is deviating sinusoidally with a frequency of modulation frequency f_m and with maximum frequency deviation of Δf. Quantity:

$$\beta = \frac{\Delta f}{f_m} \tag{15}$$

is defined as such and is called the FM modulation index and presents the maximum angle deviation that the oscillator will experience from the nominal carrier phase. The equation for V(t), which now is in the form of:

$$V(t) = V_c \sin(2\pi f_c t + \beta \sin(2\pi f_m t)) \tag{16}$$

can be rewritten in terms of Bessel first order functions as:

$$\begin{aligned} V(t) = \sum_{n=-\infty}^{\infty} J_n(\beta)\ \cos(2\pi f_c t + 2\pi n f_m t) \\ = J_0(\beta)\ \cos(2\pi f_c t) \quad + \\ J_{-1}(\beta)\ \cos(2\pi(f_c - f_m)t) \quad + \\ J_1(\beta)\ \cos(2\pi(f_c + f_m)t) \quad + \\ J_{-2}(\beta)\ \cos(2\pi(f_c - 2f_m)t) \quad + \\ J_2(\beta)\ \cos(2\pi(f_c + 2f_m)t) \quad + \\ \ldots \end{aligned}$$

since for small x values it is possible to approximate $J_n(x)$ with:

$$\begin{aligned} J_0(x) &= 1 \\ J_{-1}(x) &= J_1(x) = x/2 \\ J_{-2}(x) &= J_2(x) = 0 \quad \text{and for n} > 2 \end{aligned}$$

the relation 16 can be rewritten as:

$$V(t) = V_c[\sin(2\pi f_c t) + \frac{-\beta}{2}\sin(2\pi(f_c - f_m)t) + \frac{\beta}{2}\sin(2\pi(f_c + f_m)t)] \tag{17}$$

which says for small modulation indexes, there will be two sidebands of amplitude $\frac{\beta}{2}$ smaller than the carrier, appearing at frequency offsets of f_m above and below the frequency of the primary signal at f_c. Figure 41 shows an actual measurement of such a case where a continuous wave is frequency modulated at a small modulation index. For quantity Γ which is called Single Side Band (SSB) to carrier ratio, as long as frequency modulation is involved, one can write:

$$\Gamma = \frac{P_{SSB}}{P_c} = \frac{\beta^2}{4} = \frac{\Delta f^2}{4 f_m^2} \tag{18}$$

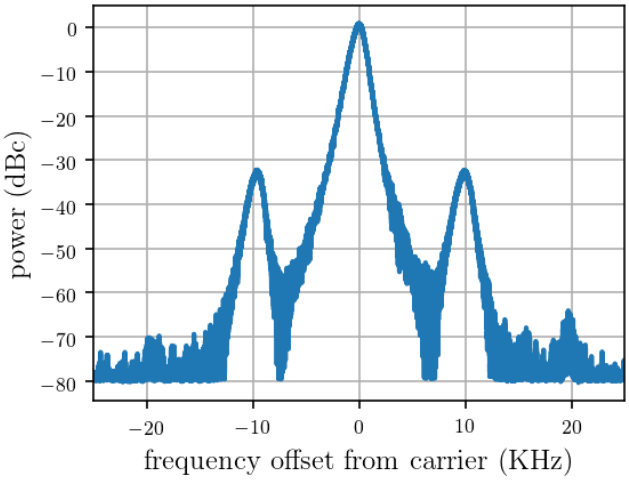

Figure 41: Modulation sidebands are the results of frequency modulation. This plot shows a 32 dB difference from carrier to sidebands at a modulation frequency of 10 kHz from the carrier. This difference corresponds to a modulation index of 0.05, i.e., the maximum frequency deviation (Δf) was 500 Hz.

note that if a frequency demodulator is in hand, Eq. (13) implies that a sinusoidal voltage appears at the output of the frequency demodulator. At the same time, quantities such as Γ and f_m can also be measured, revealing the importance of Eq. (18) for calibration matters.

3.2.1 Delay line frequency discriminator

Figure 42 represents a block diagram of a delay line frequency disciminator. The incoming voltage has an amplitude of V_0 and a carrier frequency of f_c. It is frequency modulated at a frequency of f_m with a maximum frequency deviation of Δf. Eq. (14) showed the mathematical representation of such a wave:

$$V(t) = V_c \cos(2\pi f_c t + \frac{\Delta f}{f_m} \sin(2\pi f_m t)) \tag{19}$$

As the block diagram shows, a power divider separates the signal into two paths with equal amplitude, and the delay line delays the path for the RF input of the mixer by the amount of τ. At mixer inputs of RF and LO, one has:

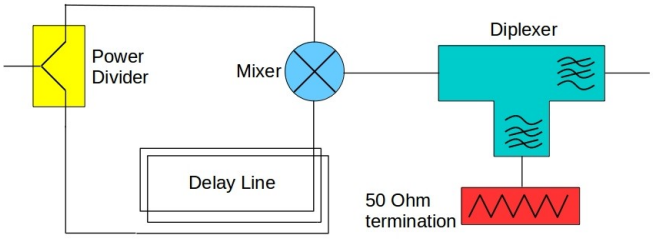

Figure 42: Block diagram of a delay line frequency discriminator

$$
\begin{aligned}
V_L(t) &= \frac{V_c}{\sqrt{2}}\cos(2\pi f_c t + \frac{\Delta f}{f_m}\sin(2\pi f_m t)) \\
V_R(t) &= \frac{V_c L}{\sqrt{2}}\cos(2\pi f_c (t-\tau) + \frac{\Delta f}{f_m}\sin(2\pi f_m (t-\tau)))
\end{aligned}
\tag{20}
$$

the mixer multiplies the two waves, which creates products with sum and difference of phase terms as:

$$
\begin{aligned}
V_m(t) = \frac{V_c L K_L}{2\sqrt{2}}[\cos[2\pi f_c(t-\tau) \quad + \\
\frac{\Delta f}{f_m}\cos(2\pi f_m(t-\tau)) \quad - \\
2\pi f_c t) \quad - \\
\frac{\Delta f}{f_m}\cos(2\pi f_m t)] \quad + \\
\cos(sumterms)]
\end{aligned}
\tag{21}
$$

Later in the calibration section of the phase locking chapter, it will be shown that the amplitude of such a beat signal is simply the phase detection sensitivity of the mixer in the given configuration, and for a consistent notation, this is denoted by K_ϕ. When these signal passes the diplexer, the sum terms which contain high frequencies at around twice the f_c are separated and dumped into a 50 Ohm load to prevent back reflections and standing wave. The output of the diplexer contains only the low-frequency parts:

$$
\begin{aligned}
V_F(t) = K_\phi[\cos[2\pi f_c(t-\tau) \quad + \\
\frac{\Delta f}{f_m}\cos(2\pi f_m(t-\tau)) \quad - \\
2\pi f_c t) \quad - \\
\frac{\Delta f}{f_m}\cos(2\pi f_m t)]]
\end{aligned}
\tag{22}
$$

which simplifies to:

$$
\begin{aligned}
V_F(t) = K_\phi[\cos[-2\pi f_c \tau \quad + \\
\frac{2\Delta f}{f_m}\sin(2\pi f_m \tau)\sin(2\pi f_m(t-\frac{\tau}{2}))]]
\end{aligned}
\tag{23}
$$

The delay line frequency discriminator is supposed to work with carrier frequency

meeting the quadrature condition meaning that:

$$2\pi f_c \tau = \frac{\pi}{2} \tag{24}$$

after applying this to eq. (23), one can write:

$$\begin{aligned} V_o(t) &= K_\phi \cos[-\frac{\pi}{2} \quad + \frac{2\Delta f}{f_m} \sin(\pi f_m \tau) \sin(2\pi f_m (t - \frac{\tau}{2}))] \\ V_o(t) &= K_\phi \sin[\frac{2\Delta f}{f_m} \sin(\pi f_m \tau) \sin(2\pi f_m (t - \frac{\tau}{2}))] \end{aligned} \tag{25}$$

for the case of small modulation indexes, $\frac{2\Delta f}{f_m} < 0.2$ and the argument of 1st sine is always small, meaning that it can be replaced by its phase as:

$$V_o(t) = K_\phi \frac{2\Delta f}{f_m} \sin(\pi f_m \tau) \sin(2\pi f_m (t - \frac{\tau}{2})) \tag{26}$$

the last sine is the time variable part, and the rest is the signal's amplitude as a function of frequency deviation. Here the usefulness of the frequency discriminator becomes clear. For the transfer response, one has:

$$\Delta V = K_\phi 2\pi \Delta f \frac{\sin(\pi f_m \tau)}{\pi f_m \tau} \tag{27}$$

for the cases where modulation frequencies are small enough, the later fraction also merges to one, leaving:

$$\begin{aligned} \Delta V &= K_\phi 2\pi \Delta f \\ &= K_{FD} \Delta f \end{aligned} \tag{28}$$

with the frequency discriminator constant being K_{FD}.

3.2.2 Similarities with Michelson interferometer

The presented delay line frequency discriminator is similar to a Michelson interferometer with unequal arms. The power divider separates the input signal in two paths, like a beam splitter in a Michelson interferometer. Then the wave travels through one non-delayed path, and another delayed one, similar to a non-equal arm-length interferometer. The mixer that mixes the two signals resembles a Michelson interferometer's beam splitter/combiner. However, in contrast to them, there is no non-linearity involved in a Michelson counterpart, which adds the two beams on top of each other. Through the delay line, the signal's frequency is preserved. However, it creates a phase shift which is a function of wavelength in the cable, and there are wavelengths that the phase difference is $\pi/2$ for them

(The zeros). The mixer output is zero for those wavelengths, while other frequencies/wavelengths experience non-$\pi/2$ phase differences, resulting in negative or positive DC voltages at the mixer's output. In conclusion, the operation is similar to a Michelson interferometer, where the intensity of the central fringe varies with wavelength variation.

3.3 Calibration

This section examines two different approaches to calibrate the delay line frequency discriminator. The first method utilizes a frequency sweep, whereas the second method feeds a known FM modulation to the frequency discriminator. In both ways measuring the response to these known input signals reveal the frequency discrimination constant.

3.3.1 Frequency sweep calibration

The frequency sweep method is straightforward: since it is a frequency discriminator, it produces different voltages at different input frequencies. One can vary the input frequency in a known way, like a frequency sweep, and then measure the output of the discriminator. Figure 43 shows the result of such a test. A single frequency sweep is fed in, and output voltage variation is measured. Points in which the output voltage is zero are frequencies that the mixer is in quadrature (Eq. (24)), meaning:

$$\phi_{LO} - \phi_{RF} = \pi/2 \tag{29}$$

At this condition, the discriminator has the most sensitivity, meaning that

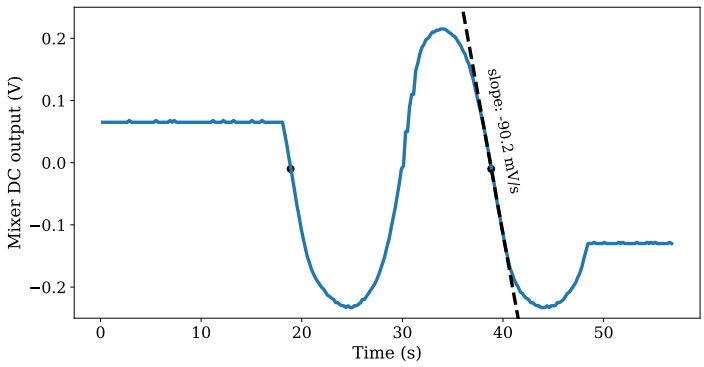

Figure 43: The delay line frequency demodulator responds to a single frequency sweep generated with a synthesizer. Sweep starts with the frequency of 385 MHz at t = 18.11 seconds and ends with the frequency of 415 MHz at t = 48.55 seconds. It can be seen that close to the zero mixer DC voltages, the slope of output voltage versus frequency (which, due to sweep, is linearly increasing with time).

the slope of voltage changes over time - due to the sweep of frequency - is also the slope of voltage changes over frequency. In the shown measurement, 30 MHz is swept in 30.44 seconds. From the slope measurement, one can write:

$$K_d = \frac{\Delta V}{\Delta t}\frac{\Delta t}{\Delta f} = 91.5[mV/MHz] \tag{30}$$

meaning that for every MHz that the input frequency changes around zero frequency, the output DC voltage will vary by 91.5 mV.

3.3.2 Frequency modulation calibration

This calibration method sends a signal with known frequency modulation to the frequency discriminator, and the resulting output voltage is measured. Relating the input FM parameters and the output voltage is the calibration of the frequency discriminator. From relation (15) one has:

$$L_{cal} = \frac{P_{SSB}}{P_c} = \frac{\beta_{cal}^2}{4} \quad = \frac{1}{4}\frac{\Delta f_{cal}^2}{f_{m,cal}^2} \tag{31}$$

with L_{cal} as single sideband to carrier ratio of calibration signal, Δf_{cal} being maximum frequency deviation of calibrating signal and $f_{m,cal}$ being modulation frequency of calibration signal product note 11729C-2 (1985). To perform a

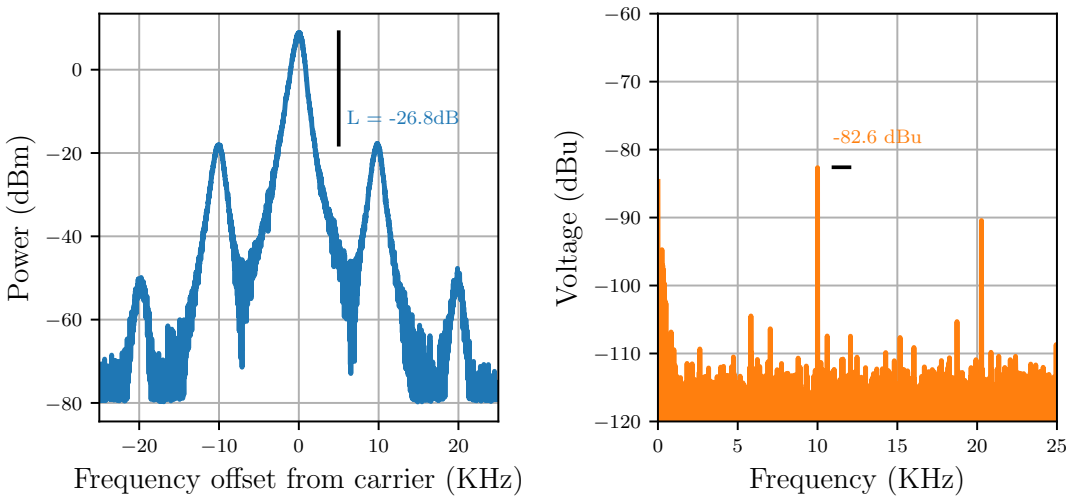

Figure 44: An example of measurements taken for FM calibration of the delay line frequency discriminator. Left: input spectrum of a frequency modulated wave at a modulation index of 0.1 and modulation frequency of 10 kHz with the resulting $\sim$ -27 dB of SSB/Carrier ratio. Right: Measured baseband spectrum at the output of the frequency demodulator revealing the modulation component at a modulation frequency of 10 kHz. The peak at 20.3 kHz is not a modulation product but from an interfering source in the lab, staying constant even with modulation frequency changes.

calibration, frequency modulation with a small modulation index is created ($\beta < 0.1$). First, the sideband to carrier ratio is measured on the spectrum analyzer. From the definition of the frequency discriminator constant, one has:

$$K_d^2 = \frac{\Delta V_{rms}^2}{\Delta f_{rms}^2} \tag{32}$$

After sending the calibration signal to the discriminator, at the output, a sinusoidal voltage shows up with an amplitude of ΔV_{rms} at the modulation frequency. Combining with Eq. (31) one can write:

$$K_d^2 = \frac{\Delta V_{rms}^2}{2 f_{m,cal}^2 10^{\frac{L_{cal(dB)}}{10}}} \tag{33}$$

Figure 44 shows an example of such calibration measurement. Repeating this for different modulation indexes is presented with different calibration points in the right plots of 44 with a value of 91.2 ± 3.9 mV/MHz as a result of the frequency discriminator constant, which is in good agreement with the value from the previous method.

3.4 Experimental setup

This section spreads some of the experimental setup's aspects. The schematic of figure 46 shows a block diagram of the experimental setup. Pumping the SLD is

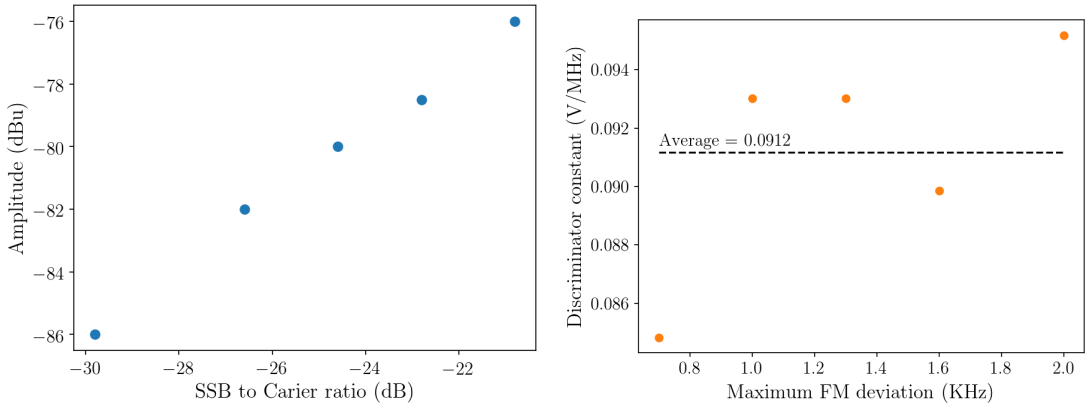

Figure 45: Calibration results from the frequency modulation (FM) method. Left: Points are taken by varying the modulation index at a fixed modulation frequency of 10 kHz. (Figure 44 corresponds only to one of these points). Note that they are all within the small modulation index approximation. The ratio of measured voltage amplitude at the output and the Single Side Band to Carrier ratio is a function of frequency discriminator constant, plotted on a logarithmic scale to resemble a line. Right: the resulting discrimination constant is plotted versus maximum FM deviation, with the average in a dashed line.

essential for performing harmonic generation and mixing. For this, a laboratory synthesizer followed by a diode multiplier chain (VDI, 2009) pumps the SLD. The diode chain increases the synthesizer's frequency through multiplication, in this case by a factor of 16. Within the SLD acting as a harmonic generator, the 26th harmonic of its input, itself 16 times the f_{synth}, is generated. The high-frequency QCL wave is then down-converted in the SLD, also playing the role of a mixer and producing the down-converted QCL signal in the SLD's IF output. This IF signal is filtered and amplified in the IF processor, preparing it for frequency discrimination. As presented earlier, a delay line, a mixer, and a diplexer form the frequency discriminator. Doing such, frequency deviation information is present on the DC and low-frequency voltages in the output. This low-frequency content is then shaped and amplified in control electronics to correct the frequency instabilities of the QCL by feeding it back to the QCL on its supply line. Figure 47 shows a fraction of the experimental setup.

3.4.1 Temperature stabilization

It will be discussed in section 3.6 that during the first runs of the experiment, the thermal runaway was a limiting phenomenon and revealed the importance of temperature stabilization, which has been done using the Cryocon temperature controller model 44C. The cryocooler being on all the time, continuously cools the QCL. In this situation, turning on and off a 50 Ohm power resistor installed next to the QCL as a heater allows the temperature controller to keep the temperature more constant at a slightly higher temperature. For this, a set of Proportional, Integral, and Derivative (PID) constants had to be chosen for the Cryocon controller. These parameters work within the following relation to

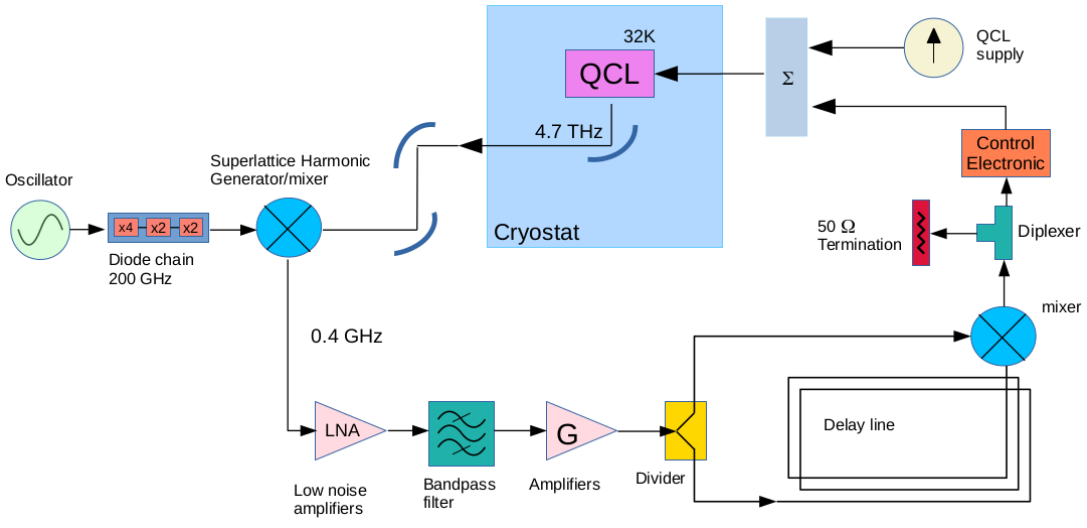

Figure 46: Schematic of delay line frequency stabilization experiment.

Constant	Value
P	15.00
I	55.50
D	7.93

Table 15: Proportional, Integral and Derivative (PID) constants for Cryocon temperature controller to stabilize the QCL bath temperature.

keep the temperature more constant:

$$p(t) = k(P\ T + D\ \frac{dT}{dt} + I\ \int_{t_0}^{t} T(\tau)\, d\tau) \tag{34}$$

where p(t) is the heat being dissipated on the thermal bath of the QCL to regulate the temperature denoted as T. The built-in auto-tuning of the Cryocon instrument helped to determine the constants. Table 15 presents the list of them.

Figure 48 presents sample results of uncontrolled versus controlled QCL bath temperatures. The temperature-controlled QCL bath still shows a standard deviation of 3.5 mK for temperature variations. This is the thermal footprint of the pulse tube, which is fast enough that the large thermal capacity of the bath

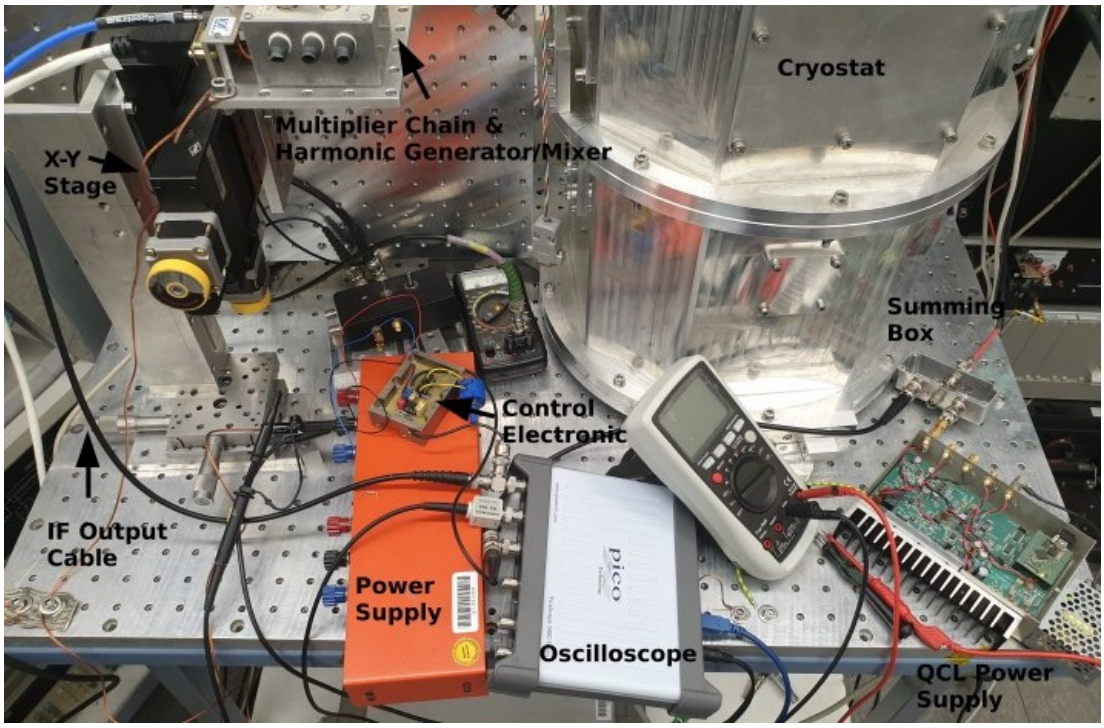

Figure 47: Photograph of the experimental setup table. Signal and noise come from the IF output cable to the control electronics on the table. The signal finally leaves the table after the summing box via the thin black line with a red starting, which contains the DC and correction currents for the QCL.

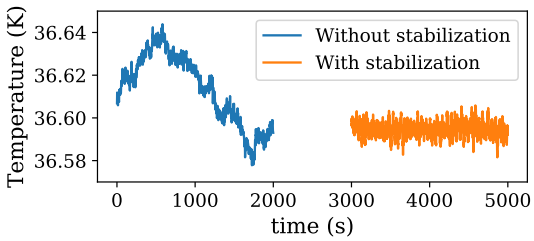

Figure 48: Comparison of longtime drifts of the QCL bath temperature with and without temperature controller. 0.3 Kelvin is subtracted from the stabilized trace to place it next to the uncontrolled trace.

does not allow the temperature controller to compensate it, because of the large thermal mass.

3.4.2 Intermediate warm optics

Chapter 5 presents the details of optical design for the 4.7 THz laboratory receiver. This experiment shares the cold parts of QCL optics up to the cryostat window. Outside, this experiment utilizes a warm flat mirror to reflect the QCL beam into a second warm but active mirror that focuses the emission into the horn of the SLD. Figure 49 presents a diagram of the experiment's optical arrangement (the high-frequency section). The SLD's horn is heavily over-modded, and no beam waist can be assigned; This experimental setup experimentally produced a better signal in the SLD's IF output. Table 16 presents the optical parameters.

3.4.3 Synthesizer, Diode multiplier chain and the Superlattice device

QCL frequency calibration revealed the QCL frequency to be 4748.6 GHz. Wishing an IF frequency at 0.4 GHz in the upper sideband fixes the LO frequency

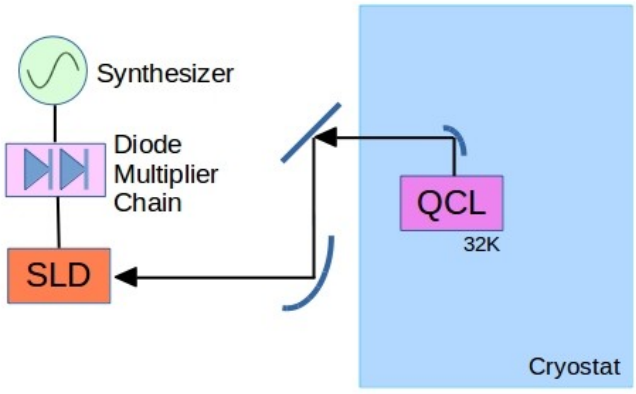

Figure 49: Schematic of the optical elements and the high-frequency part of the experiment.

Table 16: Optical parameters of the delay line experiment setup.

parameter	**value**
QCL beam waist	61 μm
distance to the QCL mirror	17.0 mm
QCL mirror focal length	16.1 mm
distance to the intermediate flat mirror	142.5 mm
distance to the SLD mirror	44 mm
SLD mirror focal length	53.6 mm
distance to the HEB beam waist	47 mm
SLD beam waist	undefined

of the SLD to 4748.2 GHz, which is created at the 26th harmonic of the diode multiplier chain output. This determines the Diode multiplier chain frequency to be 182.6224 GHz, from which, together with a multiplication factor of 16 in the diode multiplier chain, the synthesizer frequency at 11.4139 GHz can also be deduced. With the synthesizer's power set to 17 dBm, with slight changes, no observable change in the down-converted QCL signal was visible, meaning that this 50 mW of power was large enough to operate the diode multiplier chain in saturation. Moreover, power measurements revealed that the attenuation voltage of $V_{att} = 1.25V$ set on the diode multiplier chain corresponds to a pump power of 1 mW to the SLD. Table 17 briefs these parameters.

3.4.4 Intermediate Frequency settings

The power level at the IF output of the SLD for the 26th harmonic is minimal, typically less than 1 pW. The noise density at 400 MHz is around 0.1 pW/MHz, mainly from the SLD. For utmost care about this tiny signal, the first low noise amplifier (ZX60-P103 from mini-circuits) is placed to amplify the signal only a few centimeters away from the SLD. This way adds the least amount of noise, minimizes the signal loss in the cable, and prevents a highly variable standing wave pattern to be added to the IF band. After this first low noise amplifier, a longer line transfers the IF frequency band to the IF processor for further amplification, filtering, and providing monitor outputs. Figure 50 shows a photo of the IF chain.

Quantity	**Value**
f_{RF}	11.4139 GHz
P_{RF}	17 dBm
V_{att}	1.25 V

Table 17: Parameters set on synthesizer and diode multiplier chain. This enables the SLD to produce the mixing product at 0.4 GHz.

Parameter	Value/Comment
T_n of first amp	28 K
Gain of first amp	21 dB
T_n of second amp	59 K
Gain of second amp	20 dB
Total gain at 400 MHz	85 dB
Fraction of P_{mon} to P_{out}	-21 dB
Filter noise bandwidth	30.7 MHz
Filter center frequency	401 MHz
IF chain linearity status	checked: it is linear
IF chain expected frequency band	0.1 to 1 GHz
available attenuation	0 to 9 dB in 1 dB steps

Table 18: Brief parameters and specifications of the IF processor

As shown in figure 50, in the IF processor four amplifier stages amplify the signal to the needed levels for the frequency discriminator. The tunable attenuator helps to adjust the output power level in small steps of 1 dB. The directional coupler separates a small amount of power to provide IF monitor output for the spectrum analyzer and a total power measurement: the separated power from the directional coupler is divided into two equal paths by a power divider. Fi-

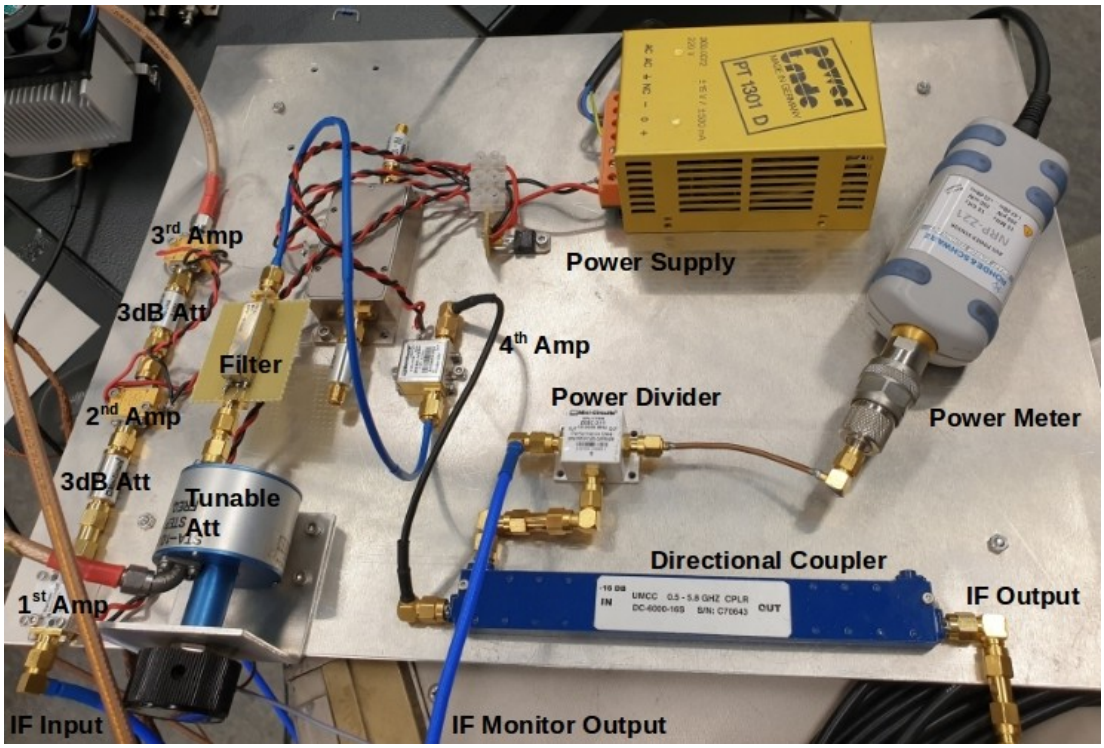

Figure 50: The Intermediate Frequency (IF) processor. Its main task is to amplify the QCL signal from the SLD's IF output while filtering out the surrounding broadband noise. This unit is placed between the SLD and frequency discriminator. Att stands for attenuator, and Amp stands for amplifier.

nally, the directional coupler's main track, which contains the most power, is optimally ready to run the frequency discriminator. Table 18 presents brief facts and specifications of the IF chain.

As mentioned, the IF filter filters out most of the broadband noise in the SLD's IF band while letting the down-converted signal pass through the experiment. For the filter, a large bandwidth will result in a severe noise level to the mixer, which may compress the mixer and reduce the delay line frequency discriminator's sensitivity. On the other hand, bandwidth should be large enough that in case of loss of lock, the unlocked QCL signal still passes through, resulting in a quick lock recapture. This experiment uses the SXBP-404+ bandpass filter from Minicurcuits, with a noise bandwidth of 30.7 MHz. The dedicated subsection on mode jumps contains a plot of this filter's bandpass (sub-section 3.6.1).

3.4.5 Delay line frequency discriminator

The goal of this sub-system is to discriminate the input frequency of the QCL signal and produce a proportional output voltage to the incoming frequency. A power divider (ZESC-2-11 from Minicircuits) separates the incoming signals into two equal paths, one of them enters the delay line.

The delay line is a 10-meter piece of RG-58/U cable. This cable type comes with Polyethylene as the dielectric material. According to its design, it should have a velocity factor (VF) of 0.66, corresponding to the wave's fractional speed of light propagation in the cable. Any given cable length permits multiple integer number of wavelength halves to fit in its total length, just like the longitudinal

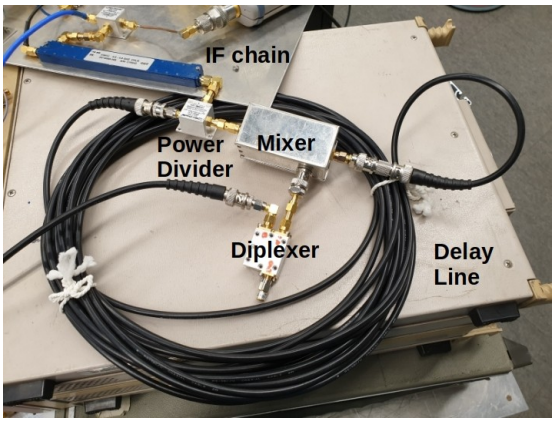

Figure 51: The frequency discriminator as implemented in the lab. It consists of a power divider with just one way passing through a lengthy cable to produce delay, and both ways end up in the balanced mixer. In order to filter the frequency sum product created in the mixer, a diplexer separates and dumps them into a matched load.

mode spacing in the cavity of a laser. For a given length, the frequency spacing of these modes, the free spectral range, is:

$$\Delta f = \frac{VF.c}{L} \tag{35}$$

which results in a frequency spacing of 20 MHz, in good agreement with the measured value of 19.7 MHz. Slight dielectric and geometric tolerances can account for the difference. Table 19 shows frequency and slope sign from some of the existing zeros (modes and modes + $\frac{1}{2}$) in the vicinity of operating frequency.

The mentioned cable length and velocity factor introduces a delay of 50.1 ns to signals traveling that path. The cable loss is measured 4.6 dB with a power meter and a synthesizer at 400 MHz. The datasheet gives an attenuation of 37.7 dB per 100 meters at this frequency, attributing 3.8 dB of the measured loss to the cable itself. The loss for connectors and cable manufacturing tolerances account for the remaining 0.8 dB Belden (2022).

An SRA-1W+ diode ring mixer from Minicircuits combines the delayed and un-delayed signals fed to the LO and RF ports (Minicircuits, 2004). This mixer exhibits an excellent conversion loss of 6 dB and a high LO to IF isolation of 36 dB at 400 MHz. The earlier relates to a larger frequency discrimination constant since it means a smaller value for K_L in the K_ϕ relation (Eq. 21). The latter prevents large output DC offset voltages Kurtz (2022).

As mentioned earlier in the theory of frequency discriminator, there is a need to filter the high-frequency components that the mixer naturally creates, especially the frequency sum-product, which shows up at twice the operating frequency at 800 MHz. A diplexer separates the high and low-frequency portions of the mixer output. High-frequency components are dumped in a 50-ohm load to prevent reflections, and the low-frequency port of the diplexer is the frequency discriminator output. Figure 51 shows the implementation of the entire delay line frequency discriminator sub-unit.

Frequency (MHz)	**Slope sign**
376.9	+
385.8	-
396.7	+
405.5	-
416.4	+
425.2	-

Table 19: Some zeros of the delay line. In the experiment, zeros with negative slope signs could stabilize the QCL frequency.

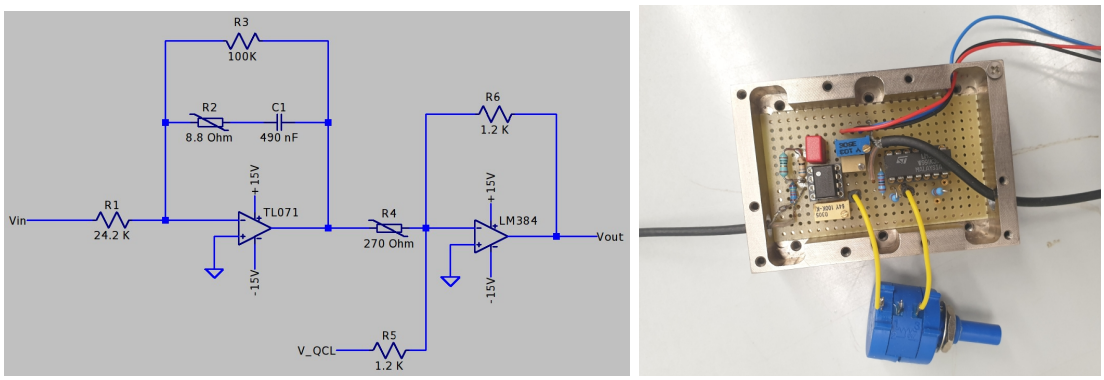

Figure 52: Left: schematic of the control electronics unit. The first OPAMP with the capacitor in the feedback path creates an integrator with low pass shape and limited gain. The second OPAMP is a variable gain block and an adding point for the DC operating offset voltage of the QCL to the OPAMP. The V_{QCL} node is the fine QCL voltage offset trimmer to set the output's offset value. Right: This figure shows the actual circuit. The signal comes in from the left via the black cable and leaves via the other black cable on the right. The blue multi-turn variable resistor is for fine gain adjustments of the setup. The yellow multi-turn potentiometer is for input offset adjustments of the first OPAMP.

3.4.6 Control Electronics

Control electronics convert the frequency discriminator output into a voltage signal that results in frequency control when applied to the QCL. The essential functions for this to happen are amplification, filtering, and managing the offsets. Operational amplifiers (OPAMPs) take over these tasks, and few potentiometers help to set the mentioned parameters manually. Figure 52 shows the schematic and photo of this sub-system.

The first OPAMP subtracts the additional offset caused by the mixer and its own input offset. It also selects a narrow band of frequencies $\sim$ 60 Hz wide starting from DC and filters out the higher frequencies. It also provides a fixed amplification to the signal. The second OPAMP provides a large tunable amplification. It also adds the control signal on top of a large desired offset voltage, such that the DC voltage of the QCL stays unchanged when attempts are made to frequency stabilize the QCL, therefore no frequency jump will happen by closing the control loop. Table 20 presents specifications of the control electronics.

parameter	**value**
Typical DC operating point	10.87 V
available variable gain	From 1 to 100
Fixed gain of 1st stage	4
Bandwidth	60 Hz

Table 20: Brief specifications of the control electronics.

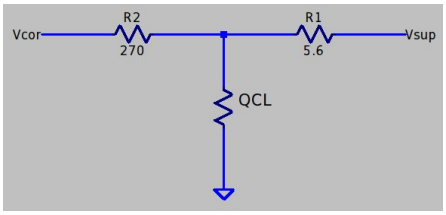

Figure 53: Schematic of the summing node to combine DC and correction currents and feed the QCL.

3.4.7 Summing box and tuning constant of the QCL

A summing box adds the generated correction current and the DC that powers up the QCL. It is as simple as a resistive current combiner. Its other role is to protect the QCL from extreme threats from the control side, such as short circuits or OPAMP saturations. Without proper protection, these can harm the QCL.

With no current from the correction port, the voltage drop across the QCL is 10.87 V; this is the number to tune the output offset of the control electronics at. Despite the DC value itself, the frequency tuning constant at the correction port is a crucial parameter for frequency stabilization of any kind. In order to measure it the set point voltage of the control electronics was varied, which resulted in a different QCL frequency. The plot in figure 54 presents this measurement.

$$K_v = 9.73(MHz/V) \tag{36}$$

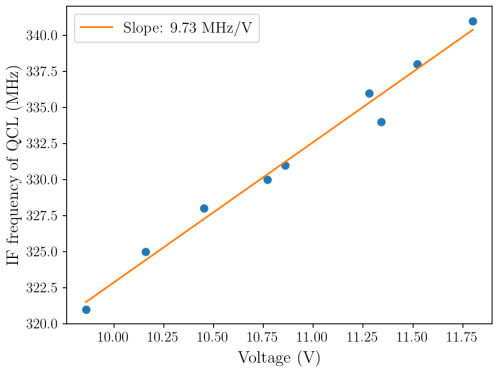

Figure 54: Measuremnet of the QCL's frequency tuning constant at the correction port. The voltage of the correction port is varied, and the corresponding change in the IF frequency of the QCL is measured on spectrum analyzer.

3.5 Results

When the experiment runs and all the necessary setting is set, the last step to close the control loop and stabilize the QCL's frequency is to increase the control

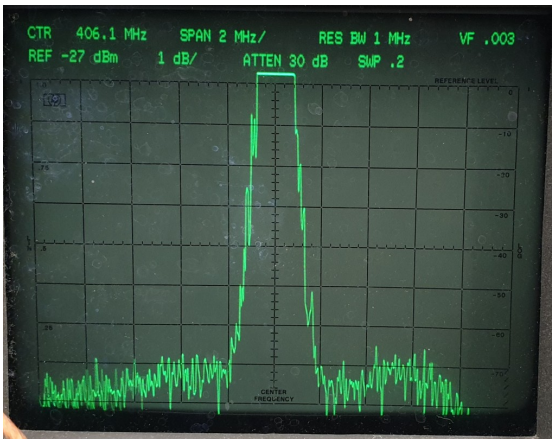

Figure 55: Frequency locked 4.7 THz QCL using a delay line frequency discriminator is visible in the center, also cropped on top. This photo is a capture from the spectrum analyzer's screen at a resolution bandwidth of 1 MHz, measuring the IF processor's monitor output.

gain. There is an upper gain range that stabilizes the QCL, while lower gains are not enough. In the middle gain settings, the amplitude of the instabilities is reduced but does not entirely vanish. Complete frequency stabilization happened only at the highest available gain, with the QCL line fully fixed in the IF monitor band. This entire process was also repeatable. Figure 55 shows the locked QCL line photographed from the spectrum analyzer's display.

In order to record the long-term behavior of the frequency stabilized line versus time, the best way is to capture the IF spectrum as a time series. a Software Defined Radio (SDR) (Nooelec SmarTee) made this possible. The SDR is tuned to the IF frequencies around 400 MHz and records a bandwidth of 2.6 MHz. The 'SDRtoRSS' software communicates the data with the SDR and integrates its vast data stream on the laptop. Simultaneously it pipes the integrated data to the 'Radio Sky Spectrograph' (RSS) software, which records and monitors the integrated data stream in a well-manageable format. Figure 56 shows a sample of such an IF measurement from the locked QCL.

In figure 56 before t = 240 seconds, the gain of the control electronics was small. With care, at the very beginning, the agile QCL line can be seen as scratches in the plot with orange color. With the sudden increase in gain at t = 240 seconds, the laser line got stable and stood at the desired frequency of 406 MHz for the remaining half an hour. The empty thin line at the center frequency is an artifact of the SDR receiver corresponding to three dead channels. The fact that stabilized frequency does not precisely match the frequency discriminator's quadrature frequency at 405.5 MHz (see table 19) is that an additional DC offset in the experiment has offset the stabilized line frequency. An observable change is also visible in the background's width, which in figure 56 roughly appears from

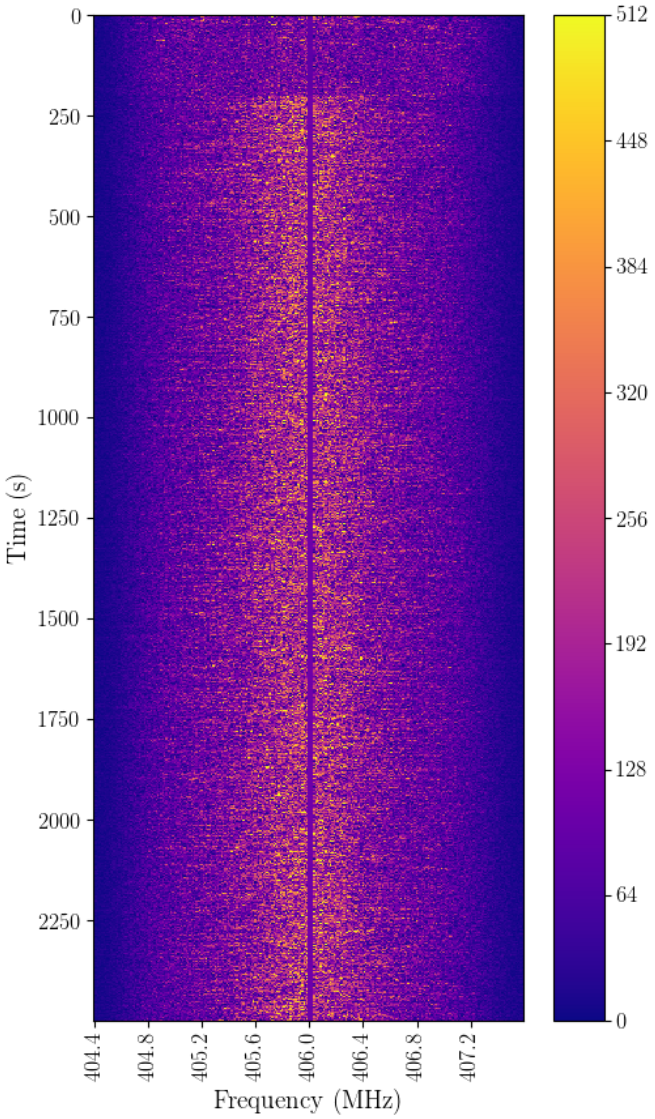

Figure 56: The waterfall spectrum of the IF frequency band vs. time shows the down-converted QCL line staying in the center when closing the control loop stabilizes the QCL frequency after t = 240 seconds. The solid narrow blue vertical line in the center is an artifact of SDR from channels that were not working.

404.8 to 407.2 MHz. The plot shows a slight but visible reduction after the frequency lock. This is understood as the concentration of the QCL energy in the center after lock, so broadened QCL line plus the frequency jitter is no further spreading its power in the IF band: causing the background to appear slightly smaller. This later can be seen more clearly in figure 57 left plot.

Figure 57 shows how a Gaussian function can be an excellent fit to the line on top of the noise floor in an integrated SDR IF measurement. THz QCLs intrinsically have a small linewidth on the order of a few kHz (REF). The measured broader linewidth arises from a large amount of noise in control electronics that also makes its way to the QCL. Initially, the SLD has added a broadband

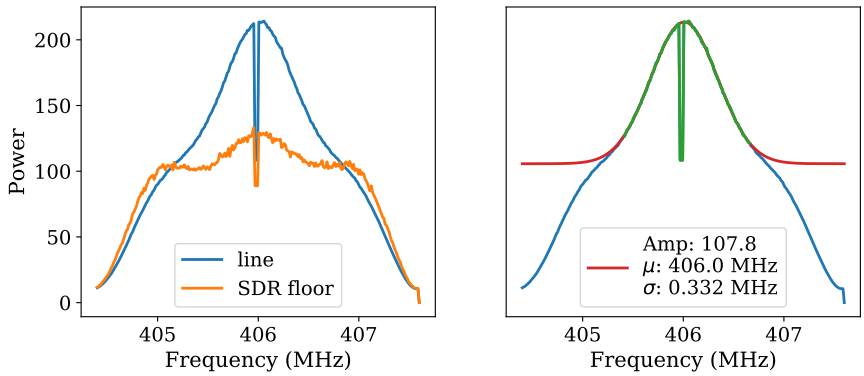

Figure 57: Left: averaged IF of floor spectrum in orange and the QCL stabilized line in blue. The fact that the line's floor is not the same as the floor measurement can arise from residual QCL emission in the floor measurement. The deep narrow dip is an artifact of the SDR receiver. Right: the same QCL stabilized line in blue. Excluding the artifacted channels, to the line part of the blue trace (shown in green) a Gaussian function is fitted (in red). The Gaussian curve gives a linewidth with an FWHM of 780 kHz.

noise to the IF, which, along with the QCL signal, is amplified and propagated through all stages in the IF and is also present at the frequency demodulator's output. When this broadband noise plus the QCL demodulated signal is used to stabilize the laser's frequency, the QCL signal cancels compensates the frequency disturbances. However, simultaneously, the noise, which initially did not exist at such a high level, broadens the QCL line. Figure 58 shows an example of the frequency discriminator's output.

At the beginning of the main plot in figure 58, large voltage deviations correspond to large frequency deviations at the frequency discriminator's input. As can be seen, this is a periodic signal with a period of 0.58 seconds (1.72 Hz, corresponding to the pulse tube cryo cooler). After t=80 seconds, the control loop is closed, and those periodic signals are no longer visible. Still, some noise is present at the demodulator's output, originating from the SLD's wide band noise and causing the QCL line broadening of 780 kHz.

More experiments were performed by inserting optical attenuators made of floppy disc film (each 3.9 dB of attenuation) in the QCL beam to study the effect of signal-to-noise ratio on the frequency locking's quality. Inserting attenuators has two effects:

1. it changes the amount of optical feedback to the laser

2. it reduces the signal-to-noise ratio

The attenuators enabled experimenting three different signal-to-noise regimes. As presented earlier, the first runs had no attenuator, with maximum optical feedback disturbances and, at the same time, with the best signal-to-noise condition.

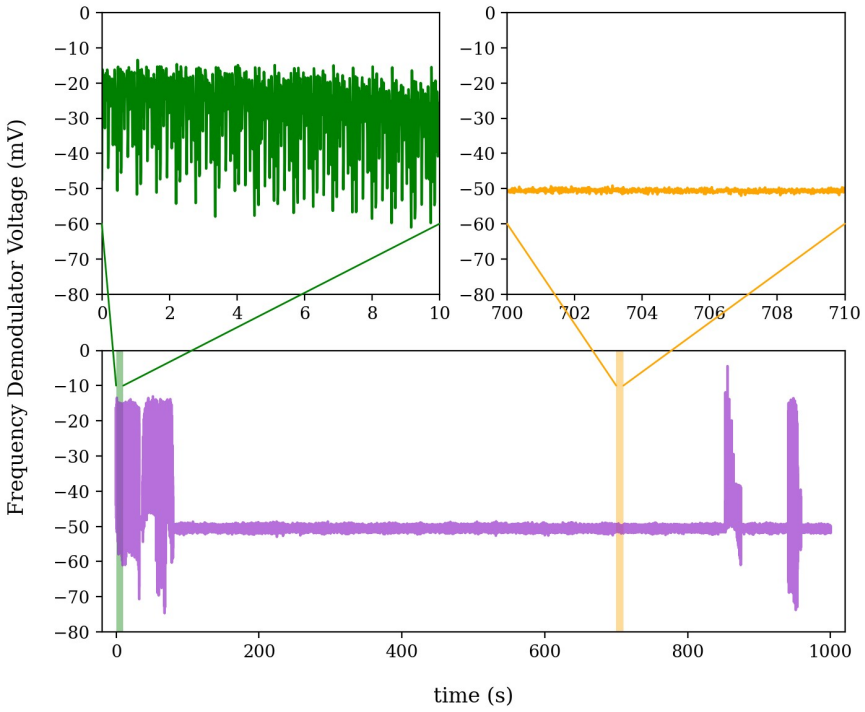

Figure 58: Example of frequency discriminator's output. In the beginning, QCL is free running, and as visible in the left-hand side zoomed subplot, the frequency discriminator gives the error information of frequency showing large deviations with a period of 0.58 seconds equal to the pulse tube period. After t = 80, an increase in the electronic control gain has stabilized the QCL's frequency, and as can be seen in the right inset, those deviations are no longer visible. At $t = 850$ seconds, a manual change in the OPAMP's offset voltage caused the OPAMP in control electronics to reach saturation voltages, so no further correction was possible to the QCL. At $t = 960$ seconds, a manual reduction in control loop's gain has unlocked the QCL for few seconds.

Afterward, tests included one and two attenuators. Figure 59 shows the spectrum analyzers view with one attenuator inserted in the QCL beam.

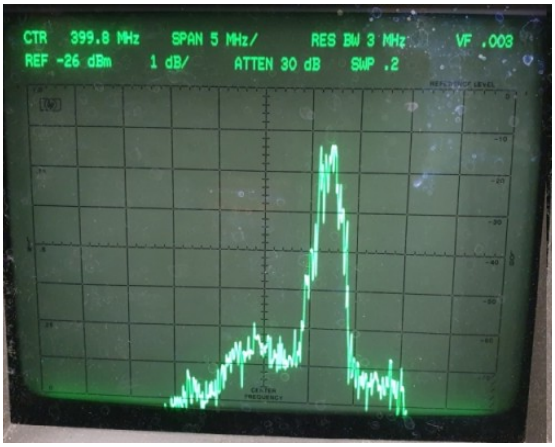

Figure 59: Frequency locked 4.7 THz QCL to the delay line at low signal-to-noise ratio, as seen in the IF.

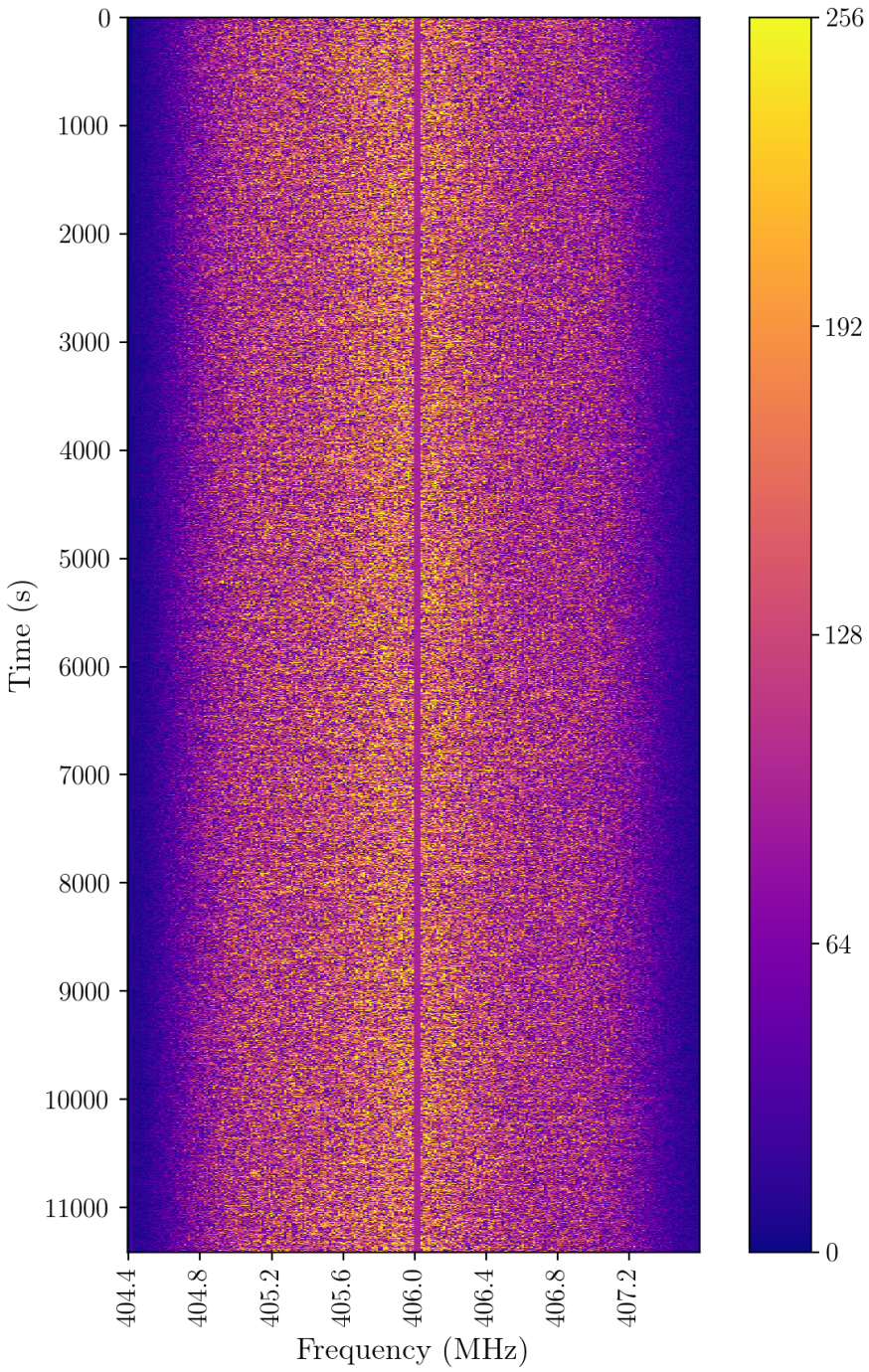

Figure 60: Waterfall plot of the IF spectrum over more than 3 hours, showing the frequency-locked QCL even at poor signal-to-noise conditions. The laser line is the faint, wide yellow vertical one. The narrow central vertical blue line is an SDR artifact.

Compared to figure 55, figure 59 shows a shorter QCL line. In both plots, the vertical scales are the same, 1dB/bin, but the frequency spans differ. At last, With two attenuators in the beam, the experiment was repeated: the signal-to-noise was the worse, but the minimum optical feedback also resulted in a smaller un-stabilized effective laser linewidth. Interestingly even with this poor signal-

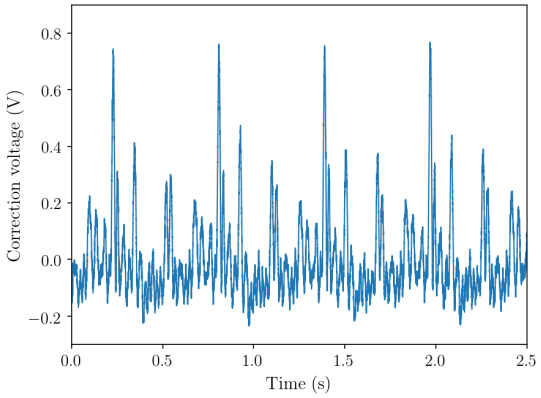

Figure 61: Example of the correction voltage waveform that is sent to the QCL. Interesting is the impulse nature of the periodic pulses.

to-noise condition of less than 2 dB over noise floor (at resolution bandwidth = 3 MHz), the experiment stabilized frequency for hours. Figure 60 shows the waterfall of the IF band in this extreme case, with the faint stabilized laser line in the center. In this case, the experiment could stay in frequency-locked condition for over 3 hours.

3.5.1 Correction signal

With the QCL's frequency controlled, the voltage at the correction port contains frequency demodulation of the QCL's frequency, containing information on the existing disturbances that the QCL is simultaneously corrected for. This voltage provides information on how the QCL would behave without frequency control. Figure 61 shows a sample of the correction voltage waveform. The high spikes can be understood as moments when a helium pulse is released into the cryo cooler

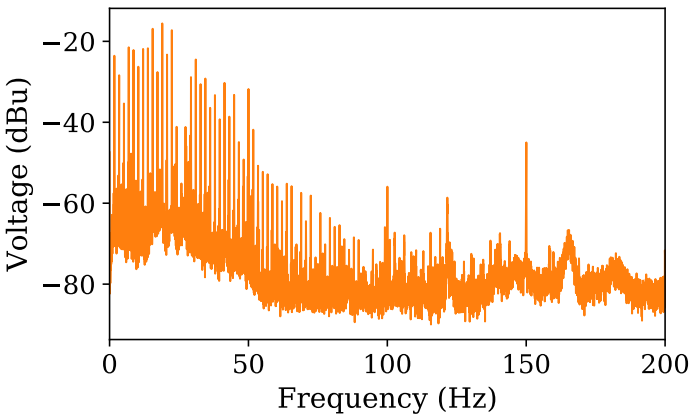

Figure 62: Spectrum of the correction voltage fed to the QCL. Harmonics of the pulse tube are visible at frequencies below 100Hz: these components are fed to the QCL to correct against disturbances from which the unlocked QCL would suffer.

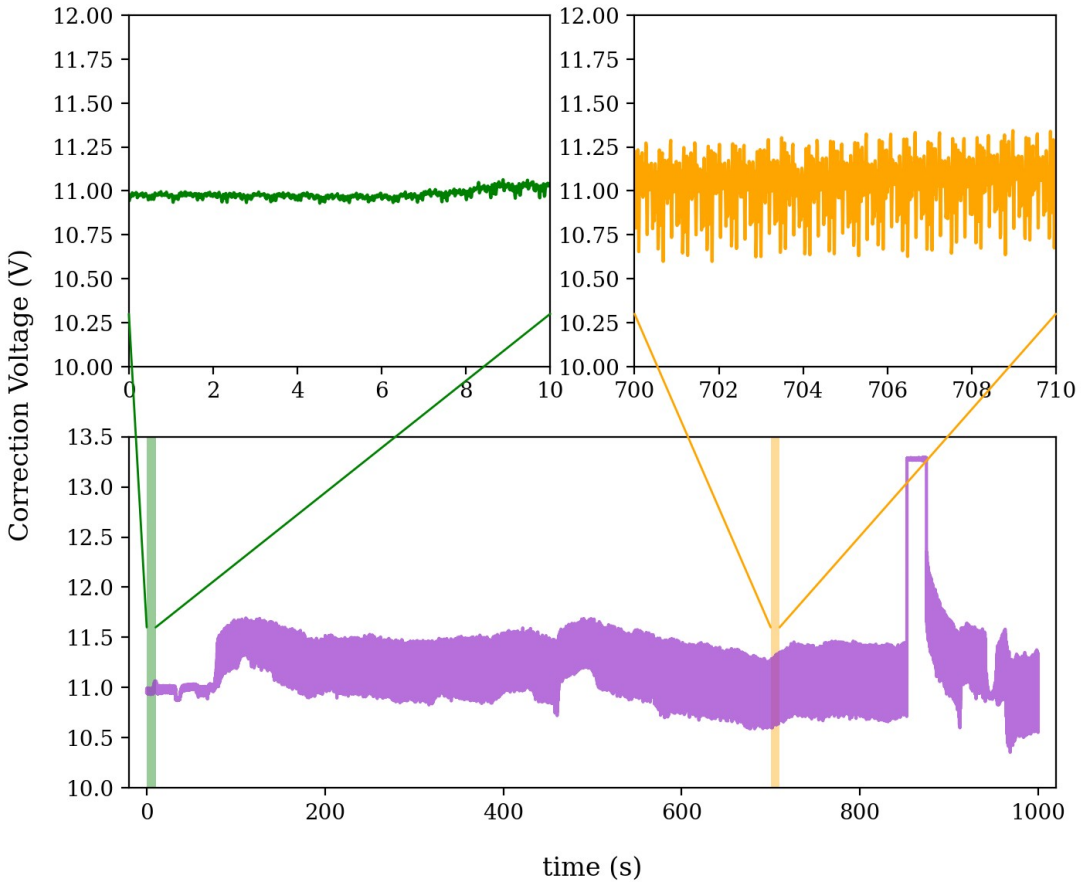

Figure 63: Waveform of the correction voltage that is fed back to the QCL. Before $t = 80$ seconds gain of the control electronics was small. As the gain increases, the correction signal's amplitude also increases, becoming sufficient for the frequency control. The periodic signal of 0.58 seconds is observable in the right inset, corresponding to the pulse tube-induced disturbances. The saturation and lowering the gain effects are also visible in the main plot here at $t = 850$ and $t = 960$ seconds, comparable with figure 58.

head, inducing relatively large mechanical movement in the cryostat resulting in a large interconnected disturbance via optical feedback. Figure 62 shows spectrum of the same correction voltage signal.

The sharp and short frequency disturbances in the correction voltage plots, as visible in figure 63, are in perfect period match with the pulse tube. This in principle can either be from mechanical and, in turn, via optical feedback or thermal fluctuations, through temperature tuning. The spectra of the demodulated disturbances, such as visible in figure 62, reveal a rich harmonic content up to even the 50th harmonic of the pulse tube. Such a rich harmonic content can not result from the thermal fluctuations of the QCL thermal bath. That is because the QCL thermal bath has a large thermal capacity resulting in a significant thermal time constant, and can therefore not follow any fast thermal changes.

In contrast to the figure 61 which showed a zoomed view of correction voltage

Table 21: The standard deviation of the frequency discriminator and the correction voltage waveforms, when the QCL is locked, at the three attenuation steps.

attenuation (dB)	$\sigma_{discriminator}$ **(mV)**	$\sigma_{correction}$ **(V)**
0	0.45	0.4
3.85	0.45	0.14
7.7	0.45	0.03

when the QCL is locked, figure 63 shows the broad picture of this voltage for both locked and unlocked QCL. This data is measured at the same time as the data shown in figure 58, the two complete each other. A quantitative analysis can be done by comparing the standard deviation that both frequency discriminator and correction voltage gives, at the three different attenuation steps. Table 21 presents the results.

As seen in table 21, the amount of locked standard deviation for discriminator output remains the same. In the locked state, the frequency discriminator's output mainly contains wideband noise. Inserting attenuators in the QCL beam changes the signal only, but the noise stays the same. In contrast, changing optical attenuation results in different optical feedback, which needs different corrections, accordingly. Therefore the standard deviation of the correction voltage is variable with attenuation.

3.5.2 Optical feedback

An interesting observation during the experiment was that coming close to the setup and stepping back and forth, right and left, changed the position of the QCL peak in the IF monitor output when the QCL was unlocked. When locked, doing so changes the amplitude and offset of correction voltage to the QCL. Along with the observation that adding an attenuator in the optical path reduced the disturbances, it could be concluded that the hypothesis of disturbances to a large part arising from the optical feedback is correct. Since the wavelength of the laser is only 63 micrometers, the setup is much susceptible to mechanical movements: either caused by the pulse tube or a person moving around the setup and creating micrometer deformations in the lab's concrete floor. Also the fact that the experiment bench was simple, with neither tip-tilt compensation nor vibration isolation, has caused the setup to be sensitive. Other works has also reported the effect of optical feedback in disturbing QCL's frequency stability, such as in (A. A. Danylov et al., 2012). Figure 64 shows an example of correction voltage change with the person moving close to the setup.

As mentioned earlier in the introduction, for the effect of optical feedback on the emission frequency of a single-mode laser, one can write:

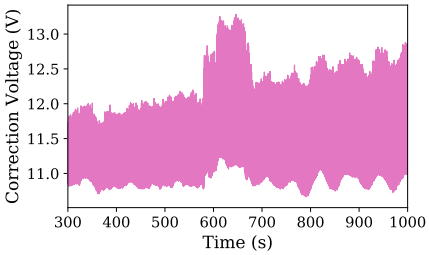

Figure 64: The increased locked QCL correction voltage at the middle of the plot between $t = 580$ to $t = 680$ seconds results from a person stepping one step forward, standing just next to the optics bench, and taking it back after ∼100 seconds. Movements changed the laboratory floor deflections, which affected the optical bench by a minimal amount, still large enough for optical feedback to react to it.

$$\nu_{QCL} - \nu_0 = -\frac{cK}{4\pi L_{ext}}[\sin\frac{4\pi\nu_{QCL}L_{ext}}{c} + \alpha_H \cos\frac{4\pi\nu_{QCL}L_{ext}}{c}] \tag{37}$$

whereas for K one has:

$$K = \epsilon(1 - R_{QCL})\sqrt{\frac{R_{SLD}}{R_{QCL}}}\frac{L_{ext}}{L_{QCL}n_{eff}} \tag{38}$$

in these equations, R_{QCL} and R_{SLD} are power reflectivities of the QCL and the SLD, α_H is the linewidth enhancement (Henry) factor, L_{QCL} and L_{ext} are the QCL ridge and external cavity lengths, n is the effective refractive index of the QCL medium, and ϵ is coupling parameter taking all optical couplings and attenuation into account. Mechanical motions appear as variations to L_{ext}, and this will be the driver for the frequency disturbances through relations of Eq. (38) and Eq. (37).

Figure 65 shows the needed correction voltages to correct against optical feedback for the locked laser as a function of optical attenuation. As evident, adding the first attenuator reduces the QCL's peak frequency deviation significantly, and the second one further reduces the QCL's peak frequency deviations. Note that in the curve showing the data with two attenuators, the harmonic fingerprint of the pulse tube is barely visible, Meaning that most of the frequency disturbances are gone.

Time domain measurements of figure 65 could also be presented in histograms, to show the occurrence of different voltage values. The voltage frequency tuning constant of the QCL can then convert those histograms to the frequency histograms. They show the corrections made on the QCL's frequency and reveal the uncorrected QCL's lineshape.

The effect of optical attenuation on the QCL frequency disturbances is appar-

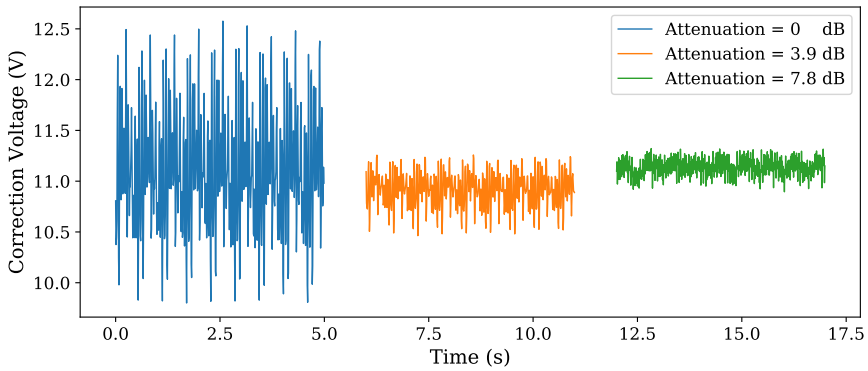

Figure 65: Effect of adding optical attenuation in the QCL's optics path on locked QCL's correction voltage. Optical attenuation reduces the optical feedback, reducing its associated frequency disturbances.

ent in figure 66. The idea may appear that one way to have an unstabilized QCL with relatively small linewidth is to use optical attenuation on the QCL's beam. As figure 66 shows, adding attenuation will help reduce the linewidth broadening caused by the optical feedback. However, The drawback is the loss of the laser's optical power. This is still possible for applications dealing with fractions of the laser's power, such as the GREAT instrument of the SOFIA telescope. A better idea is to use an optical isolator, which limits the back reflection wave to the laser. Such a device will largely maintain the output power, while keeping the back reflections small, therefore causing not much of line broadening due to optical feedback.

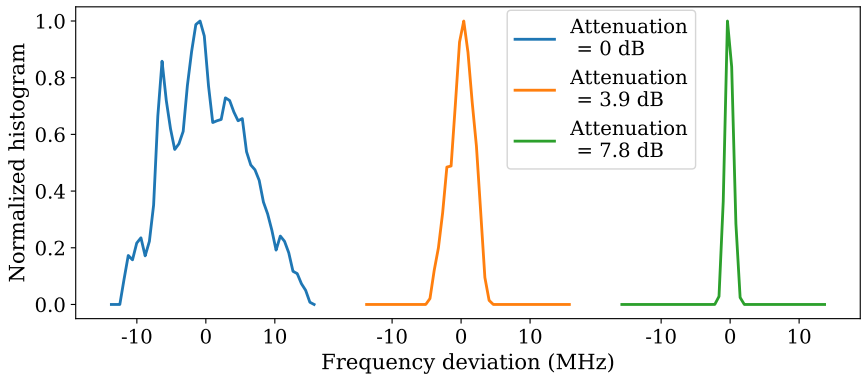

Figure 66: Result of converting the measured voltage histogram at the QCL's correction port to frequency histograms using the known voltage frequency tuning constant of the QCL; histogram of frequency disturbances. Left: no attenuation, Middle: one attenuator piece, and Right: two attenuator pieces.

3.5.3 Laser linewidth

A figure of merit for such an experiment is the laser linewidth of the frequency stabilized QCL. Three players determine it: The intrinsic laser linewidth which is in the kHz range (Baryshev et al., 2006), the leftover uncorrected modulations, which the QCL suffers from, and the additional linewidth, which the control loop has added. Since this experiment involves heterodyning, there is direct access to study the laser line. Since the lineshape of the SLD's LO convolves with the laser line, it also can cause additional line broadening. Therefore measuring the laser line in the intermediate frequency puts a direct upper limit on the laser linewidth. Figure 67 shows examples of locked laser line profiles as measured in the IF band using the SDR as a backend to record spectra.

As said earlier and visible in plots of the figure 67, the delay line method copes with different signal-to-noise and optical feedback disturbance situations and locks the QCL's frequency. It is also evident that the width of the laser line does not change much by varying the signal-to-noise ratio. As the signal is attenuated in each step by 3.9 dB, the QCL linewidth increases only by 3 percent. From an instrument design perspective, this result means no necessity for a high signal-to-noise in the IF to get a good locked linewidth. This is useful since a large part of the QCL emission can pump the mixer array, and still, the left fraction is enough to stabilize the frequency.

3.5.4 Lock time

The time that the laser stays locked is another figure of merit. To check this, best is to check the frequency demodulation and the correction voltage voltages

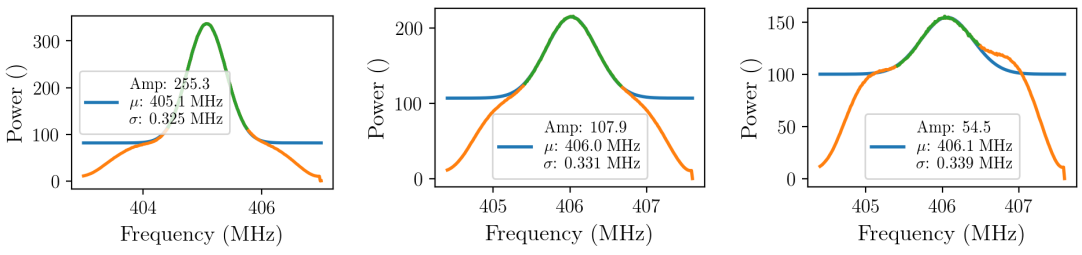

Figure 67: An integrated line of the QCL measured in the IF monitor output with an SDR. Recorded spectra are in orange; the part used for the Gaussian fit is green, and the resulting Gaussian function fit to the line is in blue. The decaying noise floor at both ends arises from the SDR's design. From left to right, measurements have no optical attenuator, one and two of them; each attenuator had an attenuation of 3.9 dB. As expected, adding attenuation results in a reduction in the line's amplitude. The Linewidth of the laser shows small dependence on attenuation, slowly increasing.

Date	Att	t_{total} (minutes)	$\frac{t_{unlock}}{t_{total}}$	Limiting phenomena
Nov 25	0	84	8.3%	OPAMP saturation and temperature not stabilized
Nov 26	0	113	0	none
Nov 29	0	59	0	none
Nov 29	1	87	2.3%	none
Nov 30	1	350	0	none
Dec 01	2	29	0	thermal control off
Dec 01	2	189	0	thermal control failed

Table 22: Samples of obtained lock time from different experiment days and at different attenuation settings.

recorded with the oscilloscope. In order to easily interpret them, the SDR data from the IF band is helpful. Table 22 briefs the details of the measured data regarding lock time.

Table 22 reveals some general behaviors. With no optical attenuation meaning strong optical feedback, the frequency discriminator method can temporarily lose control when large frequency deviations are present and control electronics settings is not best. With careful control electronics setting lock could be attained for two hours. Using one attenuator reduces the agility of the QCL line, and with reasonable control electronics settings, the QCL frequency was stabilized for hours. In the extreme case of poor signal-to-noise conditions: the QCL is calmer, but the control signal is also weaker. Even in this condition, the experiment could lock the QCL for hours. The overall impression is that only issues with the temperature controller, if existed, was limiting the experiment's performance.

3.6 Difficulties

3.6.1 uncontrolled temperature causing mode jump

One of the difficulties that appeared at the beginning of this experiment was the observation of thermal runaway in the system, followed by bi-modal frequency instability. The phenomena work as follows: due to a positive drift in the temperature, increasing the QCL's current was pulling the frequency to keep it under control. Increasing the current, in turn, slightly increases the QCL's temperature. This way, positive feedback is happening. Control of frequency is lost when the control voltage reaches the maximum that the OPAMPs of control electronics can provide, reaching saturation around 13.3 volts. Figure 68 shows an example of this behavior.

No more control is possible with the correction voltage at the maximum, and the temperature further increases. In this situation the QCL tends to lower fre-

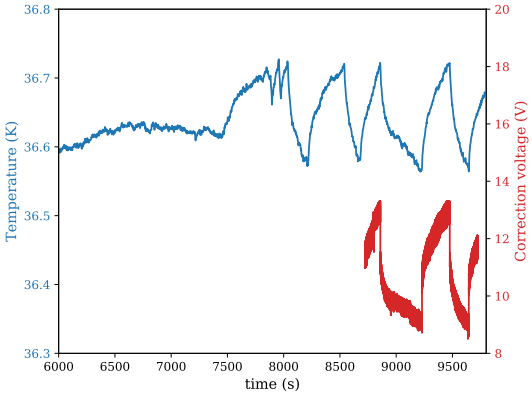

Figure 68: The blue curve presents the temperature of the QCL bath with no temperature stabilization. The red trace presents the correction voltage to the QCL. Stabilization was turned on at t $\sim$ 7400 seconds, and correction voltage was recorded only after t $\sim$ 8500 seconds. After t $\sim$ 7400 seconds, both curves show bi-stable operation between two limits. The mode jump moments are associated with the sharp vertical rise and fall in correction voltage.

quencies. Thus, it jumps to the mode at 385 MHz, and the QCL locks again since the QCL needs a lower voltage for the locked state at these higher temperatures. Now with less current, the QCL starts to cool down, and this mode continues until the QCL is cool enough that the preferred stable frequency is larger. At this point, QCL jumps back to the higher mode at 405 MHz, with frequency stabilization drawing more current and raising the temperature. The entire cycle repeats. Figure 69 shows the position of modes in the pass-band of IF.

As mentioned earlier, the SXBP-404+ filter defines the band-pass of frequencies that the frequency discriminator and the following sub-units can see. The

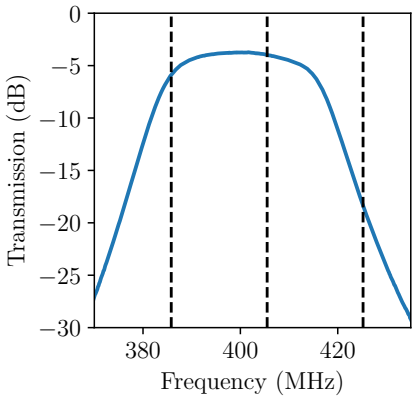

Figure 69: The blue curve shows the band-pass shape of the SXBP-404+ filter. Dashed lines show places of modes that pass the quadrature condition for the delay line frequency discriminator. The ones at 405 and 385 MHz has low insertion loss condition through the filter and are the main modes for the stabilization experiment.

frequency discriminator creates and dictates discrete modes to the system, presented in table 19 and marked with vertical dashed lines in figure 69. They should not be mixed with laser modes, which come with about 40 GHz of separation. The third mode at 425 MHz has only 5 % transmission compared to the central mode and is fragile, but still, very few times in superior signal-to-noise condition mode jumps to this mode also have been observed.

3.6.2 Synthesizer drift

Another problem at the beginning was a long-lasting drift limiting the lock time of the experiment. Correction voltage had an upward drift until the OPAMP saturates. The drift was only present at the start of the experiment every day, after turning the instruments on, and after several hours, the effect disappeared. Figure 70 presents a sample measurement of the drift.

The idea came that drift is due to the warm-up time of instruments like the microwave synthesizer that pumps the diode chain and, in turn, the SLD. On

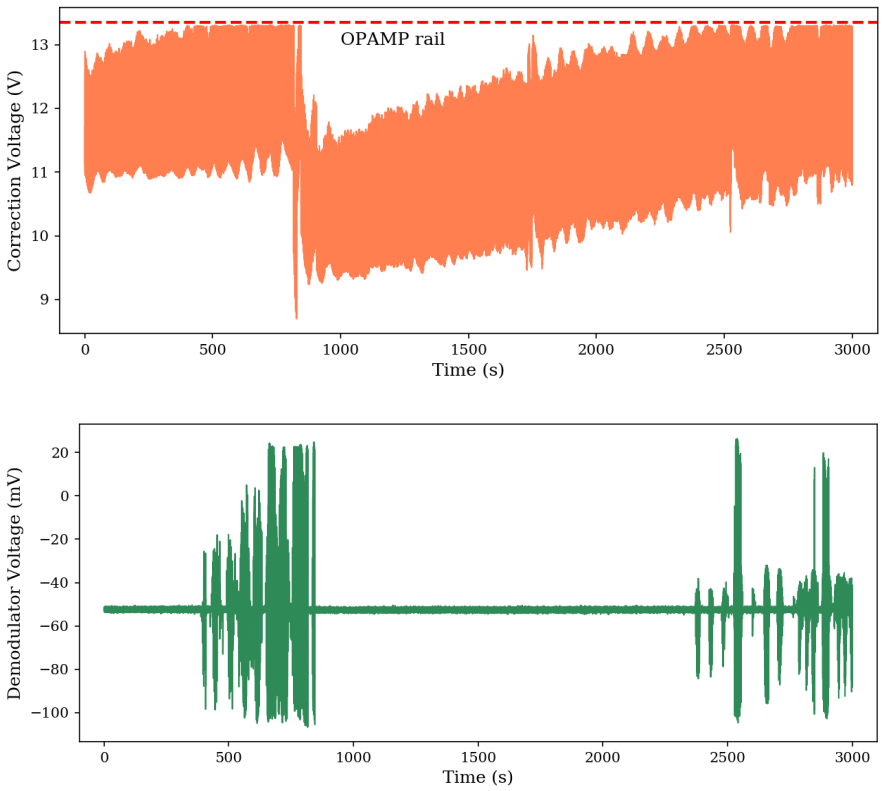

Figure 70: The top plot shows the correction voltage, and the bottom shows the frequency demodulator voltages; data sets are taken simultaneously. It shows that when the correction voltage reaches the OPAMP rail at 13.3V, the QCL unlocks, and the frequency discriminator shows a large variation corresponding to significant frequency disturbances. At t $\sim$ 850 seconds, a mode jump happens, and after a few tens of seconds, the experiment gains back the frequency control.

the following days of the experiment, all the instruments were left on overnight to keep them in thermal equilibrium with the laboratory and prevent them from the warm-up phase. Doing this vanished the drift.

Figure 71 shows the drift with a slope of $\sim 0.08\ \frac{V}{min}$. The voltage frequency tuning constant of the QCL converts this to $0.8\ \frac{MHz}{min}$ of drift. The complete diode chain and the SLD have a multiplication factor 416, and the synthesizer oscillating at 11.4 GHz. These turn the $0.8\ \frac{MHz}{min}$ of drift into 0.16 part per million (ppm) of frequency drift per minute. The datasheet of the synthesizer gives a value of $1 \times 10^{-}6$ per degree Celsius of frequency drift for each degree change in temperature of the synthesizer Rohde und Schwarz (2019). With this temperature coefficient, these calculations estimate a temperature increase rate of 1 Degree every 6 minutes for the synthesizer in the warm-up phase.

3.6.3 Presence of large noise at discriminator output

In the beginning, measurements at the frequency discriminator output with the oscilloscope suffered from an intense broadband noise, which is the amplified wideband SLD noise propagated through the IF processor. To limit this noise and be able to measure the QCL frequency disturbances and the DC value better, there was a need for low-pass noise filtering. The RC low pass filter presented in 4.3.4 sub-section has helped with these measurements.

3.7 Limits

3.7.1 Signal to noise ratio

One main limiting factor for this stabilization method is the signal-to-noise ratio. The control electronics has a finite bandwidth and passes some noise power, which will end up on the QCL and cause additional line broadening. Since the noise

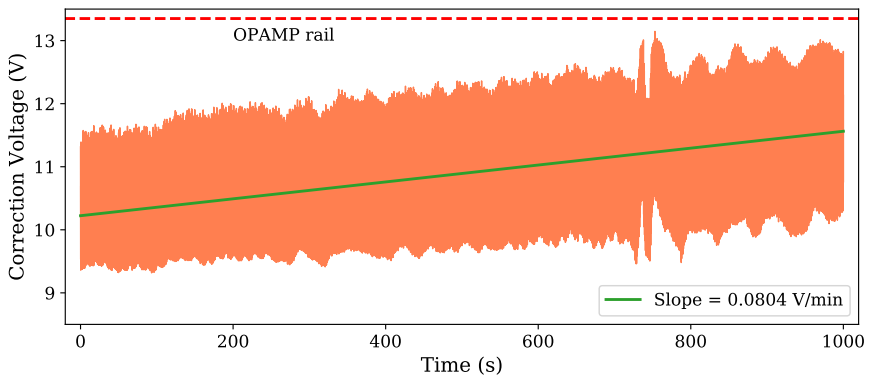

Figure 71: The drift rate is derived via a linear fit to the measured correction voltage.

is random and white, it is a good approximation if this modulation process is considered Gaussian. In a good signal-to-noise condition, less control gain is needed to build up the correction signal to control the QCL frequency. This smaller gain means less amplification for the noise and, therefore, smaller noise-induced QCL line broadening.

3.7.2 Frequency spacing of delay line modes

As seen in subsection 3.4.5, the delay line's mode spacing is a function of delay line length. As the delay line gets longer, the spacing of modes gets smaller, meaning that more modes can fit in the same IF bandwidth. In this experiment, there were two main available modes, and very few times, even locking to the third mode at 425 MHz was seen at the best signal-to-noise conditions. Reducing the IF bandwidth can help with the multi-modal issue.

3.7.3 Frequency discrimination constant

The frequency discriminator constant can be one of the limiting factors for the quality of the frequency stabilization. The smaller this constant is, the larger the gain must be to compensate for the small discrimination constant, together with the drawback of noise getting more significant. A large frequency discriminator constant is essential for a good signal-to-noise ratio. The delay line discrimination constant can be maximized depending on the frequency of choice, cable selection, and length.

3.7.4 control electronics bandwidth

The control electronics bandwidth is an essential parameter for the design. More dynamic signals require larger bandwidths since this will allow the frequency wide information of the QCL line to stay present in the control loop and correct the fast disturbances. A relevant example of a highly dynamic signal is this experiment when the optical feedback is strong.

3.7.5 Mechanical shock

The effect of strong mechanical shock was also tested with the setup. While the QCL was frequency locked, the experimenter created strong shocks by standing next to the setup, jumping up, and hitting the lab floor with both ankles. Doing this, only in some cases, the lock lost momentarily, or a mode jump was happening. This may be important for telescope systems performing fast accelerations.

4 Phase locking using warm SLD as mixer

Phase locking is a way of frequency stabilization that compares the oscillator's phase, which is to be stabilized, with the phase of a stable reference oscillator. The phase detector compares the two phases and produces a voltage proportional to the error between the two. This phase error is used to create the correction feedback for the free oscillator. When this is successful, the phase of the oscillator will follow the phase of the reference oscillator. This scheme stabilizes the phase and frequency of the oscillator, called a Phase-Locked Loop (PLL). The word loop stands for a control loop that controls the phase using feedback. Figure 72 presents this concept in a block diagram view where the Voltage Controlled Oscillator (VCO) is the oscillator of interest. [3]

As shown in the block diagram in figure 72, the phase detector takes two inputs: the reference oscillator waveform and the waveform from the oscillator to be stabilized. This block creates the error of the two and sends this to the loop filter. The loop filter changes the error signal to be ready to be sent to the oscillator for stabilization. Generally, this block gives most design freedom to get good dynamical behavior from the entire phase-locked loop system. The last block is the voltage-controlled oscillator, which is the oscillator to be stabilized, and it has to be voltage-controllable since voltage feedback will be applied to it to correct its deviations.

In this work, the voltage-controlled oscillator is the QCL. It is given, and there is little design choice regarding this element. On the other hand, a phase detector is a choice in this experiment, which should handle the problematic situation of this experiment. The loop filter is the primary choice of the experimentalist when planning and designing the QCL phase-locking experiment. In the extremely simple case, it can be a direct connection or a resistive divider network, but often it is more complicated. This chapter starts with the phase detector description and calibration methods. After that a brief PLL theory follows. The next section presents the experimental setup where the PLL design, especially the transfer function method is employed. Then a short section on noise modeling for the experiment precedes the results section.

4.1 Phase detectors

Phase-locking applications can employ many types of phase detectors. Phase detector's main branches include multiplier and sequential phase detectors. Multiplier phase detectors multiply the two inputs and generate a DC voltage in the

[3] After submitting this thesis, we achieved an excellent phase-locked QCL. This work is not included in this chapter, and we plan to publish this result in a journal paper.

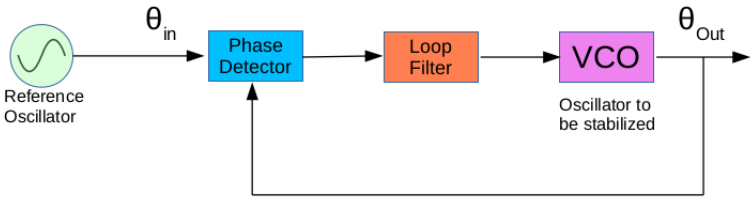

Figure 72: A phase-locked Loop (PLL) system's general block diagram showing only the fundamental elements.

output that varies as a function of the phase difference between the two inputs. Double-balanced diode ring mixers and active modulators such as Gilbert cell mixers are examples of this type. On the other branch, sequential phase detectors are based only on the relative delay between two rising edges when the inputs are digitized. Phase frequency detectors (PFD) alone or including a charge pump are examples of such phase detectors. The SRA-1W+ double-balanced diode ring mixer from Minicircuits performed well for this experiment and is chosen for phase detection in the rest of this chapter.

4.1.1 Calibration of double balanced mixer as phase detector

Phase detector converts the phase differences into voltage differences with a conversion factor:

$$\Delta V = K_{PD} \times \Delta\phi \tag{39}$$

Where K_{PD} is called phase detector gain, the main parameter of any phase detector. This section introduces two methods to calibrate and get the phase detector gain. Primary to calibration, it is worth reminding some relations from the modulation theory. As shown in chapter 3, for a mathematical model of frequency modulation, one has:

$$V(t) = V_c sin(2\pi f_c t + \frac{\Delta f}{f_m} sin(2\pi f_m t)) \tag{40}$$

The V_c and f_c were the amplitude and frequency of the main (carrier) wave, Δf was the maximum frequency deviation, and f_m was the modulating frequency. The term $\frac{\Delta f}{f_m}$ was called FM modulation index and denoted there with β:

$$\beta = \frac{\Delta f}{f_m} \tag{41}$$

FM modulation index is equivalent to the peak angle modulation when converting the earlier formalism into a phase modulation formalism, therefore:

$$V(t) = V_c sin(2\pi f_c t + \theta_p sin(2\pi f_m t)) \tag{42}$$

Where θ_p denotes for peak modulation phase. It was also shown how such modulation would create side bands on both sides of the main wave: the carrier. For the ratio of power that exists in each of these side-bands P_{SSB} compared to the carrier P_c, one has:

$$L = \frac{P_{SSB}}{P_c} = \frac{\theta_p^2}{4} \quad = \quad \frac{\Delta V_{rms}^2}{2K_{PD}^2} \tag{43}$$

Which describes the so-called single side-band to carrier ratio. Now after this brief review of phase modulation, calibration processes are presented.

4.1.2 Calibration using a beat note

In order to calibrate the phase detector: which is to understand how phase input differences result in a change in output voltage, two signals of $V_L(t) = A_L sin(2\pi f_L t + \Phi)$ and $V_R(t) = A_R sin(2\pi f_R t)$ are fed to the LO and RF port of the mixer, resulting in an output of:

$$K_L A_R[cos(2\pi(f_L - f_R)t + \phi) - cos(2\pi(f_L + f_R)t + \phi)] \tag{44}$$

Where K_L is the mixer efficiency being a function of the LO power. For phase detection applications, there is always a low-pass filter to reject the high-frequency component, so only the difference term is interesting:

$$K_L A_R[cos(2\pi(f_L - f_R)t + \phi)] \tag{45}$$

When a mixer is employed for phase detector, f_L and f_R are equal and ϕ is close to 90 °, so one has:

$$K_L A_R[cos(\phi)] = K_L A_R[sin(\Delta\phi)] = K_L A_R.\Delta\phi \tag{46}$$

Where $\Delta\phi$ is a deviation from the phase quadrature condition for small angle deviations. It shows that mixer output voltage is a function of input phase difference, and the phase detector constant is the $K_L A_R$ term which is the amplitude of the beat note signal in relation 45. So the phase detection gain is:

$$K_{PD} = \Delta V/\Delta\phi = K_L A_R(Volts/rad) \tag{47}$$

This method is a fast way of estimating a mixer's phase detection gain. Figure 73 shows such a measurement for the SRA-1W+ double-balanced mixer.

Which results in a value of:

$$K_{PD} = 0.248 \quad (Volts/rad) \tag{48}$$

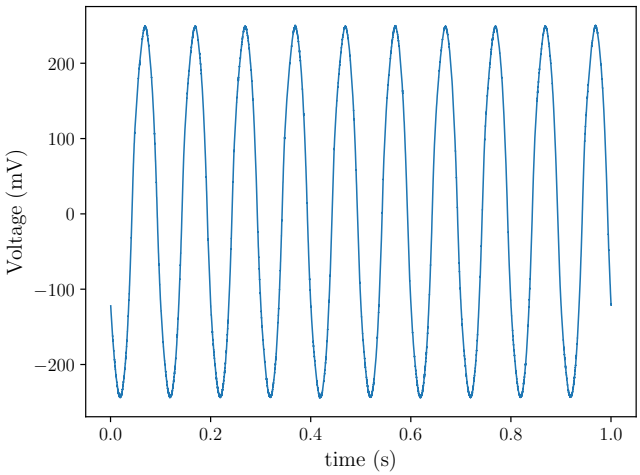

Figure 73: Beat note result from two waves at 328.00001 MHz and 328.00000 MHz, fed to the phase detector's RF and LO port. The beat note amplitude is 248 mV, equal to the phase detection constant.

The assumption here is that the shape of the frequency difference product, the beat note, being the phase detection curve, is sinusoidal. In reality, this may deviate from the ideal case, as shown for the SRA-1W+ mixer in figure 80, that close to the peaks, the curve bends and flattens faster than a sine function. A better measure of the phase detection sensitivity is by measuring the slope. This is shown in figure 74.

As can be seen, this plot shows a slope with a value of:

$$K_{PD} = 0.34 \quad (Volts/rad) \tag{49}$$

In order to make sure that the mixer operates optimally, in another test, the mixer's LO power is varied while checking the IF port's beat note voltage. The power of the mixer's RF port was kept constant at 7 dBm. The frequency of RF

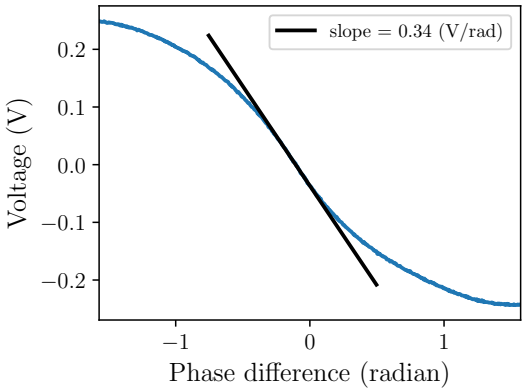

Figure 74: To be more accurate, even for non-ideal mixers, the maximum slope of the curve gives the maximum possible phase detection gain.

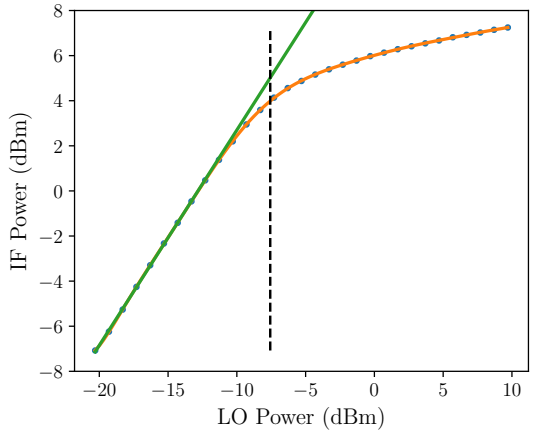

Figure 75: The LO power is varied at a fixed RF power, and the IF output's power is calculated from measured beat note voltage. The dashed vertical line shows that the mixer gain (dots and fitted curve in orange) separates by 1 dB from the linear fit to the curve's beginning (in green) at around -7.5 dBm. After this point, feeding more LO power does not increase the mixer gain much.

and LO were 328 MHz and 328.00001 MHz, respectively.

Figure 75 shows that the compression happens at an LO power of -7.5 dBm, meaning that a further increase in LO power will change the IF output's power slowly, and the same applies to the phase detector's conversion gain. After this test, the SRA-1W+ mixer for this experiment has always been used at an LO power of 7 dBm.

4.1.3 Calibration using phase modulation

As the importance of the phase detection constant implies, this second method checks the correctness of the first calibration using a test voltage-controllable oscillator. A DC voltage has set the oscillator's frequency to around 328 MHz. A noise over this DC voltage has frequency modulated the oscillator's output waveform. This waveform was measured with a spectrum analyzer and a PLL based phase demodulator, as figure 76 presents them.

The spectrum analyzer measured the disturbances around the carrier frequency at 328 MHz. On the other hand, phase demodulator measurement presents the same signals close to zero frequency called base-band. It is such that each modulation component appears at the corresponding modulation frequency. Phase demodulator is simply the phase-locked test oscillator. In such a case, the phase detector's output is a phase demodulation for the oscillator's waveform.

Visible in figure 76 are the different resolutions for the two measurements. The one measured with the spectrum analyzer suffers from the limited, relatively poor spectrum analyzer's resolution bandwidth of 30 kHz. At the same time, the base-band measurement is taken with a fast oscilloscope and taking the Fast Fourier

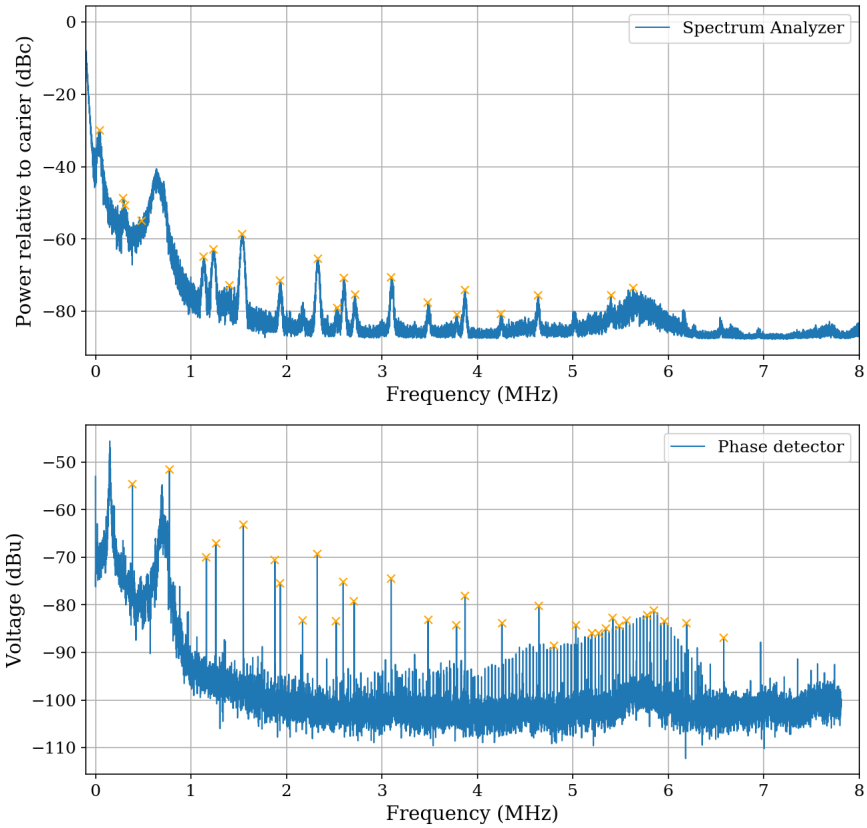

Figure 76: The noise of the test oscillator is measured with two methods (I) using a spectrum analyzer (top) and (II) using a PLL phase demodulator (bottom). The similarities in trend and, in particular, many mutual peaks are identifiable. Comparing the mutual peak values of the two measurements create calibration points.

Transform (FFT), resulting in a much finer frequency resolution. The LO that drove the mixer was a Rohde&Schwarz SMR20 synthesizer with minimal phase noise, less than -70 dBc at 100 Hz away from the carrier in one Hz bandwidth.

Figure 76 contains many mutual peaks detected by the peak detection algorithm, marked with thin yellow crosses. 13 of them are found reliable for phase detector calibration. The SRA-1W+ phase detector with a phase detection gain of K_{PD} has served the phase detector role in phase-locking the test oscillator: converting the oscillator's phase fluctuations to voltage fluctuations when measuring directly at the phase detector's output. Single side-band to carrier ratio relation of 43 is the correct formula to convert the top plot's data into phase disturbance information. One can write it in logarithmic format as:

$$10log(L)(dBc) = 20log(\Delta V_{rms})(dBV) - 20log(K_{PD}) - 3 \tag{50}$$

Figure 77 shows the comparison plot of voltage measurement at the phase detector output versus single side-band to carrier power measurement in log-

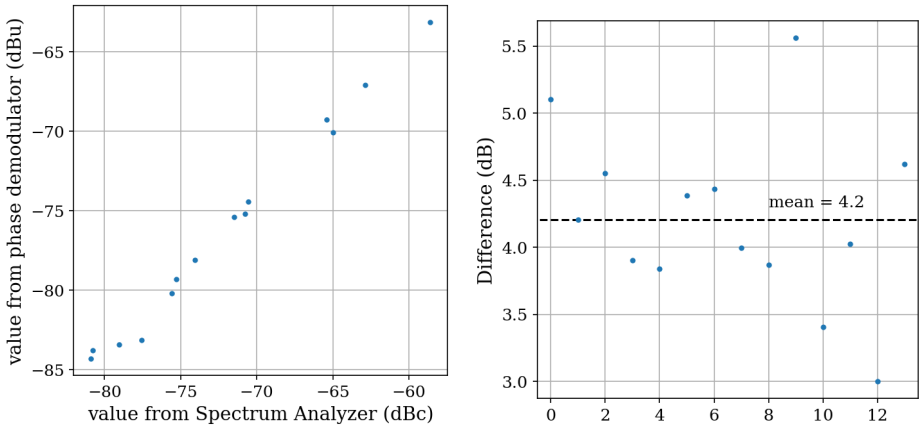

Figure 77: Left: Phase demodulated voltage value for each of those 13 points as a function of single sideband to carrier ratio on the spectrum analyzer. It shows the linear behavior of the phase detector over more than two orders of magnitude phase disturbance levels. Right: Scatter of differences for each point of the left plot, around the average of 4.2 dB.

arithmic format. For all data points in the lefthand side plot, the quantity $10log(L) - 20log\Delta V_{rms}$ is calculated and plotted in the righthand. The mean value is 4.2 dB. Voltage measurements of dBu need conversion to dBV by adding 2.2 dB. Finally, for the gain of the phase detector:

$$20log(K_{PD}) = 4.2 + 2.2 + 3 = 9.4 \quad dB \tag{51}$$

Which means:

$$K_{PD} = 0.34 \quad (V/rad) \tag{52}$$

Being in perfect agreement with the measured value in the earlier subsection (Eq. (49)).

4.2 A brief theory about PLLs

The introduction section of this chapter presented a brief operation principle of a PLL. As stated there, the goal is to lock the phase θ_o of the VCO oscillator, in this experiment specifically the QCL, to the phase of a stable reference oscillator θ_i such that the stability of the weak but stable reference is followed by the powerful THz, but inherently less stable QCL. To do this, a PLL must be formed: meaning that a phase detector and a loop filter are required. Figure 78 show a general block diagram of such a control loop, with emphasizes on the role of each unit. The following sub-sections will open some more detailed theory about these units.

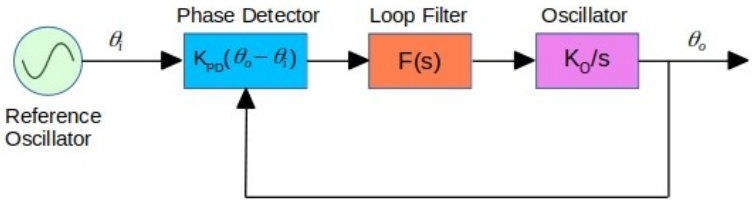

Figure 78: A PLL general block diagram, with emphasis on role of each unit.

4.2.1 Static phase error

If an oscillator is phase-locked, it follows the phase of the reference oscillator with an additional phase offset. A double-balanced mixer as a phase detector gives most of the phase detection sensitivity when the two phases from the Radio Frequency (RF) and the Local Oscillator (LO, the reference oscillator in the PLL case) are in quadrature. Due to the mentioned phase offset, there are deviations from the quadrature-phase condition. However, such a phase error is present in the control loop: it will create the control voltage to correct the oscillator's phase. This error is called the static phase error (Wolaver, 1991). Figure 79 provides a model to study this.

As presented in figure 79, in linear approximation, the phase detector can be modeled as an element subtracting the two phases to produce the phase error θ_e, followed by a gain block with the gain of the phase detector K_{PD}. In the end, an adding node adds the phase detector's offset voltage to complete the model. The loop filter of the PLL follows this phase detector's model, and then the signal reaches the oscillator. Depending on the input, the voltage-controlled oscillator produces an output frequency: At the input, the operating voltage is subtracted, then a gain block of K_V is in the path that accounts for the VCO's gain. The VCO's integrator is the last element. It integrates the input voltage and produces an increasing phase in the oscillator's output.

In steady state, the oscillator's phase is locked to the reference phase, so there is no frequency difference between the two signals. One can start from the phase

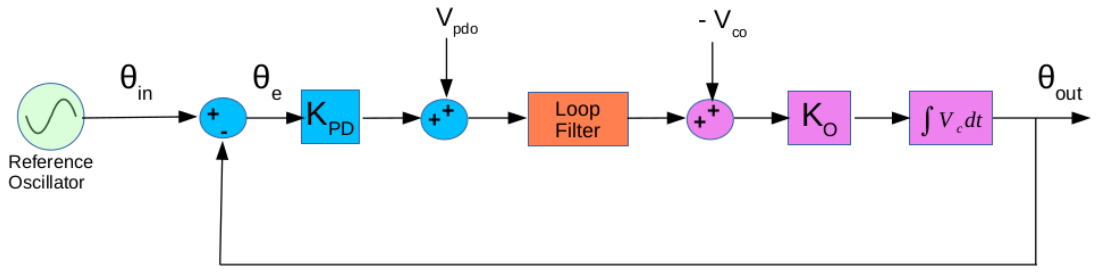

Figure 79: Static signal propagation in the linear approximation of the PLL. This model emphasizes offset voltages in the system since they are important players of the system's static state.

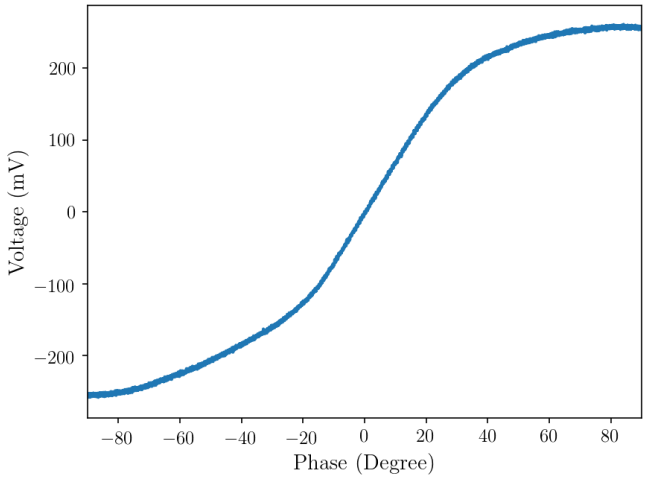

Figure 80: Two waves of 400.00001 MHz and 400.00000 MHz are fed to the RF and LO port of the phase detector. The voltage waveform at the output, created from the beat note, reveals the phase detection curve.

detector output and follow the signal propagation as follows:

$$[(\theta_e K_{PD} + V_{pdo})F_{DC} - V_{co}] \times K_O = \overline{\Delta\omega_O} = 0 \tag{53}$$

This equals zero because there is no frequency change when the oscillator is phase-locked. Then one has:

$$\frac{V_{co}}{F_{DC}} = \theta_e K_{PD} + V_{pdo} \tag{54}$$

After rearranging:

$$\overline{\theta_e} = \frac{V_{co}}{K_{PD}F_{DC}} - \frac{V_{pdo}}{K_{PD}} \tag{55}$$

The last relation helps to estimate the static phase error. As shown in figure 80, the mixer characteristic as a phase detector is neither ideal nor linear. It also reveals the importance of caring about static phase error to ensure the mixer's operation in the linear range and to have a larger phase detection gain. As a rule of thumb, it should not get larger than 1 rad for a good tracking in a PLL. It is also important to mention that a PFD + charge pump phase detector can eliminate the static phase error in the system; it is essentially zero for them (Wolaver, 1991).

4.2.2 Phase detector gain in presence of noise

The last section opened a detailed discussion about the phase detectors. Operation of the phase detectors are impaired in situations where an unwanted component is also present to them. One important case is when noise with rms

of $\theta_{e,rms}$ comes along with the phase tracking error information from the PLL. In this situation, the unwanted phase error causes the gain of the phase detector to reduce as (Wolaver, 1991):

$$K'_{PD} = K_{PD} e^{-\theta^2_{e,rms}/2} \tag{56}$$

4.2.3 Ranges for Phase locked loop

This section introduces a few ranges that are performance parameters of a PLL system, categorized into 3 different groups. Lock-in and pull-in capture ranges are frequency ranges over which slow and fast capture happens. A locked PLL maintains the lock within the hold range of the PLL. Finally, a locked PLL can handle frequency impulses without jumping out of the lock within the pull-out range. A more detailed discussion is presented in (Gardner, 2005) and (Encinas, 1993). A little more detailed presentation of these ranges now follows this brief introduction.

The hold range is the difference between the free-running oscillator frequency and the reference frequency over which the PLL holds the phase lock. This range in literature is denoted as $\Delta\omega_H$ and for this one can drive:

$$\sin\theta_e = \frac{\omega_R - \omega_O}{K_o K_{PD} F_{DC}} \tag{57}$$

Where θ_e stands for phase error from phase detector, ω_R and ω_O stand for reference and free running oscillator angular frequency, K_{PD} and K_o stand for phase detector gain and voltage tuning of oscillator constants, and F_{DC} stands for loop filter's DC gain. The sinuous function's range limits unity, resulting in the following:

$$\Delta\omega_H = K_{DC} = K_o K_{PD} F_{DC} \tag{58}$$

Hold range is the DC gain of the PLL system (K_{DC}). This result is one reason to aim for a larger DC gain.

Two capture ranges are associated with a PLL system: one for fast and the other for slow capture processes. The fast capture is called lock-in, and for a second-order lag lead loop filter, it is:

$$\Delta\omega_L = K_o K_{PD} \frac{\tau_2 \tau_D}{\tau_1(\tau_D + \tau_2)} = K \tag{59}$$

Where K denotes the PLL's loop gain. Within lock-in range, capture is a fast process. In contrast, the slow capture process, called pull-in, takes some time. For frequency differences within this range, there will be a beat note from the reference and the free-running oscillator's frequency, where the beat frequency

decreases with time. In the end, the frequency of the two will match, and the loop will fall in the lock. For the pull-in range:

$$\Delta\omega_p = \sqrt{2K_{DC}K} \tag{60}$$

An estimation of Pull-in time for a type 2 PLL can be shown to be (Gardner, 2005) :

$$T_p = \frac{\Delta\omega^2\zeta^2(1+1/4\zeta^2)^3}{16B_L^3} \tag{61}$$

with B_L and ζ being the PLL's equivalent noise bandwidth, and second-order PLL's damping factor.This relation shows that a small bandwidth PLL leads to a long pull-in time. The risk of long capture time is why many PLL systems use a sort of aid for acquiring phase-lock, for example, a frequency sweep. Using a PFD + charge pump phase detector extends the pull-in range and this is a reason for the popularity of that phase detector type.

The last range to be introduced here is the pull-out range. PLL may lose the tracking out of this range, but the PLL can acquire the tracking back again, usually with a pull-in capture. For this range, one has:

$$\Delta\omega_{po} = 1.8\omega_n(\zeta+1) \tag{62}$$

where ω_n is the second-order PLL's natural frequency. The pull-out range is a valuable quantity to consider frequency steps manageable by PLL without any loss of lock.

As a summary, it is worth comparing all four introduced ranges together. Consider that the oscillator is free running at some frequency. For a quick capture, the reference frequency should come close to the free-running oscillator's close vicinity; this is the smallest range, the Lock-in. Up to some wider frequencies, the PLL can handle some steps on the reference frequency; this is the pull-out range. Up to some larger frequency limit, if the lock is lost, a slow capture is still possible: the pull-in range. Furthermore, the widest range is the hold range, over which the locked PLL stays locked. As a comparison, one can write (Encinas, 1993):

$$\pm\Delta\omega_L \leq \pm\Delta\omega_{po} \leq \pm\Delta\omega_p \leq \pm\Delta\omega_H \tag{63}$$

4.2.4 Transfer function of Phase Locked Loop

A transfer function is a mathematical model that relates the output of a linear system/subsystem to the different inputs. In the introductory part of this chapter, it was said that the central design freedom in the PLLs occurs in the loop filter.

In this section, the goal is to write such a function for the QCL phase-locking experiment. A loop filter of Lag-Lead type with an active amplifier - implemented by an operational amplifier (OPAMP) - was chosen and designed. The schematic of the loop filter circuit is shown later in figure 86 of the experimental setup. The transfer function of this loop filter is:

$$F_(s) = G_{amp}\frac{\tau_D}{\tau_1}\frac{1+s\tau_2}{1+s(\tau_2+\tau_D)} \tag{64}$$

Where $\tau_1 = R_1C$, $\tau_2 = R_2C$, $\tau_D = R_DC$ are the time constants associated with different elements of the loop filter. S is the frequency variable being $s = j\omega$. At $s = -1/\tau_2 + \tau_D$ the pole of the transfer function is located since this is the denominator's root. Similarly, τ_2 is associated with the zero of this transfer function, and finally G_{amp} is the gain of the amplifier stage. When the control loop is closed, the open loop transfer function G(s) results the closed-loop transfer with:

$$H(s) = \frac{G(s)}{1+G(s)} \tag{65}$$

The G(s) from the Eq. (81), without the two last terms for the parasitic OPAMP pole terms as an approximation, can be used in this formula for H(s) in the form of a famous second-order system:

$$H(s) = \frac{2\zeta\omega_n s + \omega_n^2}{s^2 + 2\zeta\omega_n s + \omega_n^2} \tag{66}$$

Which is in the well-established format of a second-order system response with

$$\omega_n = \sqrt{\frac{K_{DC}}{\tau_1}} \tag{67}$$

being the natural frequency and with

$$\zeta = \frac{\omega_n}{2}(\tau_2 + \frac{1}{K_{DC}}) \tag{68}$$

being the damping factor of the system.

4.2.5 Phase tracking: response of PLL to different inputs

Knowing how the PLL responds to different changes in the reference phase in the time domain is essential. Precisely the PLL's response to a phase step, a phase ramp, or a frequency ramp, as shown in Figure 81.

To best check the PLL's ability to handle different phase input functions over time, it is helpful to form the PLL's phase error function $\theta_e(t)$ and check its response to different phase inputs. The final value theorem expresses the relation

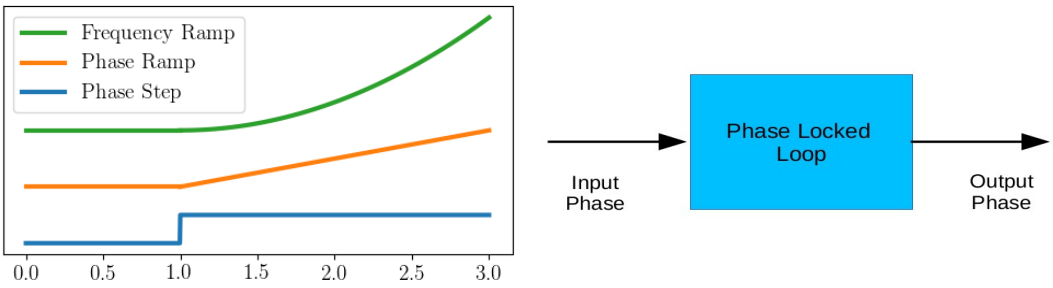

Figure 81: Examples of different phase input functions to a PLL system. The question is how the output reacts to these functions.

between the phase error as a function of time $\theta_e(t)$ and its Laplace transform $\theta_e(s)$ as a function of frequency as:

$$\lim_{t\to\infty} \theta_e(t) = \lim_{s\to\ 0} s\theta_e(s) \tag{69}$$

Where the definition of the error transfer function $E(s)$, and the defined closed-loop transfer function $H(s)$ in Eq. (65), help in calculating the $\theta_e(s)$ with:

$$E(s) = \frac{\theta_e(s)}{\theta_i(s)} = 1 - H(s) = \frac{s}{s + K_{PD}K_oF(s)} \tag{70}$$

The following Table gives three fundamental error inputs to the system and their corresponding Laplace transform.

$\theta_i(t)$	$\theta_i(s)$	
$\Delta\theta$	$\Delta\theta/s$	phase step
$\Delta\omega t$	$\Delta\omega/s^2$	frequency step
Λt^2	Λ/s^3	frequency ramp

Table 23: Fundamental phase error functions and their Laplace transforms.

Multiplying these relations for input phase error functions in the Laplace domain from the table 23 with the error transfer function E(s) results in the PLL's output phase error to that given input phase error. Then one can use the final value theorem to check the final error value. The following discusses the resulting phase error from each presented case in table 23.

4.2.6 Phase step

For the phase step, one can write:

$$\lim_{t\to\infty} \theta_e(t) = \lim_{s\to\ 0} s\theta_e(s) = \frac{s\Delta\theta}{s + K_{PD}K_OF(s)} = 0 \tag{71}$$

This means any phase step is fully corrected in the steady state of the PLL after transients are damped.

4.2.7 Phase ramp

For the case of phase ramp or equally a frequency step, one has:

$$\lim_{t\to\infty} \theta_e(t) = \lim_{s\to\ 0} s\theta_e(s) = \frac{\Delta\omega}{s + K_{PD}K_O F(s)} = \frac{\Delta\omega}{K_{PD}K_O F(s)} \tag{72}$$

The loop filter's transfer function $F(s)$ approaches F_{DC} at very low frequencies, leaving the denominator with the PLL's DC gain. As a result, the phase error caused by a frequency step is nonzero, and the larger the PLL's DC gain, the smaller this phase error will be: this is another reason to aim for large DC gains in the PLL design. The loop filter can contain an integrator to realize this in the PLL design. In practical designs, OPAMPs play the role of an integrator, and even with their finite DC gain, they still produce significant DC gains. Such a phase-locked loop that now includes two integrators: one in the loop filter and the other always in the oscillator, is called a type 2 PLL. The ability to handle frequency steps is why type 2 PLL systems are widespread. An example of the need for handling frequency steps is tuning the LO of a heterodyne receiver to a new frequency, where the input frequency jumps from one value to another.

4.2.8 Frequency ramp

As the last case for a frequency ramp, one can write:

$$\lim_{t\to\infty} \theta_e(t) = \lim_{s\to\ 0} s\theta_e(s) = \frac{\Delta\theta/s}{s + K_{PD}K_O F(s)} \tag{73}$$

The type 2 second order PLL transfer function of 66 converts this to:

$$\lim_{t\to\infty} \theta_e(t) = \lim_{s\to\ 0} s\theta_e(s) = \frac{s^3\Lambda/s^3}{s^2 + 2\zeta\omega_n s + \omega_n^2} = \frac{\Lambda}{\omega_n^2} \tag{74}$$

with Λ being the frequency rate. For a second order PLL system this equation is non-zero, and increasing the natural frequency ω_n of the second-order PLL can reduce it. As Eq (67) shows, increasing the natural frequency needs increasing the loop bandwidth, which will be seen later how this may result in a compromise. A frequency ramp can create significant static phase errors that are not acceptable by the PLL; eventually, the PLL may unlock. Different types of PLL with different loop filter transfer functions handle the frequency ramp differently. A Type 3 PLL where the loop filter contains 2 integrators will have a zero steady-state static phase error due to frequency ramps. An example of such a case is receiving

signals with variable Doppler shifts, such as an over-passing satellite in the sky.

4.3 Experimental setup

Much of this experiment is common to the delay line frequency stabilization experiment presented in chapter 3. That is because the stabilization is done with the same heterodyne signal that one gets from the QCL's down-conversion at the output of the SLD. As a result, the following parts stay the same: cryostat, warm optics, the high-frequency part including the synthesizer, the diode multiplier chain and the SLD, and the first low noise amplifier.

The complete experimental setup works as follows: The cryostat houses the QCL, and a few mirrors couple the QCL's emission into the SLD, located outside the cryostat. A laboratory synthesizer at 11.4 GHz runs a diode multiplier chain to produce 182.5 GHz to pump the SLD from its waveguide LO port. The focused QCL emission into the diagonal horn input of the SLD at 4.7THz mixes with the 26th harmonic of the SLD LO pump at 182.5GHz, down-converting the QCL's emission to 0.33 GHz at the SLD's IF output. A low-noise IF processor amplifies and prepares this low-level IF signal into a relatively powerful signal. The IF processor's output drives the double-balanced mixer as a phase detector to compare the QCL signal's phase to one from a clean reference oscillator. Mixer's output contains the phase error information of the down-converted QCL emission to the reference. A frequency-separating diplexer separates and dumps the high-frequency part of the beat note into a termination load. The low-frequency information is further processed in the PLL's loop filter. In the final stage, a resistive current combiner adds the loop filter's output signal to the QCL's supply current to close the control loop. Figure 82 presents the full schematic of the

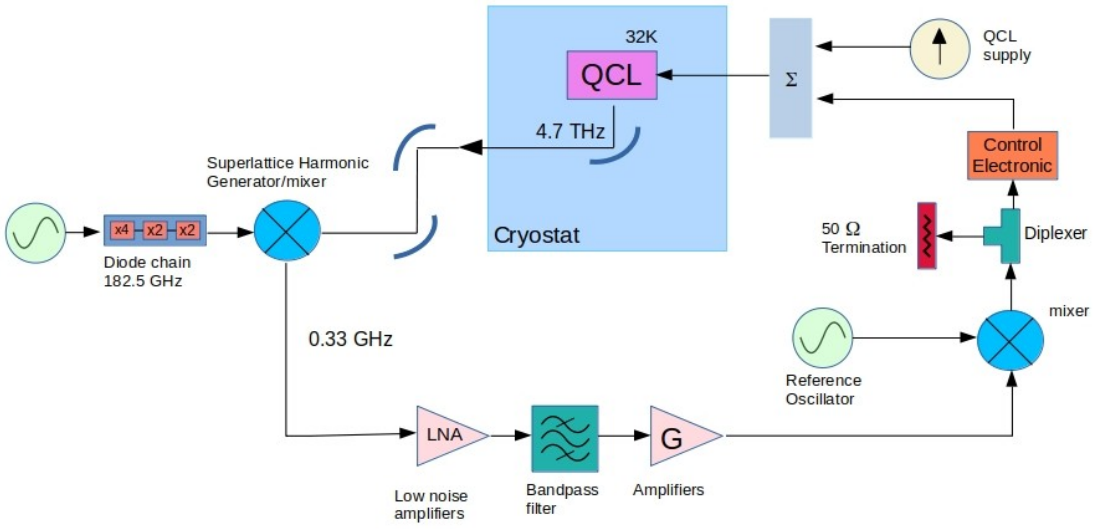

Figure 82: Schematic of QCL phase locking experiment.

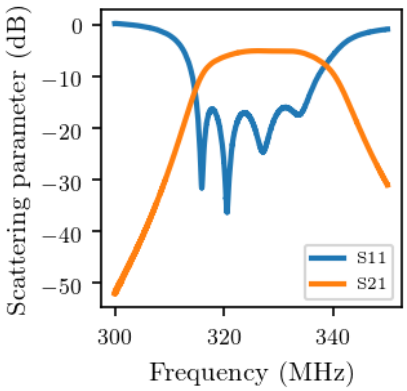

Figure 83: Transmission and reflection measurement of the IF processor's bandpass filter.

experiment. The subsections below present the new units in the experiment in somewhat more detail.

4.3.1 Intermediate Frequency (IF) processor

The Intermediate Frequency (IF) processor is almost identical to the one in chapter 3. The only difference is in the IF filter. The main task of this filter is to reduce the total amount of noise entering the phase detector. It is a linear phase filter with a relatively small bandwidth. The linear phase behavior matters for phase locking: it is gentle with phase and introduces the least phase change and distortion to the phase of the full PLL transfer function, hence not sacrificing the stability of the PLL by a large reduction in the phase stability margin. On the other hand, small bandwidth causes less wide-band noise to reach the phase detector; therefore, maintaining the signal to noise at the phase detector's input larger. Figure 83 shows the transmission and reflection measurement of the filter, and table 24 shows the filter specification.

4.3.2 Phase detector

The SRA-1W+ double-balanced diode ring mixer has been the choice for the phase detector throughout this experiment. The reference signal from a laboratory synthesizer drives the mixer's LO port, while the IF processor's output feeds

Parameter	Value
Center frequency	328 MHz
Noise bandwidth	21.1 MHz
Insertion loss	5 dB
Insertion phase slope	17.2 deg/MHz

Table 24: The IF bandpass filter's specifications.

Figure 84: The SRA-1W+ is a double-balanced diode ring mixer. The golden SMA connectors are the RF and the LO ports, while the third BNC connector extracts the IF output.

the mixer's RF port. After passing a frequency separating diplexer to dump the sum frequency component, the mixer's IF output provides the loop filter with phase correction information. Figure 84 shows this mixer inside the box. In general in very poor signal to noise conditions, multiplier type of phase detectors are more robust compared to the sequential phase detectors (Gardner, 2005). The selected double-balanced mixer provides an excellent LO-IF isolation, which means although power level at the LO input is large, it will not strongly contribute to the mixer's output offset voltage. Table 25 shows a brief characteristics of this mixer.

4.3.3 Reference oscillator

A Hewlett-Packard 8648B synthesized RF signal generator took the reference oscillator's role in this experiment; to generate a continuous pure wave at 328 MHz. The phase noise from this source is expected to be very small, and table 26 gives specifications of the synthesizer for 500 MHz. Since synthesizers synthesize the output frequency using phase-locking, one expects a similar or lower phase noise at a smaller frequency.

Parameter	**Value**
Conversion loss	5.8 dB
Phase detection gain constant	0.34 V/rad
Optimum LO power	7 dBm
typical output offset voltage	3 mV
LO - IF isolation	36 dB

Table 25: Relevant specifications of the SRA-1W+ mixer for application of phase detection.

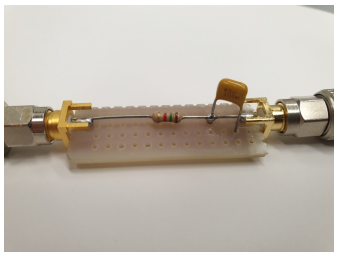

Figure 85: The low-pass RC filter with a cutoff frequency of 106 Hz to monitor the phase detector's output.

4.3.4 Phase demodulator filter

The phase detector's output is also interesting for analysis purposes; this is the phase demodulation port of the experiment. The still relatively large IF filter's bandwidth, in the order of 20 MHz, together with the fact that the noise power density is also strong, causes an extensive amount of noise. This will appear on top of any interesting signal at this output. A way to overcome this problem is by using a single-stage low-pass RC filter. With the resistor value of R = 1.49 KΩ and the capacitor value of C = 1.01 µF. The cutoff frequency is:

$$f_c = 1/2\pi RC = 106Hz \tag{75}$$

From a white noise source, this filter will allow a total noise power corresponding to the filter's equivalent noise bandwidth:

$$B_L = 1/4RC = 166Hz \tag{76}$$

Figure 85 shows a photo of this filter, and the band-pass of this filter will be visible in plots of results sections such as figure 98.

4.3.5 Loop filter

This experiment's loop filter core is a lag-lead active filter. It has one integrator, implemented with an OPAMP, followed by a variable gain stage. In order to avoid

Frequency offset	**Phase noise**
1 Hz	-70 dBc/Hz
10 Hz	-96 dBc/Hz
100 Hz	-97 dBc/Hz
1 kHz	-93 dBc/Hz
10 kHz	-116 dBc/Hz
100 kHz	-140 dBc/Hz
1 MHz	-146 dBc/Hz

Table 26: The single sideband phase noise of HP8648B synthesizer.

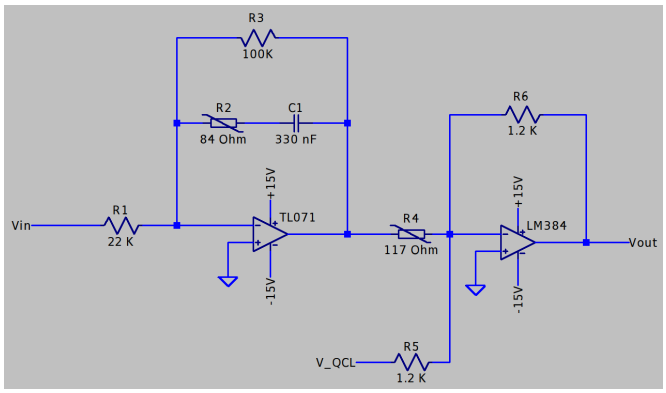

Figure 86: Schematic of the loop filter to phase lock the QCL. The first OPAMP is an Integrator with a limited DC gain, while the second OPAMP is a variable gain block for the signal path.

saturation, the gain of the integrator OPAMP is limited, and also, a potentiometer makes it possible to change the integrator's time constant. Figure 86 shows the schematic of the loop filter.

Since there is DC coupling from the loop filter's output to the QCL, it is important that while correcting the QCL disturbances within the PLL action, the QCL's DC operating voltage is not changed. Otherwise, the frequency of the laser changes while trying to stabilize it, disabling phase locking. In order to compensate for this voltage offset, the adding node at the negative input of the gain's OPAMP adds the DC operating voltage set point of the QCL, set by a potentiometer, to the signal path. Offset trimming is essential at some points to manage the DC offsets in the system: special care is taken toward the phase detector's parasitic offset and the first OPAMP's. Figure 87 shows a photo of the actual circuitry.

Different aspects are important in selecting an OPAMP for an active loop filter (Thompson, 1979).

I) OPAMPs have limited bandwidth. The corresponding quantity is the Gain Bandwidth Product (GBP), with a typical value of $\sim$ MHz. This limited band-

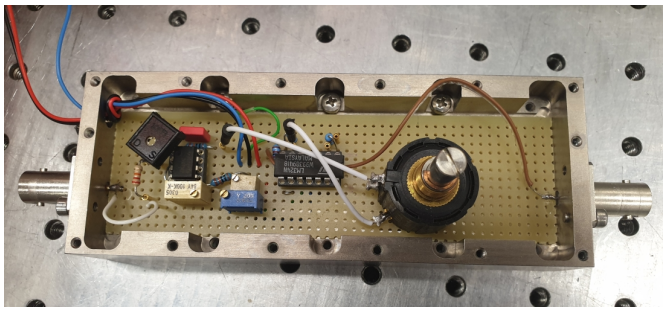

Figure 87: The implemented loop filter circuit. The output from the phase detector enters the loop filter from the left BNC connector.

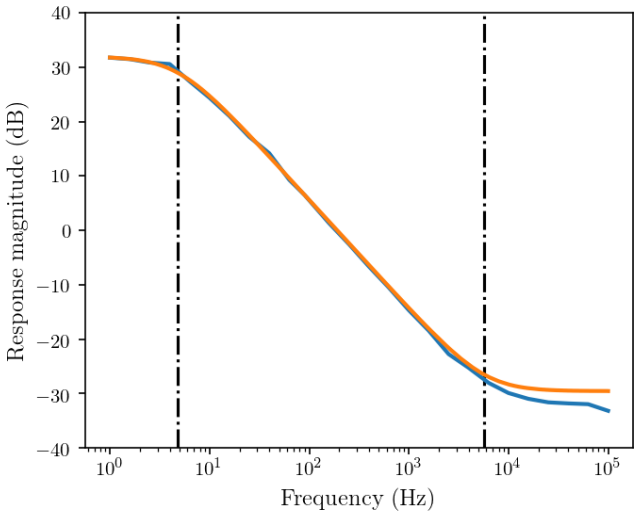

Figure 88: The measured transfer function of the loop filter. The blue curve presents the measurement, while the orange one corresponds to the simulation. The dashed line on the right represents the position transfer function's pole associated to the $\tau_2 + \tau_D$ time constant. Similarly, the left dashed line represents transfer function's zero associated with the τ_2.

width adds a parasitic pole in the PLL's open loop transfer function, as will be seen in equation 77. This parasitic pole can affect the PLL's transfer function and limit the PLL's stability.

II) Input offset voltage of the OPAMP also matters since a large DC voltage gain will amplify it, causing saturation problems. Since the QCL is a voltage-controllable oscillator, changes in the DC point will change the output frequency of the laser. If phase locked, phase locking will try to correct against it, which can put stress on the control loop and even result in loss of lock. For a robust design, the offset's temperature coefficient also has importance.

III) Loop filter's added noise can be an issue in a PLL system. The corresponding quantities are e_n, the input-referred noise voltage density with the unit of $nV/\sqrt{Hz}$, and i_n, the input-referred current noise density with the unit of $pA/\sqrt{Hz}$. Section 4.4 presents the essential tool for noise analysis in a PLL system.

As previously said in sub-section 4.2.4, one should consider the finite bandwidth of the OPAMPs for high end designs. Figure 88 shows the result of measuring the loop filter's transfer function alone. It measures the output's amplitude versus the input's amplitude at different frequencies. A sinusoidal lab signal source and a Lock-in amplifier were the equipment to measure it.

Figure 88 shows that at higher frequencies measured transfer function deviates from the simulation. The limited bandwidth of OPAMPs causes this: they have less gain at higher frequencies, which also limits the loop filter's transfer function.

OPAMP	Open loop gain	e_n	Input offset	GBP	Tech
TL071	200 $\frac{V}{mV}$	15 $\frac{nV}{\sqrt{(Hz)}}$	3 mV	4 MHz	JFET
LM324	100 $\frac{V}{mV}$	35 $\frac{nV}{\sqrt{(Hz)}}$	2 mV	1 MHz	BJT

Table 27: Specifications of the selected OPAMPs for use in the loop filter.

For a better simulation, the additional effects of the OPAMP-induced parasitic poles can be added to the loop filter's transfer function as:

$$F_(s) = \frac{\tau_D}{\tau_1}\frac{1+s\tau_2}{1+s(\tau_2+\tau_D)}G_{amp}\frac{1}{1+s\tau_{p1}}\frac{1}{1+s\tau_{p2}} \tag{77}$$

here τ_{p1} and τ_{p2} are the parasitic poles from limited bandwidth of 1st and 2nd OPAMP.

Table 27 summarizes relevant parameters of the OPAMPs used.

4.3.6 Static phase error estimation

Equation 55 and the details presented in subsection 4.2.1, along with the phase detector's specifications and design parameters as shown in table 28 can all be put together to estimate the static phase error present in the QCL phase-locking experiment. From the equation 55:

$$\overline{\theta_e} = \frac{V_{co}}{K_{PD}F_{DC}} - \frac{V_{pdo}}{K_{PD}} = 0.7 \quad rad \tag{78}$$

4.3.7 Second order system approximation

Subsection 4.2.4 introduced the preliminary formalism for a second order PLL design. Although the design is more complex, still it is worthy to have the parameter set that presents the design in a 2nd order approximation. The main parameter set can be the natural frequency ω_n, and the damping factor ζ. Alternatively the integrator's time constant τ_2 and the loop gain of the PLL could also be chosen. One can estimate the ζ and the ω_n with:

$$\omega_n = \sqrt{\frac{K_v}{\tau_1}} = 379 \quad krad/s \tag{79}$$

being the natural frequency and with

$$\zeta = \frac{\omega_n}{2}(\tau_2 + \frac{1}{K_v}) = 5.3 \tag{80}$$

being the damping factor of the system, which by being larger than unity, means that in this approximation the control loop behaves over damped and therefore a large phase margin close to 90 degrees is expected.

4.3.8 Full transfer function

Multiplying the relation 77 with the constants from the two main remaining elements of the system: the phase detector and the oscillator (the QCL), results in the open loop transfer function of the PLL system:

$$G_(s) = K_{PD} K_v G_{amp} \frac{\tau_D}{\tau_1} \frac{1 + s\tau_2}{s(1 + s(\tau_2 + \tau_D))} \frac{1}{1 + s\tau_{p1}} \frac{1}{1 + s\tau_{p2}} \tag{81}$$

The blue and orange traces of figure 89 show the simulated magnitude and phase of the open loop transfer function for the PLL of this experiment, respectively.

The open-loop gain curve asymptotes a horizontal line at very low frequencies to the DC loop gain value, which is not visible in figure 89 . In Bode plots, toward higher frequencies, passing each transfer function's zero increases the gain curve slope by 10 dB/decade, and passing each pole will reduce it by the same amount. Similarly, passing each zero will add 90 ° to the phase curve, while each pole subtracts 90 ° from it. The frequency at which the open loop gain value reaches unity (0 dB) measures the control loop bandwidth. A key quantity to check with

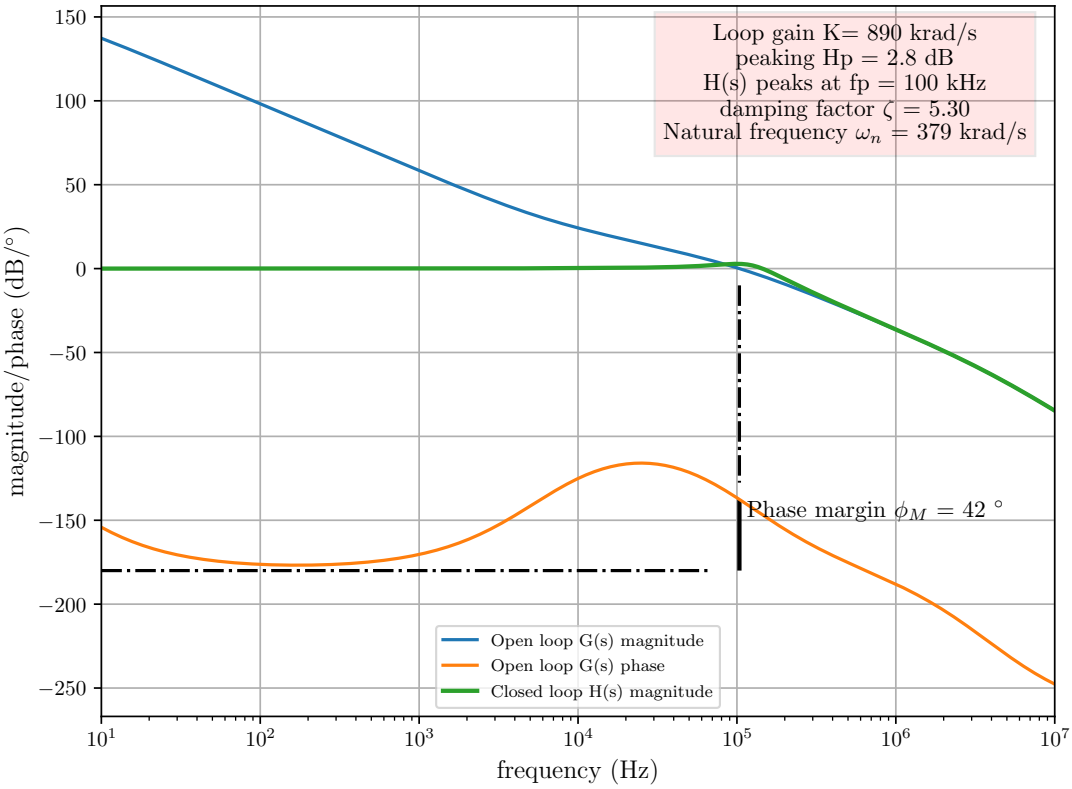

Figure 89: Simulation of the open-loop (G(s)) and closed-loop (H(s)) transfer function for phase-locked QCL. The box presents a selection of the important parameters of this PLL system. The solid and dashed black lines correspond to the phase margin estimation.

the helpf of the Bode plot is the stability phase margin, defined as the phase difference to 180 ° when the gain curve crosses unity. The black solid and dashed lines in figure 89 help to read and identify this quantity. If the phase margin reaches zero, the control loop is unstable and will oscillate since positive feedback will occur in a round trip within the control loop. Practical designs hardly risk the phase margin below 40°.

4.3.9 PLL noise bandwidth

As a requirement for PLL signal-to-noise considerations, the equivalent noise bandwidth of the closed loop transfer function H(s) has to be estimated, which defines as:

$$B_L = \int_0^\infty |H(f)|^2 df \tag{82}$$

For a 2nd order PLL of type 2, with the help of the calculated performance parameters from the table 28 (Gardner, 2005):

$$B_L = \frac{K}{4}(1 + \frac{1}{4\zeta^2}) = 231.4 \quad (kHz) \tag{83}$$

Since a second-order system approximation is behind this estimation, the noise bandwidth is calculated based on the modeled closed-loop transfer function and using Eq. 82. With the help from the more sophisticated H(s) from simulations, similar to what is presented in figure 77, figure 90 repeats the same H(s) curve, together with a demonstration of equivalent noise bandwidth which is 251 kHz.

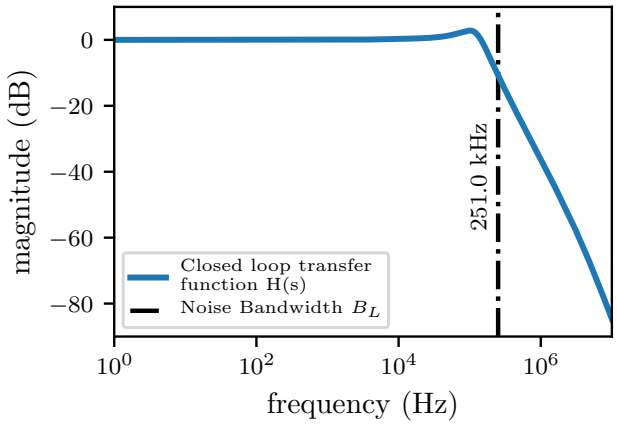

Figure 90: The integral of equation 82 is calculated for the simulated closed loop transfer function, also shown in figure 89. The dash-dotted line shows the equivalent noise bandwidth of the transfer function.

4.3.10 Corresponding PLL ranges

The four ranges introduced in the subsection 4.2.3 should also be examined in the PLL design phase (Encinas, 1993). For the Hold range:

$$\Delta\omega_H = K_o K_{PD} F_{DC} = K_v = 1.05 \times 10^9 rad/s = 167.2MHz \tag{84}$$

Which is correct for the case of no static phase error. The importance of the hold range for a QCL phase-locking experiment is when the free-running frequency of QCL deviates from the reference oscillator. This is the range over which PLL maintains the lock.

As presented earlier, two capture ranges are associated with a PLL system. The one for fast capture processes is called the lock-in range, which for a second-order lag lead loop filter, it is equal to the loop gain:

$$\Delta\omega_L = K = 890krad/s = 142kHz \tag{85}$$

The PLL immediately locks if the free-running QCL frequency lies within this range of the reference oscillator. On the other hand, within the pull-in range, lock capture is a slow process:

$$\Delta\omega_p = \sqrt{2K_{DC}K} = 43.3Mrad/s = 6.9MHz \tag{86}$$

From the subsection 4.2.3, for the time estimation of a pull-in process for a second-order loop, one recalls that:

$$T_p = \frac{\Delta\omega^2\zeta^2(1 + 1/4\zeta^2)^3}{16B_L^3} \tag{87}$$

Therefore, a large noise bandwidth and a small damping factor are preferred for a faster pull-in process.

The pull-out range deals with the frequency span over which the PLL handles the reference frequency steps without temporary loss of lock. For this range, one has:

$$\Delta\omega_{po} = 1.8\omega_n(\zeta + 1) = 4.3Mrad/s = 684kHz \tag{88}$$

The importance of this range relies on the need to change the QCL's frequency without losing the phase lock. With a step series of less than the above size and waiting for the PLL to settle down on the new frequency, one should be able to change the reference frequency safely.

4.3.11 PLL signal to noise ratio

With the signal and noise levels known from the IF processor, one can estimate the signal-to-noise ratios for a PLL system, therefore being able to consider the effect of noise on PLL's performance. The noise level at the IF processor's output has a typical noise density of -80 dBm/Hz which in a 50 Ohm system translates to a noise voltage spectral density of $N_0 = 5 \times 10^{-10}\ V^2/Hz$. Similarly the QCL peak has a typical power of -11.5 dBm corresponding to an rms voltage of $V_{i,rms} = 0.06$ V. The two form the one-sided input phase noise density of as (Gardner, 2005) (Wolaver, 1991):

$$\Theta_0 = \frac{2N_0}{V_{i,rms}^2} = 1.4 \times 10^{-7}\ rad^2/Hz \tag{89}$$

With the closed loop transfer function, the PLL passes this noise to the QCL. For the rms of QCL phase noise as a result of input noise density one can write:

$$\overline{\theta_o^2} = \Theta_0 B_L = 3.54 \times 10^{-2}\ rad^2 \tag{90}$$

Which means an rms phase noise of 0.19 rad. This estimation can also be applied to the input signal-to-noise ratio to the PLL which is:

$$SNR_i = \frac{1}{\Theta_0 B_i} = \frac{1}{2\overline{\theta_i^2}} = 0.33 \tag{91}$$

In a similar way with the relation of input signal-to-noise ratio, one can also define a loop signal-to-noise ratio as:

$$SNR_L = \frac{1}{2\Theta_0 B_L} = \frac{1}{2\overline{\theta_o^2}} = 14.2 \tag{92}$$

The noise outside of the loop pass band that has been rejected by the H(s), has to be carried by the phase detector. The fact that in this experiment, the noise bandwidth of the IF processor is much larger than the equivalent PLL noise bandwidth, leads to:

$$\overline{\theta_e^2} \simeq \Theta_0 B_i/2 = 1.49\ rad^2 \tag{93}$$

Corresponding to an rms phase noise of 1.22 rad.

As mentioned in subsection 4.2.2, additional noise present at the phase detector impairs and reduces its effective gain. With the estimated phase noise present at the input, one can estimate a gain reduction of

$$K'_{PD} = K_{PD} e^{-\theta_{e,rms}^2/2} = 0.48 \times K_{PD} \tag{94}$$

Parameter	Value	Name/Comment
τ_1	7.3 ms	time constant
τ_2	28 μs	time constant
τ_D	33 ms	time constant
K_{PD}	0.34 V/rad	damping factor
F_{DC}	4	DC gain of loop filter
K_{DC}	1.05×10^9 rad/s	PLL's DC gain
K	8.66×10^4 rad/s	Loop gain
$Peaking$	2.9 dB	Closed loop gain peaking
G_{amp}	10	2nd OPAMP's gain
ζ	5.3	damping factor
ω_n	3.79×10^5 rad/s	natural frequency
K_v	9.73 MHz/V	QCL voltage tuning

Table 28: The calculated parameters for the QCL phase locking experiment.

Which is a substantial gain reduction, due to the large present noise, the gain reduction is substantial.

4.3.12 Parameter list

At the end of this section, the parameter list resulted from the experimental setup and the corresponding simulations is presented. Most of these have been calculated based on the design of the system and with the help of the different relations presented in this chapter. Only the gain of the 2nd OPAMP was a variable to fine tune the phase lock. Table 28 shows a summary of the parameters.

4.4 Noise model for the QCL phase locking experiment

Later in this chapter, the effect of noise will be discussed in the results section. This section presents the basics of noise modeling for a PLL system as a preliminary step for that discussion. This experiment has many noise sources, and not all affect the phase-lock quality similarly. In reality, only a few are important, and one should consider them in the design phase (Robins, 1991) (Gardner, 2005). Figure 91 shows the proposed noise model for the experiment.

In general, in order to write a transfer function for the effect of each noise source on the output phase, one can use the general transfer function formalism for a closed-loop control system as following (Dorf & Bishop, 2002):

$$\frac{output}{input} = \frac{A}{1 + AB} \tag{95}$$

Where 'A' is the total gain from the noise source to the output, and 'B' is the total gain from the output to the noise source. In fact, the same relation derives

Table 29: Most powerful noise sources and their effect on the phase-locked QCL

source	source PSD	transfer function	typ/max phase PSD
Superlattice	22.4 $\frac{\mu V}{\sqrt{Hz}}$	H(s)/K_{PD}	66 $\frac{\mu rad}{\sqrt{Hz}}$ typ
1st OPAMP e_n	15 $\frac{nV}{\sqrt{Hz}}$	H(s)/K_{PD}	44 $\frac{nrad}{\sqrt{Hz}}$ typ
R1 (Nyquist)	19 $\frac{nV}{\sqrt{Hz}}$	|H(s)/K_{PD} + E(s)K_o/s|	2.5 $\frac{\mu rad}{\sqrt{Hz}}$ max
2nd OPAMP e_n	35 $\frac{nV}{\sqrt{Hz}}$	|H(s)/K_{PD} + E(s)K_o/s|	4.6 $\frac{\mu rad}{\sqrt{Hz}}$ max

the closed loop transfer function from the open loop one, seen in Eq. (65). As an example regarding noise, noise transfer of the SLD and the IF processor denoted n_{SLD} to the output point with the phase denoted θ_{Out} will consist of all blocks from the phase detector's input to output (A in relation 95), and then from output to the input of phase detector(B in relation 95, which is unity), as:

$$\frac{\theta_{Out}}{n_{SLD}} = \frac{K_{PD}F(s)G_{DC}\frac{K_{VCO}}{s}}{1 + K_{PD}F(s)G_{DC}\frac{K_{VCO}}{s}} \tag{96}$$

The nominator is only G(s), the PLL's open loop transfer function discussed in 4.2.4. The same plus 1 in the denominator changes relation 96 to the closed-loop transfer function: H(s). This means n_{SLD} affects the output noise precisely in the same way as the reference oscillator's noise does; both propagate with the same H(s) low-pass profile. Table 29 presents the most powerful noise sources present in the experiment, together with a typical resulting phase PSD from them. The table shows how the wide-band SLD noise that is present at the input, should dominate the overall noise performance of the phase-locked QCL.

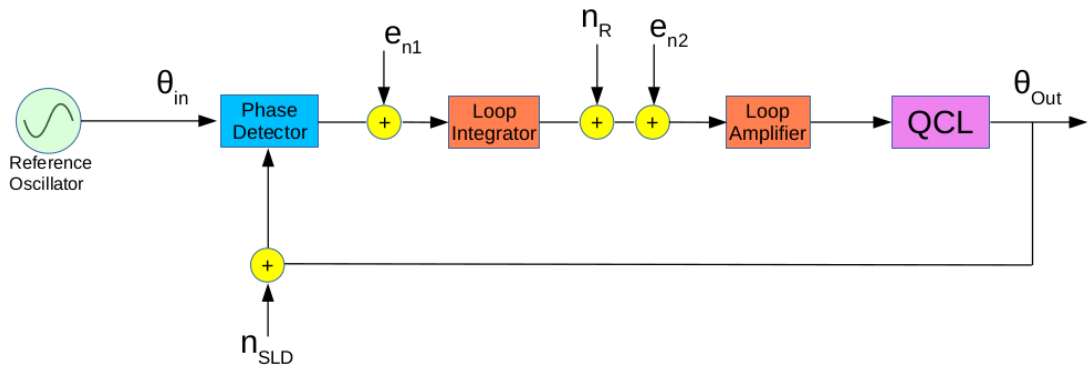

Figure 91: Noise model for QCL phase locking experiment showing only relatively strong noise sources. n_{SLD} contains both the SLD's and the IF processor's noise contribution. The voltage noise of the first OPAMP is e_{n1}, the Nyquist noise of the loop integrator's resistor is n_R, and the voltage noise of the 2nd OPAMP is e_{n2}.

4.5 Results from phase locking

The fine tuning in the QCL phase-locking experiment is done by changing the PLL's total gain using the loop filter's gain knob. While tuning, in a certain potentiometer's region, QCL can track the reference oscillator's phase, i.e., phase-locked. Figure 92 shows a photo of the stabilized QCL line in the IF monitor output visible in the middle.

In the figure 92, resolution bandwidth of the spectrum analyzer is 1 MHz, much wider than the phase-locked laser noise profile details shown in the following pages. Watching the phase-locked QCL line over a long period is an important measurement. Figure 93 shows this measurement in a waterfall plot, similar to those measurements done in chapter 3 for the frequency-locked laser line done with a Software Defined Radio (SDR) receiver. The central vertical bright line results from the SDR's artifacted channels. In contrast, the vertical line at 329 MHz with scattered emission on both sides is the phase-locked QCL line. The scattered emission on both sides of the QCL line corresponds to noises within the PLL from different sources. As visible in the waterfall plot, most of the time, the QCL is tracking the reference at 329 MHz, but sometimes it is not, during which the PLL failed to control QCL's phase. Averaging the waterfall data over time reveals the phase-locked QCL's power spectrum over the SDR's noise floor. Figure 94 shows this plot.

The spectrum in figure 94 has a much finer resolution of 12.5 kHz per spectral channel compared to 1 MHz seen in figure 92. It shows the fine energy distribution close to the QCL's peak at 329 MHz, arising from the phase noise present in the system. Although still the SDR's resolution is limiting in this measurement, but one can read an upper limit on QCL line's FWHM of 7 kHz from this data.

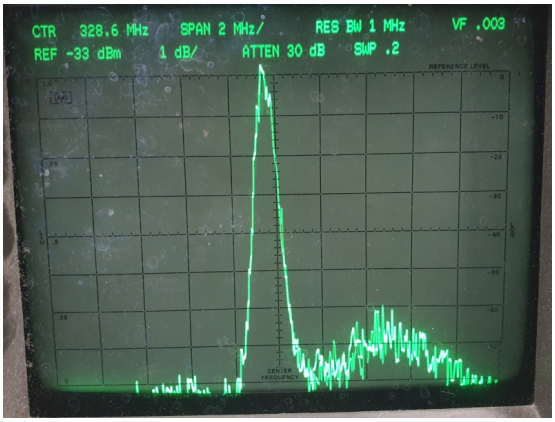

Figure 92: The phase-locked QCL line visible in the IF monitor output, at a low-resolution bandwidth. The high peak in the center corresponds to the QCL line. The noise floor is also noticeable, and the locked QCL line is about 8 dB over the noise floor.

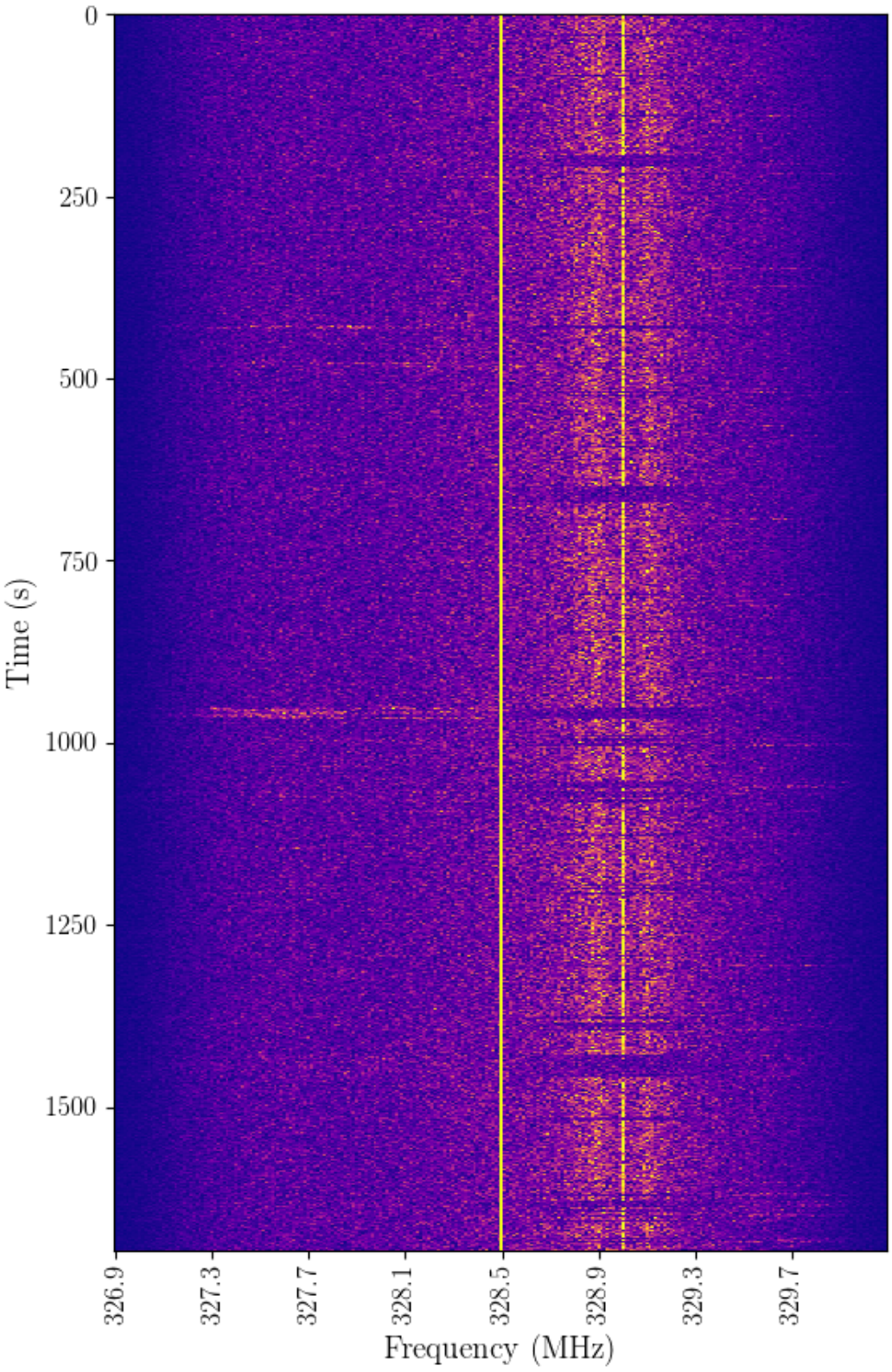

Figure 93: Waterfall spectrum of the phase-locked QCL as measured in the IF monitor output with the help of an SDR. The line at the frequency of 329 MHz corresponds to QCL emission, and the haze on both sides is the phase noise. This plot also shows that sometimes the QCL has jumped out of the lock, where gaps are visible along the QCL and noise shoulders.

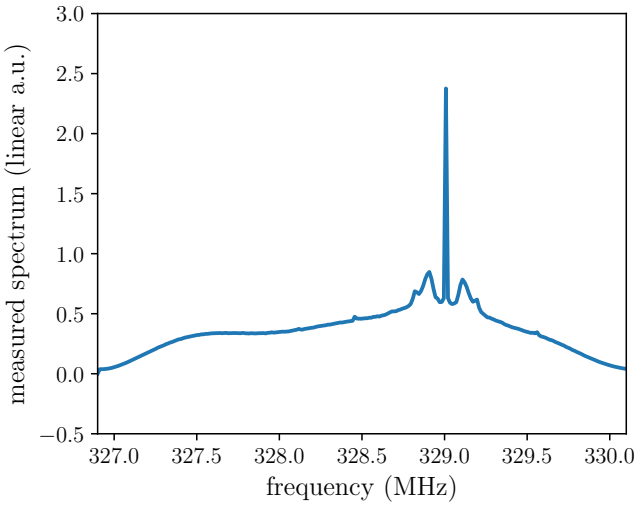

Figure 94: The phase-locked QCL is visible in the IF monitor's averaged data. The tall and narrow line is the QCL's line, with the phase noise visible on both sides, and it has little bumps which correspond to the noise-peaking behavior in the PLL and additional noise components. Interpolation has removed the artifacted channels of the SDR.

4.5.1 Phase noise spectrum

In figure 94, the phase noise haze is visible on the QCL's both sides. From the exact figure, the spectrum in one side of the QCL is extractable, and figure 95 shows this data, with the QCL line, the carrier, observable on the rightmost side, and the phase noise on the left side and next to that. The phase noise of the phase-locked QCL is visible from the QCL line at 329 MHz down to 328 MHz in the plot. Two noise peakings are observable closer to the carrier, one larger

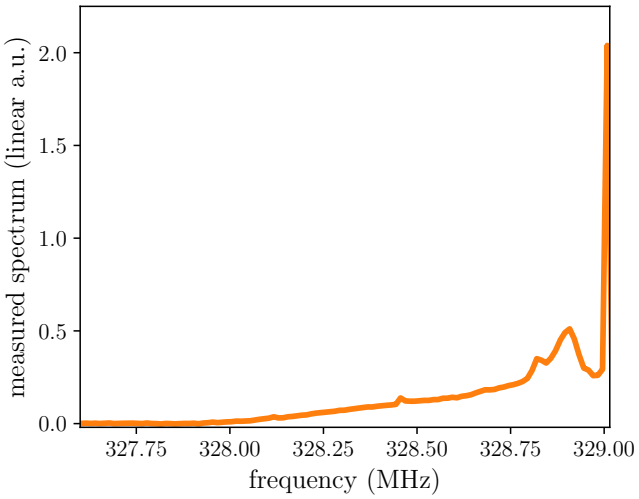

Figure 95: The one-sided phase noise spectrum from the phase-locked QCL experiment. The QCL peak (the carrier) is on the rightmost side at 329 MHz. The phase noise is visible down to about 1 MHz away from the carrier.

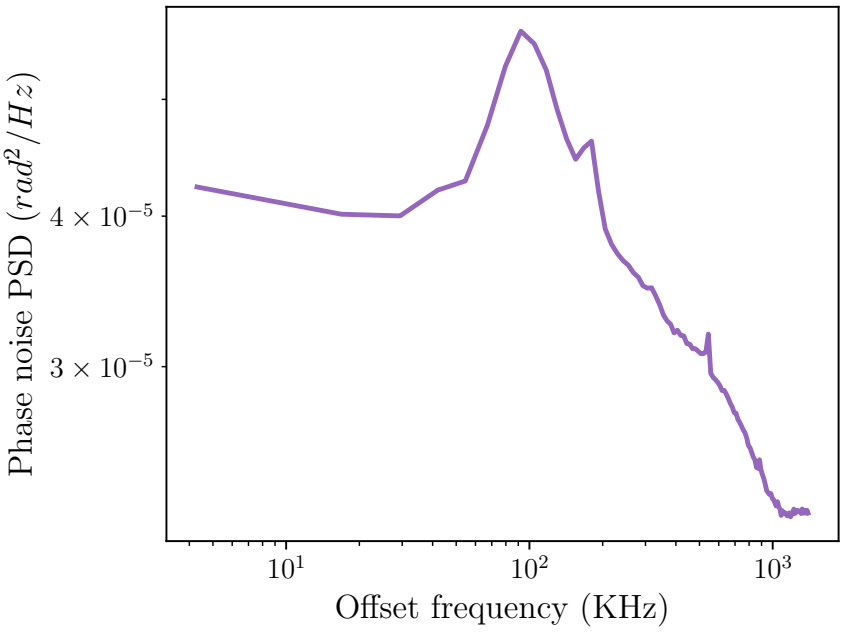

Figure 96: Extracted one sided phase noise power spectral density of the QCL with the help of spectrum measurements using the SDR.

than the other. Also, a third little noise modulation component is further away at more distant offset frequencies, visible atop the phase noise continuum. Table 30 presents some measured carrier-to-noise ratio and offset frequencies of data shown in figure 95.

4.5.2 Comparison of measured phase noise with noise model

Section 4.4 introduced a noise model for phase-locked QCL along with a list of the powerful noise sources. Now with the spectrum measurement of the locked QCL line, it is instructive to have a closer look at the QCL line and try to compare it with the noise model. From the one-sided phase noise spectrum shown in

Table 30: Offset frequencies and carrier-to-noise ratio for observable noise features of figure 95.

parameter	**value**
modulation frequency of 1st noise peak	100 kHz
Ratio of carrier to the 1st noise peak	2.8
modulation frequency of 2nd noise peak	188 kHz
Ratio of carrier to the 2nd noise peak	3.5
modulation frequency of 3rd noise peak	552 kHz
Ratio of carrier to the 3rd noise peak	5
modulation frequency of phase noise to reach noise floor	1.08 MHz
Ratio of carrier to the noise floor	7.1
QCL frequency in the IF	329 MHz

figure 95, one can calculate the two sided spectrum and by dividing it with the measurement bandwidth, form the phase noise PSD. Figure 96 shows this plot. If one assumes the first peak as noise peaking, the one at 100 kHz offset from the carrier, a noise peaking of around 3 dB is readable from the plot. Without considering the phase detector gain deterioration due to input noise, as presented in sub-section 4.2.2, these values are in good agreement with the calculated transfer function done in sub-section 4.3.8 and shown in figure 89. Sub-section 4.3.11 predicted that the wideband noise should reduce the loop gain to half, meaning that the good agreement of the calculated and measured noise peaking should have not happened. However, this missing factor of two can be accounted for the different loop gain potentiometer setting, between the measured day and the day the spectra are recorded. It is worth repeating that PLL was operational in a range of potentiometer settings, and this can account for this factor of two.

4.5.3 Phase detector's output

When the QCL is phase-locked, the phase detector's output contains phase demodulation information of the QCL line, plus a wide-band noise. In order to measure the phase demodulation, the 106 Hz filter preceded the oscilloscope. Figure 97, top, shows this phase demodulated signal, which contains the pulse-tube-induced frequency disturbance remaining with a period of 0.58 seconds. The constant DC voltage corresponds to the equilibrium tuning voltage of the QCL.

The bottom plot of figure 97 contains phase demodulation output with unlocking happening in the middle. The noise apparent at the unlocked time is the wideband noise of the IF output, whereas the rest additionally contain the demodulated periodic QCL disturbances plus the phase noise of the phase locked QCL. The phase detector converts phase fluctuations to voltage fluctuations with a K_{PD} conversion factor. Therefore, voltages at the phase detector's output can be directly assigned to phase deviations. At this point, it is worth looking at the power spectrum of demodulated phase disturbances. One can use the Fast Fourier Transform (FFT) algorithm to obtain the power spectrum of time series measurement in the top plot of figure 97, presented in figure 98.

The overall noise floor behavior of figure 98 shows the effect of the 106 Hz low-pass filter on the measurement. Lines appearing below 40 Hz arise from leftover QCL disturbances. Lines appearing at 50 Hz and harmonics are leakages of the mains electricity to the experiment, showing presence of a relatively strong ground loop. The high noise floor level within the filter's pass-band corresponds to the wide-band noise in the IF. On the other end, for frequencies greater than 1 kHz, one observes the oscilloscope's noise floor (not visible in the figure 98).

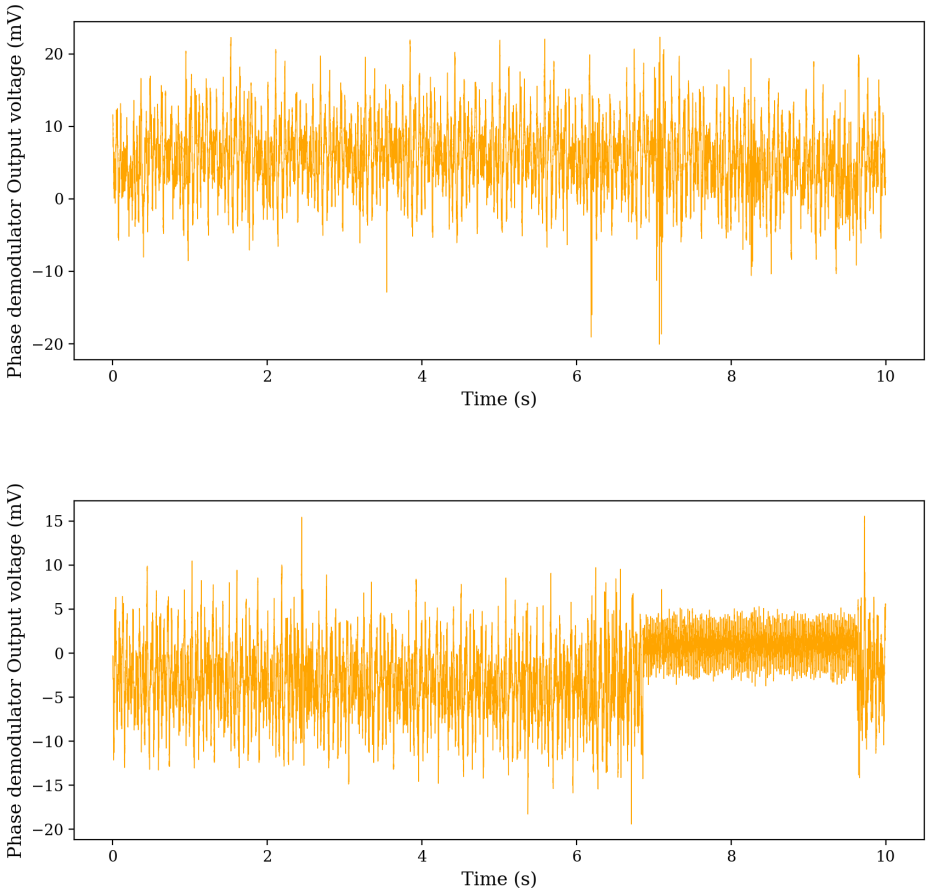

Figure 97: Time series record of the phase detector output measured with oscilloscope after the 106 Hz filter. Top: remaining phase modulations from pulse-tube disturbances are visible with a period of 0.58 seconds. The QCL is entirely in lock condition throughout this measurement. Bottom: Same measurement when a loss of lock has happened for 2.5 seconds, starting from t $\sim$ 7 seconds.

4.5.4 phase error estimation

As figure 98 shows, the total phase error has two main contributors. One is the uncorrected QCL line's phase disturbance leftover from the pulse tube. The other one is the wide-band noise that the PLL passes through. There are 17 full pulse-tube cycles in the top plot of figure 97, with a peak-to-peak mean of 29.9 mV. One can convert this to:

$$\theta_{pk-pk,\ pulse-tube} = V_{pk-pk} \times K_{PD} = 88 \quad (mrad) \tag{97}$$

of phase disturbances measured at phase demodulator's output. To consider the effect of the wide-band noise, the low-frequency part of figure 98 that contains most of the noise floor's energy is again plotted in figure 99. The main difference is the normalization to the FFT frequency bin's bandwidth, resulting in Power

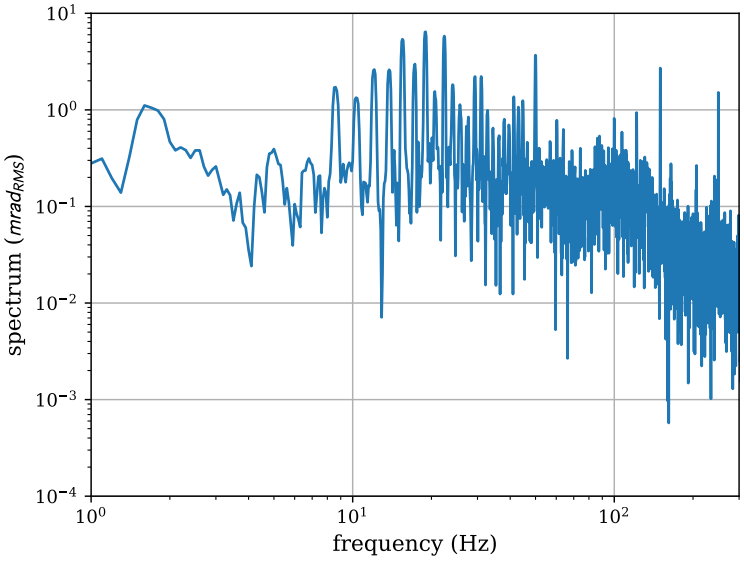

Figure 98: Voltage power spectrum of the phase detector output. Harmonics of the pulse tube from a fundamental of 1.72 Hz are visible up to $\sim$ 40 Hz.

Spectral Density (PSD). In order to estimate the noise floor PSD of the wide-band noise, the region between 51 and 99 Hz is used for averaging. The reason is that this area is relatively free of pulse-tube and mains electricity lines; therefore, most of the power there should come from the noise floor.

Figure 99 reveals a PSD of 0.22 $mrad^2/Hz$, marked in the plot with a thick solid black line. Multiplying this number with a relevant bandwidth helps to estimate the total noise floor's contribution. For the spectrum shown in figure 99, the filter's noise bandwidth is 166 Hz, giving a phase disturbance variance of:

$$\theta^2_{rms} = PSD \times BW = 36 \quad mrad^2 \tag{98}$$

Which corresponds to phase disturbances of only 6 mrad rms, much smaller than the 88 mrad from the pulse tube, meaning that in this small bandwidth, the pulse tube dominates the phase disturbances. In the next step, with applying the PLL noise bandwidth to the noise PSD:

$$\theta^2_{rms,\ wide-band\ noise} = PSD \times BW = 0.219 \times 2.51 \times 10^5 = 54969 \quad mrad^2 \tag{99}$$

Corresponding to a phase standard deviation of 234 mrad. Since the pulse tube disturbances and the SLD's wide-band noise does not correlate, one can calculate the variance of total induced phase disturbance as:

$$\theta^2_o = \theta^2_{rms,\ pulse-tube} + \theta^2_{rms,\ wide-band\ noise} = 62713 \quad mrad^2 \tag{100}$$

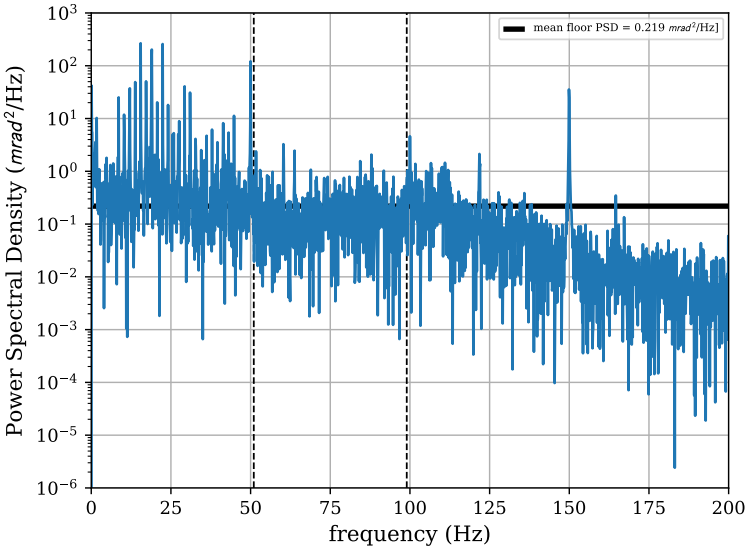

Figure 99: The phase Power Spectral Density (PSD) from the phase detector output after the 106 Hz filter, helpful for noise floor analysis.

Which corresponds to a total rms phase disturbance of 250 mrad. This value is acceptable for the PLL's operation. If the phase rms of QCL gets large enough to be comparable with 2π, QCL may miss one or more cycles and tracks back the references phase after that, this phenomena is called cycle slip (Gardner, 1979). The phase disturbance rms of 0.25 rad means that on some occasions, the QCL's phase will cycle slip. Analysis of practical PLLs has shown that for cases with $\theta_{o,rms} < 0.3rad$, cycle slipping is not a serious problem (Wolaver, 1991). Anyway with the uncertainties of these analysis, this may not completely be true and there is room for more work.

4.5.5 Loop signal to noise ratio

Sub-section 4.3.9 presented the definition of the loop noise bandwidth, with the new phase noise spectral density one can estimate the loop SNR as:

$$SNR_L = \frac{1}{2\theta_o^2} = 8 \tag{101}$$

As long as PLL's operation is questioned in respect of noise, when SNR_L is larger than 4, PLL operates well, and at around SNR_L 1, PLL completely loses the lock due to the extreme noise. The estimated loop signal to noise ratio reveals a relative good balance here. Loop bandwidth seems wide enough for better tracking and acquisition capability, but still larger than the limit in that noise impairs the PLL's operation.

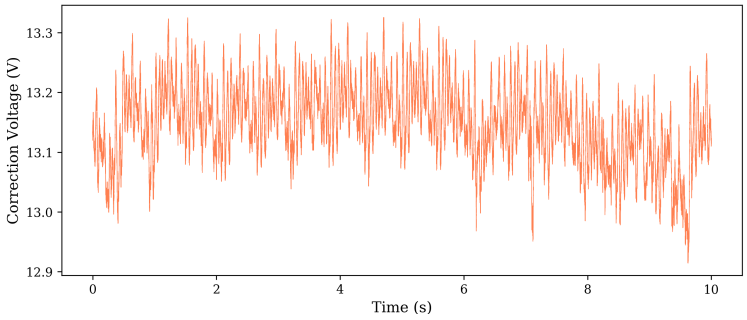

Figure 100: The measured correction port voltage, recorded along with the top plot of figure 97.

4.5.6 Correction voltage

The correction voltage to the QCL holds the necessary information to correct against the QCL frequency instabilities. Analyzing it reveals the unstable nature of the QCL. Figure 100 shows a relatively short measurement of this voltage over 10 seconds. The pulse tube-induced disturbances cause the periodic nature of the waveform.

With the frequency tuning constant of QCL at the correction port, the measurement shown in figure 100 can directly be transferred to the lineshape that the QCL would have had if it was not phase-locked over the measurement period of 10 seconds. Converting that data set to a histogram and transforming the voltages to the corresponding frequency is done and shown in figure 101. The measurement shows a peak frequency deviation of around 2 MHz, and an FWHM of 1.4 MHz could be assigned to the line in the figure 101. Compared to the locked QCL FWHM with an upper limit of 7 kHz, this shows the inherent power of phase locking to reduce the laser line broadening.

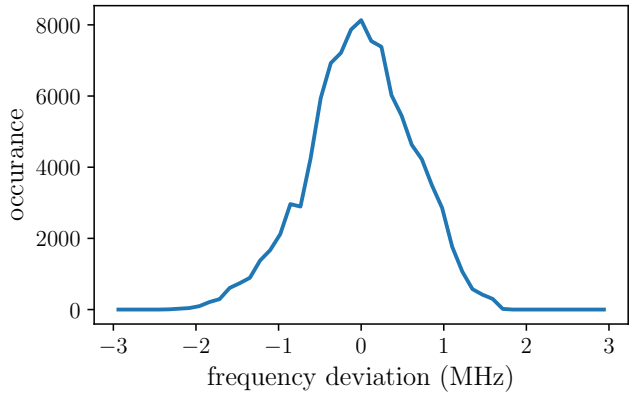

Figure 101: Histogram of the waveform shown in figure 100, converted to frequency units.

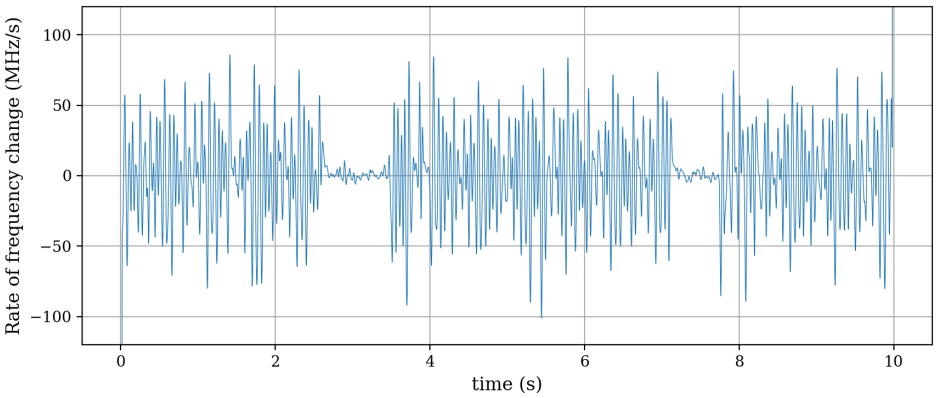

Figure 102: Rate of QCL's frequency change over time. Phase locking should be able to correct these changes. The two middle parts with y values close to zero are when the QCL is unlocked.

4.5.7 Frequency rate handling

Section 81 discussed that a frequency ramp is something that PLLs may be unable to handle. Figure 102 presents the measured frequency rate in the phase-locked QCL, including two regions where the lock was lost. The known voltage tuning coefficient of the QCL and the correction voltage fed to the QCL are used to generate this plot.

This data shows that the phase-locked QCL compensates for a peak frequency rate of 100 MHz/s. The relation of Eq. (74) can be used to check the handleability of such signals for the PLL. Although this relation comes from second-order PLL analysis, still, it is worth checking the caused phase stress due to tracking the worst observed frequency ramp case, as:

$$\lim_{t\to\infty} \theta_e(t) = \frac{\Lambda}{\omega_n^2} = 0.004\ rad \tag{102}$$

Which is a small and manageable error angle for the PLL system. Looking at figure 102 also does not show events of unlock after strong frequency ramp spikes. Therefore probably, frequency ramps were not the limiting factor in the experiment.

4.5.8 Phase-locked QCL time matters

As already seen in previous data, the QCL jumps out of phase lock state in some occasions, and this has to by analysed. Better than the spectra recordings via the SDR, are the phase detector and correction voltages with their finer time resolution. Figure 103 shows these waveforms on the top and middle sub-plots, where clearly loss of lock are identifiable with a strong decrease in the variance

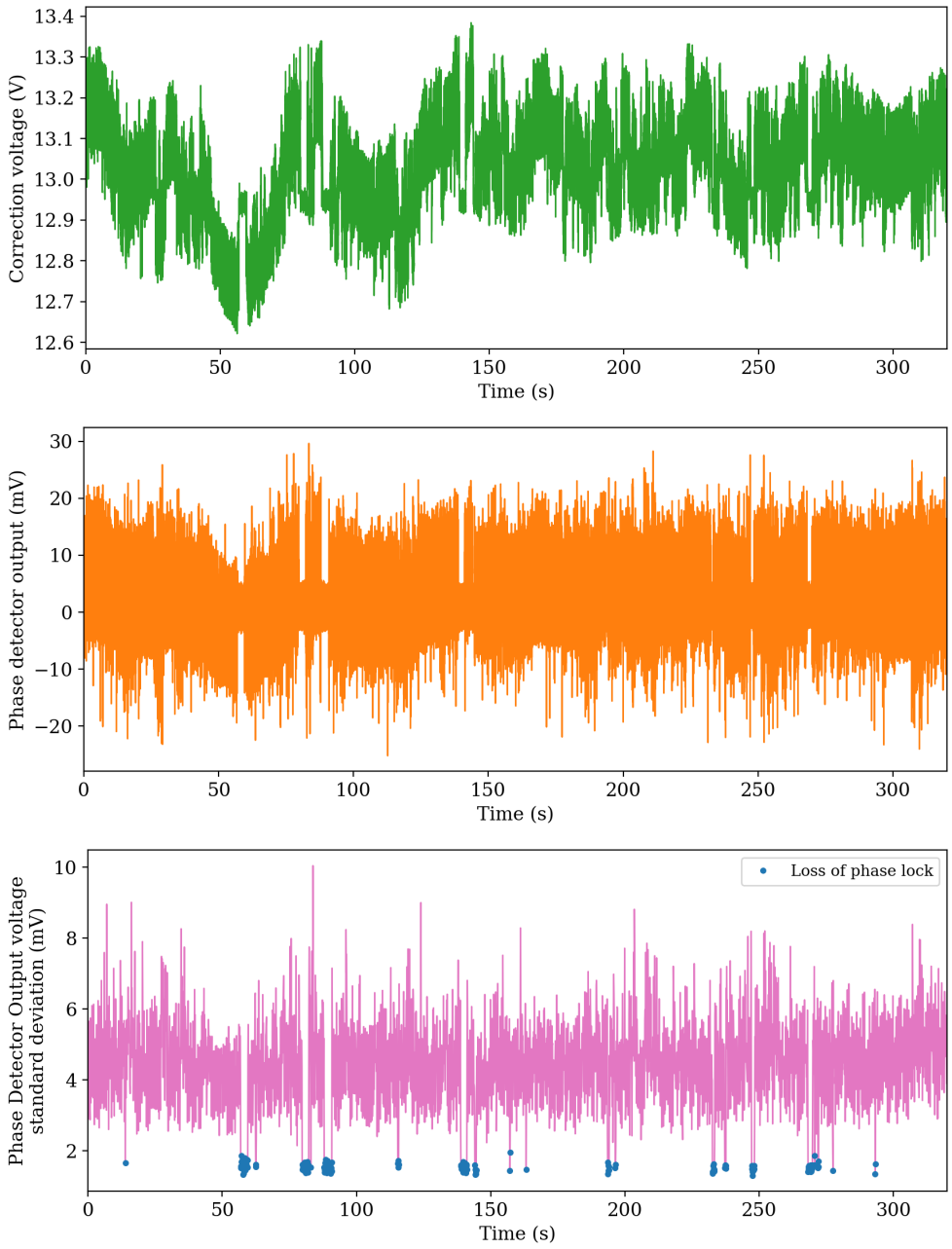

Figure 103: Top: Correction voltage to the QCL over 320 seconds. In this sample, QCL was in a locked state most of the time, and the unlocking is visible in sharp jumps to 12.95 Volts with a significantly smaller voltage variance. Middle: Phase demodulator output measured over the same time. Narrow gaps are where phase lock is lost, so only wideband noise is passed through the filter. It is in contrast to the phase-locked state when the demodulator output also contains error information of the QCL, which is simultaneously corrected. Bottom: Demodulator output after a standard deviation filter, revealing the events at which PLL lost the lock, here marked with blue circles.

of the recorded noise. The bottom sub-plot shows the phase detector's standard deviation, in which the loss of lock events of longer than 0.1 seconds are identified by condition of the standard deviation to fall below 2 mV.

Analysing the loss of lock as shown in figure 103, gives an example on statistic of lock loss. Figure 104 shows a histogram presentation of loss of lock events, plotted about their length. It shows that there are more events of shorter lock loss, compared to longer ones. The presented equation of 61 is a tool to analyse this data. For example, for the event in which the QCL was unlocked for 1 seconds, one can estimate:

$$\Delta\omega = \sqrt{\frac{16T_p B_L^3}{\zeta^2(1+1/4\zeta^2)^3}} = 126\ Mrad/s = 20\ MHz \tag{103}$$

To be the frequency difference between the QCL and the reference that the PLL had to compensate the voltage offset, to bring the QCL back to the lock. Although the presented calculation is a simple 2nd order system approximation for a normal oscillator, not one like the QCL with all the frequency disturbances, but still the order of magnitude for the created frequency steps after unlocking that has to be compensated, seems reasonable.

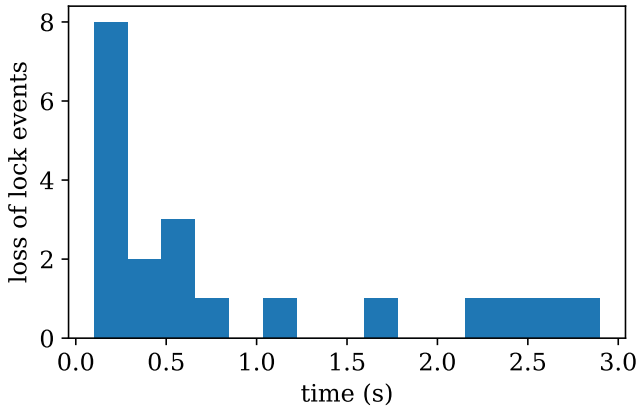

Figure 104: Histogram presentation of loss of lock events versus loss duration

5 Laboratory receiver at 4.7 THz

The first section of this chapter describes the cryostat that has been developed for this work, and it is also the platform that hosts the lab receiver at 4.7 THz. The next sections describe the experimental setup of the receiver plus some of its performance measures. The last section describes methanol emission line measurement undertaken for frequency calibration of the receiver.

5.1 Cryostat

The cryostat provides the essential cryogenic environment that few elements of this experimental setup need for their operation. The design has been shaped around an SRP-082B2 cold head with two cooling stages (Sumitomo Heavy Industries (SHI), 2023). The first and second stages can cool to around 30 K and 4 K, respectively. This cold head runs with pressurized helium from an F-70 helium compressor. The first stage of the cold head cools the radiation shield and accommodates thermal dissipation of the QCL. The second stage of the cryostat hosts the HEB detector and the Low Noise Amplifier (LNA).

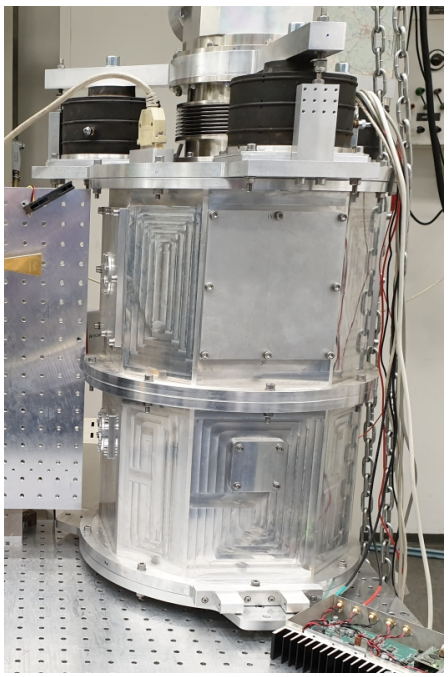

Figure 105: Photo of the cryostat on the experiment bench. More oversized windows on the upper section provide access to the 1st stage of the cooler, while smaller windows on the lower section are only to guide the optical beams in/out toward the 2nd stage's thermal bath.

5.1.1 Design

The cryostat has a design of a cylindrical shape. It has a diameter of 35 and a height of 60 cm. It is made of aluminum and is created by milling on a cylindrical shell. The cylinder is made in two parts, each 30 cm high. The outside walls are cut in an octagonal shape to ease the installation of the vacuum windows and fixture of optical elements to the cryostat's body. The top and bottom lid of the cryostat are also made of aluminum. The vacuum feedthroughs, the cold head, and the air cushion dampers are located on the top lid. In contrast, the bottom lid holds only one vacuum window on the center and three ball end grub screws to provide an adjustable three-point standing of the cryostat on the optical bench. Figure 105 shows a photo of the closed and figure 106 show schematic of the cryostat.

The pulse tube cryo cooler is installed vertically from the top, entering the cryostat from the top lid. It works based on an effect called surface heat pumping (Gifford & Longsworth, 1964). The process relies on generating helium pulses with a synchronous motor; in this case, creating 29 helium pulses during every

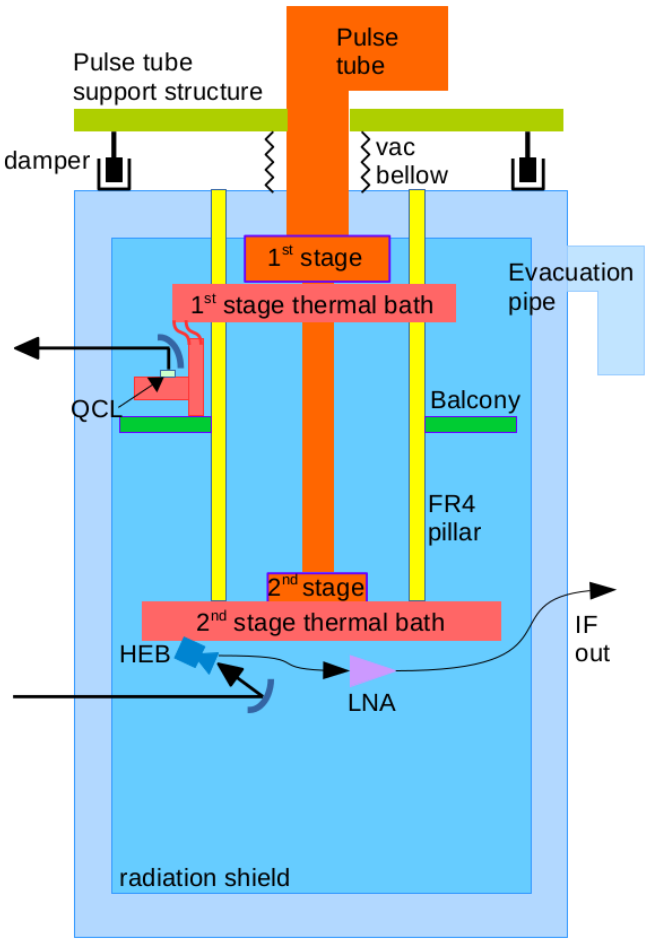

Figure 106: Schematic of the cryostat

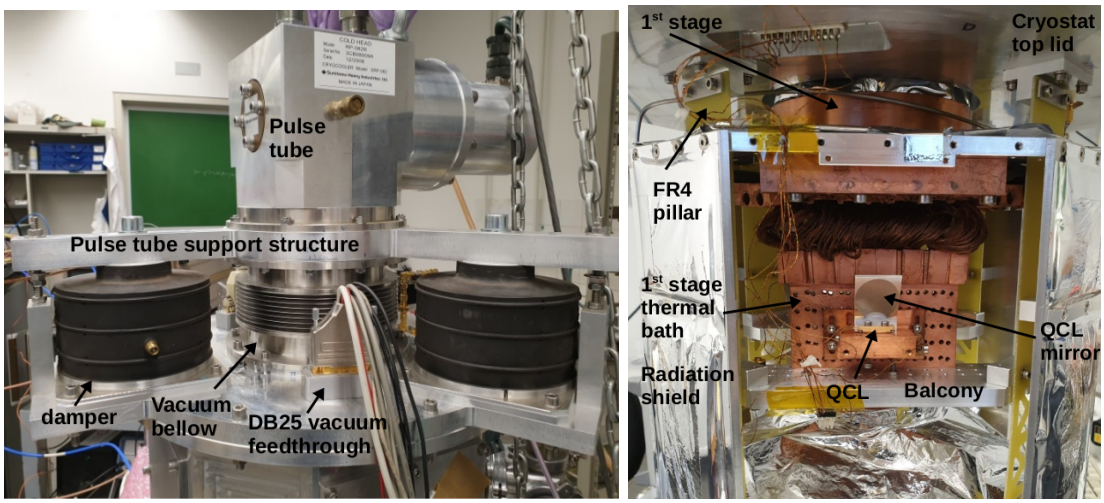

Figure 107: Left: The upper elements of the cryostat: the air cushions as dampers, the vacuum bellow, the vacuum feedthrough for electronics and the cold head pulse tube are visible in this photo. Right: Photo of the cryostat's inside. The pulse tube's 1st stage and the connected thermal bath, the QCL unit, the balcony, the radiation shield and the FR4 pillars are visible. Note the copper braid connections between copper blocks to isolate forced motions and conduct heat.

50 cycles of the mains line. This results in helium pulses with a period of 0.58 seconds (frequency of 1.72 Hz) being released toward the 1st and 2nd cooling stages. The mechanical movements of the cold elements is a known disadvantage of the method, therefor reducing them was foreseen in the design: Three air-filled cushions deployed as dampers, decouple the cold head movements from the cryostat's body on the cold head insertion point and hold the weight of the cold head at the same time, visible in figure 107. In the figure, the vacuum bellow can also be seen, creating the flexible boundary between the cryostat and the cold head, which is essential to isolate the forced motions. Connection of all these elements are done with the pulse tube support structure.

The thermal baths that the experiment's elements are installed on are made of 5N (99.999 %) oxygen-free high-purity copper (OFHC). A generic hole pattern is drilled on them to ease the installation of different parts. In addition, the second stage's thermal bath is also gold-coated to prevent oxidation. The thermal baths and the radiation shield are all thermally connected and mechanically decoupled from the cold head using copper braids. Braids are pressed into the blocks of copper to benefit the best thermal conductivity. All thermal baths are held inside the cryostat with the help of four vertical FR4 composite pillars that mechanically support them with a firm connection to the top lid of the cryostat. The 1st stage's thermal baths are hold on two pieces of aluminum block, called the balconies, that connect mechanically each couple of FR4 pillars for more stiffness against bending. The braid thermal connections complete the mechanical decoupling of

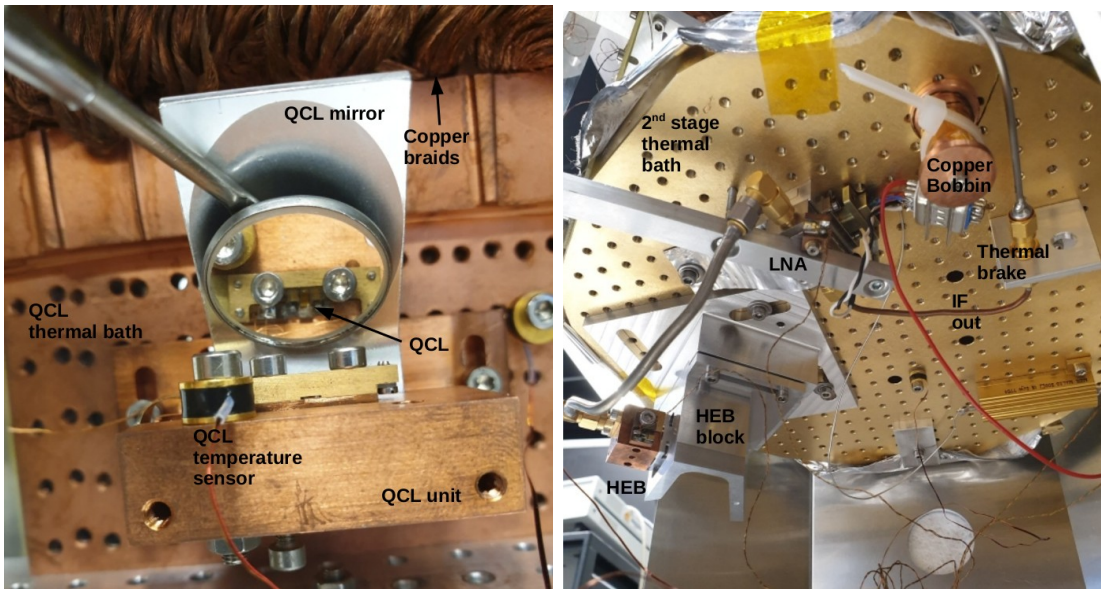

Figure 108: Left: QCL unit is installed on one of the 1st stage thermal baths and the QCL is visible with the help of the dental mirror. Copper braids are visible on top of the image; they connect this thermal bath to the 1st stage of the cryo cooler. Right: Assembly of the elements installed on the 4 K thermal bath. HEB block is visible in the lower left, and the LNA is visible approximately in the center.

thermal baths. Figure 107 right, shows these elements inside the cryostat.

Two DB25 vacuum feedthrough provide 50 wire connections between in and out of the cryostat, suitable for low-frequency currents. One of them is visible in figure 107. One is dedicated to temperature monitoring, with a standard connector defined by the Lakeshore Model 218 temperature monitor instrument (Lakeshore cryotronics, 2017). The other DB25 holds the signals for all the other purposes, including heater currents for temperature stabilization, HEB bias lines, QCL drive current, accelerometer, additional temperature sensors, and the LNA drive current. Phosphor Bronze quad (Lakeshore WQT-36-100) or double wires are used inside the cryostat to minimize thermal conduction and pickup noise: the wire diameter is 0.13 mm, corresponding to gauge number nr.36 AWG. All wires are thermally connected to the 1st stage by winding around a copper bobbin. The relevant ones are then continued to the second stage, where another copper bobbin cools the wires before touching the experiment's elements (figure 108). In addition to the DB25 feedthroughs, three SMA feedthrough provide high-frequency connections inside the cryostat. In this experiment, only one of them is holding the LNA's output, the HEB's IF band, to the outside. This coax cable (SC-219/50-SS-SS from Coax Co) (visible in figure 108, after the thermal brake) has both center and outer conductors made of stainless steel to minimize thermal conduction, and Poly-tetra-fluoro-ethylene (PTFE) serves as

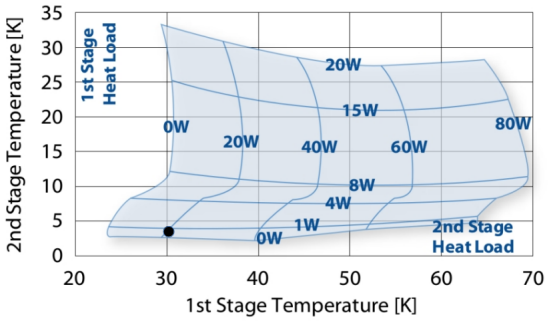

Figure 109: Heat load capacity map for the SRP-082B2 cold head from Sumitomo. After (Sumitomo Heavy Industries (SHI), 2023)

the dielectric. This cable is thermally connected to the radiation shield to dump the thermal conduction from the room-temperature cryostat wall.

There is only one radiation shield layer between the room temperature cryostat wall and the 2nd stage bath at 4 K, visible in figure 107. The shield skeleton is made of 2 mm thick aluminum sheets, fitting together to create an octagonal cylinder. The sheets are individually covered with a multi-layer insulator (MLI) made of 10 aluminized Mylar sheets with spacer sheets in between. The radiation shield, with the help of copper blocks and braids, is connected to the 1st stage of the cryo cooler for cooling. The radiation heat load from outside to the shield plus the direct radiation shining on the radiation shield through the holo optical window on the cryostat walls, construct the total radiation thermal load that is dumped to the 1st stage. Similarly, there is radiation load from the cooled radiation shield to the second stage of the cryo cooler, plus the radiation through the holo optical window on the shield. The total thermal loads to each stage determine the operating temperature of both cryo cooler stages. Figure 109 presents the cooling capacity map.

5.1.2 Cooling performance

Cryostat is cooled down in 6 hours and needs about two days to warm up. Figure 110 shows the cool-down and warm-up curves of the cryostat. In the cool-down curve, the sudden drop of temperature after t = 5.2 hours is understood to be a result of an increase in OFHC copper's thermal conductivity at few tens of Kelvin temperatures (Ekin, 2006), which helps in extracting the heat from the material and with a constant cooling power such a temperature drop has resulted. The cryo cooler senses the excessive heat load generated from this, resulting in a temporal temperature increase at the same time on the 1st stage of the cooler. On the warm-up curve, an increase in warming rate is observable at t = 2 hours, which is thought to be due to the release of Oxygen and Nitrogen from the frozen state on the cold surfaces, into a gaseous phase, at melting points of 54 and 63 K. The

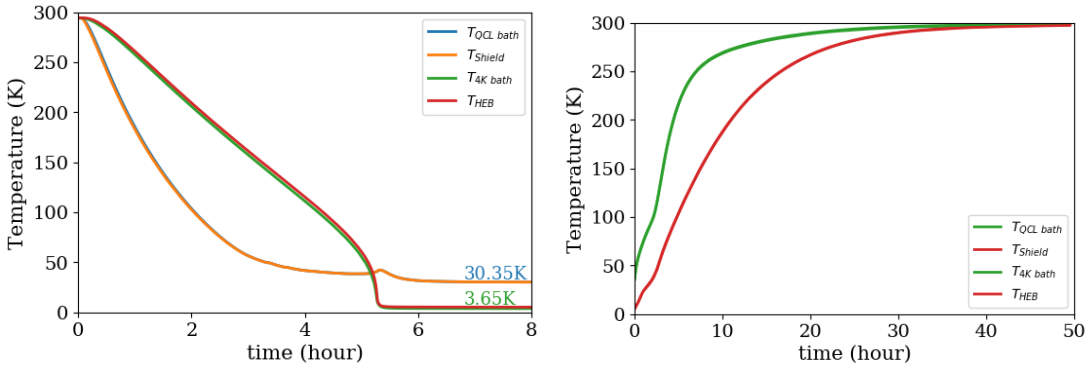

Figure 110: Left: the cool-down curve. Right: the warm-up curve for the cryostat.

gases then contribute to thermal conduction between the cryostat walls and 1st stage and between the 1st and the 2nd stage elements of the cryostat. During a few cool-down runs of this project, low helium pressure in the compressor resulted in very long cool-down times, which got fixed after a helium refill.

5.1.3 Vacuum performance

In order to evacuate the cryostat, two vacuum pumps are used: one is a rough rotary pump (Leybold TRIVAC D4B), and the other one is a turbo-molecular pump (Leybold TURBOVAC 151). The vacuum flanges are KF40. The pump unit stands next to the cryostat, and valves control the gas flow between the cryostat and the pump unit. A Pfeiffer MPT-100 pirani-penning vacuum gauge reads the pressure in the pipes between the cryostat and the pump unit.

Figure 111 shows an example measurement of cryostat evacuation. The blue part of the curve shows the rough pumping stage when only the rotary pump is on; in contrast, the orange part shows the high vacuum pumping when both turbo-molecular and rotary pumps are working. Interpretation of the orange

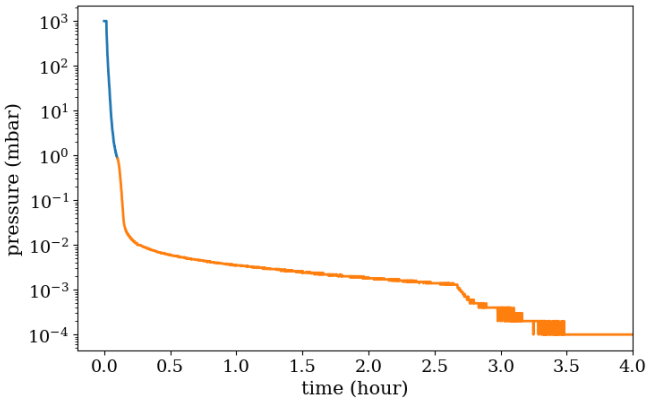

Figure 111: Evacuation curve for the cryostat, with blue part showing the rough pumping and orange part showing the medium and high vacuum pumping.

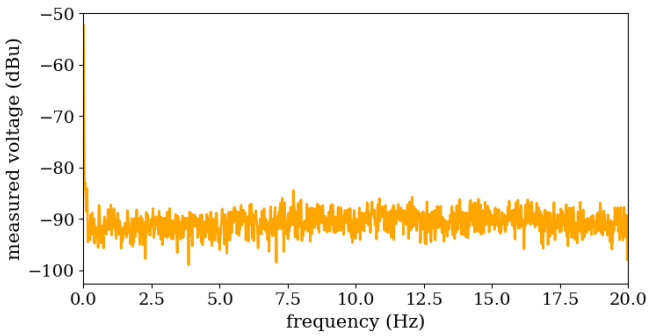

Figure 112: Measurement of voltage variations on the temperature sensor's read-out voltage to check any periodic detectable temperature variations of the QCL's thermal bath.

curve is that a dominant gas is being evacuated until t = 2.6 hours, and when that is out, gases with lower pumping speeds start to evacuate. The switching to the penning gauge of the vacuum gauge was not functional; therefore, only Pirani measurements are taken, which is why the pressure stays at $10^{-4} mbar$. A vacuum leakage rate of 3.3 mbar/day has been measured for the warm cryostat.

5.1.4 Thermal bath temperature fluctuations

As stated in the introduction chapter, the QCL frequency is temperature-dependent, and any temperature variations lead to a frequency variation. In order to check for existing temperature fluctuations, the QCL temperature sensor was used separately with an oscilloscope to monitor its output. In order to do this, a battery was providing the sensor bias current, and an operational amplifier (OPAMP) based gain block was amplifying the probable tiny signals with a gain of 10 and removing the DC component simultaneously. The FFT function was used on the oscilloscope to detect any periodic signal. The resulting spectrum can be seen in figure 112, which shows no evidence of such a periodic signal. At 1.72 Hz, the peak of the noise floor is around -88 dBu. Taking the gain of 10 into account, this puts an upper limit of 4.4 μV on peak voltage disturbances at this frequency. The DT670 sensor is specified to have a sensitivity of 1.76 μV/mK at the bath temperature of 33K (Lakeshore cryotronics, 2023), which converts the calculated upper limit to 2.5 mK to be the upper limit for the peak temperature variations of the QCL.

5.1.5 Forced motions due to pulse-tube

As stated in the introduction chapter, optical feedback can be another source of frequency instabilities. In order to check the mechanical motions of the QCL, the ADXL203 which is a dual axes MEMS accelerometer sensor was installed on

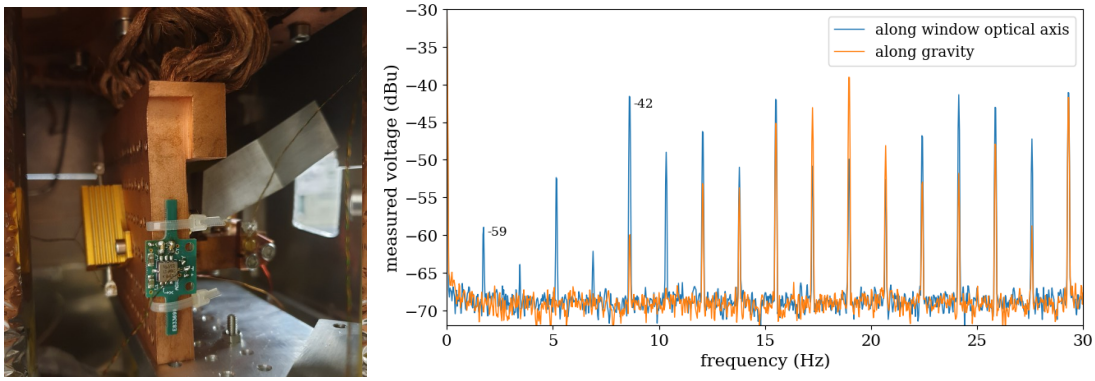

Figure 113: Left: photo of the accelerometer as installed on the QCL thermal bath. Right: spectrum of the measured acceleration, presented in the frequency domain to emphasize the presence of the pulse tube harmonics.

the QCL thermal bath, as seen in figure 113 (Analog Device, 2018). A similar approach to the subsection 5.1.4 was used to read this sensor. The sensor had two channels to read the acceleration along two perpendicular axes, one in the QCL beam propagation direction from the window toward out and another in gravity's direction. The result can be seen in figure 113, which shows a rich spectrum of the pulse tube harmonics on the acceleration. It is notable that since acceleration is the second derivative of position, the movement amplitude of the pulse tube at each frequency should be scaled with $\frac{1}{f^2}$. This results in a displacement of 0.94 μm from 110 μg at the fundamental harmonic, which can be compared to a displacement of 0.3 μm from 870 μg at the 5th harmonic. The given 1 mV to 1 mg conversion factor of the sensor has been used to drive these values, without taking the sensor's conversion factor changes due to the low temperature of the sensor into consideration.

5.2 Experimental Setup

Figure 114 shows a schematic of the experiment. The QCL is free running and is producing the 4.7 THz beam, which is guided outside of the cryostat until reaching the beam combiner of the receiver. The beam combiner adds a fraction of the QCL power to the receiver input's beam. The overlay of the two beams goes through the cryostat windows and reaches the HEB detector. The HEB detector, which is electrically biased at the good bias point, takes the QCL power portion as the LO and is pumped. With this, the input beam to the receiver is down-converted to the IF output of the HEB. The HEB's IF output is first amplified with a cryogenic Caltech CITLF4 Low-Noise Amplifier (LNA) (S. Weinreb, 2009) and is then processed by the IF processor outside the cryostat. Ultimately, the IF band of interest reaches the XFFTS spectrometer, which samples and creates

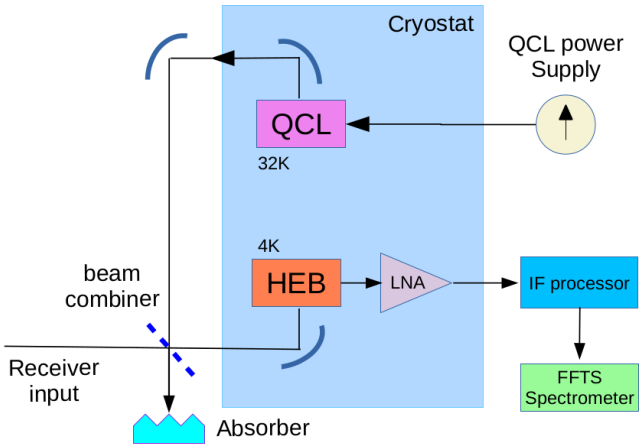

Figure 114: Schematic of the heterodyne laboratory receiver at 4.7 THz.

the IF spectrum and communicates this with the measurement PC. Figure 115 show photos of the experimental setup.

5.2.1 Optics

The QCL and the HEB are optical elements in this setup with fixed beam parameters, and based on them, the rest of the design is developed. The Gaussian beam initiating from the QCL is from a beam waist size comparable to the wavelength; thus, it is a fast diverging beam. The QCL's mirror transforms this divergent and fast beam into a slower beam with a beam waist far away from the cryostat. The beam exits the cryostat via the HDPE QCL window with 3 cm diameter. The straight beam is cut and bent downward with the help of a flat mirror. Before reaching the optical bench in front of the HEB window, a beam combiner

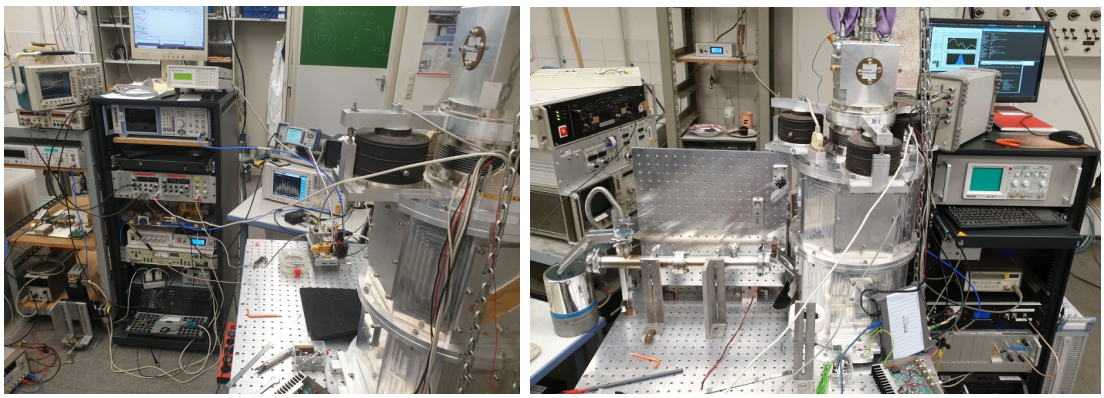

Figure 115: Left: A view of the experimental setup, which primarily emphasizes basic instruments that are needed, including the HEB bias box, the lock-in amplifier for small signal measurements, and the spectrum analyzer to check the output band of the mixer. Right: A heterodyne gas cell measurement is carried out in this particular setup, and the IF processor, XFFTS and measurement PC are on the rack on the right

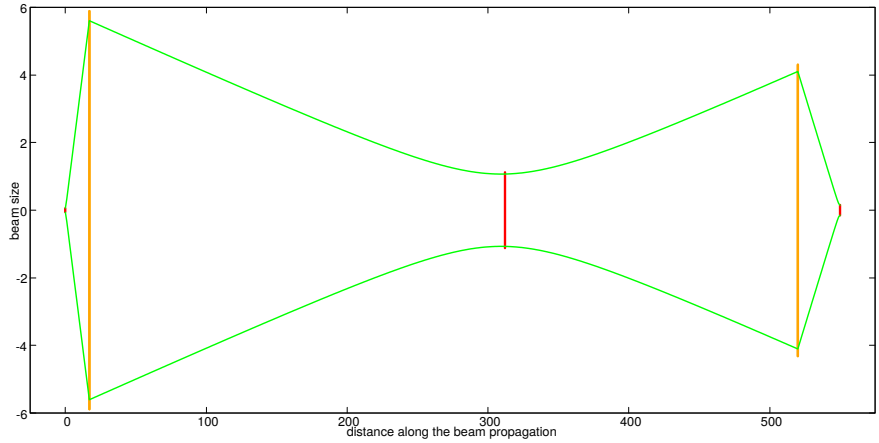

Figure 116: Schematic of the optical design, a drawing of the design presented in table 31. The green curves correspond to the beam size, the red lines are beam waists, and orange lines are active mirrors.

consisting of a 12 μm mylar film that, in the P polarization, reflects only 6 % of the QCL power into the cryostat and, at the same time overlays 94 % of the direct beam to the HEB window of the cryostat, being the receiver's input beam (the sky port in case of a heterodyne astronomical instrument). The HEB's mirror, built into the HEB block, is the last active mirror in the optical path and matches the combined two beams to the beam waist of the HEB mixer at the correct position. The schematic of the optical setup can be seen in figures 114. To tune the optical power that pumps the HEB, the alignment screws of the flat mirror holder are used to fine-tune the power coupling between the HEB and the QCL. Table 31 and figure 116 present and show the full optical parameters and the corresponding design.

Table 31: Optical parameters of the 4.7 THz heterodyne receiver optics.

parameter	**value**
QCL beam waist	61 μm
distance to the QCL mirror	17.0 mm
QCL mirror focal length	16.1 mm
distance to the intermediate beam waist	295 mm
intermediate beam waist size	1.08 mm
distance to the HEB mirror	208 mm
HEB mirror focal length	26.5 mm
distance to the HEB beam waist	30.0 mm
HEB beam waist	150 μm

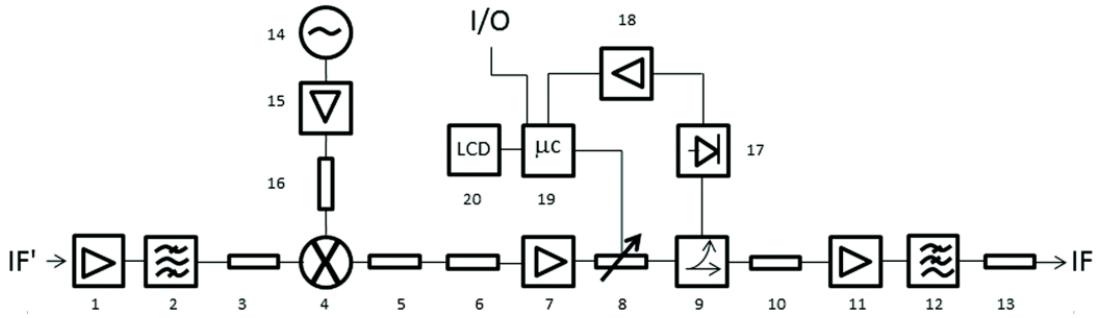

Figure 117: Diagram of the Intermediate Frequency (IF) processor used in this experiment. For details please refer to the text. Adopted from (Wehres et al., 2018)

5.2.2 IF chain

The IF processor first amplifies the signal with 25 dB (shown with number 1 in figure 117) and then band-pass filters (2) the band in the range of 5.1 to 7.6 GHz. For better matching, an attenuator is used (3) before reaching the RF port of the IF mixer (4). For the LO port of the same mixer, a Direct Digital Synthesizer (DDS) (14) generates 7.6 GHz, which, after amplification (15) and attenuation (16), down-converts the RF input signal of the mixer to the 0 to 2.5 GHz band. This band is further attenuated (5,6) to limit the standing wave and is then amplified by 24 dB (7). A micro-controller (19) controlled step attenuator (8) regulates the power of the passing signal, from which 99 % is transmitted and one % is separated with the help of a directional coupler (9), for total power measurement (17,18) of the band. The passing signal after small attenuation (10) is amplified (11) for the third time by 24 dB, then it is band-pass filtered (12), and after another attenuation (13), the frequency band reaches the output.

5.2.3 XFFTS spectrometer back-end

The Fast Fourier Transform Spectrometers (FFTS) does the end measurement of the IF frequency band: by integrating and measuring it as a function of frequency (Klein et al., 2012). This is done digitally with the help of a fast Analog to Digital Converter (ADC) that samples the incoming waveform of the IF band with 2.5 GHz bandwidth. For the XFFTS generation of these spectrometers, the ADC samples at 5 billion samples per second, with a resolution of 10 bits. The resulting samples are then communicated with a Xilinx Virtex-6 LX240T Field Programmable Gate Array (FPGA) capable of handling the massive data stream from the ADC and calculating the Fast Fourier Transform of the signal. The 2.5 GHz band is sampled into 32768 spectral channels with an 88.5 kHz noise equivalent bandwidth. For its operation in the lab spectrometer, the user had to ensure that the total IF power into the XFFTS does not exceed -2 dBm power

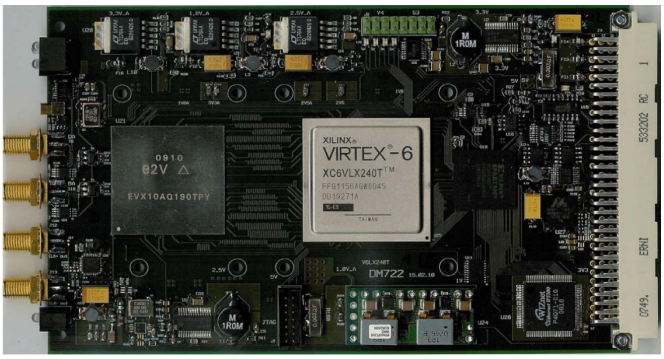

Figure 118: Photo of the electronic board of the XFFTS spectrometer. The IF data comes via the gold SMA connectors on the left. The ADC chip, the gray square, samples the input IF band. The FPGA chip, the silver square, calculates the FFT. The final spectrum data stream comes out from the right side. (Credit: B. Klein, MPIfR, Bonn)

level, corresponding to a peak-to-peak voltage of 500 mV in the 50 Ohms input impedance of this system. A dedicated computer reads the final data.

5.2.4 Beam maps

One can measure the receiver beam map at the receiver's input port when operational. For this, a Lock-in Amplifier (LIA) reads the total power from the receiver. An MIRL17-900 which is a dedicated IR source with modulation capability, was modulated with a square wave of 9.6 Hz and the same waveform was used at the LIA's reference input (Electro Optical Technologies (EOT), 2006). This detector radiates with a typical temperature of 750 K, with an effective area

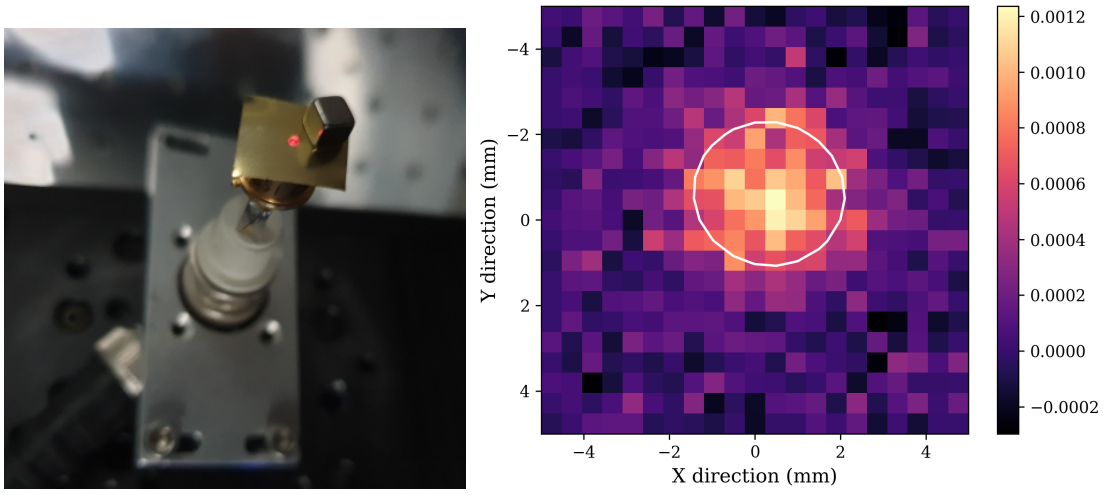

Figure 119: Left: The infrared source is installed on the x-y stage to measure the HEB beam profile. The iris is installed to reduce the spatial size of the source in order to measure a more realistic beam. Right: Beam map of the HEB that is measured with the source and the corresponding total power of the receiver. The drown circle shows the 75 % contour of the Gaussian fit.

of 1.7×1.7
mm^2. In this experiment scheme, the LIA's output only detects the receiver's total power signal generated by the this IR source. The spatial size of the source could be reduced with a pinhole (0.5 mm diameter) to obtain a better spatial resolution. The source was mounted on a controllable XY stage that scanned the IR source in the expected beam position of the receiver. Figure 119 shows a photo of the IR source and the resulting beam map. This beam map is obtained at a distance of 19.8 cm from the cryostat with the ellipse (almost circle) showing the 75 % contour. The fitted 2-dimensional Gaussian corresponds to a Gaussian sigma of 1.58 and 1.49 mm in the ellipse's long and short axis directions, corresponding to an eccentricity of 0.33, which can be a result of slight miss-alignment of the XY stage scanning plane referenced to the HEB beam.

5.3 Receiver Performance

5.3.1 Receiver noise temperature

Even whit no signal present at the receiver input port, the heterodyne receiver will still measure some temperature called receiver noise temperature. It is a figure of merit for a heterodyne receiver and is usually measured with a hot-cold method, where two absorbers with two different known temperatures are placed at the receiver's input port. From this, the input temperature to the receiver is known, and thus using a linear fit, the offset will be the receiver's noise temperature. If by placing the hot and the cold absorbers at temperatures of T_H and T_C, the receiver measured power is P_H and P_C, the Y factor is defined as $\frac{P_H}{P_C}$ and the receiver noise temperature T_{rec} is then:

$$T_{rec} = \frac{T_H - YT_C}{Y - 1} \tag{104}$$

This measurement is done for the receiver of this study, with the hot absorber being at room temperature and the cold absorber being dipped into liquid nitrogen. Figure 120 shows the result of switching between these two absorbers at the receiver's input port. For this measurement, an IF bandwidth from 1 to 2 GHz of the receiver has been used, and measured data corresponds to a total power receiver noise temperature of 3920 ± 90 K, which does not take the cryostat window, beam combiner loss and air absorption, into account. The measured value is obtained with both of the sidebands contributing equally to the result, so it is the double sideband (DSB) noise temperature. The HEB detector is expected to dominate the receiver noise temperature in this experiment. (D. Büchel et al., 2015) has reported a record value of 980 K for the minimum noise temperature

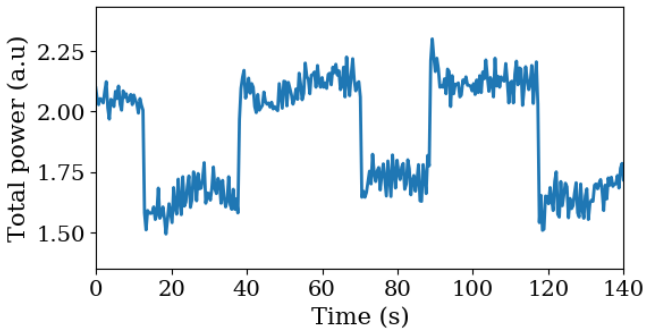

Figure 120: Doing a lock-in hot-cold measurement to determine the receiver noise temperature. larger values correspond to the total power with warm absorber present at the receiver's input beam, and smaller values correspond to the cold absorber in a similar way.

from these HEB detectors.

Instead of total power, repeating the same type of Y-factor measurement is possible to determine the DSB receiver noise temperature at all spectral channels of the heterodyne receiver in the IF. Figure 121 presents the results of such a measurement for an IF band from 5.1 to 7.6 GHz for this receiver. The plot shows a minimum receiver noise temperature of around 5000 K at 5.1 GHz. The plot shows an overall increase in the receiver noise temperature as a function of frequency, which is expected from the general performance of the HEB detectors. The The HEB detector is designed for an operating frequency of 0.1 to 2.5 GHz and has an IF filter circuitry rejecting higher frequencies from passing through the IF. Therefore the loss is increased for higher frequency signals, which increases the receiver noise temperature (D. Büchel et al., 2015). It should also be mentioned that the loss in the optical power combiner, air, and vacuum window has already added to the measured receiver noise temperatures; thus, these numbers are only upper limits.

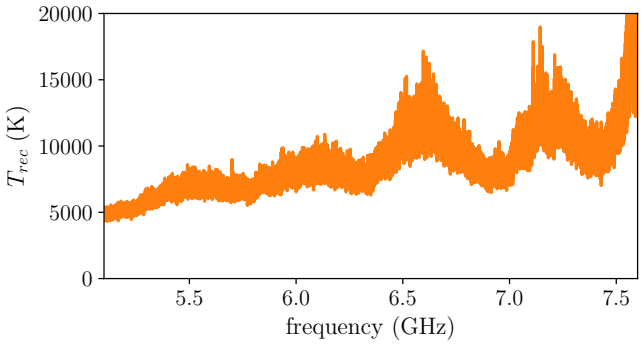

Figure 121: The DSB receiver noise temperature as a function of the IF frequency. This operating frequency is much larger than the intended IF frequency of the HEB detector.

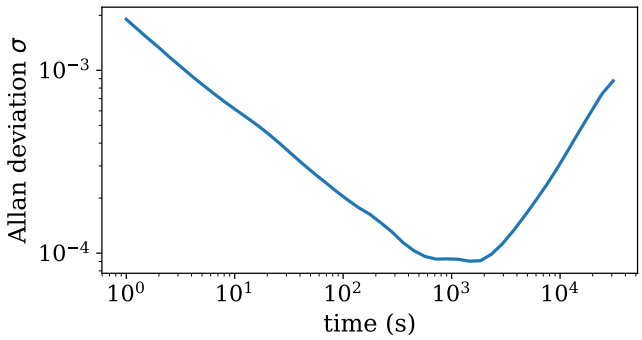

Figure 122: Allan deviation of the total power monitor output from the laboratory receiver.

5.3.2 Allan stability

Allan's variance of the total power monitor output from the IF processor has been studied to measure the receiver's stability with time (Kooi, 2008). One can calculate the Allan variance for a given sample length τ as the square of the difference between two consecutive samples. The Allan deviation, the square root of Allan time, is a function of sample length. The measured Allan deviation plot can be seen in figure 122. The descending -0.5, the horizontal, and the ascending +1 slope in the plot correspond to the white frequency noise, flicker frequency noise, and the frequency random walk, respectively. The so-called Allan time is defined as the time at the white frequency noise stops to dominate the Allan deviation, which for this receiver, one can read an Allan time of 500 seconds from the plot (for the total power). This example can be compared to the GREAT instrument, which had an spectroscopic Allan time of 100 seconds (Heyminck et al., 2012).

5.3.3 Receiver sensitivity

A heterodyne receiver can reach a certain sensitivity in measuring the intensity of the incoming light, which is a function of the receiver noise temperature and integration time. The relationship between these quantities is expressed with the radiometer equation as (Wilson & Rohlfs, 1996):

$$\Delta T = \frac{T_{sys}}{\sqrt{\Delta\nu t}} \times 2 \tag{105}$$

where T_{sys} is the system DSB noise temperature, $\Delta\nu$ is the measurement bandwidth, and t is the integration time. With an integration time of 10 seconds, a measurement bandwidth of 88 kHz for a single FFTS channel, and a T_{sys} of 10000 Kelvin, this receiver can reach an rms noise level of 21 Kelvin.

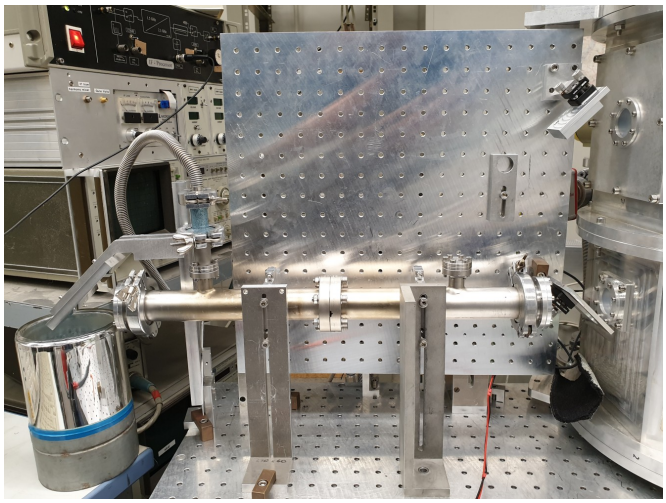

Figure 123: The experimental setup to measure the emission lines from the methanol gas. The gas cell is visible in the center, the cryostat on the right, and the absorber bucket filled with LN2 on the left.

5.4 Methanol Spectroscopy with receiver at 4.7 THz

As an example of this heterodyne receiver in measuring emission lines, a series of methanol line measurements had been carried out to calibrate the unknown frequency of QCL nr.2. Experimental setup includes the heterodyne receiver at 4.7 THz, with a gas cell installed on the input port of the receiver, which is followed by a mirror that reflects the input beam into an LN2 cooled absorber. Figure 123 shows a photo of this setup. Measurement is done with evacuated or methanol vapor filled gas cell. Table 32 shows a summary of the methanol and the gas cell's parameters.

5.4.1 Measurement procedure

For a clear view and to check if the emission lines are there or not, the FFTS software has a special function to measure and waterfall plot the (on - off)/(off) which corresponds to (line - background)/(background). In figure 124 the detected methanol lines are visible as vertical lines, and the horizontal displacements of the lines are caused by a change in QCL current. The lines that shift in opposite direction belong to the different side-bands of the mixer.

parameter	**value**
Length	50 cm
Window diameter	4 cm
Window material	High Density Poly Ethylene (HDPE)
typical methanol pressure readout	1.2 mbar

Table 32: A summary of parameters regarding the gas cell.

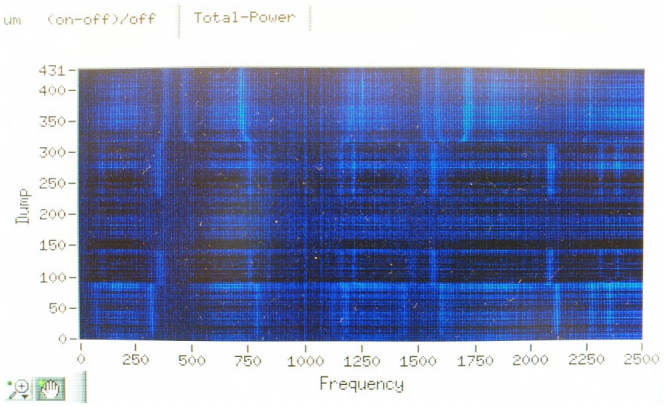

Figure 124: photo from the computer screen while waterfall measuring methanol gas lines in (on - off)/(off) mode.

To measure the emission from the methanol gas, the following procedure was performed:

1. optimally pumping the HEB with fine tuning of th LO power
2. measuring the cold load with transmission through the evacuated gas cell
3. measuring the cold load plus methanol emission

In order to minimize effect of receiver baseline drifts, usually 2nd and 3rd steps are repeated several times in series.

5.4.2 QCL frequency calibration with methanol emission lines

Measurements are line - vac, containing the fingerprint of the lines in the recorded IF spectrum. The measured IF spectrum contains both Lower SideBand (LSB) and Upper SideBand (USB) signals. With a slight QCL frequency shift, the measured lines shift their position to either right or left. With a positive QCL

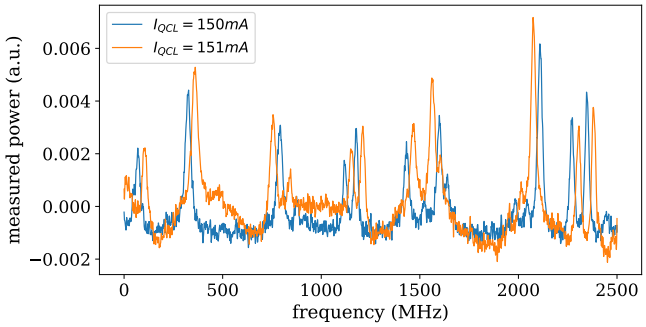

Figure 125: Comparison of the integrated measured IF spectrum for two QCL currents of 150 and 151 mA. A Hann 10-point filter, has reduced the excess floor noise of the measurements.

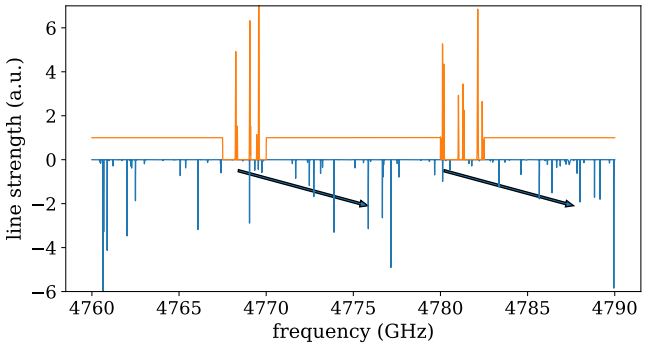

Figure 126: The plot in which the QCL frequency calibration got successful. The overlay of the measured lines in orange vs. the JPL database spectrum from 4760 to 4790 GHz in blue. The arrows show the first lines of the LSB and the USB bands that match. Only the database lines are in the correct frequencies.

frequency step, lines in the USB shift to the right side, whereas LSB lines shift leftward. Figure 125 shows this effect.

Now that one has separate the lines in the LSB and the USB bands, one can compare the measured IF spectrum with the database lines for line identification. A series of plots were created with the measured frequency unknown spectrum plotted on top, whereas at the bottom, pieces of the JPL database with lines of known frequencies were plotted piece-by-piece in many small bands. This method reduced the density of lines in each plot, and identification of the lines became easier. Finally, figure 126 revealed the patterns that matched.

With only frequency translation, the measured spectrum can be fitted to the predicted spectrum from the JPL database. The plot in figure 127 show this match between the two spectra. By doing this, the middle point between the LSB and USB sidebands corresponds to the LO frequency. As can be seen, the QCL frequency is 4782.7 GHz, measured at a current of 151 mA and a bath temperature of 33 K.

In detail, one can compare the LSB and the USB with the prediction of

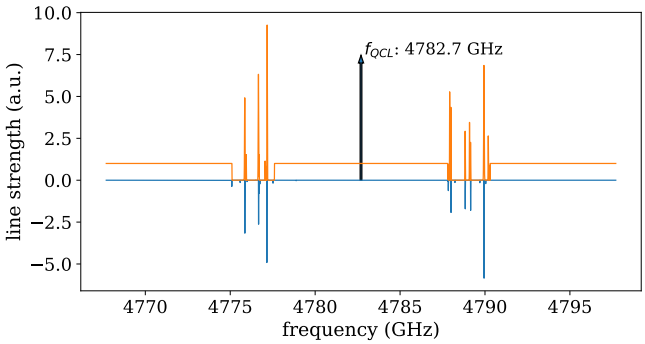

Figure 127: Comparison of the measured and the JPL database spectrum. The QCL frequency is located between the two measured bands at 4782.7 GHz.

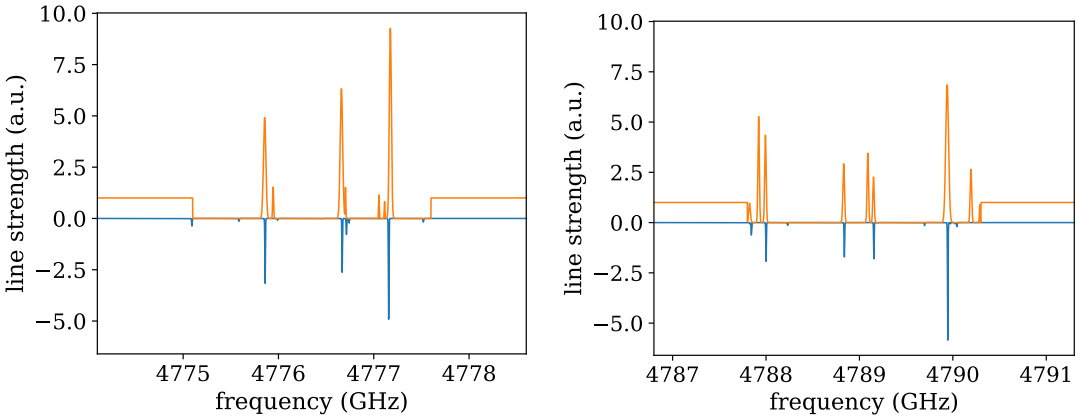

Figure 128: Zoom view to the measured vs. database line spectrum for the LSB on the left and the USB on the right

lines from the JPL database. figure 128 presents the band-to-band comparisons. Some measured lines are not predicted in the database. The mismatch can be explained by the complexity of the methanol molecule, which makes the energy level calculations from the model inaccurate. In addition to that, these lines can arise from possible contamination in the gas cell, for example from residual water vapor.

6 Summary

SOFIA is an airborne observatory that observes sub-mm and far-IR waves. SOFIA is mighty in studying dust and the emission of cooling lines of the interstellar medium, such as CII emission. The GREAT instrument of this telescope has dedicated channels to observe different spectral lines at very high resolving powers such as 10^7. This is possible only with the heterodyne method, primarily based on mixing the received sky signal with the Local Oscillator (LO) in a highly nonlinear mixer device and down-converting the sky signal to much lower Intermediate Frequencies (IF). The 4.7 THz channel of GREAT is dedicated to observing the Oxygen's fine structure line ($^3P_1 - ^3P_2$) at ground electronic state, with associated photons at 63 μm/4.745 THz. For this, the High-Frequency Array (HFA) of upGREAT instrument has 7 Hot Electron Bolometer (HEB) detectors to increase the mapping speed, and the LO is a Quantum Cascade Laser (QCL). The achieved receiver noise temperature and the IF bandwidth for HFA are 1500 K and 4 GHz, respectively.

The fact that in a heterodyne receiver, the sky and LO signals convolve with each other inside the mixer, depicts that LO's lineshape copies to every spectral element of the sky signal down-converting to the IF spectrum. This fact initiates two essential requirements for the LO signal quality. One is that the LO linewidth should be small, adding no additional broadening to the source's observed spectrum. At 4.7 THz, a spectral resolution of 1 MHz corresponds to resolving a velocity of 63 m/s; this is well below the width of typical spectral elements of sources in the galaxy since they have much larger velocities. However, such a resolution is needed within the solar system when observing planetary atmospheres, for example. The second requirement is its spectral purity, meaning that the LO should be monochromatic and free of spikes and spurs. Ideally, one likes to have any spectral impurity be 1000 times smaller than the LO line's power. As for the third requirement, since the LO is a free-running laser in the HFA's case, it lacks an absolute frequency reference. Locking the frequency or phase of the LO to a reference, therefore, improves the frequency accuracy. For the atomic oxygen line at 4.7 THz, the telluric line from the same atom, up to date, has been used as a frequency reference. However, high-velocity winds in the earth's stratosphere limit the absolute accuracy.

QCLs rely on intersubband transitions. They are capable of producing continuum THz emission with advantages including compactness, ease of operation and high power. This work uses two QCLs, produced by the Institute for Quantum-optics at ETH in Zurich and designed explicitly for single-mode operation at 4745 GHz. Their active medium is a superlattice structure: a sandwich

of GaAs/AlGaAs with a total thickness of 9.2 μm grown by the Molecular Beam Epitaxy (MBE) technique. The laser frequency is tunable with current, temperature, and optical feedback. In the tested setups, these devices showed the most frequency tuning to the current with a positive tuning slope, somewhat smaller to the temperature with a negative tuning slope, and only a tiny tuning with optical feedback. These tuning mechanisms also help to calibrate the lasers, by doing methanol absorption spectroscopy and cross-match of the recorded spectrum with the JPL database for molecular spectroscopy. During the project, laser nr. 2 showed an unexpected mode jump from 4744 GHz to 4785 GHz, which was challenging to calibrate again after the mode hope. The laser also showed multimoding emission at higher currents. Only frequency stabilization utilizing a methanol gas absorption line was performed with this laser, and the two other heterodyne experiments used the laser nr. 1.

Generating a heterodyne product is crucial for the performed delay line frequency locking and the phase locking methods used in this work. Generating this heterodyne product needs a stable frequency reference. Combining this reference with the QCL emission in a mixer creates a different frequency term useful for QCL frequency stabilization. The first element to generate this reference is the diode multiplier chain, the VDI AMC-S177, consisting of an active quadrupler, an amplifier, and a couple of doublers. This translates an input frequency of 11.4 GHz to an output frequency of 182.5 GHz, up to a power level of 25 mW, capable of pumping a harmonic generator and mixer, the second element to generate the reference.

The harmonic generator and mixer used in this work is a Superlattice Device (SLD) which, like the QCL, is also made by MBE and is a superlattice of GaAs/AlAs. The device shows a strong non-linear current-voltage (I-V) relation, making the generation of high harmonics and, at the same time, mixing two submm waves possible. In both experiments of this work, the SLD plays two roles: as a harmonic generator and mixer. The QCL THz emission and the diode chain's mm-wave pump power enter the SLD block separately, and the mixing product is available at the device's IF port. At the beginning of this work, a fourth method of heterodyne detection of the SLD's emission at 4.7 THz with a Hot Electron Bolometer (HEB) was also foreseen. To realize this, the experimental setup also implements the HEB detector, such that the QCL's emission pumps this detector. The HEB also has limited sensitivity as a total power detector, which is detectable over the device's bias current. The first experiment of this work utilizes this latter possibility to stabilize the QCL's frequency with the help of a methanol gas absorption line.

The first experiment uses a methanol gas absorption line as the frequency

discriminator. The idea is that the QCL's emission passes through a gas cell, and with the help of current tuning, the QCL's frequency is always corrected such that QCL is emitting at the absorption line's dip and the transmission through the gas cell is minimum. To realize this in the experimental setup, one must detect that the QCL is located on which side of the absorption dip. Applying a known frequency modulation to the QCL and using the same modulator waveform as a reference to a Lock-in Amplifier (LIA) enables the setup to probe the slope of the Methanol's absorption line. In fact, by inserting the HEB detector's current monitor output into LIA's input and measuring the LIA's output, one generates the absorption line's 1st derivative, with a positive slope that crosses zero volts when the QCL frequency equals the frequency of the methanol line's dip; This is a frequency discriminator. Control electronics offset correct, amplify, and filter this to create the correction signal, which feeding it back to the QCL corrects the QCL's frequency disturbances.

One can monitor the frequency discriminator's output to learn about the frequency disturbances present in the experiment before and after activating the frequency stabilization. When the QCL frequency is in the linear range of the frequency discriminator, strong pulses are visible in its output with a period of 0.58 seconds, 1.72 Hz, equal to the cryostat's pulse tube cryo cooler. The pulse shape includes many sharp parts, not a simple waveform, but to a very good extent, it is periodic. Analysing histograms of this waveform reveal that before and after closing the control loop, a Full Width at Half Maximum (FWHM) of 320 and 36 kHz are assigned to the laser linewidth. The frequency modulator used in the experiment itself broadens the QCL line to an FWHM of 2.12 MHz, estimated to be the total QCL's linewidth as well, and showing that the modulator is dominating the final linewidth. The frequency demodulator waveform analyzed with the Fast Fourier Transform (FFT) revealed many harmonics of the pulse tube present in this signal, meaning that apart from the pulse tube's fundamental harmonic, faster components are also involved in disturbing the QCL's frequency.

This work's second and third experiments are heterodyne experiments, which use the down-converted QCL's emission as the primary signal. It is at an IF frequency between 0.3 to 0.4 GHz, being 10 dB (measured at 3 MHz resolution bandwidth) over the the SLD's generated noise. The IF processor handles this tiny signal by amplifying it to the needed power levels and filtering the noise out. The IF processor's output signal is ready for any frequency or phase discrimination to achieve different stabilization schemes.

The first heterodyne experiment uses a delay line frequency discriminator to produce a correction voltage. The frequency discriminator consists of a power divider that divides the input frequency band, centered at 405 MHz from the IF

processor, in two equal amplitude signals. Only one passes through a 10 m long coax cable as the delay line, and then both signals are mixed in a diode ring balanced mixer. The frequency of both signals is equal, but their relative phase is a function of the frequency. When the QCL frequency varies due to instability, its IF frequency also varies, and the diode ring mixer output DC voltage varies accordingly. To calibrate the frequency discriminator, two methods of feeding a frequency sweep and applying a known frequency modulation have been used, and both led to a frequency discrimination constant of 91.5 mV/MHz. The frequency discriminator's output signal is further processed in the control electronics to be filtered, amplified, and offset-corrected to create the correction voltage, which adds a tiny correction current to the QCL's DC current.

The delay line frequency discriminator could successfully stabilize the QCL's frequency. The experiment could control frequency deviations as large as 10 MHz during the measurement while being stable for a couple of hours. In addition to the initial experiment, the effect of adding optical attenuations of each 3.9 dB in the QCL beam could be studied. Interestingly, attenuating the optical beam reduced the QCL's disturbances. Frequency locking is still possible, for hours long, even after adding two attenuators, leaving less than 2 dB of signal over noise, for frequency stabilization. The observations with attenuators showed that the primary disturbing mechanism of the QCL's frequency is the optical feedback to the laser. The locked laser line showed a Gaussian lineshape with an FWHM of 780 kHz. Disturbing the setup, including strong mechanical shocks and QCL temperature drifts, could cause the experiment to jump to the other delay line's mode at 386 MHz. Active temperature stabilization of QCL's thermal bath helped to eliminate this effect.

The second heterodyne experiment locks the QCL's phase to the one from a stable laboratory synthesizer as a reference. This technique is called Phase Locked Loop (PLL). Principle of operation is the following: a phase detector compares the phase of the QCL with the reference and creates an error voltage. A loop filter processes this error voltage to a suitable control current, which is fed to the QCL. The applied correction current compensates against the frequency disturbances and keeps the QCL's phase locked to the reference. In this experiment, a diode ring balanced mixer plays the role of phase detector; these mixers are among the best choices in the presence of large amounts of noise. Two calibration measurements, including beat note and phase noise methods, in perfect agreement with each other have determined 0.34 V/rad as this mixer's phase detection gain.

The design of a PLL involves the transfer function method, which for each system's element, compares the amplitude and phase of the output to the input. Putting the individual transfer functions together, leads to the open loop transfer

function (G(s)), which is key to examining the system's bandwidth and stability. Regarding stability, at unity gain, the phase difference should be above 180° , and in practical cases, consistently above 140° , leaving at least a so-called 40° of phase margin. The loop filter is the main element in setting the G(s). After feeding the QCL's phase back to the phase detector, closing the control loop, A complete PLL has a closed loop transfer function (H(s)) that transfers QCL's output phase to the reference's input phase. The H(s) has a low pass profile, to which an equivalent noise bandwidth B_L can be assigned. B_L is a relevant quantity in specifying the signal-to-noise in PLLs, and the initial value from the design is 251 kHz. A second-order PLL system is a well-understood case often used in PLL design, with its natural frequency and damping factor as performance measures. In this experiment, the initial design values for loop gain, phase margin, natural frequency, and damping factor are 890 krad/s, 42° , 379 krad/s, and 5.3, respectively.

There are many noise sources in a PLL system that are not equally important. The transfer function method is powerful in estimating the propagation of the noises in a PLL system. Not surprisingly, among this experiment's noise sources, the SLD's wideband noise present in the IF processor's output with a noise density of 66 $\mu rad/\sqrt{Hz}$ is dominant. Noise propagation analysis reveals that it propagates to the output with H(s), similar to the reference's phase, estimated to produce a QCL phase variance of $0.035 rad^2$. The loop signal-to-noise ratio, defined as half of this variance's inverse, is therefore estimated to be 14.2, a reasonable number regarding the noise's effect on PLL's behavior. The rest of the SLD's noise, not tracked by the PLL, stresses the phase detector and causes sensitivity lose. Estimating a root mean square of 1.22 rad for this noise, it is expected to reduce the phase detector's sensitivity to 48% of the original value, one of the effects not foreseen in the design.

The QCL's phase locking is successful. After closing the control loop, on a spectrum analyzer and in spectra recorded with the Software Defined Radio (SDR), a thin solid line replaces the jittering unstable QCL line. Phase locking is possible over periods of around half an hour. During each measurement set, on occasions, loss of lock is observable from sub-seconds to about a few seconds. On both sides of the QCL line, phase noise peaking shoulders also appear, with a peaking value of 3 dB at an offset frequency of 100 kHz from the QCL line, in agreement with the transfer function simulations. An oscilloscope measures the phase detector's output as a phase demodulator, and its waveform, which is periodic again with 0.58 seconds, after processing with FFT, reveals the existence of pulse tube harmonics to frequencies as high as 50 Hz, and in a phase noise floor density of $0.219 mrad^2$/Hz. As new estimations, the latter results in a total

QCL's phase rms of 0.25 rad and a loop signal-to-noise ratio of 8. These numbers are marginal but still OK for the loop's performance. Measurements of QCL's correction voltage made it possible to estimate the QCL's uncorrected linewidth. An FWHM of 1.4 MHz is measured for the QCL's linewidth over 10 seconds, which, compared to the phase-locked QCL's FWHM of a few kHz, emphasizes the potential of the PLL in linewidth reduction.

The thesis's last chapter presents the heterodyne laboratory receiver at 4.7 THz, initially developed to host all experiments of this work, plus the phase locking experiment with the HEB detector as a mixer (remaining open for more work). This work's cryostat is based on a pulse tube cold head unit. It has an actively cooled radiation shield and provides access to both cryo cooler's cooling stages via three thermal baths. The pulse tube operation of these cold heads are known to produce mechanical motions. Hence the design foresaw dampers, a vacuum bellow, and decoupling copper braids. An ADXL203 MEMS accelerometer estimated a motion amplitude on the order of 1 μm for the fundamental harmonic of the pulse tube at 1.72 Hz, along with many higher harmonics at lower amplitudes, at QCL's installation location. The optical design helps to couple the QCL's emission, located on one of the 1st stage's thermal baths, to the HEB placed on the 2nd stage's thermal bath. In front of the HEB's vacuum window, a beam combiner combines 6% of the QCL's power with 94% of the signals from the so-called receiver's sky port. After the HEB, a low noise amplifier amplifies the HEB's IF band by 36 dB while adding only 11 K to the receiver's noise. The IF band from 5.1 to 7.6 GHz exits the cryostat and gets further processed in the IF processor, which at the end, an eXtended Fast Fourier Transform Spectrometer (XFFTS) integrates and measures its spectrum. Hot-cold receiver noise temperature measurement resulted in a receiver noise temperature of around 5000 K at the IF frequency of 5.1 GHz, considering none of the window, air, and beam combiner losses. Using the IF processor's total power detector, an Allan variance stability time of 500 seconds is measured for this receiver. As proof of the heterodyne receiver's operation, Methanol gas's emission could be measured in front of a liquid nitrogen cooled absorber, with the setup. In total, 15 methanol lines were identified, and with their help, the QCL nr. 2 could finally be frequency calibrated after the mode hop.

References

Analog Device. (2018, May). *ADXL203: precision single/dual axis accelerometer datasheet.*

Barkan, A., Tittel, F. K., Mittleman, D. M., Dengler, R., Siegel, P. H., Scalari, G., ... Ritchie, D. A. (2004). Linewidth and tuning characteristics of terahertz quantum cascade lasers. *Optics Letters*, *29*(6), 575-577. doi: https://doi.org/10.1364/OL.29.000575

Baryshev, A., Hovenier, J. N., Adam, A. J. L., Kašalynas, I., Gao, J. R., Klaassen, T. O., ... Reno, J. L. (2006). Phase locking and spectral linewidth of a two-mode terahertz quantum cascade laser. *Applied Physics Letters*, *89*(3). doi: https://doi.org/10.1063/1.2227624

Beck, M., Hofstetter, D., Aellen, T., Faist, J., Oesterle, U., Ilegems, M., ... Melchior, H. (2002). Continuous wave operation of a mid-infrared semiconductor laser at room temperature. *Science*, *295*(5553), 301-305. doi: https://doi.org/10.1126/science.1066408

Belden. (2022). *RG-58/U cable datasheet.*

Betz, A. L., Boreiko, R. T., Williams, B. S., Kumar, S., Hu, Q., & Reno, J. L. (2005). Frequency and phase-lock control of a 3 THz quantum cascade laser. *Optics Letters*, *30*(14), 1837-1839. doi: https://doi.org/10.1364/OL.30.001837

Bonzon, C., Benea Chelmus, I. C., Ohtani, K., Geiser, M., Beck, M., & Faist, J. (2014). Integrated patch and slot array antenna for terahertz quantum cascade lasers at 4.7 THz. *Applied Physics Letters*, *104*(16). doi: https://doi.org/10.1063/1.4871369

Bosco, L. (2019). *THz quantum cascade laser: astrophysical applications and high temperature performance* (PhD thesis). ETH Zurich.

Bosco, L., Bonzon, C., Ohtani, K., Justen, M., Beck, M., & Faist, J. (2016). A patch-array antenna single-mode low electrical dissipation continuous wave terahertz quantum cascade laser. *Applied Physics Letters*, *109*(20). doi: http://dx.doi.org/10.1063/1.4967836

Bulcha, B. T., Hesler, J. L., Valavanis, A., Drakinskiy, V., Stake, J., Dong, R., ... Barker, N. S. (2015). Phase locking of a 2.5 THz quantum cascade laser to a

microwave reference using THz schottky mixer. proceedings of the 40th International Conference on Infrared, Millimeter and Terahertz Waves (IRMMW-THz). doi: https://doi.org/10.1109/IRMMW-THz.2015.7327689

Büchel, D., Pütz, P., Jacobs, K., Schultz, M., Graf, U. U., Risacher, C., ... Stutzki, J. (2015). 4.7-THz superconducting hot electron bolometer waveguide mixer. *IEEE Transactions on Terahertz Science and Technology*, *5*(2), 207-214. doi: http://dx.doi.org/10.1109/TTHZ.2014.2382434

Büchel, D. F. (2017). *Hot electron bolometer mixers for thz arrays* (PhD thesis). University of Cologne.

Cologne Database for Molecular Spectroscopy (CDMS). (2019). *https://cdms.astro.uni-koeln.de/.*

Danylov, A., Erickson, N., Light, A., & Waldman, J. (2015). Phase locking of 2.324 and 2.959 terahertz quantum cascade lasers using a Schottky diode harmonic mixer. *Optics Letters*, *40*(21), 5090-5092. doi: http://dx.doi.org/10.1364/OL.40.005090

Danylov, A. A., Light, A. R., Waldman, J., Erickson, N. R., Qian, X., & Goodhue, W. D. (2012). 2.32 THz quantum cascade laser frequency-locked to the harmonic of a microwave synthesizer source. *Optics Express*, *20*(25), 27908-27914. doi: https://doi.org/10.1364/oe.20.027908

Dorf, R. C., & Bishop, R. H. (2002). *Modern Control Systems* (9th ed.). Prentice Hall.

Durán, C. A., Güsten, R., Risacher, C., Görlitz, A., Klein, B., Reyes, N., ... Lis, D. C. (2021). 4GREAT-a four-color receiver for high-resolution airborne terahertz spectroscopy. *IEEE Transactions on Terahertz Science and Technology*, *11*(2), 194-204. doi: http://dx.doi.org/10.1109/TTHZ.2020.3042714

Eichholz, R., Richter, H., Wienold, M., Schrottke, L., Hey, R., Grahn, H. T., & Hübers, H.-W. (2013). Frequency modulation spectroscopy with a THz quantum-cascade laser. *Optics Express*, *21*(26), 32199-32206. doi: https://doi.org/10.1364/OE.21.032199

Ekin, J. W. (2006). *Experimental Techniques for Low-Temperature Measurements*. Oxford University Press.

Electro Optical Technologies (EOT). (2006, Sep). *MIRL17-900: pulsed broadband infrared light source datasheet.*

Encinas, J. (1993). *Phase Locked Loops*. Chapman and Hall.

Ennico, K., Becklin, E. E., Le, J., Rangwala, N., Reach, W. T., Rhodes, A., ... Zavala, E. (2018). An overview of the stratospheric observatory for infrared astronomy since full operation capability. *Journal of Astronomical Instrumentation*, *7*(4). doi: https://doi.org/10.1142/S2251171718400123

Esaki, L., & Tsu, R. (1970). Superlattice and negative differential conductivity in semiconductors. *IBM Journal of Research and Development*, *14*(1), 61-65. doi: 10.1147/rd.141.0061

Faist, J. (2018). *Quantum Cascade Laser*. Oxford.

Faist, J., Capasso, F., Sivco, D., Sirtori, C., Hutchinson, A., & Cho, A. (1994). Quantum cascade laser. *Science*, *264*(5158), 553-556. doi: https://doi.org/10.1126/science.264.5158.553

Faist, J., Gmachl, C., Capasso, F., Sirtori, C., Sivco, D., Baillargeon, J., & Cho, A. (1997). Distributed feedback quantum cascade lasers. *Applied Physics Letters*, *70*(20), 2670-2672. doi: https://doi.org/10.1063/1.119208

Gardner, F. M. (1979). *Phaselock Techniques* (2nd ed.). John Wiley and Sons.

Gardner, F. M. (2005). *Phaselock Techniques* (3rd ed.). John Wiley and Sons.

Gifford, W. E., & Longsworth, R. C. (1964). Pulse-tube refrigeration. *Journal of Engineering for Industry*, *86*(3), 264-268. doi: https://doi.org/10.1115/1.3670530

Gordy, W., & Cook, R. L. (1984). *Microwave Molecular Spectra*. John Wiley & Sons, Inc.

Graf, U. U., Honingh, C. E., Jacobs, K., & Stutzki, J. (2015). Terahertz heterodyne array receivers for astronomy. *Journal of Infrared, Millimeter, and Terahertz Waves*(36), 896-921. doi: https://doi.org/10.1007/s10762-015-0171-7

Green, R. P., Xu, J.-H., Mahler, L., Tredicucci, A., Beltram, F., Giuliani, G., ... Ritchie, D. A. (2008). Linewidth enhancement factor of terahertz quantum cascade lasers. *Applied Physics Letters*, *92*(7). doi: https://doi.org/10.1063/1.2883950

Hayton, D. J., Khudchenko, A., Pavelyev, D. G., Hovenier, J. N., Baryshev, A., Gao, J. R., ... Vaks, V. (2013). Phase locking of a 3.4 THz third-order distributed feedback quantum cascade laser using a room-temperature superlattice

harmonic mixer. *Applied Physics Letters*, *103*(5). doi: https://doi.org/10.1063/1.4817319

Heyminck, S., Graf, U. U., Güsten, R., Stutzki, J., Hübers, H. W., & Hartogh, P. (2012). GREAT: the SOFIA high-frequency heterodyne instrument. *Astronomy and Astrophysics*, *542*(L1). doi: 10.1051/0004-6361/201218811

Higgins, R. D., Teyssier, D., Pearson, J. C., Risacher, C., & Trappe, N. A. (2010). Calibration of the Herschel HIFI instrument using gas cell measurements. proceedings of the 21st International Symposium on Space Terahertz Technology (ISSTT).

Jet Propulsion Laboratory (JPL) database for molecular spectroscopy. (2022). *https://spec.jpl.nasa.gov/.*

Justen, M., Bonzon, C., Ohtani, K., Beck, M., Graf, U., & Faist, J. (2016). 2D patch antenna array on a double metal quantum cascade laser with >90% coupling to a gaussian beam and selectable facet transparency at 1.9THz. *Optics Letters*, *41*(19), 4590-4592. doi: https://doi.org/10.1364/OL.41.004590

Kazarinov, R., & Suris, R. (1971). Possibility of the amplification of electromagnetic waves in a semiconductor with a superlattice. *Soviet Physics-Semiconductors*, *5*(4), 707-709.

Khalatpour, A., Paulsen, A. K., Addamane, S. J., Deimert, C., Reno, J. L., Wasilewski, Z. R., & Hu, Q. (2022). A tunable unidirectional source for GUSTO's local oscillator at 4.74 THz. *IEEE Transactions on Terahertz Science and Technology*, *12*(2), 144-150. doi: https://doi.org/10.1109/TTHZ.2021.3124310

Khosropanah, P., Baryshev, A., Zhang, W., Jellema, W., Hovenier, J. N., Gao, J. R., ... Hesler, J. L. (2009). Phase locking of a 2.7-THz quantum cascade laser to a microwave reference. *Optics Letters*, *34*(19), 2958-2960. doi: https://doi.org/10.1364/OL.34.002958

Khudchenko, A., Hayton, D. J., Pavelyev, D. G., Baryshev, A. M., Gao, J. R., Kao, T.-Y., ... L., V. V. (2014). Phase locking a 4.7-THz quantum cascade laser using a super-lattice diode as harmonic mixer. proceedings of the 39th International Conference on Infrared, Millimeter and Terahertz Waves (IRMMW-THz). doi: http://dx.doi.org/10.1109/IRMMW-THz.2014.6956455

Khudchenko, A., Pavelev, D. G., Vaks, V. L., & Baryshev, A. M. (2018). Overview of techniques for THz QCL phase-locking. proceedings of 3rd Interna-

tional Conference: Terahertz and Microwave Radiation: Generation, Detection and Applications (TERA-2018). doi: 10.1051/epjconf/201819504003

Klein, B., Hochgürtel, S., Krämer, I., Bell, A., Meyer, K., & Güsten, R. (2012). High-resolution wide-band fast Fourier transform spectrometers. *Astronomy and Astrophysics*, *542*(L3). doi: https://doi.org/10.1051/0004-6361/201218864

Kloosterman, J. L., Hayton, D. J., Ren, Y., Kao, T. Y., Hovenier, J. N., Gao, J. R., ... Reno, J. L. (2013). Hot electron bolometer heterodyne receiver with a 4.7-THz quantum cascade laser as a local oscillator. *Applied Physics Letters*, *102*(1). doi: http://dx.doi.org/10.1063/1.4774085

Kooi, J. W. (2008). *Advanced receivers for submillimeter and far infrared astronomy* (PhD thesis). University of Groningen.

Kraus, J. D. (1986). *Radio Astronomy* (2nd ed.). Cygnus-Quasar Books.

Kurtz, S. R. (2022). *Mixers as phase detectors* (Tech. Rep.). The communications edge.

Lakeshore cryotronics. (2017, Jul). *Model 218: Temperature Monitor User's Manual.*

Lakeshore cryotronics. (2023). *DT-670 silicon diode datasheet.*

Lang, R., & Kobayashi, K. (1980). External optical feedback effects on semiconductor injection laser properties. *IEEE Journal of Quantum Electronics*, *16*(3), 347-355. doi: http://dx.doi.org/10.1109/JQE.1980.1070479

Mahdizadeh, S., Graf, U. U., Justen, M., Faist, J., Beck, M., Olariu, T., & Stutzki, J. (2023). Frequency stabilization of a 4.7 THzquantum cascade laser using a delay line frequency discriminator. *IEEE Transactions on Terahertz Science and Technology*, *13*(6). doi: https://doi.org/10.1109/TTHZ.2023.3320948

Mahdizadeh, S., Graf, U. U., Justen, M., & Stutzki, J. (2022). Frequency locking of a 4.7 THz quantum cascade laser using a delay line. proceedings of the 32nd International Symposium on Space Terahertz Technology (ISSTT).

Maiwald, F., Drouin, B. J., Pearson, J. C., Mehdi, I., Lewen, F., Endres, C., & Winnewisser, G. (2005). Planar diode multiplier chains for THz spectroscopy. proceedings of 16th International Symposium on Space Terahertz Technology (ISSTT).

Minicircuits. (2004, Feb). *SRA-1W+: level 7, plug-in double balanced mixer datasheet.*

Ohtani, K., Turčinková, D., Bonzon, C., Benea-Chelmus, I.-C., Beck, M., Faist, J., ... Stutzki, J. (2016). High performance 4.7 THz GaAs quantum cascade lasers based on four quantum wells. *New Journal of Physics*, *18*(12). doi: 10.1088/1367-2630/18/12/123004

Oppenheim, A. V., Willsky, A. S., & Nawab, S. H. (1996). *Signals and Systems* (2nd ed.). Prentice Hall.

Paveliev, D., Koshurinov, Y. I., Ivanov, A. S., Panin, A. N., Vax, V. L., Gavrilenko, V. I., ... Zhukov, A. E. (2012). Experimental study of frequency multipliers based on a GaAs/AlAs semiconductor superlattices in the terahertz frequency range. *Physics of Semiconductor Devices*(46), 121-125. doi: https://doi.org/10.1134/S1063782612010150

Paveliev, D. G., Koschurinov, Y. I., Ustinov, V. M., Zhukov, A. E., Lewen, F., Endres, C., ... Hübers, H.-W. (2008). Short GaAs/AlAs superlattices as THz radiation sources. proceedings of the 19th International Symposium on Space Terahertz Technology (ISSTT).

Pavelyev, D. G., Vasilev, A. P., Kozlov, V. A., Obolenskaya, E. S., Obolensky, S. V., & Ustinov, V. M. (2018). Increase of self-oscillation and transformation frequencies in THz diodes. *IEEE Transactions on Terahertz Science and Technology*, *8*(2), 231-236. doi: 10.1109/TTHZ.2017.2785043

Pavelyev, D. G., Vasilev, A. P., Kozlov, V. A., Obolensky, E. S., Obolensky, S. V., & Ustinov, V. M. (2017). The diode heterostructures for THz devices. proceedings of the 28th International Symposium on Space Terahertz Technology (ISSTT).

Petermann, K. (1988). *Laser Diode Modulation and Noise*. Kluwer Academic Publishers, Advances in Optoelectronics (ADOP) series.

Philipp, M., Graf, U., Wagner-Gentner, A., Rabanus, D., & Lewen, F. (2007). Compact 1.9 THz BWO local-oscillator for the GREAT heterodyne receiver. *Infrared Physics and Technology*, *57*(1), 54-59. doi: https://doi.org/10.101/j.infrared.2006.10.034

P. Minguzzi, P., Tonelli, M., Carrara, G., & di Lieto, A. (1985). CH3OH and CH3 81Br self-broadening measurements with a millimeter-wave stark interferometer. *Journal of Molecular Spectroscopy*, *102*(2), 395-401. doi: https://doi.org/10.1016/0022-2852(85)90322-4

Pozar, D. M. (2005). *Microwave Engineering* (1st ed.). John Wiley and Sons.

product note 11729C-2. (1985). *Phase noise characterization of microwave oscillators* (Tech. Rep.). Hewlett Packard.

Rabanus, D., Graf, U. U., Philipp, M., Ricken, O., Stutzki, J., Vowinkel, B., ... Faist, J. (2009). Phase locking of a 1.5 terahertz quantum cascade laser and use as a local oscillator in a heterodyne HEB receiver. *Optics Express*, *17*(3), 1159-1168. doi: https://doi.org/10.1364/OE.17.001159

Ravaro, M., Jagtap, V., Manquest, C., Gellie, P., Santarelli, G., Sirtori, C., ... Barbieri, S. (2013). Spectral properties of THz quantum-cascade lasers: Frequency noise, phase-locking and absolute frequency measurement. *Journal of Infrared, Millimeter and Terahertz Waves*, *34*, 342-356. doi: 10.1007/s10762 -013-9981-7

Ren, Y., Hayton, D. J., Hovenier, J. N., Cui, M., Gao, J. R., Klapwijk, T. M., ... Reno, J. L. (2012). Frequency and amplitude stabilized terahertz quantum cascade laser as local oscillator. *Applied Physics Letters*, *101*(10). doi: https:// doi.org/10.1063/1.4751247

Ren, Y., Hovenier, J. N., Cui, M., Hayton, D. J., Gao, J. R., Klapwijk, T. M., ... Reno, J. L. (2012). Frequency locking of single-mode 3.5THz quantum cascade lasers using a gas cell. *Applied Physics Letters*, *100*(4). doi: https://doi.org/ 10.1063/1.3679620

Renk, K. F., Rogl, A., Stahl, B. I., Meier, A., Koschurinov, Y., Pavel'ev, D., ... Vasilyev, A. (2006). Semiconductor-superlattice frequency mixer for detection of submillimeter waves. *International Journal of Infrared and Millimeter Waves*, *27*, 373-380. doi: https://doi.org/10.1007/s10762-006-9074-y

Renk, K. F., & Stahl, B. I. (2011). Operation of a semiconductor superlattice oscillator. *Physics Letters A*, *375*(27), 2644-2651. doi: https://doi.org/10.1016/ j.physleta.2011.05.038

Renk, K. F., Stahl, B. I., Rogl, A., Janzen, T., Pavel'ev, D. G., Koshurinov, Y. I., ... Zhukov, A. (2005). Subterahertz superlattice parametric oscillator. *Physical Review Letters*, *95*(12). doi: https://doi.org/10.1103/PhysRevLett.95.126801

Rezac, L., Hartogh, P., Güsten, R., Wiesemeyer, H., Hübers, H. W., Jarchow, C., ... Netty, H. (2015). First detection of the 63 μm atomic oxygen line in the thermosphere of Mars with GREAT/SOFIA. *Astronomy and Astrophysics*, *580*(L10). doi: https://doi.org/10.1051/0004-6361/201526377

Richter, H., Greiner-Bär, M., Günther, B., Rösner, K., & Hübers, H.-W. (2010). A 4.7-THz gas laser local oscillator for GREAT on SOFIA. proceedings of the 21st International Symposium on Space Terahertz Technology (ISSTT).

Richter, H., Pavlov, A. D., S. G. Semenov, Mahler, L., Tredicucci, A., Beere, H. E., Ritchie, D. A., & Hübers, H. W. (2010). Submegahertz frequency stabilization of a terahertz quantum cascade laser to a molecular absorption line. *Applied Physics Letters*, *96*(7). doi: https://doi.org/10.1063/1.3324703

Richter, H., Wienold, M., Schrottke, L., Biermann, K., Grahn, H. T., & Hübers, H.-W. (2015). 4.7-THz local oscillator for the GREAT heterodyne spectrometer on SOFIA. *IEEE Transactions on Terahertz Science and Technology*, *5*(4), 539-545. doi: 10.1109/TTHZ.2015.2442155

Risacher, C., Güsten, R., Stutzki, J., Hübers, H.-W., Bell, A., Buchbender, C., ... Wiesemeyer, H. (2016). The upGREAT 1.9 THz multi-pixel high resolution spectrometer for the SOFIA observatory. *Astronomy and Astrophysics*, *595*(A34). doi: https://doi.org/10.1051/0004-6361/201629045

Risacher, C., Güsten, R., Stutzki, J., Hübers, H.-W., Büchel, D., Graf, U. U., ... Rosner, S. (2016). First supra-THz heterodyne array receivers for astronomy with the SOFIA observatory. *IEEE Transactions on Terahertz Science and Technology*, *6*(2), 199-211. doi: 10.1109/TTHZ.2015.2508005

Robins, W. P. (1991). *Phase Noise in Signal Sources* (2nd ed.). Peter Peregrinus Ltd.

Rohde und Schwarz. (2019). *SMF100A Microwave Signal Generator Specifications.*

S. Weinreb. (2009, Oct). *CITLF4: cryogenic SiGe low noise amplifier datasheet.*

Schomburg, E., Brandl, S., Hofbeck, K., Blomeier, T., Grenzer, J., Ignatov, A. A., ... Kop'ev, P. S. (1998). Generation of millimeter waves with a GaAs/AlAs superlattice oscillator. *Applied Physics Letters*, *72*. doi: https://doi.org/10.1063/1.121038

Schrottke, L., Lü, X., Röben, B., Biermann, K., Hagelschuer, T., Wienold, M., ... Grahn, H. T. (2020). High-performance GaAs/AlAs terahertz quantum-cascade lasers for spectroscopic applications. *IEEE Transactions on Terahertz Science and Technology*, *10*(2), 133-140. doi: http://dx.doi.org/10.1109/TTHZ.2019.2957456

Slocum, D. M., Xu, L.-H., Giles, R. H., & Goyette, T. M. (2015). Retrieval of methanol absorption parameters at terahertz frequencies using multispectral fitting. *Journal of Molecular Spectroscopy*, *318*, 12-25. doi: http://dx.doi.org/10.1016/j.jms.2015.09.008

Stutzki, J., & Güsten, R. (2022). Velocity resolved [CII] observations - a 40 year long story. Proceedings of the 7th Chile-Cologne-Bonn symposium.

Sumitomo Heavy Industries (SHI). (2023). *Cryocooler product catalogue.*

Thompson, A. R. (1979). *VLA electronics memorandum no. 180: Phase lock loop parameters of f2 and f3 modules* (Tech. Rep.). National Radio Astronomy Observatory.

van Marrewijk, N., Mirzaei, B., Hayton, D., Gao, J. R., Kao, T. Y., Hu, Q., & Reno, J. L. (2015). Frequency locking and monitoring based on bi-directional terahertz radiation of a 3rd-order distributed feedback quantum cascade laser. *Journal of Infrared, Millimeter, and Terahertz Waves*, *36*, 1210-1220. doi: https://doi.org/10.1007/s10762-015-0210-4

VDI. (2009, Mar). *VDI-AMCS177: 1 THz amplified multiplier chain datasheet.*

Virginia Diodes, Inc. (2022). *https://www.vadiodes.com/en/.*

Ward, J., Schlecht, E., Chattopadhyay, G., Maestrini, A., Gill, J., Maiwald, F., ... Mehdi, I. (2004). Capability of thz sources based on schottky diode frequency multiplier chains. proceedings of the IEEE MTT-S International Microwave Symposium Digest. doi: https://doi.org/10.1109/MWSYM.2004.1338884

Wehres, N., Maßen, J., Borisov, K., Schmidt, B., Lewen, F., Graf, U. U., ... Schlemmer, S. (2018). A laboratory heterodyne emission spectrometer at sub-millimeter wavelengths. *Physical Chemistry Chemical Physics*, *20*, 5530-5544. doi: http://dx.doi.org/10.1039/C7CP06394F

Wilson, T. L., & Rohlfs, K. (1996). *Tools of Radio Astronomy* (2nd ed.). Springer-Verlag.

Wolaver, D. H. (1991). *Phase-Locked Loop Circuit Design* (1st ed.). Prentice Hall.

Zhang, W., Khosropanah, P., Hovenier, J. N., Gao, J. R., Bansal, T., Klapwijk, T. M., ... Faist, J. (2008). Towards detection of OH line at 3.5 THz using a HEB mixer and a distributed feedback quantum cascade laser. proceedings of the 19th International Symposium on Space Terahertz Technology (ISSTT).